Computational and Experimental Study on Conversion of Biogas into Valuable Fuels and Useful Chemicals Using Non-thermal Plasma

by

Chao Xu

Thesis submitted for the degree

Of

Doctor of Philosophy

Department of Electrical Engineering and Electronics

Liverpool, November 2018

Declaration

Chao Xu declares that this thesis is his own work. All the reproduced and cited contents have been acknowledged in the references. Neither this thesis nor any part of it have been submitted to any other university or institution for the application of another degree or qualification.

Liverpool, August, 2017

Signature:

Acknowledgement

I would like to gratefully thank my primary supervisor Prof. Xin Tu for his guidance and support during the full course of this project. Prof. Xin Tu's overwhelming support and enthusiasm as well as constructive suggestions are essential and inestimable for completing my PhD project.

I would like to gratefully thank my internal examiner Prof. James Walsh for his recommendations and suggestions on the viva and correcting list of my thesis. Prof. James Walsh's constructive suggestions are very important for completing my PhD thesis.

I would like to gratefully thank my external examiner Prof. Meihong Wang for his recommendations and suggestions on my thesis. Prof. Meihong Wang's constructive suggestions are very important for completing my PhD project.

I would like to thank Dr. Yuxuan Zeng for his help with discussion on the academic problems, and the suggestions on the manuscripts of my thesis.

I would like to thank Dr. Weizong Wang for his help with discussion on the problems about modelling of chemical reactions.

I would like to thank the members of my research group, Dr. Danhua Mei, Dr. Li Wang, Dr. Hao Zhang, Shiyun Liu, Yichen Ma, Jia Sun, Fengsen Zhu, Yuxing Tian for their important assistances on my work.

List of Publications

Y. Yi, C. Xu, L. Wang, J. Yu, Q. Zhu, S. Sun, X. Tu, C. Meng, J. Zhang, H. Guo. "Selectivity control of H_2/O_2 plasma reaction for direct synthesis of high purity H_2O_2 with desired concentration", *CHEMICAL ENGINEERING JOURNAL*, 313:37-46, 2017. In this work, I co-operated with Dr. Yi. to investigate the optimum operating conditions for synthesis of H_2O_2¸while I focused on the simulation works to calculate the mean electron energy and electron density, and to define the possible pathways of generation of H_2O_2.

L. Wang, S.Y. Liu, C. Xu, X. Tu. "Direct conversion of methanol to n-C_4H_{10} and H_2 in a dielectric barrier discharge reactor", *GREEN CHEMISTRY*, 18(20):5658-5666, 2016. In the co-operation with Dr. Wang, I calculated the electron density, electron energy and densities of the related species (i.e. CH_3) to explain the mechanism of generation of n-C_4H_{10}.

C. Xu, X. Tu, "Plasma-assisted methane conversion in an atmospheric pressure dielectric barrier discharge reactor", *Journal of Energy Chemistry*, 22(3):420-425, 2013. This was the first research of my PhD study, so my supervisor Prof. Xin Tu helped me perform the experiments to investigate the effects of the operating conditions (i.e. discharge power and residence time) on conversion of CH_4 in a DBD reactor at atmospherics pressure.

Abstract

This project has studied reforming of biogas into fuels and valued chemicals using non-thermal plasma through experiments and simulations. CH_4, CO_2 and H_2 are used as the inlet gas. All simulation results have been validated by the experimental results. Different reactions which are relevant to reforming of biogas, including pure CO_2 splitting, hydrogenation of CO_2, dry reforming of CH_4 and steam reforming of CH_4, have been investigated and the mechanisms of them have been clearly defined by the simulations. The overall aim of this project is to investigate the effects of the different operating conditions, including discharge power, residence time, compositions of inlet gas, etc., on conversion of biogas and reaction pathways for the desired products in a dielectric barrier discharge (DBD) reactor.

The major challenge to simulate DBD plasma-assisted reactions is the power description. Apart from the existing researches, the project raises a novel method to describe the DBD plasma power using the technique of advanced signal process. All simulations in this project are performed in a Fortran 90 language environment using the ZDPlaskin.

Vibrational excitations of CO_2 play significant roles in CO_2 splitting and their contributions to decompose CO_2 are enhanced with an increasing discharge power. In terms of hydrogenation of CO_2, a higher H_2/CO_2 ratio has a positive effect on conversion of CO_2. The mechanism to generate CH_4 is difficult to be defined by the common method based on sensitivity analysis due to the slow generation of CH_4, so a reverse educing method is used to summarise the pathways of the hydrogeneration process. Besides, C_2H_2 and C_2H_6 are the major gas-products observed in dry reforming methane. According to the simulations, 60.3% of CH_3 radicals are consumed by recombination to produce C_2H_6, while more than 99% of CH_2 radicals are consumed by oxidisation reactions to generate aldehydes. This project also investigates the steam reforming of methane in a high/low steam environment. By doping deuterium, in form of D_2O, into the DBD reactor, a compound-specific isotope analysis (CISA) is performed to identify the contributions of methane and steam to produce hydrogen gas and trace the radicals released from steam to define a clearer and more accurate mechanism.

List of Figures

List of Tables

List of Abbreviations

DBD	Dielectric barrier discharge
DRM	Dry reforming of methane
SRM	Steam reforming of methane
AD	Anaerobic digestion
MSW	Municipal solid waste
WGS	Water gas shift reaction
RWGS	Reverse water gas shift reaction
MR	Membrane reactor
GHGs	Greenhouse gases
GTL	Gas to liquid
LTE	Local thermodynamic equilibrium
LPG	Liquefied Petroleum Gas
GD	Glow discharge
DC	Direct current
AC	Alternating current
RF	Radio frequency
GA	Gliding arc
MW	Microwave
ATRB	Autothermal reforming of biogas
SRB	Steam reforming of biogas
DRB	Dry reforming of biogas
GHSV	Gas hourly space velocity
WHSV	Weight hourly space velocity
OSC	Oxygen storage capacity
SDC	samaria doped ceria
0D	0-dimensional
1D	1-dimensional
2D	2-dimensional
DFT	Density functional theory
MD	Molecular dynamics
EEDFs	Electric energy distribution functions

VOCs	Volatile organic compounds
MFC	Flow rate controller
TCD	Thermal conductivity detector
FID	Flame ionisation detector
GC	Gas chromatograph
VV	Asymmetric vibrational excitation modes of CO_2
VT	Symmetric vibrational excitation modes of CO_2
BE	Boltzmann equation
CISA	Compound-specific isotope analysis

Nomenclature

ΔH	Enthalpy
λ	Mean free path
n	Gas density
n_e	Electron density
σ	Collisional cross section
σ_k	Cross section of the target particle
σ_m	Total momentum-transfer cross section
r_1, r_2	Radii of colliding partner
α	1st Townsend ionisation coefficient
E	Electrical field
C_k	Gas composition
k_{ion}	Ionisation rate coefficient
E/n	Reduced electric field
p	Gas pressure
eV	Electron volt
T_e	Electron temperature
T_v	Temperature of vibrationally excited molecule
T_g	Gas temperature
T_0	Temperature of neutral particle
T_i	Temperature of ion
ε_{glass}	Dielectric constant of glass
ε_{vacuum}	Dielectric constant of vacuum
ε_{air}	Dielectric constant of air
$\varepsilon_{plasma\text{-}gas}$	Dielectric constant of plasma gas
ε_0	Dielectric constant of barrier
ε_p	Permittivity of barrier
V_b	Breakdown voltage
f	Function of electron energy distribution
m	Electron mass
q	Elementary charge
v	Mean electron velocity

$C[f]$	Change rate of the electron energy distribution function
$N_{i=1\ldots i\max}$	Dynamic densities for species in plasma
Q_{ij}	Source term to describe contribution from each diverse reaction
t	Time
R	Reaction rate
k_j	Reaction rate constants for reactions in plasma
A_j	Pre-exponential factor
B_j	Temperature factor
E_j	Activation energy
C_d	Capacitance of coaxial barrier
C_g	Capacitance of gas
L	Discharge length
a	Inner diameter of coaxial barrier
b	Outer diameter of coaxial barrier
U_g	Gas voltage
U_a	Applied voltage
U_d	Voltage on external capacitor
$I_\mathrm{t,a}$	Total current
$I_\mathrm{p,g}$	Discharge current
$I_\mathrm{v,g}$	Displacement current
T_s	Sampling period
ω_s	Sampling frequency
ω_m	Frequency of signal
ω_c	Cut-off frequency
$P(t)$	Discharge power
X	Conversion rate
η	Energy efficiency
S	Selectivity
Y	Yield
$\hbar\omega_i$	Quantum energy
$\mathrm{M}_{(\mathrm{R})}$[a]	Rotational excited molecule
$\mathrm{M}_{(\mathrm{v})}$[a]	Vibrational excited molecule
$\mathrm{M}_{(\mathrm{e})}$[a]	Electronic excited molecule

E_v	Energy of vibrational excited molecule
ω_i x_{ij}	Spectroscopic constants
d	Degeneracies of the vibrational excitation
l_2	Special quantum number
z	Position coordinate
f_0	Isotropic perturbation
f_1	Anisotropic perturbation
x_k	Mole faction of target particle
$\overline{v}_i$	Net production frequency
D	Diffusion coefficient
μ	Mobility of electron
α_r	Spatial growth rate of electron
θ	Dihedral angle
x_p	Total proportion of hydrocarbons and carbohydrates containing deuterium element

a: M stands for a molecule (i.e. CO_2, CH_4, etc.).

Chapter 1: Introduction

1.1 Aim of the work and outline of the thesis

The aim of this PhD dissertation is to contribute to the central research on conversion of biogas into value-added chemicals and/or fuels using non-thermal plasma. The entire process is very complex and requires a multidisciplinary and integrated approach, involved in plasma chemistry, electrical engineering, materials science, etc, so it is necessary to focus on obtaining answers to some questions related to specific aspects of this process. Many researches in this area are still based on assumptions of the plasma and chemical processes, especially for revealing mechanism of a plasma-assisted reaction. Therefore, modelling is an important tool to investigate reaction mechanism and even more importantly to enhance the existing experiments.

This PhD work began with an experiment on conversion of methane in a dielectric barrier discharge (DBD) reactor, while some of the results of that work/paper were explained by assumptions and the reaction mechanism was difficult to be defined. Therefore, I realised that this PhD work required more theoretical knowledge of plasma chemistry and swerved the research orientation to modelling of reactions in DBD reactors to obtain a better understanding of plasma-assisted reforming of biogas after the 1st year of my PhD study.

In **Chapter 2**, a literature review of the reforming of biogas is made to understand the achievements and limits in this area. Through the literature review, higher conversion rates of CH_4 and CO_2 have the positive effects on the reforming process. Therefore, this PhD, afterwards, investigates the different processes to convert CH_4 and CO_2.

Reaction mechanism cannot be defined without simulations which can identify the most important reactions during the entire reforming process, while experiments can validate whether the model used for simulations is accurate or not. Both the models and experiments will be described in **Chapter 3**.

The first step to study on the DBD plasma-assisted reforming of biogas is taken through the research on CO_2 splitting in **Chapter 4**, where the effects of discharge power, inlet flow rate and discharge length are investigated. Attention is mainly focused on the influence of excited CO_2 on the conversion of CO_2.

Chapter 5 investigates the process of the combined conversion of CO_2 and H_2, so-called hydrogenation, in a DBD reactor. The mechanism is concluded by the investigation of important species and reverse educing method through several sub-sensitivity analysis.

In **Chapter 6**, the work investigates dry reforming of methane (DRM) in a DBD reactor. The effects of discharge power and the most active radicals are analysed through simulations and experiments. Based on these results, the mechanism of DRM is clearly defined.

Finally, a study on steam reforming of methane (SMR) in a DBD reactor is performed, in **Chapter 7**. This is done in two stages. Firstly, the concentration of steam is set to a low value to investigate the effect on discharge power of the SMR process. Secondly, a new mechanism is defined when the concentration of steam is increased. Deuterium is used to identify the proportion of hydrogen production generated from the steam. These four main processes are performed to draw conclusions and provide a better understanding of the reaction mechanisms of DBD plasma-assisted reforming of biogas.

1.2 Prospect and background of conversion of biogas

Currently, serious environmental pollution is an issue which cannot be underestimated and should be solved urgently. The pollutants are mainly from animal manure, sewage sludge, municipal solid waste (MSW), etc. Fermentation and Anaerobic Digestion (AD) of the biodegradable organics can be considered as the suitable and effective treatments for those biological wastes, while biogas is the indispensable product of these two processes [1-3]. The contents of biogas are summarised in **Table 1.1** and it is obvious that CH_4 and CO_2 are the two major compounds of biogas.

Table 1.1 The major composition of biogas [3, 4].

Composition	Chemical Formula	
Methane	CH_4	40-70 (%vol)
Carbon dioxide	CO_2	29-41 (%vol)
Nitrogen	N_2	0-15 (%vol)
Hydrogen sulfide	H_2S	0-2000 (ppm)
Oxygen	O_2	0-2.9 (%vol)

There is an ever-increasing demand for a sustainable power source, instead of the non-renewable fossil sources. Biogas is renewable and can be combusted as a fuel directly for heating and producing electricity. Compared with another prospective fuel – "H_2", firstly, storage and transportation of biogas are much easier [5, 6]. As such, biogas is a suitable source for hydrogen fixation. Secondly, as mentioned above, biogas is eco-friendly and the generation of it reduces soil and water pollution [7]. Thirdly, the by-product of biogas generation (i.e. organic fertiliser with lower toxic effect) is also valuable [8, 9]. Finally, the reason why biogas is considered as a promising fuel is that the generation of biogas is simple and low-cost [10, 11], and the process is illustrated in **Figure 1.1**.

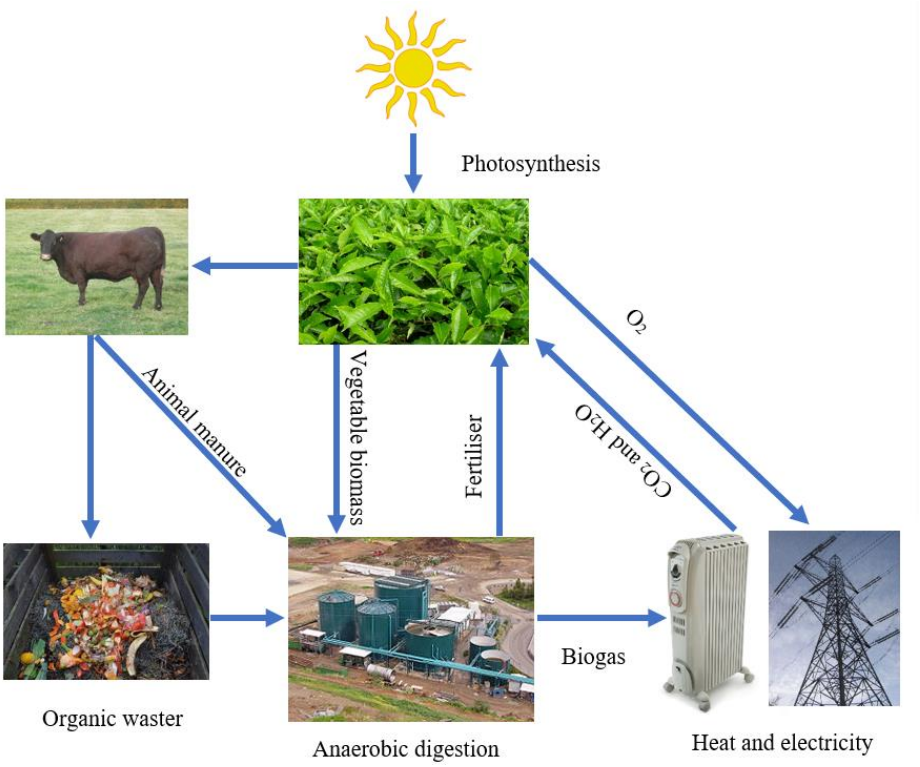

Figure 1.1 Schematic of biogas generation [4, 8, 11].

The equipment used to generate biogas is very easy to set up, causing a small scale of investment. The cost for collecting the organic waste, including, the household waste and animal manure, is relatively low [2]. The biochemical pathways rely on the natural photosynthesis which converts light into biomass [12]. Obviously, all the raw materials for biogas reforming are cheap and renewable. The combustion process of biogas is clean, and the products are H_2O and CO_2 which are important for photosynthesis [13]. Instead of over an open fire, cooking on a gas stove can prevent the respiratory disease [14-16].

An unfortunate disadvantage of biogas is that the biogas generation is not efficient [17]. Many governments are not that interesting on the recaches on new technologies of biogas generation. Therefore, the production of biogas cannot supply for a large population. Moreover, compared with H_2, the purity of biogas cannot be guaranteed, because of the impurities [18, 19]. The impurities (i.e. sulphide) may corrode some metal parts of the engine. In addition, H_2 used in industry is mostly generated by the chemical reactions (i.e. water gas shift reaction, WGS) with the controllable operating conditions, while the biogas generation, nowadays, is still based on the AD process which is dramatically relied on the weather [19, 20].

The impact of weather to generate biogas using a biochemical method is difficult to be controlled currently. However, the issue of the impurities of biogas can be solved by reforming of biogas into H_2 fuel and valuable chemicals. To reforming biogas efficiently, it is worthy to conduct researches on the conversions of the major contents of biogas which are CH_4 and CO_2.

1.3 Conversion of CO_2

The energy-related CO_2 emission has been reported of ~32.2 Gt in 2016 across the world and it has increased by more than 7 Gt from 2010. Therefore, America pledges to reduce the greenhouse gases (GHGs) emissions by 26 - 28 % by 2015 compared with the levels of 2005, while the EU promises to cut emission of GHGs by at least 40 % by 2030 [21].

1.3.1 Pure CO_2 splitting

The chemical structure of CO_2 is stable with the dissociation energy of ~178 kcal/mole (7.6 eV) [22]. Therefore, conversion of CO_2 using traditional thermal method is not very efficient, considering about the commercial benefit. On one hand, the required energy is fairly high (operating temperature > 2500 K) and the maximum conversion rate of CO_2 is lower than 20 % (based on the thermal equilibrium calculation) [23]. On the other hand, the reverse reaction among products of CO_2 splitting (i.e. $2CO + O_2 \rightarrow 2CO_2$) can restrict CO_2 conversion under that high temperature [24-38]. The overall reaction of CO_2 splitting is written as:

$$CO_2(g) \rightarrow CO(g) + \tfrac{1}{2} O_2(g), \Delta H = +283 \text{ kJ/mol} \quad (1.1)$$

The high value of the enthalpy, ΔH, determines that CO_2 splitting is a strongly endothermic chemical reaction. The equilibrium of this reaction lies strongly to the left without removing

one of the products: CO or O_2 [23]. There is no an effective technology to separate CO and O_2 at high temperature to avoid the occurrence of the reverse reaction. Therefore, the thermal-catalytic CO_2 splitting is difficult to be applied on the industrial scale [23, 39].

Non-thermal plasma is a preeminent source for CO_2 conversion to provide (re)active species, such as ions and radicals, under a much lower temperature. Many different types of plasma used for CO_2 splitting have been reported, including DBD, microwave discharge, as well as gliding arc discharges [40-43]. However, the researches based on simulations to investigate the effects of electron energy, electron density and (de)excitations on CO_2 splitting are few.

1.3.2 Hydrogenation

The other feasible method to convert CO_2 is hydrogenation of CO_2 which is thermodynamically process written as:

$$CO_2(g) + 4H_2(g) \rightarrow CH_4(g) + 2\ H_2O(g),\ \Delta H^0 = -165.3\ kJ/mol \quad (1.2)$$

CH_4 is one of the products during the hydrogenation process. Currently, 95 % of the H_2 production is generated from the SMR process, causing a problematic flawed loop [44]. Therefore, the commercial benefit of the hydrogenation process cannot be improved unless H_2 can be effectively produced from a renewable source (i.e. biogas).

Except for CH_4, methanol is also the value-added product of the hydrogenation process. In industry, the annual production of methanol by using this process is around 70 M metric tons (in 2015) and the relevant reactions are [45-47]:

$$CO_2(g) + H_2(g) \rightarrow CO(g) + H_2O(g),\ \Delta H = +40.9\ kJ/mol \quad (1.3)$$

$$CO_2(g) + 2H_2(g) \rightarrow CH_3OH(g),\ \Delta H = -90.8\ kJ/mol \quad (1.4)$$

$$CO_2(g) + 3H_2(g) \rightarrow CH_3OH(g) + H_2O(g),\ \Delta H = -49.9\ kJ/mol \quad (1.5)$$

Equation 1.5 determines the overall reaction of CO_2 hydrogenation to produce methanol which is an exothermic process. Equation 1.3 is well-known as the reverse water gas shift reaction (RWGS) which can be considered the activation of CO_2 [47]. The generated CO by RWGS will further react with H_2 to produce CH_3OH. Obviously, doping metals which often are used as the catalysts in the RWGS reaction can promote the CO_2 hydrogenation [48].

1.4 Conversion of CH_4

The structure of CH_4, known as the simplest alkane and organic, is in tetrahedral with four C-H covalent bonds with different dissociation energies which are 104 kcal/mole (CH_3-H), 106 kcal/mole (CH_2-H), 106 kcal/mole (CH-H) and 81 kcal/mole (C-H), respectively [49, 50]. In the view of the dissociation energies, conversion of CH_4 is easier to be ignited using thermal catalytic method, compared with conversion of CO_2. Moreover, the conversion rate can reach ~20 % (maximum) under 500 K, while the operating temperature is usually over 700 K to maximise the conversion of CH_4 [51]. Currently, the most adopted processes for conversion of CH_4 are DRM and SRM. Certainly, these processes are often combined to achieve the steam-CO_2 dual reforming of CH_4 [52, 53]. People have paid more attentions on plasma-catalytic conversion of CH_4 in the last decade. Plasma could break any chemical bond to produce lots of radicals. With the increasing of the variety of products (i.e. hydrocarbons, aldehydes, alcohols and acids), the selectivity of desired product(s) becomes more significant.

1.4.1 Steam reforming of methane

The SMR process is mature and leading technique for hydrogen production in industry under harsh operating conditions [54] and the relevant reaction is written as:

$$CH_4(g) + H_2O(g) \rightarrow CO(g) + 3H_2(g),\ \Delta H^0 = +206\ kJ/mol \quad (1.6)$$

Usually, after the reforming process (under 800-1000 ^oC and 1.5-2.0 MPa), the outlet gas still needs to pass two WGS reactors for removal of CO, because CO could poison the catalyst [55-57]. With development of membrane reactors (MR), SMR can be performed under relative milder operating conditions at a much lower operating temperature (500-600 ^oC). Additionally, the selectivity of H_2 can be effectively enhanced by using Pd-based in a MR [58-61].

1.4.2 Dry reforming of methane

The combined conversion of CH_4 and CO_2 is also known as DRM. Apart from SMR, CO_2 is an oxidised and thermodynamic stable molecule. Hence, DRM requires a higher operating temperature and can be written as:

$$CH_4(g) + CO_2(g) \rightarrow 2\ CO(g) + 2H_2(g),\ \Delta H^0 = +247\ kJ/mol \quad (1.7)$$

The traditional DRM has been investigated for many years, and the selectivity of H_2 can reach more than 80 %, while the operating temperature is usually increased up to more than 700 ^oC to accomplish high-performance DRM with a certain catalyst (i.e. supported nickel with(out) different promoters and bimetallic metals [62-64]. Moreover, formation of coke is an important reason why DRM cannot be applied in industrial scale to produce H_2 [65-68].

1.5 Target chemicals of biogas reforming

The most important product of biogas reforming is synthesis gas (syngas), consisting of H_2 and CO. H_2 of syngas is a renewable and clean fuel. Except for directly using as a fuel, H_2 is a very important raw material for the industrial applications, such as metallurgy and ammonia synthesis [69-71].

Syngas can be used in fuel cell, which converts the chemical energy of fuels to electric energy through redox reactions [72], while it can also be converted to useful chemicals in liquid phase through Gas-To-Liquid (GTL) process. The most famous application of GTL is the Fischer-Tropsch process to produce hydrocarbons, methanol, acetone and Liquefied Petroleum Gas (LPG) which is clean and provides a lower viscosity and longer life-time [73-81]. The GTL process is a derivative of biogas reforming and completely renewable, whereas it also contributes to reduce the GHGs indirectly.

1.6 Plasma

The term “plasma” was first introduced by Irving Langmuir in the 1928 [82]. With the increasing temperature, molecules exist in the different phase: solid, gas, liquid and the fourth state of matter – plasma [83]. Plasmas, consisting of balanced charges of ions and electrons, occur in either nature or the laboratory (natural: stars, solar wind, solar, etc.; man-made: glow discharge, gliding arc, DBD, etc.). Typically, the electron temperatures of most plasma are from 1 eV to 20 eV (1eV = 11,600 K) with the electron density in the range of 10^6 -10^{18} cm^{-3}. Electrons are the first part of elements receiving the energy from electric field during mean free path, λ, which defines the distance of an electron released from an electrode passing through the plasma gas without any colliding with the other particles [83].

$$\lambda = \frac{1}{n\sigma} \tag{1.8}$$

where n is the gas density, σ is the collisional cross section which is equal to π ($r_1 + r_2$), while r_1 and r_2 are the radii of colliding particles.

Accelerated electrons distribute energy to the other particles, whereas the first step for ionisation is to ionise neutral species (i.e. atoms, molecules and radicals) into ions [83]. Consequently, electron density, electron temperature and energy distribution, can strongly affect the plasma, and the ions would be the second feature of the plasma. Most of plasma involve in Townsend mechanism which is the electron avalanche produced by a single electron released from cathode (equation 1.9) [84].

$$\frac{\alpha}{n} = f(\frac{E}{n}, Ck) \tag{1.9}$$

Where α is the first Townsend ionisation coefficient, E is electric field, and C_k represents gas composition. Additionally, α can also be defined by the ionisation rate coefficient k_{ion}, reduced electric field (E/n) and the electron mobility μ_e (equation 1.10) [83]:

$$\alpha = \frac{1}{\mu_e}\frac{k_{ion}(E/n)}{E/n} \tag{1.10}$$

Based on the degree of ionisation, man-made plasma can be distinguished into two major groups. The first group is the high-temperature plasmas, so called fusion plasmas, which are completely ionised, while the main applications of them are tokomaks, stellarators, plasma pinches, focuses, etc [83]. This project studies on the second group which consists of the weakly ionised plasmas, providing a suitable environment for chemical reactions.

Beside the degree of ionisation, plasmas can also be divided into thermal and non-thermal plasmas. The criterion to classify them is based on whether the plasma is in thermal equilibrium and will be discussed later in the next section.

1.6.1 Thermal plasma

The plasma temperature is mainly defined by the average energy of heavy particles and electrons and the value of $(\frac{E}{p})^2$, where p is the total pressure of plasma gas [83]. In addition, only if the value of E/p is small, the temperature of electrons and particles will approach to each other, causing local thermodynamic equilibrium (LTE) [83]. For the thermal plasma, the temperatures of all species are almost same and in the LTE state. The LTE can be achieved by

the different methods (with a higher gas temperature or a lower mean electron temperature). One of them is to generate plasma at a high temperature (4,000 K to 20,000 K), while the other method is to increase the gas pressure of plasma. As mentioned above, electrons receive energy from the electric field during the mean free path and lose a portion of energy through the collisions with heavy particles. The transfer of Joule heating occurs during this collision process at the same time [83]. A high gas temperature increases the temperatures of all species in plasma, so the temperatures of heavy particles and electrons can be equilibrated to reach LTE. A lower electron temperature can be obtained at a high gas pressure. When the density is high, the mean free path becomes shorter, leading to a lower electron energy received from the electric field. In addition, electrons lose more energy with the increment of collisions.

The advantages of thermal plasmas are its high temperature, high intensity non-ionising radiation and high energy density [83, 85]. Because the thermal plasmas can reach the temperature of 20,000 K, they are already used for many applications (i.e. coating technology, fine powder synthesis, etc) [85]. However, some reactions (i.e. DRM) are still difficult to be performed using the thermal plasma-assisted technique, because the operating temperature is high, causing deactivation of the catalysts, and the reactions still occur in the LTE.

1.6.2 Non-thermal plasma

Electrons and heavy particles in non-thermal plasmas or cold plasma are far from the LTE [83]. Based on value of E/p, non-thermal plasmas can be achieved by either high electric field or low gas pressure. A longer mean free path provided by a low gas density and higher electric field are important to increase electron temperature. There exist many different species in non-thermal plasmas with the individual temperature, and the temperature of electron (T_e) is the highest, followed by the vibrationally excited molecules (T_v). Moreover, the temperatures of gas (T_g), neutral species (T_0) and ions (T_i) are approximately same. Therefore, the order of them can be written as: $T_e >> T_v > T_g \approx T_0 \approx T_i$. For most non-thermal plasmas, the electron temperature is in the range of 1eV to10 eV, while the gas temperature can remain near to the ambient temperature [83].

Because of the high electron temperature of non-thermal plasmas, (re)active species can be generated through the electron-impact dissociation and excitation. This is the key advantage of non-thermal plasma: the unreactive reactant (i.e. CO_2) can be activated at room temperature, reducing coke deposited and preventing sintering of catalyst. In addition, the flexibility

indicates another advantage of non-thermal plasmas. The discharge can be switched on and off instantaneously and the associated reactions are easily initiated by adjusting the applied electric field, while there is no requirement of an external heating source for the non-thermal plasma-assisted reactions.

Non-thermal plasma can provide a good non-equilibrium condition with different (re)active species for reactions, but it is difficult to control the selectivity of the desired product(s). Radicals generated by electron-impact reactions can recombine into many different products, depending on the different chemical reaction rate coefficients. Therefore, non-thermal plasma-catalysis is the desirable technology for most of chemical reactions.

1.6.2.1 Glow discharge

The glow discharge (GD), which is luminous in contrast to the low power dark discharge, is the most famous type of non-thermal plasma, and it is a self-sustained continuous discharge ignited by a direct current (DC) power with a cold cathode which is the source for the first electron emission [83]. Moreover, the secondary emission is induced by positive ions. A schematic diagram of a common glow discharge is illustrated in **Figure 1.2**.

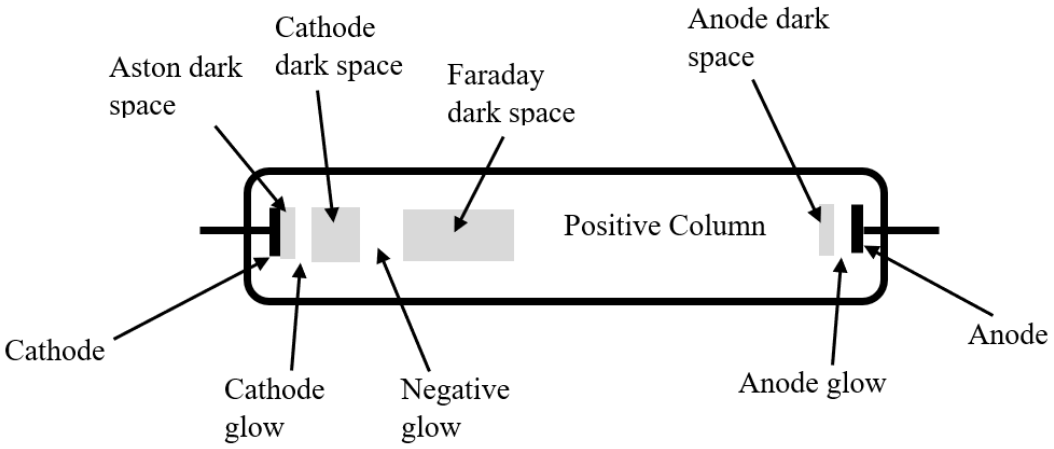

Figure 1.2 The structure of the glow discharge [83].

From the cathode to the anode, the first layer of glow discharge is the Aston dark space which is adjacent to the cathode [83]. Electron energy of this layer is low and not enough for ionisations or excitations of heavy particles, causing a thin dark layer. Then there is a thin glow layer, so-called the Cathode glow [83]. In this layer, the heavy particles can be excited by

electrons with the enough energy. However, the excited heavy particles will fall back to the ground state or a lower excitation level and release the obtained energy through the emission of light. The gas voltage drop of the Cathode dark space is the largest, because electron energy in this area is enough to ionise the plasma gas [83]. The electrons produced by secondary emission via the ionisation diffuse to the anode, while the positive ions are directed to the cathode, causing emission of new electrons by colliding the surface of the cathode. The Negative glow comes after the Cathode dark space [83, 86]. In this zone, the electron density is increased dramatically due to the ionisation, leading to the enhancement of the recombination (between electrons and positive ions) and intensity of light through the bremsstrahlung radiation process [87], which will make Negative glow become less bright until fully dark, resulting in the Faraday dark space [83]. If the distance between the cathode and anode is long enough, a quasi-neutral plasma with a low electric field, as known as “Positive column”, is formed by the cathode layer (consisting of the Aston dark space, Cathode glow, Cathode dark space and Negative glow) and anode [83]. The positive column is the traditional weakly ionised non-thermal plasma at a low pressure. Finally, near the anode, the intensity of the electric field will increase, and the electron density will decrease, causing the Anode glow and Anode dark space, respectively [83].

1.6.2.2 Corona discharge

Corona discharge is another typical example of non-equilibrium discharge generated by either continuous or pulse DC power with a relatively lower discharge power, taking place at the atmospheric pressure in the regions of high electron field near sharp edges, points, or thin wires [83]. An example of corona discharge is shown in **Figure 1.3**.

Figure 1.3 Image of a corona plasma discharge [83].

Negative corona can be formed when the high electric field is located around the cathode, while if the high electron field is applied around the anode, positive corona will be produced. **Figure 1.4** illustrates the typical positive and negative corona discharges generated between a needle and plate. With increasing of the applied voltage, the spark, leading to local overheating and non-uniformity of discharge, will be formed, limiting the practical application. The man-made corona discharge applied by a pulsed DC power can solve this problem when the duration of pulse width is shorter than 100-300 nanoseconds with the distance of electrodes of around 1-3 cm. Negative corona can be ignited by secondary electron emission, while positive corona only can be generated when the electric field is greater than the threshold value defined as: E_{cr} [88].

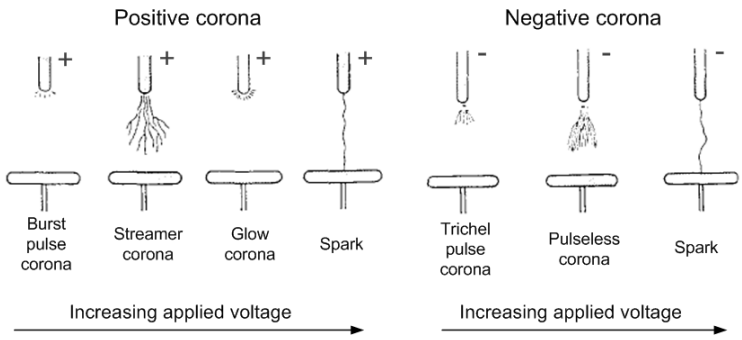

Figure 1.4 Schematic of corona discharge types in positive and negative corona discharges [88].

1.6.2.3 Dielectric barrier discharge

DBD, so-called silent discharge, is important for this project and all simulations/experiments will be performed using DBD plasma, while it has been widely used in the plasma chemistry

for many years. DBD can be mainly classified into planar DBD (**Figure 1.5**) and cylindrical DBD.

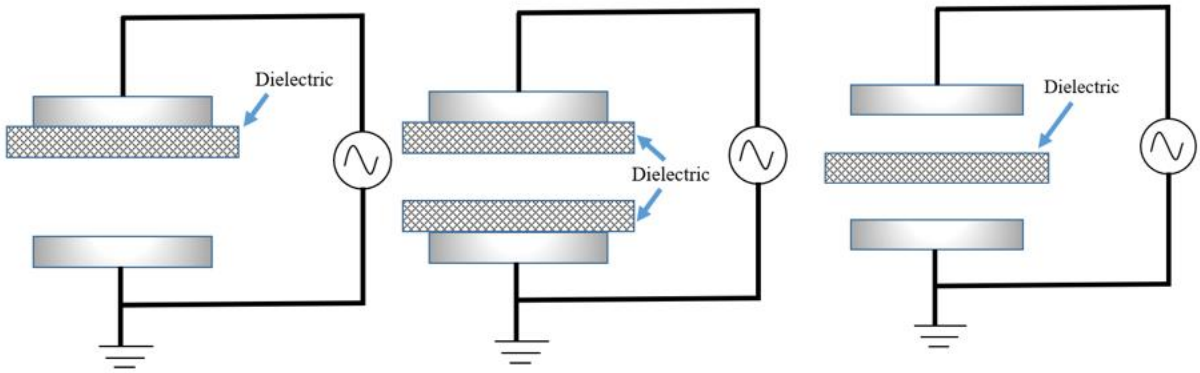

(a) (b) (c)

Figure 1.5 Major configurations of planar DBD plasmas. (a) and (c): Single dielectric; (b): double dielectrics [89].

For planar DBD, it consists of two parallel planar electrodes with one or two dielectric layer(s) positioned in the discharge gap, while a single dielectric layer can also be suspended between the two electrodes. Cylindrical DBD plasma which is generated in two coaxial cylindrical electrodes with one (or two) electrode covered by a coaxial cylindrical dielectric, shown in **Figure 1.6**. The reactors used in the project are based on cylindrical DBD and quartz tubes were used as the cylindrical dielectrics which were adjacent to the outer electrodes, as illustrated in **Figure 1.7**.

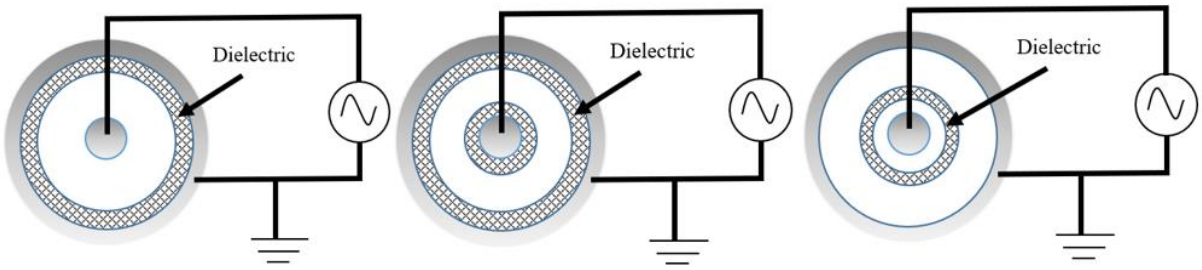

(a) (b) (c)

Figure 1.6 Major configurations of cylindrical DBD plasmas. (a) and (c): Single cylindrical dielectric; (b): double cylindrical dielectrics [89].

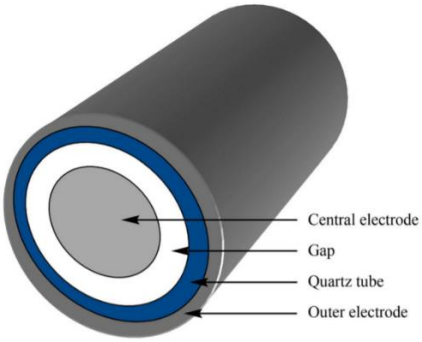

Figure 1.7 Basic pattern of the reactors used in this project based on cylindrical DBD [90].

Sparking and electric arc cannot be formed, because of the existence(s) of dielectric barrier(s) [91]. The dielectric barrier layer can be made of many materials. The most common materials are glass, quartz (used in this project) and titanium dioxide. The ability of a material to receive and store electric energy from electric field can be represented by the dielectric constant (ε) [92]. The dielectric constant of vacuum is 1, while the dielectric constants of other materials are represented by ratio of it against the dielectric constant of vacuum (i.e. ε_{glass} = 4.5-10). Additionally, the dielectric constants of (plasma) gases are much lower and slightly higher than the ones of vacuum (i.e. ε_{air} = 1.00054), while $\varepsilon_{plasma\text{-}gas}$ is often approximated to ε_{vacuum} [93].

The typical power sources of DBD plasma are alternating current (AC) power and radio frequency (RF) high-voltage. The DBD reactors used in this project were supplied by an AC power. Because of the characteristics of AC power, the breakdown of gas occurs repeatedly. When the gas voltage reaches breakdown voltage, V_b, it falls back to a very low value and the discharge current is generated by a large number of micro-discharges, known as the filament discharges [83]. A subsequent filament may appear again in the same position, because of the "memory effect" [94]. These bright filaments are statistically distributed in space and time within the scale in nanosecond. The volume of these micro-discharges indicates plasma volume of DBD, comprising about 1-10 % of the total gas volume, while the rest of gas is not ionised and served as a carrier to store and absorb the energy dissipated in the filament discharges and to transport the species with a longer life-time produced by the micro-discharges [95].

DBD can provide an non-LET environment for reactors at a low gas temperature. Catalysts are easily packed into a DBD reactor, because of the configurations of DBD, as well known as Packed Bed DBD Reactor (more details will be discussed in the following section). The larger plasma volume can be obtained with a higher frequency of AC power, caused by the increasing number of micro-discharges, but more desired species could be dissociated again due to the

enhancement of electron-impact reactions. Therefore, in the most cases of DBD plasma-assisted reactions, selectivity of desired product(s) cannot be guaranteed, and it is important to improve the selectivity by placing (a) suitable catalyst(s) in a DBD reactor.

1.6.3 Warm plasma

A transitional type of plasma, so-called “warm plasma”, operates at the boundary of both thermal and non-thermal plasmas, so it provides a high power/electron density and non-equilibrium environment with a high electron temperature [83]. Warm plasmas provide active species for chemical reactions, working as the non-thermal plasmas, and increase the gas temperature to a relatively higher level (2,000 K to 3,000 K) [96].

1.6.3.1 Gliding arc discharge

Gliding arc (GA) discharge is a traditional type of warm plasma and a transient type of arc discharge. A GA discharge is generated between at least two diverging electrodes placed in a fast gas flow, resulting in an oscillating phenomenon [97]. A classical GA is illustrated in **Figure 1.8**.

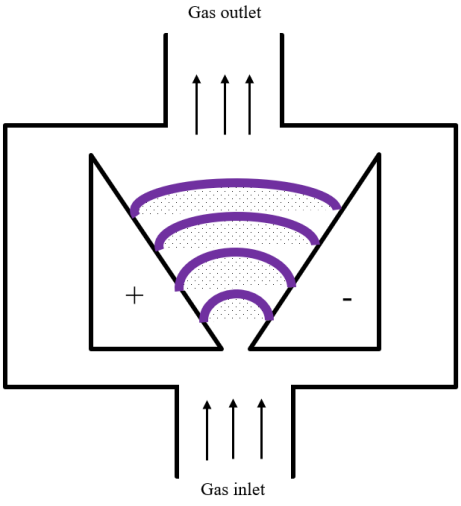

Figure 1.8 Schematic representation of the classical GA discharge [97].

The high electric field applied on the electrodes breaks down the inlet gas at the shortest distance between the electrodes, generating an arc column. The arc is pushed downstream by the gas flow and the length of it is elongated until the arc cannot be sustained by the electric

field [98]. After the extinguishment of the arc, a new arc will be generated immediately at the narrowest gap. During the extinguishing process, the LET state of the discharge cannot be sustained due to the heat losses from the arc, resulting in a rapid transition to a non-LTE state. The high electron temperature (around 1 eV) can maintain the conductivity of GA plasma, even if the discharge cools fast to gas temperature [96].

A GA discharge combines the advantages of thermal and non-thermal plasmas with a relatively high power density and electron temperature, through the transition between LTE and non-LTE states. However, the major drawback of GA in the area of plasma chemistry is the short residence time caused by the high flow rate of inlet gas, leading to an inadequate reaction of reactants. Therefore, it is necessary to pay more attentions on the conversion rate(s) of the inlet gas(es) when chemical reactions are performed using GA discharge.

1.6.3.2 Microwave discharge

There are many different types of Microwave discharge (MW), including cavity induced plasmas, free expanding atmospheric plasma torches, electron cyclotron resonance plasmas, surface wave discharges, etc [83]. MW discharges, belonging to the group of warm plasma, are electrode-less and applied by the electric power of microwaves (i.e. electromagnetic radiation in the frequency range of 300 MHz to 10 GHz) [99]. **Figure 1.9** shows a typical configuration of a surface wave discharge reactor.

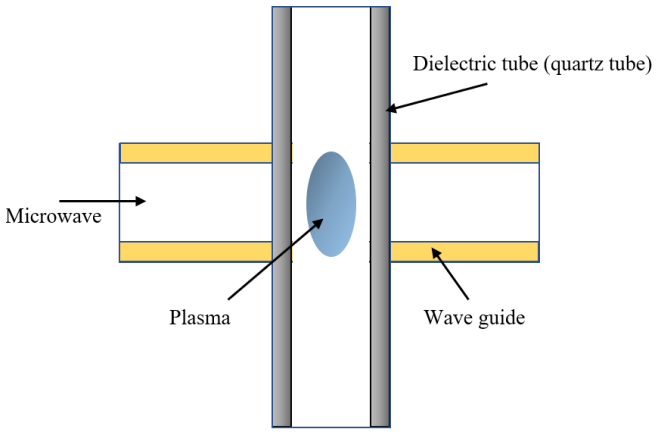

Figure 1.9 Schematic view of a MW reactor [100].

In such a reactor, a MW, generated by a magnetron with a certain wavelength (i.e. 815 MHz or 2.45 GHz), is induced by a wave guide to the reactor chamber. The discharge, absorbing the energy from the MW, is formed when the gas flows through the quartz tube.

1.7 Plasma chemistry

In the view of Fridman [83], the ionisation in plasma chemistry can be generally classified into five groups. The first one is direct ionisation of neutral, atoms, radicals and molecules by an energetic electron within one collision. Secondly, the preliminary excited neutral species can be ionised again through stepwise ionisation. Thirdly, ionisation by collisions of heavy particles (i.e. CO_2 ionised by excited Argon, Ar*) occurs when the energy of the collision partners exceeds the ionisation potential. Fourthly, photon-ionisation takes place in collisions between neutrals and photons (*hv*). Finally, surface ionisation is known as the electron emission which is caused by the collision between electron/photo and a surface.

In this project, the effects of photon reactions are neglected due to the lack of data on their reaction rate coefficients, while assumptions, that no surface reactions and recirculation appeared in the DBD reactor, are made to solve the Boltzmann Equation (BE) (see more details in **Chapter 3**). Therefore, the plasma mechanism used to build the models of this project is mainly based on the processes of direct ionisation, stepwise ionisation and heavy particles.

Elastic and inelastic are the two major types of collisions occurring in a plasma. Momentum transfer occurs during the inelastic collisions and cannot transfer the kinetic energy to the internal energies of the colliding particles. As mentioned above, there are a wide variety of species existing in plasmas, so it is necessary to understand the different time scales for the species reacting with each other. The electron-impact excitation, dissociation and ionisation are the primary processes of plasmas occurring within a time scale of around nanoseconds to produce the active species, including radicals, excited species and ions. Moreover, chemical reactions (i.e. reactions among neutral radicals) often take place after these primary processes and are usually completed within about 10 milliseconds. **Table 1.2** lists the major processes of plasma chemistry.

Table 1.2 The main processes of plasma chemistry. A and B stand for atoms and M represents a temporary colliding partner [83].

Electron-impact reactions (in nanosecond)	
Excitations	$e^- + AB \rightarrow AB^* + e^-$
Rotational	$e^- + AB_{(V_1)} \leftrightarrow AB^-_{(V_i)} \rightarrow AB_{(V_2)} + e^-$
Vibrational	$e^- + AB_{(R_1)} \leftrightarrow AB^-_{(R_i)} \rightarrow AB_{(R_2)} + e^-$
Electronic	$e^- + AB_{(E_1)} \leftrightarrow AB^-_{(E_i)} \rightarrow AB_{(E_2)} + e^-$
Dissociations	$e^- + AB \rightarrow A + B + e^-$
	$e^- + AB \rightarrow A + B^* + e^-$
Polar Dissociation	$e^- + AB \rightarrow A^+ + B^- + e^-$
Attachments	$e^- + AB \rightarrow AB^-$
	$e^- + A + B \rightarrow A^- + B$
Dissociative attachment	$e^- + AB \rightarrow (AB^-)^* \rightarrow A^- + B$
Non-dissociative ionisation	$e^- + AB \rightarrow AB^+ + e^- + e^-$
Dissociative ionisation	$e^- + AB \rightarrow A^+ + B + e^- + e^-$
Step-wise ionisation	$e^- + A \rightarrow A^* + e^- \rightarrow A^+ + e^- + e^-$
Electron-ion recombination	$e^- + AB^+ \rightarrow AB$
Dissociative electron-ion recombination	$e^- + AB^+ \rightarrow (AB)^* \rightarrow A^* + B$
Radiative electron-ion recombination	$e^- + A^+ \rightarrow A^* \rightarrow A + h\nu$
Detachment	$e^- + AB^- \rightarrow AB + e^- + e^-$
Ion-neutral and neutral to neutral reactions (in millisecond)	
Penning dissociation	$M + AB \rightarrow A + B + M$
Penning ionisation	$M^* + AB \rightarrow AB^+ + M + e^-$
Charge transfers	$A^+ + B \rightarrow A + B^+$
	$A^- + B \rightarrow A + B^-$
Ion-ion recombination	$A^- + B^+ \rightarrow AB$
Neutral-neutral reaction	$A + B + M \rightarrow AB + M$
Detachment	$A^- + B^* \rightarrow A + B + e^-$
Associative detachment	$A^- + B \rightarrow (AB^-)^* \rightarrow AB + e^-$
Atomic decomposition	$A^* + B_2 \rightarrow AB + B$
Electronic synthesis	$A^* + B \rightarrow AB$
Atomic synthesis	$A + B \rightarrow AB$

1.7.1 Plasma catalysis

As discussed in **section 1.6.2**, selectivity of a plasma-assisted reaction is often out of control due to the wide variety of species. This issue can be solved by the technique of plasma catalysis which can be achieved when the set-up of plasma is combined with a packing catalyst, while the purpose of using this technique is to optimise the plasma reactions. On one hand, inert species (i.e. CO_2 molecules) can be activated by plasma for further reactions under a milder condition. On the other hand, the active species can selectively recombine at the surface of catalyst(s) to generate the desired product(s). Currently, there are two major configurations to perform the plasma-catalytic reactions: single-stage and two-stage configuration, shown in **Figure 1.10** [101, 102]. In terms of the single-stage configuration, the catalyst is placed into the plasma zone directly, causing a direct interaction between the catalyst and discharge, and can be fully or partially packed into the plasma zone [103]. Moreover, for the two-stage configuration, there are two processes defined by the different positions for placing catalyst near to the plasma zone. The pre-process is defined as that the plasma is located upstream the catalyst, while if the plasma is located downstream the catalyst bed, the post-process will be formed. The former process, which is the most adopted two-stage configuration, can provide reactive species for further catalytic reactions, while in the latter case, the major function of plasma is to destroy the unwanted species generated by thermal catalytic reactions [104].

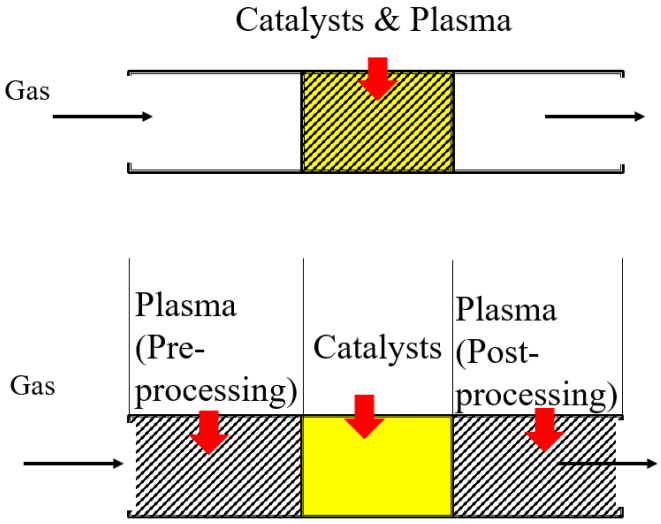

Figure 1.10 Schematic diagrams of single-stage (top) and two-stage (bottom) configurations of plasma catalysis [102, 105].

1.7.1.1 Packed bed DBD reactor

Packed bed DBD reactor is a typical derivate/application of single-stage plasma catalysis and consists of packing pellets between the electrodes (**Figure 1.11**). The packing pellets are usually made of ferroelectric materials (i.e. $BaTiO_3$) and can be either catalytic or non-catalytic, while even if the pellets are non-catalytic, they can still affect the plasma reactions by changing the characteristics (i.e. reduced electric field) of DBD [106].

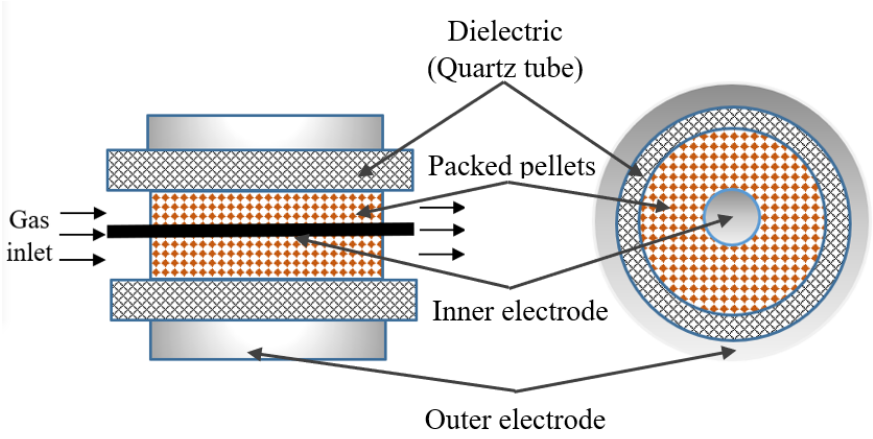

Figure 1.11 Configurations of cylindrical packed bed DBD reactor [107].

The electric field is intensified not only at the contact point between the packing pellets but also at the contact point between the pellets and electrodes/reactor wall, because the spontaneous polarization of the ferroelectric materials caused by the applied voltage forms a strong local electric field at the contact points. The increased intensity of electric filed can improve the electron energy around the contact points, resulting in a higher Townsend ionisation coefficient (defined in equation 1.9 and equation 1.10) of DBD plasma, and generate micro-discharge inside the pores of the pellets. Meanwhile, DBD could be changed into surface discharge because of the presence of insulating surface (of pellets) [83, 106].

1.7.1.2 Synergetic effects

Synergetic effects, caused by interactions between plasma and catalyst, are often used to determine whether the output parameters, including conversion rate, selectivity, yield and energy efficiency, of a reaction are improved by plasma catalysis or not. These effects can be termed as “synergy” only when the combined effect between plasma and catalyst is larger than the sum of plasma-only effect and catalytic effect on a reaction [108].

The synergetic effects on the conversion rates of CH_4 and CO_2 were obtained in Zhang et al.'s [109] work on the DBD plasma-catalytic DRM, shown in **Figure 1.12**. In their case, the conversion rate of CH_4 was observed of around 70 % and larger than the sum of conversion rates of plasma-only (~12 %) and catalytic (~10 %) DRM, while the conversion rate of CO_2 was also improved dramatically and up to ~ 75 % by the synergetic effects.

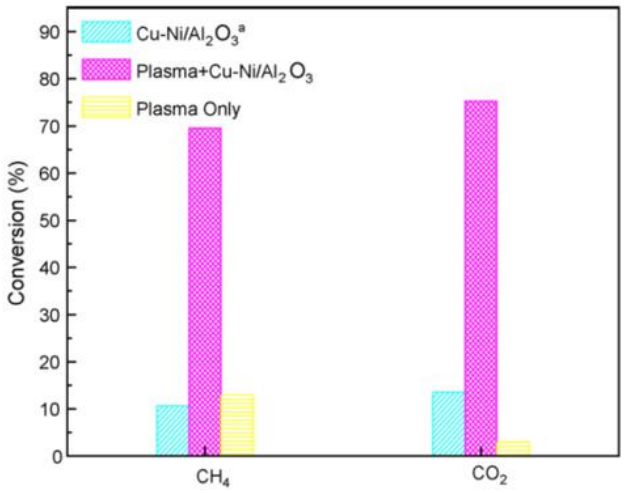

Figure 1.12 Synergetic effects in a DBD plasma-catalytic DRM process from Zhang et al.'s work [109].

Most of researches to report the synergetic effects are performed for the single-stage DBD plasma catalysis. As mentioned above, DBD plasma and catalyst can react with each other directly in a single-stage configuration, leading to the complex interactions. These major interactions are summarised in **Table 1.3**.

Table 1.3 The possible effects of the catalyst on plasma and vice versa [83, 110, 111].

Effects of catalyst on plasma	**Effects of plasma on catalyst**
1. Enchantment of electric field 2. Formation of micro-discharge 3. Change of discharge type	i. Change of physicochemical properties - change of characteristics of catalyst - higher adsorption probability - reduction of metal oxide - reduced coke formation ii. Activation by photons iii. Lower activation barrier iv. Change of surface reaction pathways

As discussed above, the presence of the catalyst results in the changes of plasma by several factors: (1) the electric field can be intensified around the contact points; (2) micro-discharges are formed which provide more channels to convert species in plasma; (3) the presence of the insulating surface promotes the formation of surface discharge.

Catalyst will also be affected by plasma during plasma-catalytic process: (i) the special surface area and dispersion of catalyst are changed by discharges, possibly causing a higher absorption probability at the surface of catalyst, while plasma can promote the reduction of metal oxide catalyst to its metal form, providing a longer life-time of catalyst, and reduce the coke formation; (ii) catalyst can also be activated by photons emitted by the excited species in plasma; (iii) the chemical bonds of species can be activated with a lower energy due to vibrational excitations caused by plasma; (iv) the original reaction pathways occurring at surface of catalyst are changed due to a wide variety of (re)active species produced by plasma.

Plasma and catalyst influence each other continuously during the plasma-catalytic process, causing a various changes of reaction pathways for (un)desired products and reactants. Therefore, there is a risk that the synergetic effects do not occur on a reaction. However, it is still recommended and worthy to perform the plasma-catalytic reactions, rather than simply relying on traditional catalytic process, because reactions could be enhanced dramatically once the synergetic effects occur.

Chapter 2: Literature reviews

2.1 Autothermal reforming of biogas

According to the major compositions of biogas (see **Table 1.1**), currently, most researches of autothermal reforming of biogas (ATRB) are performed based on the DRM process (with a low concentration of H_2S). Besides the high energy consumption, development of the suitable catalysts for ATRB is another challenge, because of the carbon deposition and poisoning of catalysts caused by sulphides. **Table 2.1** summarised the ATRB evaluations. X and Y represent conversion rates of CH_4 and CO_2, respectively.

Table 2.1 Catalyst performance summary investigated for ATRB

Catalyst	X_{CH_4} (%)	X_{CO_2} (%)	Y_{H_2} (%)	Y_{CO} (%)	Temp (^oC)	CH_4/CO_2	Ref.
25 wt.% Ni/MgAlCe	52	48	72.7	12	873	1.5	[112]
1.5 wt.% NiO/CeO_2	97.5	90.5	96.3	1.3	800	1.5	[113]
5 wt.% Ni/Mg0.4Al_2O_3	99	15	-	-	1073	1.5	[114]
13 wt.% NiO/Ce-Zr-Al_2O_3	99.0	34.4	67.1	1.5	800	1.5	[115]
1 wt.% RhO_2-13 wt.% NiO /Ce-Al_2O_3	99.1	39.1	75.3	1.7	800	1.5	[115]

To date, the number of researches on ATRB is limited and Ni supported on different carriers are the most adopted catalyst used in ATRB process with a CH_4/CO_2 ratio of 1.5. Arkai et al. performed an investigation of ATRB using a 30 wt.% Ni/Al_2O_3 catalyst. The maximum conversion rate of CH_4 was observed of 90 % with S/C ratios of 1.5 at 750 ^oC [116]. Redox cycle among Ni, NiO and Ni_2O_3 is very import to develop the Ni-based catalysts with a longer useful time. More steam was generated by the oxidation of N_i to Ni_2O_3, reducing the activity of the catalyst [117]. Vita et al. also investigated ATRB over a Ni/CeO_2 catalyst. The conversion rates of CH_4 and CO_2 reached 99.6 % and 90.5 %, respectively, using a 17.6 wt.% Ni/CeO_2 catalyst at 850 ^oC. The catalysts were deactivated slightly after 150 hours. A higher NiO dispersion on catalyst surface can maintain activity of the catalyst, but aggregation of Ni particles was limited [113]. Lzquierdo et al. conducted a study on ATRB using 13 wt.% Ni/Ce-Zr-Al_2O_3 at the temperature of 800 ^oC. Addition of O_2 in the system can improve conversion

of CH_4, because partial oxidisation of CH_4 could occur at the same during ATRB, causing a lower yield of H_2 [115].

2.2 Steam reforming of biogas

Steam reforming of biogas (SRB) is very similar to steam-CO_2 dual SRM with a certain concentration of H_2S. **Table 2.2** summarised the evaluations of catalysts used for SRB, where S/C stands for inlet ratio of steam and carbon.

Table 2.2 Catalyst performance summary evaluated for SRB

Catalyst	X_{CH_4} (%)	X_{CO_2} (%)	Y_{H_2} (%)	Y_{CO} (%)	S/C	Temp (^oC)	CH_4/CO_2	Ref.
10 wt.% Ni/Ce-Zr-La	43	12	47.2	2.1	3	550	1	[118]
5 wt.% NiO/CeO_2	64.6	36.2	35.8	10.5	1.3	800	2	[119]
15 wt.% Ni/Al_2O_3	82	8.5	-	-	2	1073	1.2	[120]
0.09 wt.% [Pd-Rh] /Ce-ZrO_2-Al_2O_3	90	6.5	71.2	0.8	1.5	1073	1.5	[121]
1.3 wt.%Pd-Rh/CeZrO2- Al_2O_3	93.9	5.0	-	-	1.2	800	1.5	[121]
4 wt.% RhO_2 /3 wt.% La_2O_3-Al_2O_3	93	10.5	2.62	0.98	1.3	685	1	[122]
$Ni_{0.4}Ce_{0.8}O_2$	96	40	72.4	5	2	700	3	[123]
7.5 wt.% Ni/CeO_2	99	4	55	29	1	900	1.5	[124]

Ahmed et al. evaluated the SRB process using a wt.% RhO_2/3 wt.% La_2O_3-Al_2O_3 catalyst under the temperature of 590-685 ^oC with a S/C ratio of 1.28 – 3.86 and CH_4/CO_2 ratio of 0.55 –1.51. The range of Gas Hourly Space Velocities (GHSV) used in their work was set to 9,180 – 27,000 h^{-1}. The lowest conversion rate of CO_2 was observed under the temperature of 650 ^oC with S/C of 1.32 and GHSV of 9810 h^{-1}. A lower operating temperature promoted the WGS reaction and inhibited DRM, causing a lower conversion rate of CO_2, while the yield of H_2 was imporved by a higher concentration of steam [122].

Effendi et al. compared the effects of a fixed bed reaction and fluidised bed reactor on SRB over a 11.5 wt.% Al_2O_3 catalyst under the temperature of 750 ^oC with a S/C ratio of 2.2 and a GHSV of 18,000 h^{-1}. The performance of SRB was improved by 5-15 % using the fluidised

bed reactor. A higher inlet flow rate of biogas resulted in a poor fluidisation in the reactor, causing the severe coke formation which could be reduced by an increasing concentration of steam [125].

Izquierdo et al. investigated the effects of using different supports on Ni and bimetallic RhNi on SRB under the temperature of 800 ^{o}C with the CH_4/CO_2 ratio of 1.5 and Weight Hourly Space Velocity (WHSV) of 131,800 gas·cat^{-1}· h^{-1}. The maximum conversion rates of CH_4 and CO_2 were observed at the S/C ratio of 1 over a 13 wt.% Ni/Ce-Zr-Al_2O_3 catalyst. DRM was also inhibited by a higher concentration of steam in their case. By using this catalyst, a higher H_2 yield was obtained, rather than using of the Ni/Ce-Al_2O_3 and Ni/Zr-Al_2O_3 catalysts [126].

Sulphur from sulphides (i.e. H_2S) can react with active metal sites to reduce the activity of catalysts, while non-selective side reactions could happen, if the stable metal-adsorbate bonds are formed. However, although H_2S could poison metallic-based catalysts, adding a suitable amount of it can improve the reforming activity of the catalysts [127].

According to the research performed by Laosiripojana et al., Ce-O-S phases (i.e. $Ce(SO_4)_2$, $Ce_2(SO_4)_3$ and Ce_2O_2S) were formed by addition of H_2S during the SRB over a 5 wt.% Ni/CeO_2 catalyst. As reported, the Oxygen Storage Capacity (OSC) was improved by the generation of $Ce(SO_4)_2$, which reduced the total reforming rate of biogas [128].

However, sulphur poisoned the 15 wt.% Ni/Al_2O_3 catalyst in Appari et al.' work, causing 98 % loss of the activity of the catalyst. Steam removed the sulphur from H_2S at a higher temperature of 800 ^{o}C and the activity of the catalyst was easily recovered by steam at this temperature [129].

Ashrafi et al. supported Appari et al.' opinions by using the same catalyst in SRB. They increased the temperature from 700 ^{o}C to 800 ^{o}C and found that the regeneration of the catalyst activity was enhanced by 29 % with the higher temperature [129, 130].

Angeli et al. tried to perform the SRB process under a relatively lower temperature (400-500 ^{o}C) over the Ni and Rh with different supports, while they indicated that the conversion rate of CH_4 was increased by using the CeZrLa as the support of the catalyst [118].

2.3 Dry reforming of biogas

Dry reforming of biogas (DRB) is performed by introducing the mixture gas of biogas and CO_2 into a reactor. Therefore, this process is extremely approximate to DRM and the catalysts used in DRM (i.e. Ni-based catalysts) are the good references to develop the catalysts for DRB, shown in **Table 2.3**.

Table 2.3 Catalyst performance summary for DRB

Catalyst	X_{CH_4} (%)	X_{CO_2} (%)	Y_{H_2} (%)	Y_{CO} (%)	Temp (^oC)	CH_4/CO_2	Ref.
75Ni-25Co/Al_2O3	25	0	0	0.6	600	1	[131]
15wt.%Ni-5wt.%CoO_2 /MgO-Al_2O_3	57.1	-	90	-	900	1.25	[132]
13 wt.% NiO/Ce-Zr-Al_2O_3	60.1	94.4	63.5	63	800	1.5	[115]
1wt.%RhO_2-13 wt.%NiO /Ce-Al_2O_3	64.5	85.6	57.5	51.8	800	1.5	
8wt.%NiO/20wt.%CeO_2-Al_2O_3	70.5	97	76.5	60	860	1.5	[64]
20 wt.% NiO/MgO	80	85	-	-	750	1.5	[133]
26 wt.%Ni/La_2O_3	80	82	-	-	700	1.5	[134]
$Ni_{0.4}Ce_{0.8}O_2$	83	78	-	-	700	3	[123]
7NiO-3CoO_2/La_2O_3-Al_2O_3	>90	>90	95	96	800	1	[135]
9wt.%NiO/$Ce_{0.82}Sm_{0.18}O_{1.91}$	98	97	0.8	-	800	1	[136]
$Ce_{0.7}La0_{.2}Ni_{0.1}O_2$	98	80	38	70	800	1.04	[137]

The major advantage of DRB is to convert two GHGs (CH_4 and CO_2) at same time, but the coke formation of it is increased due to the lack of steam-carbon reactions, causing clogging of reactors. Xu et al. studied on DRB using a Ni-Co/La_2O_3-Al_2O_3 catalyst, while the maximum conversion rates of CH_4 and CO_2 were observed of 94.5 % and 97.0 %, respectively with the H_2 selectivity of 92.7%, under the temperature of 800 ^oC and CH_4/CO_2 ratio of 1. The reduction of Ni and Co occurred around 500 ^oC, resulting in the formation of active sites of the catalyst, which were formed in the reductive atmosphere of H_2 and CO [138]. Arbag et al. performed a similar research and they found that a higher amount of Co in the catalyst reduced the catalytic activity due to the formation $CoAl_2O_4$ [9]. However, activity of catalyst can be improved by the addition of Co with a lower amount to Ni-based catalyst, while Saha et al. performed DRB

over the 5 wt.% Co and 15 wt.% Ni supported by $MgO-Al_2O_3$. The authors reported a 57.1 % conversion rate of CH_4 with the H_2 selectivity of 97% [132].

Asencios et al reported a best catalytic activity for CH_4 conversion (98 %) using a 20 wt.% $Ni/MgO-ZrO_2$ catalyst. Addition of ZrO_2 to the support promoted the partial oxidisation of CH_4 and MgO showed a strong preference for DRB [133].

Juan-Juan et al. doped potassium (K) element into a10 wt.% Ni/Al_2O_3 catalyst to develop a carbon-resisted catalyst. The authors indicated that the addition of K (by 0.2 wt.% K_2O) enhanced the activity of the catalyst, because the reducibility of NiO was improved due to the modified interaction between NiO and Al_2O_3. The size and the structure of Ni particles were not changed, but more than 90 % coke was reduced [139].

Bereketidou and Goula doped Al_2O_3 with CeO_2 to develop the 8 wt.% $Ni/CeO_2-Al_2O_3$ catalyst for DRB. The maximum conversion rates of CH_4 and CO_2 were reported as 95 % under the temperature of 850 ^oC with a CH_4/CO_2 ratio of 1.5, while the authors found that the addition of CeO_2 to Al_2O_3 can improve the stability of catalyst [64]. Moreover, Charisiou et al conducted a study on DRB using the same catalyst with increased flow rate and operating temperature and exhibited a 40 % reduction of the conversion rate of CH_4. It seemed that the performance of the catalyst was restricted by higher flow rate of reactants [140].

Zmiciz et al. prepared the Ni-based catalyst using a different support which was samaria doped ceria (SDC) for the DRB process. The conversion rates of CH_4 and CO_2 were observed of over 95 % with H_2 yield of 80 % under the temperature of 800 ^oC with a CH_4/CO_2 ratio of 1. The authors indicated that a higher CH_4/CO_2 ratio decreased the conversion rate of CH_4 [136].

$La_2O_2CO_3$ will be formed by adding La_2O_3 to Al_2O_3 and it can establish the equilibrium on surface of Ni crystallites [127]. Li et al. used a 5 wt.% Ni/nano-rod shaped La_2O_3 for SRB and they found that La_2O_3 increased the adsorption and activation of CO_2, resulting in a higher conversion rate of CO_2 [134]. Catalytic activity occurred in the inter-phase of $Ni-La_2O_2CO_3$, leading to a lower carbon deposition due to the generation of the oxy-carbonate species [127].

The pre-treatment is very important for preparing catalysts. Instead of the traditional method, in Zhao et al.'s work, $NiO-CO_2O_3/Al_2O_3$ was pre-reduced by H_2 and followed by a treatment with CO_2, resulting in the formation of $Ni(HCO_3)_2$ which can be decomposed to release oxygen. The released oxygen would then react with the carbon deposited on the Ni surface, causing a

longer life-time of the catalyst. The conversion rates of CH_4 and CO_2 were increased from 87 % to 95 % and 95 % to 99 %, respectively, with the catalyst pre-treated for 1 hour [141].

The methods of preparing catalyst also play a key role to provide a higher catalytic performance for DRB. Goula et al evaluated the performance of Ni/Al_2O_3 catalysts prepared by different methods, including wet impregnation, incipient wetness and equilibrium deposition. A higher Ni dispersion was obtained by using of equilibrium deposition method, causing a higher catalytic activity, while the traditional impregnation caused an uncontrolled precipitation on the surface of catalyst [142].

2.4 Plasma-catalytic reforming of biogas

Because of the severe coke formation and high requirement of the operating temperature for catalytic reforming of biogas, people start to pay more attentions on non-thermal (i.e. DBD) plasma-catalytic biogas reforming. Different catalysts also play an important role in this hybrid technique, and suitable catalyst (i.e. supported Ni, Co, and some of noble metals) can deploy the distributions of products effectively [103, 143, 144]. To date, the number of researches on using this technique to convert biogas is limited. However, it is worthy to perform more researches on that, because, as mentioned above, the biogas reforming could be enhanced dramatically if the synergetic effects happen, as Zhang et al.'s work [109].

Recently, plasma has been reported as a potential technique for hydrogen generation via reforming of hydrocarbons/carbohydrate (i.e. biogas, methane, methanol, heavy oil, etc). The effect on hydrogen yield of the inlet ratio of S/C is prominent, and a higher steam concentration can inhibit the generation of the poisonous gas CO (less than 30-vol.%) [145]. The energy yield of hydrogen production for industrial process is reported at 60 $g(H_2)/kWh$ [146], while, as reported, plasma technique has ability to enhance the hydrogen yield up to 225 $g(H_2)/kWh$ [147]. Different discharge types (i.e. DBD, microwave discharge, gliding arc, etc) have been used in plasma-catalytic reforming of biogas [148, 149], while the electron energy distribution functions (EEDFs) of plasma play a significant role in plasma-catalytic reactions and they can be affected by many factors, including different compositions of inlet gas, applied voltage, discharge gap, discharge length and flow rate [150, 151].

2.4.1 Corona discharge plasma-catalytic reforming of biogas

Dai et al. performed a plasma-assisted reforming of biogas using a pulsed corona discharge without catalyst. They found the conversions of CH_4 and CO_2 can be improved by the pulsed voltage with the major products of CO and C_2 compounds. The maximum conversion rates of CH_4 and CO_2 were observed of 58.4 % and 61.1 %, respectively, with feed flow rate of 25 ml/min and CH_4/CO_2 ratio of 2 at the applied voltage of 38 kV and discharge power of 42 W with frequency of 88 Hz. Under these operating conditions, the yields of CO and C2 hydrocarbons reached to 34.1 % and 9.0 %, individually [152].

Li et al. investigated effects of different discharge types of corona discharge on the conversions of CH_4 and CO_2. The authors identified that positive corona has the strongest positive effect on the reforming of biogas, followed by the AC corona, while the reforming process was inhibited using a negative corona [153, 154].

The development of catalyst is necessary to induce the synergetic effects between catalysts and plasmas. Aziznia et al. studied on corona plasma-catalytic reforming of biogas over the Ni/Al_2O_3 catalyst to determine the hybrid effect between a corona discharge. In comparison to the plasma-alone system, placing the Ni-based catalyst into the plasma rector increased the conversion rates of CH_4 and CO_2, causing a higher selectivity of CO and inhibiting the generations of hydrocarbons and oxygenates [155].

Zhang et al. performed a pulsed corona plasma-catalytic reforming of biogas using La_2O_3/Al_2O_3 as the catalyst. The highest conversion rate of CH_4 was obtained of 24.9 % with a selectivity of C_2 hydrocarbons of around 72.8 % at the input power of 30 W. They found that C_2H_2 was the major hydrocarbon with a concentration of 76.4 mol %, while doping palladium (Pd) to the La_2O_3/Al_2O_3 catalyst modified the pathways for generations of C_2 compounds and C_2H_4 became the major C_2 product [156].

2.4.2 DBD plasma-catalytic reforming of biogas

The interaction between catalyst and plasma in a DBD reactor is more complex due to the presence of catalyst pellets with packed bed, causing the change of discharge type (as defined in **section 1.7.1**). Eliasson et al. investigated on the DBD plasma-catalytic reforming of biogas over a NaX zeolite catalyst. The authors found that placing the NaX zeolite reduced total

conversion rates of CH_4 and CO_2, resulting in the higher concentrations of C_2, C_3 and C_4 products. There were no synergetic effects observed in their work [157].

Zhang et al. tried to investigate DRB at low temperature and atmospheric pressure using DBD plasma over different catalysts, including quartz fleece, zeolite x, zeolite HY and zeolite NaY. They found that zeolite NaY catalyst promoted the conversion of biogas, resulting the highest yield of syngas [158]. Apart from Zhang et al.'s work, Jiang et al obtained a higher selectivity of light hydrocarbons ($C_2 – C_4$) during the plasma-catalytic DRB over a zeolite catalyst which efficiently reduced the coke deposition and polymers generated by plasma on the surface of catalyst [159].

Ni-based catalysts have been widely used in ATRB, SRB and DRB, so many research groups tried to perform the plasma-catalytic reforming of biogas using these catalysts. Song et al. reported the DBD plasma-catalytic DRB over a $Ni/\gamma\text{-}Al_2O_3$ catalyst. They found that the selectivity of CO and conversion rate of CO_2 were improved by the presence of the catalyst, with a negligible effect of loading amount of Ni on catalyst [160]. Apart from Song et al.'s work, there was an around 20 % increment on CH_4 conversion and the selectivity of syngas was also improved, by using the 20% Ni/Al_2O_3 catalyst in Wang et al.'s work [161]. Zeng et al. doped Mn, Co and Cu into the Ni-based catalyst, they defined that the conversion of CH_4 was dramatically enhanced using the $Mn\text{-}Ni/\gamma\text{-}Al_2O_3$, while these catalysts had a neglectable effect on conversion of CO_2 [162]. Lee et al. also performed the DBD plasma-catalytic DRB over a $Ni/\gamma\text{-}Al_2O_3$ catalyst, but they increased the operating temperature to 573 K to investigate the heating effect on generation of syngas. The conversion rates of CH_4 and CO_2 reached 97.5 % and almost 100 %, respectively at the input power of 80 W [163]. The obvious synergetic effects occurred in their work, while such high conversion rates of the reactants cannot be achieved in the catalytic DRB at this low temperature.

The different martials of electrodes of reactors can also affect the performance of DBD plasma-catalytic reactions. Li et al. designed the DBD reactor using different materials of electrodes. The authors introduced CH_4 and CO_2 separately into the reactor to define the activities provided by the electrodes for CH_4 and CO_2 conversions, while the orders were in the relationship: Ti = Al > Fe > Cu (for CH_4) and Al > Cu > Ti > Fe (CO_2). When CH_4 was doped to CO_2 as the inlet gas, the electrode made of Ti exhibited the best performance for the reforming process [164].

Packing method of the packed bed placed in DBD reactors can modified not only the properties of catalyst but the discharge type of DBD. Wang et al. designed three different contact modes

of catalyst and discharge to investigate the effect of packing method on DBD plasma-catalytic DRB, shown in **Figure 2.1**. In the first mode, the catalyst was placed 15 millimetres after the discharge zone (pre-process of two-stage configuration of plasma catalysis); in the second mode, the catalyst was placed at the end of the discharge zone; in the third mode the catalyst was fully placed in the plasma zone. According to the authors' opinions, the synergetic effects were only observed when the packed bed was fully placed in the plasma zone [161].

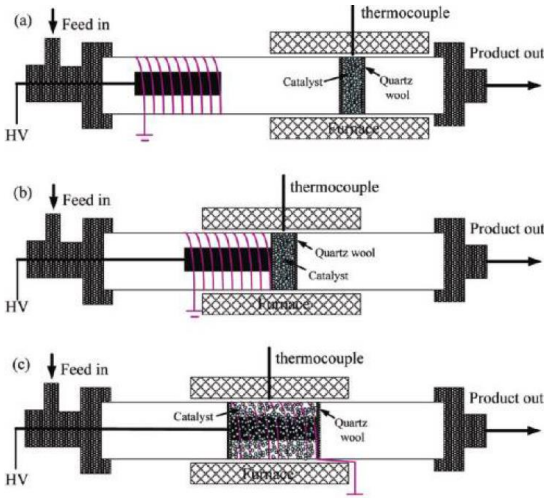

Figure 2.1 DBD reactors designed by Wang et al with different contact modes [161].

Tu et al. also investigated the effect of packing method in a DBD reactor using a Ni/γ-Al_2O_3 catalyst, as illustrated in **Figure 2.2**. In the mode A, the pellets were fully packed into the discharge gap; in the mode B, the pellets were partially packed into the discharge zone; in the Mode C, some pieces of the catalysts were place along the bottom of the reactor. They found that the discharge type was modified when discharge zone was fully packed with pellets, while there were strong filaments observed in the DBD reactor with partially packing method, so the discharge type was still dominated by DBD. Besides the packing method, they also investigated the effect of the calcination temperature for preparing the catalyst, while a lower calcination temperature (300 ^{o}C) had a positive effect on the synergy between the catalyst and discharge [103].

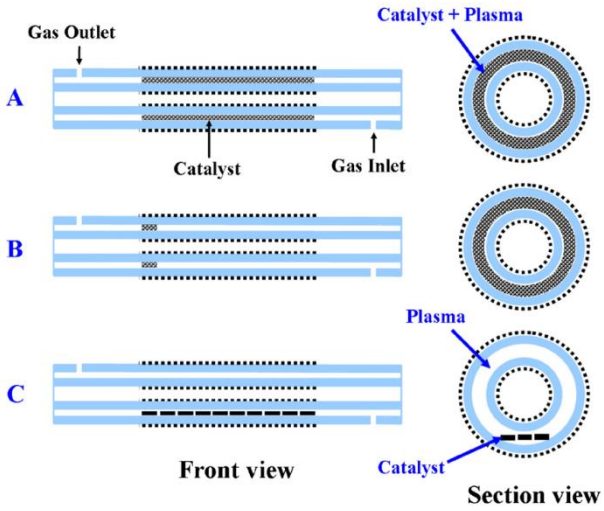

Figure 2.2 DBD reactors designed by Tu et al with different packing methods [103].

2.4.3 GA discharge plasma-catalytic reforming of biogas

As mentioned above, GA is a warm plasma with relatively higher gas temperature and moderate electron temperature (around 1 eV). Bo et al. performed a GA plasma-catalytic DRB without catalyst. The major products were syngas, C_2H_2 and C_2H_4, and C_2H_6 was not observed in their work due to the dehydrogenation process caused by GA discharge, while a higher CH_4/CO_2 (> 2) resulted in a high H_2/CO ratio of syngas and severe coke deposition on the electrodes [165].

Indarto et al. studied DRB using a GA reactor at the discharge power of 190 W with the frequency of 20 kHz. The maximum conversion rates of CH_4 and CO_2 were obtained of 40 % and 31 %, respectively, with the selectivity of H_2 and CO of 50 % and 62 %. Apart from the Bo et al.'s work only C_2H_2 was observed as the by-products with a selectivity of 12 % [166].

Tu et al. focused on the production of carbon nano-materials from the GA plasma-catalytic DRB, while many useful and value-added by-products were found in their work, including spherical carbon nanoparticles, multi-wall carbon nanotubes and amorphous carbon [36].

2.5 Modelling

2.5.1 Plasma alone

Reaction pathways become highly complex in plasma environment. During the previous years, many models have been built to simulate the plasma reactions for different applications, including the processes of plasma-assisted removal of volatile organic compounds (VOCs) [167-170] and conversion of CH_4/CO_2 [25, 40, 171-174]. These simulations were conducted without catalysts. Most of these simulations are 0-dimension (0D) by solving certain balance equations (i.e. particle continuity equation, energy balance equation, etc.), so spatial transport in plasma is neglected. Generally, the simulation results in a 0D model can provide all densities of the species existing in the plasma and a clearer reaction mechanism, but the accuracies of these simulations are restricted by the assumptions of plasma behaviour. Most of simulations on DBD plasma-catalytic reactions were performed by 0D model and the main challenge is to correctly describe DBD power, due to its filamentary discharge characteristic.

Aerts et al. built a model to investigate DBD plasma-assisted CO_2 splitting, while they described the discharge power by implementing a triangular with the duration of 30 nanoseconds per microsecond, shown in **Figure 2.3**. According to the authors' opinions, the number of pulses for one molecule passing through the reactor in real residence time was unknown, so one major objective of their work was to evaluate the effect of the number of micro-discharges on the performance of the simulation [25].

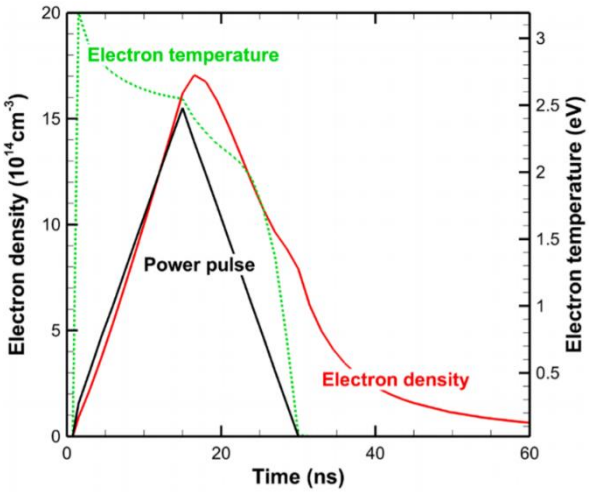

Figure 2.3 Power description and calculated electron energy/density of Aerts et al.' work [25].

Besides 0D simulations, 1,2-dimension (1D and 2D) are also suitable to simulate the plasma-assisted reactions [175, 176]. For 1D and 2D models, the diffusions of the species are considered, as well as the effects of the reactor wall. However, the microscopic information of surface reactions cannot be defined simply through the 1D or 2D model. The important results of plasma chemistry, including conversion, selectivity and energy efficiency, can also be calculated, but the sizes of 1D and 2D models are smaller than the one of 0D. Therefore, sometimes, the species with less effect on reaction mechanism are moved out of the 1D and 2D models to reduce simulation time, resulting in a slight loss of accuracy. Therefore, all simulations in this project are performed by 0D model to focus on the investigation of reaction mechanism.

2.5.2 Catalysis alone

Simulations on thermal catalytic reactions have been widely used to understand the reaction mechanism on the surface of catalysts, while they are often in the atomic scale. There are two most adopted methods: density functional theory (DFT) and classical molecular dynamics (MD) [177].

For DFT calculations, based on quantum mechanical computational calculation, are often used in physics chemistry and material science. The high accuracy is the major advantage of DFT. The calculations can clearly show reaction mechanisms and corresponding activation energy barriers, which are very important factors to calculate a new rate constant of a surface reaction. However, the system size of DFT is very small (in picosecond) and can only contain hundreds of atoms [178]. The typical simulations using DFT are the research on water gas-shift reaction with different metallic catalysts (i.e. Co, Ni, Cu, etc.) [179] and CO_2 reduction on Fe, Co, Ni and Cu [180].

Apart from DFT calculations, the system size of MD is much larger. The number of involved atoms can reach millions and the operating time is in nanosecond(s). Moreover, classical MD simulations are relied on the integration of the equations of motion of all atoms. However, the interatomic potential used in MD limits accuracy of calculation [177]. Goddard et al. [181] conducted classical MD simulations to investigate the mechanism of conversion of propene to acrolein using different catalysts (i.e. MoO_3, Bi_2O_3, $Bi_2Mo_3O_{12}$ and V_2O_5) and they found that V_2O_5 had the most positive effect on the conversion of propene, resulting in the selective pathways to generate acrolein. Somers et al [182-184] investigated mechanism of CH_x radicals

in a CH_4 background plasma over Ni-based catalysts. They found that the activities of CH_x radicals were in the sequence of: $CH_3 < CH_2 < CH$, while H_2 can only be formed on the Ni (111) surface when the temperature was increased to 1400 K. At the high temperature, the coke formation was severe, resulting in a much shorter life-time of the catalyst.

Chapter 3 Description of the model and experimental set-up

3.1 Physical description of the model

All simulations used in this project employ a 0D model using ZDPlaskin, which is a Fortran 90 module designed to follow the time evolution of the species densities and gas temperature in a non-thermal plasma with an arbitrarily complex chemistry. The chemical module can be written in any text format file (i.e. word and notepad). The Bolsig+ solver is incorporated in the ZDPlasKin for solving the BE to obtain the EEDFs. The entire process is depicted graphically in **Figure 3.1** [185].

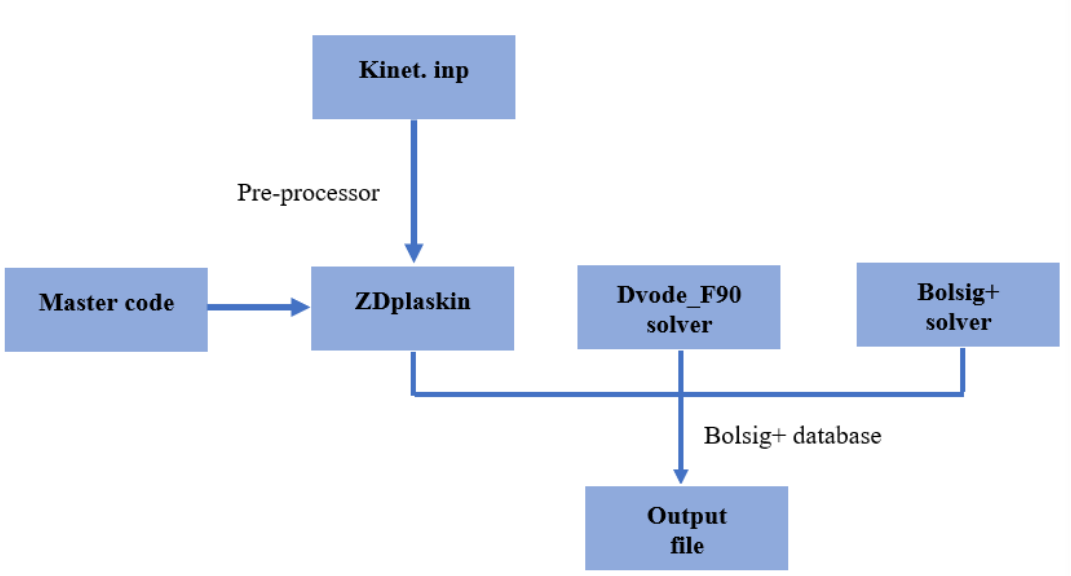

Figure 3.1 Block diagram of the modules of the 0D ZDPlaskin model used in this project [185].

As mentioned above, the 'kinet.inp' file is used to define the chemical module, including the elements, species and reactions involved in the simulation. The 'Pre-processor' will afterwards convert the 'kinet.inp' into a Fortran 90 file prepared for ZDPlaskin.

The user should provide a special master code to call ZDPlasKin library routines which perform the time integration and update electron transport and electron-impact reaction rate coefficients used in Bolsig+. The reaction operating conditions is also defined in the 'master code'. The traditional method to define the operating conditions reads an external table which provides the information (i.e. discharge power, gas voltage, initial electron density, etc.) for

Bolsig+ solver, while this project upgrades the master code and makes it possible to define the operating conditions as a function inside the 'master code' module. Additionally, the output file is extracted automatically in a '.txt' file clearly displaying the densities of all particles after upgrading the master code.

Equation (3.2) will be integrated in time using 'Dvode_F90' module performed as Variable-Coefficient Ordinary Differential Equation solver. The time steps can be set dynamically to capture the changes of densities of all species involved in the system at any time.

Before starting the simulations, there is an assumption that no surface reactions and recirculation appear in the DBD reactor so that all species can satisfy the conditions for solving BE (equation 3.1) [186].

$$\frac{\partial f}{\partial t} + v \cdot \nabla f - \frac{q}{m} E \cdot \nabla_v f = C[f] \tag{3.1}$$

where m is the electron mass, f is the EEDF, q is the elementary charge, v is the average electron velocity and $C[f]$ represents the change rate of the EEDF.

The dynamic densities of all species, $N_{i=1\ldots i\max}$, can be expressed as the equation (3.2). The source term Q_{ij} describes the contribution from each diverse reaction, $j = 1 \ldots j_{\max}$, and it is defined by user input file ('Kinet.inp') [185].

$$\frac{d[N_i]}{dt} = \sum_{j=1}^{j_{\max}} Q_{ij}(t) \tag{3.2}$$

Here is an example of the reaction (3.3) in order to provide a better understanding. The reaction rate can be calculated in equation (3.4). Therefore, the source terms are expressed as equation (3.5).

$$a\mathrm{A} + b\mathrm{B} \rightarrow a'\,\mathrm{A} + c\mathrm{C} \tag{3.3}$$

$$R = k_j[\mathrm{A}]^a[\mathrm{B}]^b \tag{3.4}$$

$$\mathrm{Q_A} = (a' - a)R,\ \mathrm{Q_B} = -bR,\ \mathrm{Q_C} = cR \tag{3.5}$$

where R is the reaction rate. Additionally, calculations of the rate constants, k_j, are different. For the neutral-neutral reactions, the rate constants can be obtained from the three-parameter Arrhenius form (3.6) [187, 188].

$$K_j(T) = A_j T^{Bj} \exp\left(-\frac{Ej}{RT}\right) \tag{3.6}$$

The unit of K_j is in cm^3/s. T is gas temperature in Kelvin. The three parameters of A_j, B_j and E_j represent pre-exponential factor, temperature factor and activation energy respectively. However, for the electron-impact reactions, E/n is used to solve BE (3.1) to obtain the EEDF and mean electron temperature, while the rate constants for all electron-impact reactions can be calculated by equation (3.7).

$$k_j = G \int_0^\infty \varepsilon \sigma_k f d\varepsilon \tag{3.7}$$

where σ_k is the cross-section of the target particle and ε ($\varepsilon = (v/G)^2$) is the electron energy in volt ($G = \sqrt{2q/m}$). The cross sections of the radical $CH_{y,(y=1,2,3)}$ and species $C_xH_{y,(x=2,3;y=2,4,6,8)}$ are adopted from literatures and added into the local databased of ZDPlaskin to upgrade the model [189, 190], while the cross sections of some familiar species (i.e. CH_4, CO_2, O_2, CO, H_2…) are collected from Morgan and Puech database [191, 192]. On the other hand, all reaction rate constants for neutral-neutral reactions used in this project are summarised from NIST database [193].

3.2 Description of the discharge power

The temporal dynamic discharge voltage is a very important inlet parameter to obtain the reduced field for this project, while all reactions involved in this project are under DBD environment. Typically, DBD exhibits as filamentary regime with lots of filaments, while the width (duration) of each filament is in nanosecond scale. These micro-discharge filaments perform most of dissociation, ionisation and excitation processes, which are essential for electron-impact reactions. Unfortunately, it is impossible to simulate the behaviour of all species during each filament, because the modalities of filaments are different. However, if the filaments can be treated as a smooth and continuous function in time, the temporal dynamic gas voltage can be obtained. Moreover, in order to get the temporal dynamic reduced electric field (E/n), unit of Td, the total gas density is also required to be set as a temporal dynamical value to perform a more accurate simulation. These processes have been achieved after modifying the master code in ZDPlaskin.

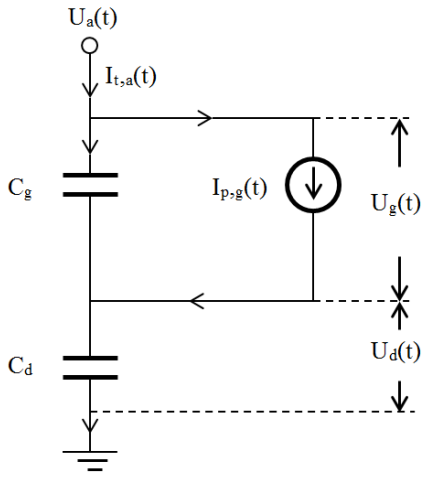

Figure 3.2 Equivalent circuit of the DBD electrode configuration

According to the basic theorem of DBD (described in **Chapter 1**), the equivalent circuit of the DBD reactor is shown in **Figure 3.2**, where C_g and C_d represent the capacitances of gap and dielectric barrier, respectively. $I_{t,a}$ is the total current flowing through the DBD circuit, while $I_{p,g}$ and $I_{v,g}$ are defined as the discharge current and displacement current. Moreover, the capacitance of the coaxial barrier is calculated as equation (3.8) [83].

$$C_d = \frac{2\pi\varepsilon_0\varepsilon_p L}{\ln(\frac{b}{a})} \tag{3.8}$$

where ε_0 and ε are the dielectric constant and permittivity of the barrier individually. L is the discharge length, while a is the inner diameter, and b is the outer diameter of the reactor. Based on **Figure 3.2**, the temporal dynamic U_d can be expressed as [94]:

$$U_d\left(t+\frac{T}{2}\right) = \frac{1}{C_d}\int_0^{t+\frac{T}{2}} I_{t,a}(\tau)d\tau + U_d(0) = \frac{1}{C_d}\int_0^{\frac{T}{2}} I_{t,a}(\tau)d\tau + \frac{1}{C_d}\int_{\frac{T}{2}}^{t+\frac{T}{2}} I_{t,a}(\tau)d\tau + U_d(0) =$$

$$\frac{1}{C_d}\int_0^{\frac{T}{2}} I_{t,a}(\tau)d\tau - \frac{1}{C_d}\int_0^{t} I_{t,a}(\tau)d\tau + U_d(0) = -U_d(t) \tag{3.9}$$

However, according to Kirchhoff's laws [194], U_d can be written as:

$$\frac{dU_d(t)}{dt} = \frac{I_{t,a}(t)}{C_d} \tag{3.10}$$

Then, equation (3.10) can be rewritten into equation (3.11):

$$U_d(t) = \frac{1}{C_d}\int_0^t I_{t,a}(\tau)d\tau + U_d(0) \tag{3.11}$$

Therefore, $U_d(0)$ can be obtained by substituting equation (3.9) to equation (3.11):

$$U_d(0) = -\frac{1}{2C_d}\int_0^{\frac{T}{2}} I_{t,a}(\tau)d\tau \tag{3.12}$$

Finally, $U_d(t)$ can be obtained (equation 3.13), while it can be subtracted from the applied voltage, U_a, to get the gas voltage (equation 3.14), $U_g(t)$:

$$U_d(t) = \frac{1}{C_d}\int_0^t I_{t,a}(\tau)d\tau - \frac{1}{2C_d}\int_0^{\frac{T}{2}} I_{t,a}(\tau)d\tau \tag{3.13}$$

$$U_g(t) = U_a - \frac{1}{C_d}\int_0^t I_{t,a}(\tau)d\tau + \frac{1}{2C_d}\int_0^{\frac{T}{2}} I_{t,a}(\tau)d\tau \tag{3.14}$$

It is clear that the function of $I_{t,a}$ in time should be obtained in advance for the calculation of $U_g(t)$. Nevertheless, the filaments of DBD appear as a discrete signal during each individual half AC power cycle, shown in **Figure 3.3**.

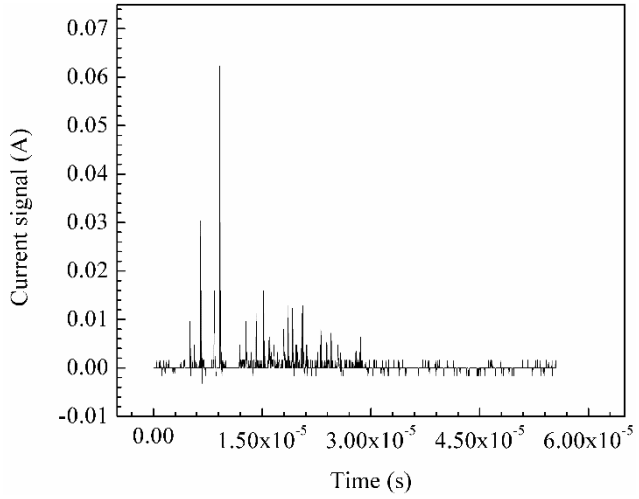

Figure 3.3 Original current signal in a half AC power cycle. (This sample was taken from the dry reforming of methane (in **Chapter 6**); CH_4: CO_2 = 1:1, total flow rate = 40 ml/min; discharge power = 10 W; room temperature and atmospheric pressure).

Obviously, a signal processing technique is required to convert the original current signal into a continuous signal. The discrete current signal is required to be considered as a sampled digital signal (equation 3.15) [195]:

$$I_{t,a}(t) = \sum_{n=-\infty}^{\infty} I(nT_s)\delta(t - nT_s) \tag{3.15}$$

where T_s is the sampling period. For the reconstruction, the original signal needs to pass through a low-pass filter with the cut-off frequency of ω_c (3 kHz).

$$h(t) = \frac{\omega_c T \sin(\omega_c t)}{\pi \omega_c t} \tag{3.16}$$

Reconstruction processing [195]:

$$I_{t,a}(t) \times h(t) = \frac{\omega_c T}{\pi} \sum_{n=-\infty}^{\infty} I(nT) \frac{\sin[\omega_c(t-nT)]}{\omega_c(t-nT)} \quad (3.17)$$

Therefore, it is possible to obtain a smooth and coherent curve of gas voltage with the defined function.

According to the Nyquist-Shannon sampling theorem [196, 197], discrete digital signals can be reconstructed integrally without any distortions, if sampling frequency, ω_s, is greater than twice the maximum frequency, ω_m, of original signals ($\omega_s > 2\ \omega_m$). In fact, the intervals and durations of those filaments are unclear, but it is obvious that the frequencies of these pulses (sampled signals) are much higher than ω_m with different amplitudes. Therefore, this work satisfies the Nyquist-Shannon sampling theorem and the original current signal (illustrated in **Figure 3.3**) can be completely reconstructed, shown in **Figure 3.4**.

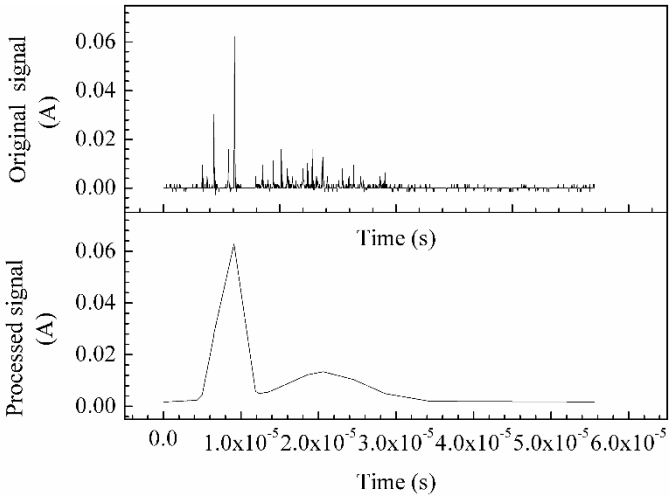

Figure 3.4 Reconstructed continuous signal from the original current signal for half AC cycle. (This sample was taken from the dry reforming of methane (chapter 6); CH_4: CO_2 = 1:1, total flow rate = 40 ml/min; discharge power = 10 W; room temperature and atmospheric pressure).

Finally, the temporal dynamic discharge power can be obtained in equation (3.18):

$$P(t) = U_g(t) \times I_{p,g}(t) \quad (3.18)$$

3.3 Experimental set-up and model description

3.3.1 Power measurement

The energy consumption of the DBD reactor is determined by measuring the input power and discharge power. The input power, known as the applied power, is the electric power applied on the entire system, including the power consumed by the transformer, AC high voltage power supply, DBD reactor (i.e. the barriers) and heating caused by the electric current or heating device (if installed) and reflects the operational cost of the entire system. In this project, the input power was measured by a power meter. The discharge power, which is used to calculate the energy efficiency of the system, is the electric power only consumed by DBD plasma. In this project, the discharge power is calculated by using Lissajous figure. The Lissajous method was firstly proposed by Manley in 1943 [198]. The measurement of input voltage and total charge transferred through the reactor are the essential parameters for the Lissajous method. It is done by connecting an external capacitor in series to the DBD reactor and recording the voltage applied on this capacitor. When the full cycle of the input voltage is recorded, a Q-U Lissajous figure can be obtained by the charge versus the input voltage and the area encircled by the figure is the discharge power [199].

3.3.2 CO_2 splitting

The coaxial quartz tube was used as the DBD reactor for this experiment, as illustrated in **Figure 1.7**. The external and inner diameters were 22 mm and 19 mm, respectively. The length of the discharge zone can be changed from 90 to 200 mm with a fixed discharge gap of 2.5 mm. A stainless-steel rod with an outer diameter of 14 mm was set in the centre of the reactor as the high voltage inner electrode, which was connected to the high voltage probe (Testec, HVP-15HF) to record the AC input voltage with a peak-to-peak voltage of 10 kV and frequency of 50 Hz. A current monitor (Bergoz CT-E0.5) was used to record the discharge current. An aluminium foil was wrapped on the surface of the quartz tube as the external electrode wired to the external capacitor (0.47 μF) to calculate the discharge power using *Q-U* Lissajous method. Pure CO_2 gas was introduced in the reactor from the gas cylinder with gas flow of 15-45 ml/min, passing through a mass flow rate controller (MFC).

The product was analysed by a gas chromatograph (Shimadzu GC-2014), equipped with a thermal conductivity detectors (TCD) and a flame ionisation detector (FID). An ozone monitor

(2B, Model 106-M) was used to measure the concentration of ozone. In order to minimise the measurement error, every measurement was repeated three times. The main products of O_2, CO and unreacted CO_2 can be detected by means of the TCD channel for calculating the conversion rate (X), as well as the energy efficiency (η).

For the CO_2 splitting, the conversion rate is defined as:

$$X_{CO_2}(\%) = \frac{CO_2 \text{converted}(\text{mol}\cdot s^{-1})}{CO_2 \text{introduced}(\text{mol}\cdot s^{-1})} \times 100 \quad (3.19)$$

And the energy efficiency, E, is calculated as:

$$\eta(\%) = \frac{CO_{2}\text{converted}(\text{mol}\cdot s^{-1})\cdot \Delta H(\text{kJ}\cdot\text{mol}^{-1})}{\text{Discharge power(kW)}} \times 100 \quad (3.20)$$

where ΔH is the reaction enthalpy of 279.8 kJ/mol.

The maximum value of E/n was observed up to 120 Td. The model can be divided into four main blocks: eleven neutral-neutral reactions; 103 electron-neutral/radical reactions, including momentum transfer, (de)excitation, dissociation and ionization; 5 electron-ion reactions; and 39 ion-neutral/radical/ion reactions (shown in **Appendix 9.1**). All species involved in this model were presented in **Table 3.1**.

Table 3.1 Summary of all species included in the model.

Neutrals and radicals	CO_2, CO_2^*(all excited states), CO, O_2, O_3, C_2O, O
Ions	CO^+, CO_2^+, CO_2^-, O_2^+, O_2^- , O^+, O^-, CO_3^-, CO_3^+, $C_2O_4^+$

3.3.3 Conversion of CO_2 with H_2

The experimental set-up was clearly described in our group's previous work [200]. The simulation results can be validated using the experimental results of that work. The experiment was carried out at atmospheric pressure. The reactor consisted of a pair of coaxial cylinders and two coaxial electrodes. The inner high-voltage electrode was a stainless-steel rod with the out diameter of 13 mm, installed along the axis of the glass tube. The shell of the inner cylinder was a quartz tube, acting as the dielectric barrier. The outer cylinder was wrapped around by a

stainless-steel mesh used as the ground electrode. The discharge length was 100 mm with a fixed discharge gap of 1.5 mm. CH_4 and CO_2 were introduced into the reactor from the gas cylinder with a total gas flow of 69.2 ml/min, passing through MFCs. The DBD reactor was connected to an AC power with a frequency of 9 kHz. The electrical signals were recorded by the four-channel digital oscilloscope (Tektronix, MDO 3024) equipped with a high-voltage probe and a current probe.

The selectivity of the major gas-phase products is written as:

$$S_{CH_4}(\%) = \frac{\text{moles of } CH_4 \text{ produced}}{\text{moles of } CO_2 \text{ converted}} \times 100\% \tag{3.21}$$

$$S_{CO}(\%) = \frac{\text{moles of CO produced}}{\text{moles of } CO_2 \text{ converted}} \times 100\% \tag{3.22}$$

The maximum value of *E/n* was observed up to ~122 Td. This chemical model for this simulation included 263 electron-impact reactions, 348 neutral-neutral reactions and 65 ion-neutral/radical/ion reactions. All simulated species were shown in **Table 3.2**.

Table 3.2 Summary of all species involved in the model.

Ground-state Neutrals & Radicals	CH_4 CH_3 CH_2 CH C C_2H_6 C_2H_5 C_2H_4 C_2H_3 C_2H_2 C_2H C_2 C_3H_8 C_3H_7 C_3H_6 C_3H_5 C_3H_4 C_3H_2 C_4H_2 C_4H_{10} CO_2 CO H_2 H O_2 O H_2O HO_2 OH H_2O_2 CH_2O CH_3CHO CH_2CHO CH_2CO C_2HO CH_3OH CH_3CO CH_2OH CH_3O HCO CH_3O_2 CH_3COOO C_2H_5OO CH_3COOOH CH_3COOH C_2H_5OH CH_3CHOH CH_3COCH_3 HCOOH COOH CH_3COCH_2 CH_3COO
Excited Neutrals & Radicals	$CH_4(v)$ $CO_2(v_{1\text{-}8})$ $CO_2(e_{1\&2})$ $C(^1D)$ $C(^1S)$ $CO(v_{1\text{-}10})$ $CO(e_{1\text{-}5})$ $H_2(j_{0\text{-}2})$ H_2 $(j_{1\text{-}3})$ H_2 $(v_{1\text{-}3})$ H_2 $(e_{1\&2})$ $H_2(\Sigma)$… $H_2(\Pi)$ $O_2(v_{1\text{-}4})$ $H_2(r_{1\&2})$ $O(^1D)$ $O(^1S)$ $H_2O(v_{1\text{-}3})$ $C_2H_2(v_{2,5\&31})$ $C_2H_2(e_{1\&2})$ $C_2H_4(v_{1\&2})$ $C_2H_4(e_{1\&2})$ $C_2H_6(v_{13\&24})$ $C_3H_6(v)$ $C_3H_6(v_{1\&2})$ $C_3H_6(e)$
Charged Species	CH_4^+ CH_3^+ CH_2^+ CH^+ C^+ C_2^+ $C_2H_6^+$ $C_2H_6^+$ $C_2H_6^-$ $C_2H_5^+$ $C_2H_4^+$ $C_2H_3^+$ $C_2H_2^+$ C_2H^+ $C_3H_8^+$ $C_3H_8^-$ $C_3H_6^+$ $C_3H_6^-$ O_2^+ O_2^- O^+ O^- H_2^+ H^+ H^- H_2O^+ CO_2^+ CO^+ OH^-

3.3.4 Dry reforming of CH_4

The experiment was carried out in same DBD reactor as described in **section 3.3.2** at atmospheric pressure. CH_4 and H_2 were introduced into the reactor from the gas cylinder with a total gas flow of 40 ml/min. The DBD reactor was connected to an AC power supply with a peak-peak voltage of 15.8 kV and frequency of 9 kHz.

Notably, the selectivity of C_xH_y was calculated as:

$$S_{CxHy}(\%) = \frac{x \times \text{moles of C}x\text{H}y \text{ produced}}{\text{moles of CH}_4 \text{ converted + moles of CO}_2 \text{ converted}} \times 100\% \quad (3.23)$$

However, 100% carbon balance cannot be achieved for the experiment, because of the coke deposition and residual liquid products in the reactor. Therefore, the selectivity of the liquid products can be calculated as:

The total selectivity of liquid products (%)

$$= 1 - (S_{CO} + S_{CxHy}) - \text{ca.10\% carbon deposition} \quad (3.24)$$

The selectivity of $C_xH_yO_z$ (%)

$$= \text{carbon of C}x\text{H}y\text{O}z \text{ (mol\%) in the liquid product } \times \text{ eq.(3.24)} \quad (3.25)$$

where the carbon deposition is assumed to be 10% in the equation (3.24). Moreover, equation (3.26) was for obtaining the simulation results of the selectivity of liquid products.

$$S_{CxHyOz}(\%) = \frac{x \times \text{moles of C}x\text{H}y\text{O}z \text{ produced}}{\text{moles of CH}_4 \text{ converted + moles of CO}_2 \text{ converted}} \times 100\% \quad (3.26)$$

The maximum value of E/n was observed up to 120 Td. This model included 263 electron-impact reactions, 348 neutral-neutral reactions and 65 ion-neutral/radical/ion reactions. All simulated species were shown in **Table 3.3**.

Table 3.3 Summary of all species included in the model.

Ground-state Neutrals & Radicals	CH_4 CH_3 CH_2 CH C C_2H_6 C_2H_5 C_2H_4 C_2H_3 C_2H_2 C_2H C_2 C_3H_8 C_3H_7 C_3H_6 C_3H_5 C_3H_4 C_3H_2 C_4H_2 C_4H_{10} CO_2 CO H_2 H O_2 O H_2O HO_2 OH H_2O_2 CH_2O CH_3CHO CH_2CHO CH_2CO C_2HO CH_3OH CH_3CO CH_2OH CH_3O HCO CH_3O_2 CH_3COOO C_2H_5OO CH_3COOOH CH_3COOH C_2H_5OH CH_3CHOH CH_3COCH_3 HCOOH COOH CH_3COCH_2 CH_3COO
Excited Neutrals & Radicals	$CH_4(v)$ $CO_2(v_{1\text{-}8})$ $CO_2(e_{1\&2})$ $C(^1D)$ $C(^1S)$ $CO(v_{1\text{-}10})$ $CO(e_{1\text{-}5})$ $H_2(j_{0\text{-}2})$ $H_2(j_{1\text{-}3})$ $H_2(v_{1\text{-}3})$ $H_2(e_{1\&2})$ $H_2(\Sigma)$… $H_2(\Pi)$ $O_2(v_{1\text{-}4})$ $H_2(r_{1\&2})$ $O(^1D)$ $O(^1S)$ $H_2O(v_{1\text{-}3})$ $C_2H_2(v_{2,5\&31})$ $C_2H_2(e_{1\&2})$ $C_2H_4(v_{1\&2})$ $C_2H_4(e_{1\&2})$ $C_2H_6(v_{13\&24})$ $C_3H_6(v)$ $C_3H_6(v_{1\&2})$ $C_3H_6(e)$
Charged Species	CH_4^+ CH_3^+ CH_2^+ CH^+ C^+ C_2^+ $C_2H_6^+$ $C_2H_6^+$ $C_2H_6^-$ $C_2H_5^+$ $C_2H_4^+$ $C_2H_3^+$ $C_2H_2^+$ C_2H^+ $C_3H_8^+$ $C_3H_8^-$ $C_3H_6^+$ $C_3H_6^-$ O_2^+ O_2^- O^+ O^- H_2^+ H^+ H^- H_2O^+ CO_2^+ CO^+ OH^-

3.3.5 Steam reforming of CH_4

The reactor consisted of a quartz tube (13 mm od × 10 mm id). A stainless-steel rod as the inner high-voltage electrode with the out diameter of 5 mm was installed along the axis of the glass tube. A stainless-steel mesh was wrapped around the tube as the ground electrode and the discharge length was 100 mm with a fixed discharge gap of 2.5 mm. The DBD reactor was supplied by a high-voltage AC power supply with a maximum peak-peak voltage of ~17 kV and frequency of 9 kHz.

CH_4 was introduced from the gas cylinder and passed through a bottle (filled with water) which was immersed in a water bath (from ambient temperature to 70 ^oC) to carry and mix with steam. Correspondingly, the range of steam concentration was from 2.5% to 31%. The total flow rate was fixed at 40 ml/min.

The conversion of D_2O was written as:

$$\text{Conversion of } D_2O = \frac{n_{D_2O,in} - n_{D_2O,out}}{n_{D_2O,in}} \times 100\% \quad (3.27)$$

$$\text{Yield of } C_xH_y = \frac{x \times n_{CxHy,out}}{n_{CH_4,in}} \times 100\% \quad (3.28)$$

$$\text{Yield of CO} = \frac{n_{CO,out}}{n_{CH_4,in}} \times 100\% \quad (3.29)$$

$$\text{Yield of } H_2 = \frac{n_{H_2,out}}{2 \times n_{CH_4,in} + n_{D_2O,in}} \times 100\% \quad (3.29)$$

where x = 1, 2, 3…, y = x, 2x or 2x+2 (i.e. C_2H_2, C_2H_4, C_2H_6…). Additionally, all heterogeneous isotope carriers were considered, when these output parameters were calculated. The isotope carriers of CH_4 contained CD_4, CHD_3, CH_2D_2, and CH_3D (isotope carriers of more species will be listed in the following sections). The maximum value of *E/n* was observed up to ~119 Td. The cross sections for D/D_2 are adopted from the literature [189, 190, 201].

However, owing to adding of deuteroxide was the reactant, the model had to be upgraded, including 274 electron-impact reactions, 442 neutral-neutral reactions and 65 ion-neutral/radical/ion reactions. All simulated species are shown in **Table 3.4**.

Table 3.4 Summary of all species included in the model.

Ground-state Neutrals & Radicals	CH_4 CH_3 CH_2 CH C C_2H_6 C_2H_5 C_2H_4 C_2H_3 C_2H_2 C_2H C_2 C_3H_8 C_3H_7 C_3H_6 C_3H_5 C_3H_4 C_3H_2 C_4H_2 C_4H_{10} CO_2 CO H_2 H O_2 O H_2O HO_2 OH H_2O_2 CH_2O CH_3CHO CH_2CHO CH_2CO C_2HO CH_3OH CH_3CO CH_2OH CH_3O HCO CH_3O_2 CH_3COOO C_2H_5OO CH_3COOOH CH_3COOH C_2H_5OH CH_3CHOH CH_3COCH_3 HCOOH COOH CH_3COCH_2 CH_3COO D D_2 D_2O OD HD DO_2 DCO HDO HDO_2 D_2O_2 CD_4 CD_3 CD_2 CD CH_3D CH_2D_2 CHD_3 CHD CHD_2 CH_2D C_2D_6 C_2D_5 C_2D_4 C_2D_3 C_2D_2 C_2H_5D C_2H_4D C_2HD_4 C_2H_3D $C_2H_2D_2$ C_2HD_2 C_2HD C_2D COD_3 CD_2O CD_2OD CD_3CDO COD_3C C_2H_4OD CHDO COD_3H C_2H_5OD COD_3CD
Excited Neutrals & Radicals	$CH_4(v)$ $CO_2(v_{1\text{-}8})$ $CO_2(e_{1\&2})$ C(^1D) C(^1S) $CO(v_{1\text{-}10})$ $CO(e_{1\text{-}5})$ $H_2/D_2(j_{0\text{-}2})$ $H_2/D_2(j_{1\text{-}3})$ $H_2/D_2(v_{1\text{-}3})$ $H_2/D_2(e_{1\&2})$ $H_2/D_2(\Sigma)$… $H_2(\Pi)$ $O_2(v_{1\text{-}4})$ $H_2(r_{1\&2})$ O(^1D) O(^1S) $H_2O(v_{1\text{-}3})$ $C_2H_2(v_{2,5\&31})$ $C_2H_2(e_{1\&2})$ $C_2H_4(v_{1\&2})$ $C_2H_4(e_{1\&2})$ $C_2H_6(v_{13\&24})$ $C_3H_6(v)$ $C_3H_6(v_{1\&2})$ $C_3H_6(e)$

Charged Species	CH_4^+ CH_3^+ CH_2^+ CH^+ C^+ C_2^+ $C_2H_6^+$ $C_2H_6^+$ $C_2H_6^-$ $C_2H_5^+$ $C_2H_4^+$ $C_2H_3^+$ $C_2H_2^+$ C_2H^+ $C_3H_8^+$ $C_3H_8^-$ $C_3H_6^+$ $C_3H_6^-$ O_2^+ O_2^- O^+ O^- H_2^+ H^+ H^- H_2O^+ CO_2^+ CO^+ OH^- D_2^+ D^+ D^-

Using computer simulations in combination with experiments, this PhD work contributes to investigation of several DBD plasma-assisted reactions for a better understanding of the complex plasma chemistry and illuminating the major reaction mechanisms.

Chapter 4 Computational study of effect of vibrational excitations on CO_2 conversion in a DBD reactor

This chapter is to analyse pure CO_2 splitting process in a DBD reactor at atmospheric pressure by means of computer simulations, while the experiments conducted under the same operating conditions can validate this model to investigate the mechanism. O_2 and CO are the valuable gases for the chemical industry. As a result, it is necessary to obtain the optimum operating conditions for CO_2 splitting and advanced computer simulation is very helpful tool to define these conditions, corresponding to the highest conversion rate and energy efficiency. Simulation of CO_2 splitting has been revealed by many groups with eminent explanations on the vibrational kinetics, but few researchers have investigated the transfer process among each excitation level of CO_2, especially for the deexcitation process. Except for dissociating the OC=O bond (~178 kcal/mole, around 7.6 eV) directly, in plasma, CO_2 can be split by the vibrational excitations, if the stored energy of OC=O bonds reach 5.5 eV. Obviously, not all electrons can gain the sufficient energy (> 5.5 eV or 7.6 eV) from the electric field to decompose the CO_2 molecules, based on the EEDFs [26, 27, 42, 202-209]. Vibrational excitations make a significant contribution to the energy accumulation on C=O chemical bonds for CO_2 dissociation. However, the real life-time of the excited CO_2 molecules is extremely short. In the other words, the deexcitations waste the accumulated energy and decline the energy efficiency.

The major reactions involved in CO_2 splitting were simulated to expound the effects on CO_2 conversion of the operating conditions, including discharge power, inlet flow rate and discharge length. Moreover, this chapter then focused on the analysis of the effects of different excitation levels on CO_2 conversion, calculated by quantum energy of CO_2 molecules, to determine the dominated excited state for decomposing CO_2 molecules. Finally, CO_2 could be decomposed by the methods of either vibrational excitations or dissociation of C=O chemical bond, so this work determined the contribution of these two major methods for CO_2 splitting, considering about all the deexcitation reactions of CO_2.

4.1. Excitation levels.

According to Fridman's work [83], there are three main vibrational excitations of CO_2: symmetric stretching mode (n00), bending mode (0n0), and asymmetric stretching mode (00n). According to the quantum energy ($\hbar\omega_i$, i =1, 2 and 3), these three modes also can be characterised into v_1, v_2, v_3, with $\hbar\omega$= 0.17 eV, 0.08 eV and 0.30 eV, respectively. As an example of bending mode, "010" represents the 1st bending of the vibrational excitation. The rule for notation remains the same as for asymmetric and symmetric modes. Moreover, for the bending mode and symmetric stretching mode, the CO_2 vibrational levels can be calculated by means of anharmonic oscillator approximation formula (4.1) and angular momentum of the quasi-rotation is characterised by a special quantum number "l_2", which assumes the values as: $l_2 = v_2, v_2 - 2, v_2 - 4, \ldots, 1$ or 0

$$\frac{E_{CO_2}}{hc} = \sum_i \omega_i(\upsilon_i + d_i/2) + \sum_{j\geq i} x_{ij}(\upsilon_i + d_i/2)(\upsilon_j + d_j/2) + x_{l_2 l_2} l_2^2 \tag{4.1}$$

where ω_i, x_{ij} and $x_{l_2 l_2}$ are spectroscopic constants defined by Friedman [83] and $d_i = (d_1 d_2 d_3)$ are the degeneracies of the three vibration modes. For the 1st bending mode, d_i is equal to the number of 010 and the energy level is equal to 0.08 eV after calculating. However, when the d_i is set to (020) for the calculation of 2nd bending mode, the energy level observed is 0.17 eV. Therefore, the 1st symmetric stretching could take place at the same time in the plasma process, and the excited state can be considered as "020+100 = 120 = d_i". After calculating the value of di, the excitation energy level and certain excitation mode can be obtained. However, if the energy level exceeded $\hbar\omega_3$ = 0.30 eV, the asymmetric stretching would happen. Therefore, the energy level of 0.30 eV can be treated as an interval between higher and lower excitation levels, while the total vibrational energy at lower excitation levels can be written as (4.2) [83]:

$$Ev(v1, v2, v3) = \hbar\omega_1(v_1 + 0.5) + \hbar\omega_2(v_2 + 1) + \hbar\omega_3(v_3 + 0.5) + x_{11}(v_1 + 0.5)^2 + x_{22}(v_2 + 1)^2 + g_{22}l_{22} + x_{33}(v_3 + 0.5)^2 + x_{12}(v_1 + 0.5)(v_2 + 1) + x_{13}(v_1 + 0.5)(v_3 + 0.5) + x_{23}(v_2 + 1)(v_3 + 0.5) \tag{4.2}$$

where $x_{11} = -0.47 \times 10^{-3}$ eV, $x_{22} = -0.08 \times 10^{-3}$ eV, $x_{33} = -1.6 \times 10^{-3}$ eV, $x_{12} = 0.45 \times 10^{-3}$ eV, $x_{13} = -2.4 \times 10^{-3}$ eV, and $x_{23} = -1.6 \times 10^{-3}$ eV are anharmonicity coefficients and g_{22} is the energy coefficient depend on the quantum number l_2. In this project, because of the lack

of data for higher asymmetric excitation modes, the "00n" mode excitations are calculated by using the total vibrational energy, *Ev*, of CO_2 (4.3) subtracting the total value of vibrational energy, $E_{sym,}$ from all symmetric modes in harmonic approximation (4.4).

$$Ev(v_a, v_s) = \hbar\omega_a v_a + \hbar\omega_s v_s - x_a v_a^2 - x_s v_s^2 - x_{as} v_a v_s \quad (4.3)$$

$$Esym = \hbar\omega_1 v_1 + \hbar\omega_2 v_2 = \hbar\omega_2 (2v_1 + v_2) = \hbar\omega_s v_s \quad (4.4)$$

where x_a is the coefficients of anharmonicity for total excitation levels, and x_{as} = 12 cm^{-1}.

Therefore, all excited modes and energy levels can be obtained and summarised in **Table 4.1**. All excited CO_2 molecules were notated by this project in the own method to simplify the simulation. Moreover, the 7.0 eV level was simulated as the electronic excitation, considering about the impact of the electrons with higher electron temperature (> 5.5-7 eV) existing in the plasma gas.

Table 4.1 Excitation levels and excited modes simulated in the model [83].

Model Notation	States	Energy Levels (eV)
CO_2	(000)	0.00
CO_2v_a	(010)	0.08
CO_2v_b	(020) + (100); (110) + (010)	0.17
CO_2v_c	(030) + (110)	0.25
CO_2v_d	(001); (120) + (030); (130) + (020)	0.29
CO_2v_1	(001)	0.34
CO_2v_2	(002)	0.4
CO_2v_3	(003)	0.5
CO_2v_4	(004)	2.5
CO_2v_5	(005)	5.5
CO_2e	Electronic excitation	7.0-10.5

Generally, the asymmetric vibrational modes (VV) of CO_2 molecules are predominantly generated under electron energy of 1 – 3 eV, and the relaxation rate is much faster than the symmetric modes (VT). Moreover, the VT relaxation can help VV mode accumulate more energy for decomposition of CO_2. However, VV modes intensify the excited vibrational states dramatically and contribute more population to dissociation of CO_2.

4.2 Effect of discharge power

In this case, the discharge power played a significant role in the CO_2 conversion. The range of discharge power for the experiments and simulations was between 10 W and 90 W. Additionally, the inlet flow rate and discharge length were fixed at 25 ml/min and 100 mm, respectively. In **Figure 4.1**, the experimental and simulation conversion rates and energy efficiency of CO_2 were illustrated versus different discharge powers. In terms of the conversion rate, it increased with the discharge power, but then stayed at a saturated maximum value of ~ 26 %. Indeed, the effect of the growing discharge power mostly can be neglected after 70 W. when the discharge was stable, the electric field on gas and mean electron energy approximately remained as a constant. However, the electron density can be raised at a higher discharge power, because of the increment of channels of filamentary discharges. Moreover, the maximum efficiency (9.8 %) was obtained with a lowest discharge power (10 W) and it obviously decreased dramatically in the power range between 10 and 50 W. It seemed that a considerable part of input energy had been wasted. More details on the effects of discharge power would be discussed later, based on the excitations of CO_2. However, before that, the first speculation for the power consumption was momentum transfer (elastic collision), corresponding to the excited state of "000".

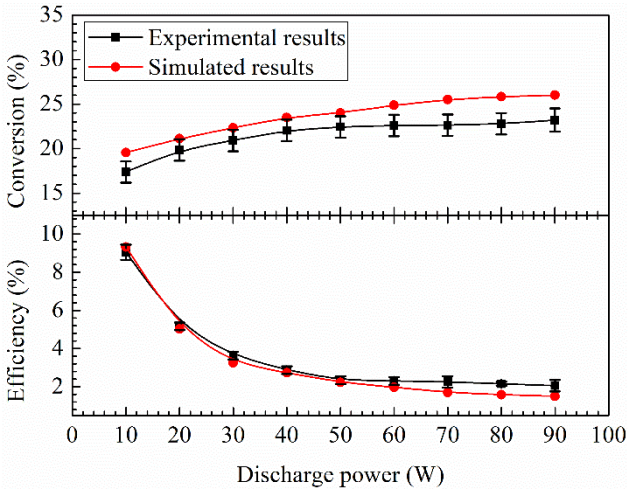

Figure 4.1 Effect of discharge power on CO_2 conversion and energy efficiency at a flow rate and discharge length of 25 ml/min and 100 mm with a fixed discharge gap of 2.5 mm.

Elastic collisions occured instantaneously when the electrons collide with other particles in plasma gas, causing the waste of energy immediately, and there was no energy transferred to the C=O bonds. All reaction rate coefficients for the elastic collision versus the increasing discharge power were plotted in **Figure 4.2**. This figure clearly disclosed that the energy loss

fraction and reaction rate coefficient became larger at a higher discharge power. The increasing energy loss fraction could be explained by deexcitations.

Deexcitations occurred during the entire process, caused by collisions among either low-energy-stored electrons or neutrals. A higher electron energy can be provided by a longer mean free path. On one hand, because the gas density increased with a higher conversion rate of CO_2 ($2CO_2 \rightarrow 2CO + O_2$), the mean free path was shortened and the proportion of the electrons with lower energy was increased. It increased the possibility that excited CO_2 was deexcited by collision with electrons. On the other hand, with the increasing density of neutrals, the probability of collision between excited CO_2 and neutrals was also increased. All these reasons can increase the energy loss due to deexcitation of CO_2 to a lower level state (< 5.5 eV) or even to the ground state ("000" excitation state). Therefore, a lower pressure and higher operating temperature can provide a lower gas density for better conversion rate of CO_2.

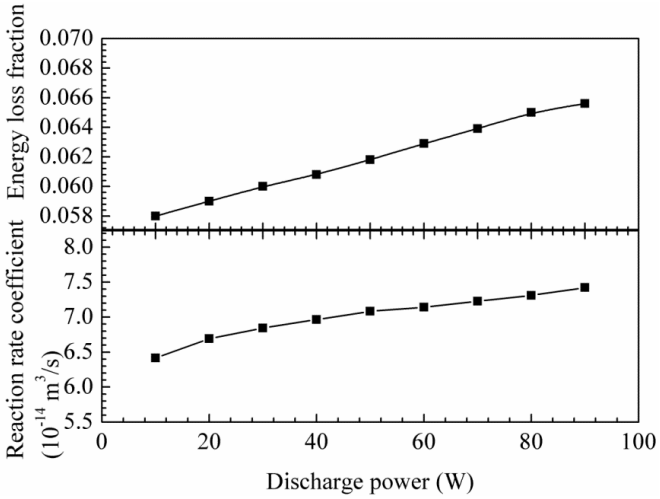

Figure 4.2 Effect of discharge power on the varied energy loss fractions and reaction coefficients of elastic collision ("000" excitation state).

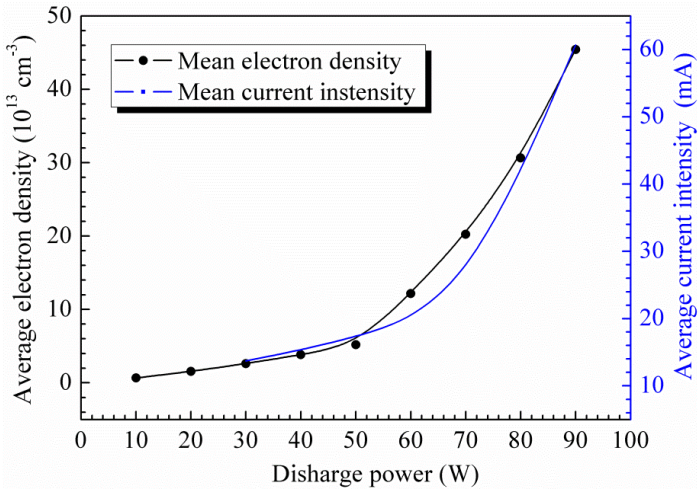

Figure 4.3 Average simulation electron density under different discharge power.

When the plasma gases were broken down, the gas voltage reached a very low value and would recover to the breakdown voltage gradually, because of the applied voltage. The mean electron energy is not improved rapidly by the increasing discharge power/voltage, because the breakdown voltage in this case was not changed dramatically. This enhancement of conversion rate of CO_2 was caused by the improvement of electron density. As a result, the electron density under various discharge powers was investigated using this model. Based on the spherical coordinates in velocity, the equation (3.1) can be written as:

$$\frac{\partial f}{\partial t} + v cos\theta \frac{\partial f}{\partial z} - \frac{e}{m} E \left(cos\theta \frac{\partial f}{\partial v} + \frac{sin^2\theta}{v} \frac{\partial f}{\partial cos\theta} \right) = C[f] \tag{4.5}$$

The equation above can be written as equation (4.6), using the basic two-term approximation (in terms of Legendre polynomial of cosθ) [186].

$$f(v, \cos\theta, z, t) = f_0(v, z, t) + f_1(v, z, t) \cos\theta \tag{4.6}$$

$$\frac{\partial f_1}{\partial t} + \mathrm{G}\sqrt{\varepsilon}\frac{\partial f_0}{\partial z} - E\mathrm{G}\sqrt{\varepsilon}\frac{\partial f_0}{\partial \varepsilon} = -N\sigma\mathrm{G}\sqrt{\varepsilon} f_1 \tag{4.7}$$

where z is the position coordinate, f_0 represents the isotropic part and f_1 is an anisotropic perturbation. Usually, in order to solve the BE, it is still needed to make assumptions about f_0 and f_1 on temporal and spatial dependence, individually.

$$f_{0,1}(\varepsilon, z, t) = \frac{1}{2\pi \mathrm{G}^3} F_{0,1}(\varepsilon) n(z, t) \tag{4.8}$$

For the temporal growth of the electron density, it corresponds to Pulsed Townsend experiments[186], and it is related to the net production frequency $\overline{\nu}_i$

$$\frac{1}{n_e}\frac{\partial n_e}{t} = \overline{v}_i \equiv NG\int_0^\infty (\sum_{ionisation} x_k\,\sigma_k - \sum_{attachment} x_k\,\sigma_k) \times \varepsilon F_0 d\varepsilon \quad (4.9)$$

However, as mentioned above, this case was focussed on steady-state simulation, corresponding to Steady-state Townsend experiments. The electron density will then increase exponentially with a rate α_r in terms of the spatial growth.

$$\alpha_r \equiv -\frac{1}{n}\frac{\partial n}{\partial z} = -\frac{\overline{v}_i}{v} \quad (4.10)$$

It needs to be noticed here, *v* is the mean electron velocity defined by F_1. Using of the definition of α_r and equation (4.8), F_1 can be obtain:

$$F_1 = \frac{1}{\sigma_m}\left(\frac{E}{n}\frac{\partial F_0}{\partial \varepsilon} + \frac{\alpha_r}{n}F_0\right) \quad (4.11)$$

Here, the total momentum-transfer cross section:

$$\sigma_m = \sum_k x_k \sigma_k \quad (4.12)$$

$$v = \frac{1}{3}\gamma\int_0^\infty F_1 \varepsilon d\varepsilon \equiv -\mu E + \alpha_r D = -\frac{\overline{v}_i}{\alpha_r} \quad (4.13)$$

where D is the diffusion coefficient. The growth of electron density was illustrated in **Figure 4.3**. Both the number of filamentary discharge and amplitude were enhanced, so the current density would not appear as a linear growth trend and the increment of electron density was also non-linear. The filamentary discharge became much more intensive at the discharge power from 50 W to 70 W, causing a dramatic rising of the electron density.

4.3 Effect of inlet gas flow rate

This work performed more experiments using different inlet gas flow rates (or residence time) to validate the model and observe the influences of inlet gas flow on conversion of CO_2. The range of flow rate was set from 25 to 125 ml/min with a constant discharge power of 50 W and discharge length of 100 mm. In **Figure 4.4**, an increasing inlet flow rate provided a lower conversion rate and higher energy efficiency. The conversion rate at the flow rate of 125 ml/min was only half of the one at 25 ml/min. Moreover, the effect of inlet flow rate on energy efficiency was not very distinct when the flow rate was greater than 105 ml/min and reached the saturated value of 5 %. Less energy was accumulated on the C=O bonds under a shorter residence time and all electron-impact which can decompose CO_2 molecule were weakened,

so the improvement of energy efficiency was restricted. More details of the influence of the electron-impact process will be discussed in the next section.

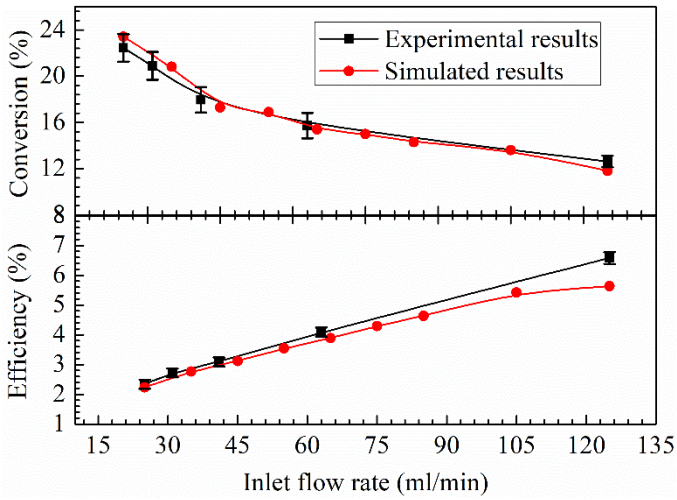

Figure 4.4 Effect of inlet flow rate on CO_2 conversion and energy efficiency at a discharge power and discharge length of 50 W and 100 mm with a fixed discharge gap of 2.5 mm.

4.4 Effect of discharge length

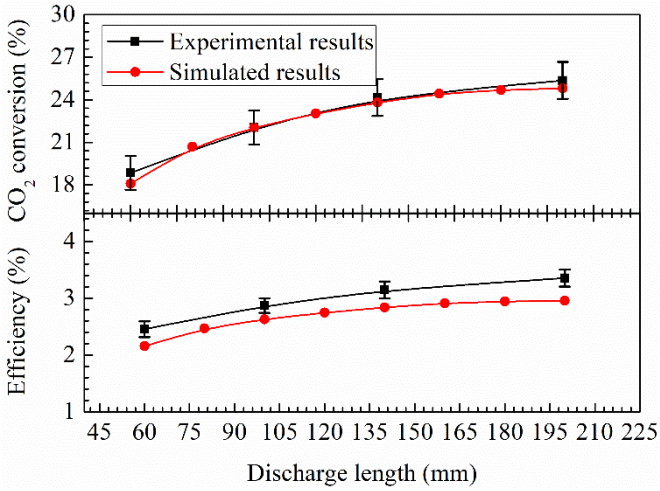

Figure 4.5 Effect of discharge length on CO_2 conversion and energy efficiency at a discharge power and inlet flow rate of 40 W and 25 ml/min with a fixed discharge gap of 2.5 mm.

The effect of the discharge length was very similar to the effect of inlet flow rate. A higher resident time can be obtained under a longer discharge length. However, the power density can be decreased with a longer discharge length or larger volume. That was the reason why the CO_2

conversion and efficiency energy were enhanced slightly. The maximum conversion rate under discharge power of 40 W and flow rate of 25 ml/min was around 24%.

Through the experiments, the model was validated. All simulation results reached a consensus with the experimental ones. Therefore, for a better understanding of the CO_2 splitting, the mechanism of CO_2 splitting would be investigated in the next section.

4.5 Vibrational effects on CO_2 splitting

This section invesigate the behaviour of the excited CO_2 at different excitation levels for CO_2 splitting, including (de)excited processes. If energies of all electrons in the DBD were greater than the C=O bond dissociation energy (7.6 eV), all CO_2 would be decomposed by dissociating the C=O bonds or ionised directly. However, based on the EEDF in this case, as shown in **Figure 4.12**, the density of electrons with a lower energy (< 5.5 eV) was higher. Therefore, many electrons cannot break down the C=O bond of CO_2 directly. However, as mentioned above, CO_2 molecule can also be dissociated by the vibrational excitations, written in equation (4.14).

$$CO_2^* \Rightarrow CO + O,\ E = 5.5\ eV \qquad (4.14)$$

CO_2 was excited from ground state to higher states by collision with electrons and started to accumulate energy on C=O bond up to 5.5 eV by continuous collisions with other electrons. **Figure 4.6** illustrated all rate coefficients of the excitation reactions.

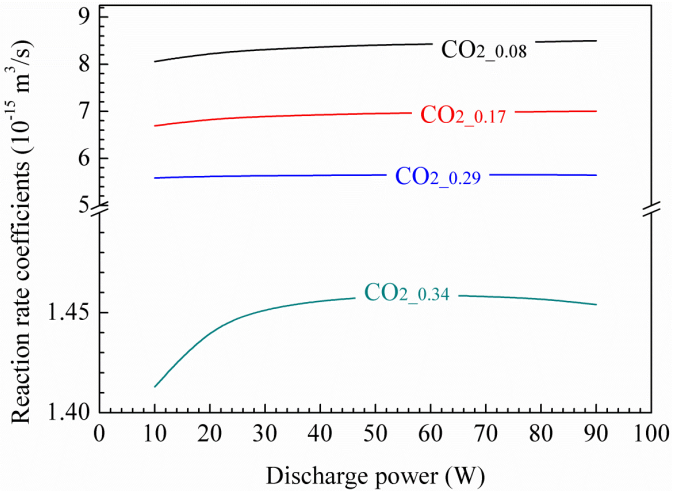

(a)

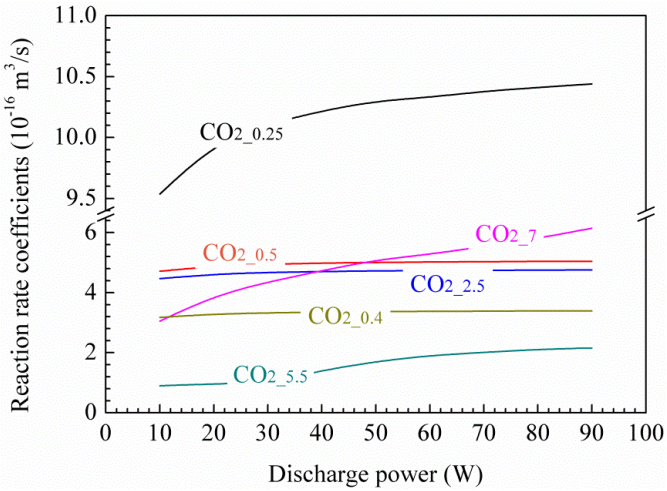

(b)

Figure 4.6 Reaction rate coefficient for each excited level.

Generally, the rate coefficients of asymmetric stretching modes (VV) were much lower than the ones of the symmetric stretching and bending (VT) excited modes, thus the fractions of CO_2 in VT modes should rise faster. These figures clearly indicated that all rate coefficients increased with an increasing plasma power, but the excitation process was dominated by the VT excitation modes, causing a lower energy stored in excited CO_2 molecules. In other words, more reactive species with lower energy were generated during the plasma-assisted CO_2 splitting process.

Clearly, under the same operating conditions, the generation rate of excited CO_2 at level of 5.5 eV (dissociation limit) was the lowest, because excited CO_2 was decomposed with stored-energy of 5.5 eV. However, 5.5 eV can be achieved by excitation of CO_2 from either the ground state or a lower excited state (energy accumulation), whereas CO_2v_5 excited from ground state can be decomposed directly. The deexcitation processes occurred during the energy accumulation before the energy reached the dissociation limit. Additionally, if the CO_2 splitting by vibrational excitations became more significant, more energy would be consumed by transitions among every excited level. Therefore, as the effects of deexcitations cannot be ignored, the reaction rates coefficients of deexcitations were required to be investigated.

Figure 4.7 showed the calculated reaction rate coefficients for the simplest deexcitation, where excited CO_2 was deexcited by electron collisions to the ground state directly. Firstly, this figure expounded that the rate coefficients of excitation processes were much faster than the ones for deexcitations. A longer residence time would make more CO_2 molecules become reactive

species with higher stored energy and it testified why the conversion rates of CO_2 were improved by the falling inlet flow rate and rising discharge length in **Figure 4.4 and Figure 4.5**. Secondly, all coefficients decreased with a higher discharge power. A higher input energy increased the number of discharge channels (filaments) of DBD, thus CO_2 molecules were very likely to be excited again by the electrons. Hence, higher electron density provided a higher possibility of excitations. Finally, CO_2 in the VT were more likely to be deexcited to the ground state. As mentioned above, deexcitations of excited CO_2 may occur after any electron collision, thus a higher electron density could promote the deexcitation process. However, CO_2 with higher stored energy (> 5 eV) was more difficult to be deexcited back to the ground state, so these excited CO_2 molecules still existed in plasma at the lower excitation levels after deexcitations. Except for the ground state, excited CO_2 could also be deexcited to any lower states through a more complex process. In order to understand the relationship, the representative deexcited rate coefficients chosen from VT and VV modes were investigated.

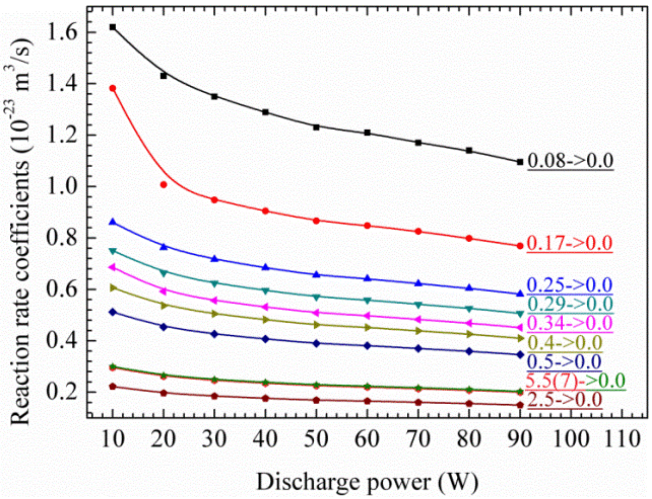

Figure 4.7 Reaction rate coefficients for excited CO_2 at all levels being deexcited back to ground state directly.

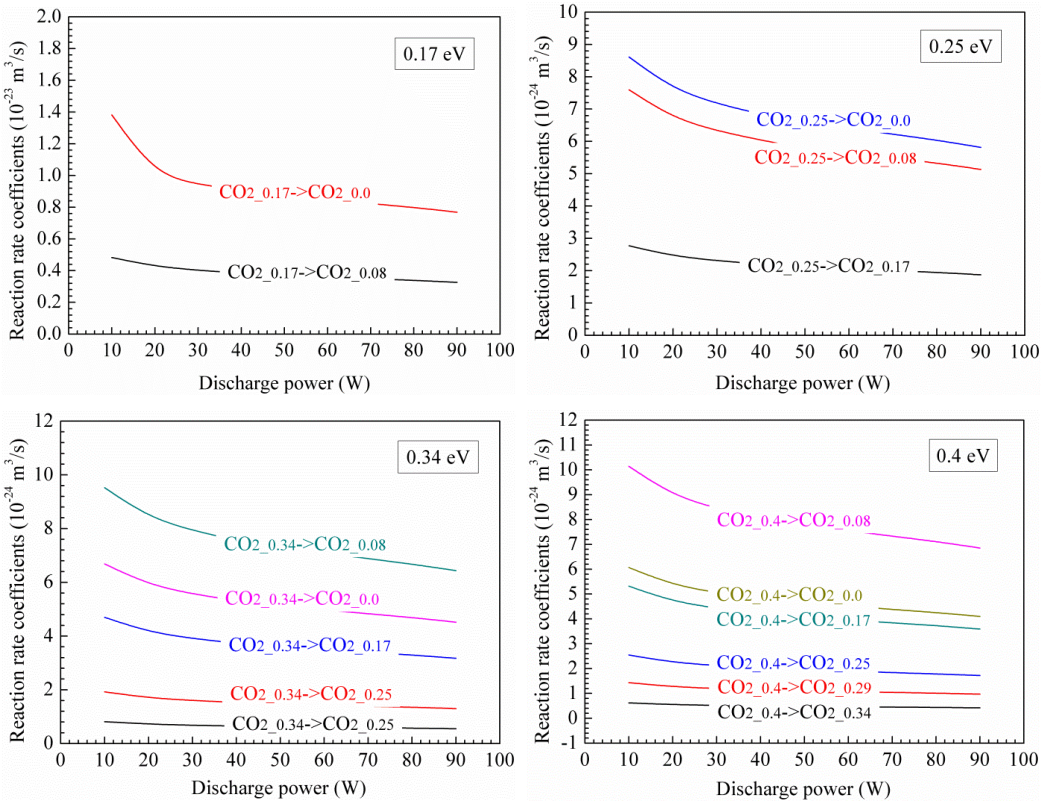

Figure 4.8 Different deexcitation rate coefficients for excited CO_2 at various energy levels. (VT modes: 0.17 & 0.25 eV; VV modes: 0.34 & 0.4 eV)

This work calculated the all rate constants among the deexcited processes. **Figure 4.8** showed the examples from the VT (0.17 eV and 0.25 eV level) and VV (0.34 eV & 0.4 eV level) modes of excited CO_2 to the ground state or a lower state. All rate coefficients declined with an increasing discharge power. Thus, it verified that discharge power made the deexcitations slower. It is worthwhile noting that the VT mode excitations were deexcited back to the ground state faster than being deexcited to a lower state. Inversely, most of the excited CO_2 with VV modes (with higher stored energy) were deexcited back to 0.08 eV level rather than to the ground state. For excitation process, 1st bending mode with the energy of 0.08 eV was the dominated excitation type under various discharge power, according to the rate constant, as shown in **Figure 4.6 (a)**. It implied that the 0.08 eV excitation state (1st bending) could be the major excitation type during CO_2 splitting. The energy of CO_2v_a was still much lower than the dissociation limit, so the energy consumed on excitation of CO_2v_a was large. However, a higher discharge power improved the density of the excited CO_2 with higher stored-energy as the reactive species.

The fractions of the excited CO_2 at every level were calculated to provide a more accurate analysis. **Figure 4.10** illustrated that the densities of species at the power of 10-50 W were from 10^{16} to 10^{17} cm^{-3} and up to 10^{19} cm^{-3} at the power of 90 W. The fractions of CO_2 at higher vibrational levels (VV modes) were much lower. The density of CO_2 at the 0.25 eV level classified as VT mode appeared very low. The reaction rate coefficient of this level was greater than the coefficients of VV mode, while the deexcitation rate coefficient was lower than the 1st bending mode. Therefore, the density of 0.25 eV should be larger than the densities of VV mode as expected. The reason for this phenomenon could only be explained by the energy loss fraction on this type of excitation, thus this work carried out an investigation to demonstrate this assumption, as shown in **Figure 4.9**.

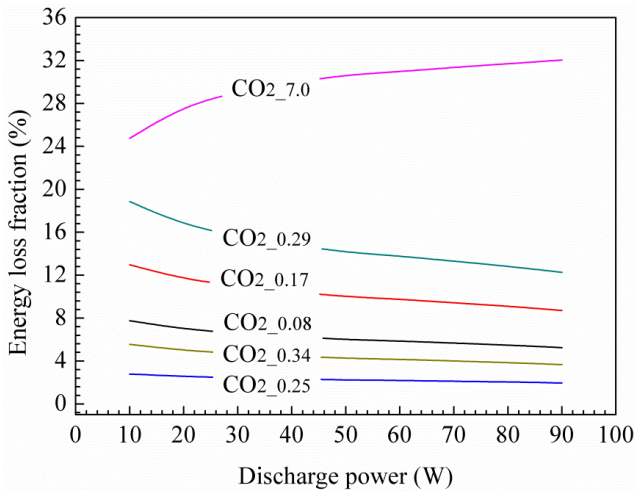

Figure 4.9 Energy loss fractions on examples of VT and VV modes.

Clearly, energy loss fraction of 0.25 eV excitation level was the lowest among the VT modes and some of VV mode excitations. Thus, its generation rate would not be high, even if its reaction rate coefficient was high with a low deexcitation rate coefficient. Therefore, the density of excited CO_2 at 0.25 eV would not be affected by discharge power dramatically. There was another important phenomenon observed in **Figure 4.10**. More than 33% of electron energy was used for electronic excitations of CO_2 splitting at a discharge power of 90 W, causing more ionisation of CO_2. Comparing 5.5 eV to 7.0 eV excitation level, the production rate coefficients were equal at the discharge power of ~50 W with a similar deexcitation rate, but the density of CO_2 at 7.0 eV level was almost 3 times larger than the one at 5.5 eV. Therefore, it implied that the relaxation rate of 5.5 eV excited level was almost 3 times faster than the 7.0 eV. Based on the energy loss fraction in **Figure 4.9**, the production fractions of

high-level excitations should rise significantly. Nevertheless, the distribution of high-level excitations only improved slightly (less than 1%) with the increasing discharge power. It also indicated that a higher discharge power can raise the density of the reactive species remarkably, but undue high electron density and low-energy-stored species restricted the generation of CO_2 at high level excitations, due to redundant electron collisions.

The density of inlet CO_2 was fixed, because of the constant operating temperature and pressure. Moreover, the reaction rate constant of each electron-impact only changed slightly (±10 %) under various discharge powers, thus all reaction rates of electron-impact reactions were strongly relied on the electron density. The electron density rose rapidly at the discharge power of 50 W, so there was a significant rise in the density of the excited CO_2 under all levels. The total density of VT mode excitations was much larger than the one of the VV mode under various power conditions.

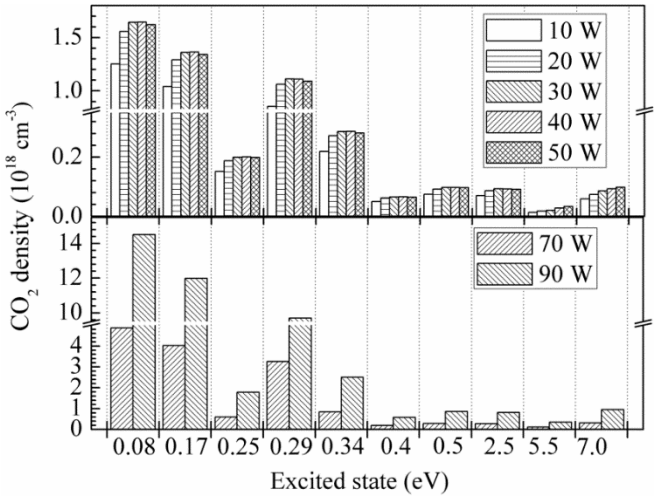

Figure 4.10 Distribution of excited CO_2 at individual level under different discharge powers.

After investigation of the excitations within each excited level, it was still needed to understand how the vibrational excitations affect the overall CO_2 splitting process. There was an assumption that all CO_2v_5 molecules would be dissociated by vibrational excitations, and then the reaction (equation 4.14) was removed from our model to determine the quantity of CO_2v_5 generated during the whole residence time. As such, the calculation of contribution of vibration excitations was available, as defined in **Figure 4.11**.

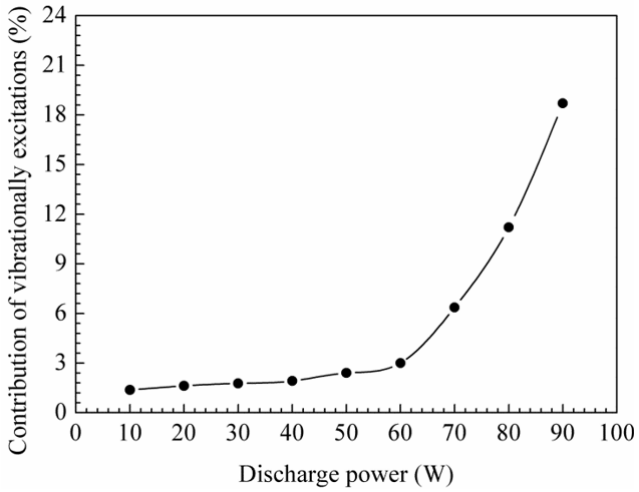

Figure 4.11 Contributions of vibrational excitations for CO_2 splitting under different powers.

Figure 4.11 clearly indicated that the contribution of vibrational excitations for CO_2 splitting was affected by the discharge power or electron density of plasma. In this case, when the electron density reached the maximum value of 3.9×10^{14} cm^{-3}, 18.7 % of converted CO_2 was caused by vibrational excitations. If one mole (2.68×10^{19}) of CO_2 molecules inlet to our DBD reactor, 5.24×10^{18} of CO_2 molecules (at room temperature and atmospheric pressure) would be converted under discharge power of 10 W with the energy efficiency of 9.8 %, while 6.97×10^{18} molecules can be converted under discharge power of 90 W. Therefore, from 10 to 90 W, the ~tenfold energy was required to improve 33 % increment of CO_2 conversion due to the enhancement of deexcitations. Moreover, if all C=O bonds of CO_2 were dissociated by vibrational excitations (5.5 eV), the energy efficiency could be improved. The electron density with the energy of 5.5eV was more than 5 times the one with the energy of 7.6 eV, shown in **Figure 4.12** (represented in $\log_2$ base). Therefore, taking account into the reaction rate (equation 3.4), more CO_2 molecules were dissociated by vibrational excitations rather than by dissociation of the C=O bond. However, the energy efficiency was decreasing with a higher discharge power, and deexcitation processes, caused by redundant collisions of electrons, restricted the enhancement of the energy efficiency. Therefore, based on this work, it is claimed that CO_2 conversion can be improved dramatically by a better EEDF with higher high-energy-stored electron density rather than increasing the discharge power (or electron density). As the electric field applied on discharge gap stayed almost unchanged at a saturated level under the same operating pressure and temperature, the enhanced EEDFs for CO_2 can only be obtained by a different gas composition. The composition of plasma gas would not be affected considerably in the plasma-only reaction due to a relatively lower conversion rate, so the mixture with a carrier gas, such as argon (Ar), was a viable method to optimise the EEDFs.

The various calculated EEDFs with different ratio of CO_2/Ar were illustrated in **Figure 4.12**. Obviously, the probability density of the electrons with high energy (> 5.5) was increasing with a decreasing concentration of CO_2. Hence, energy consumption can be enhanced under the same discharge power or electron density.

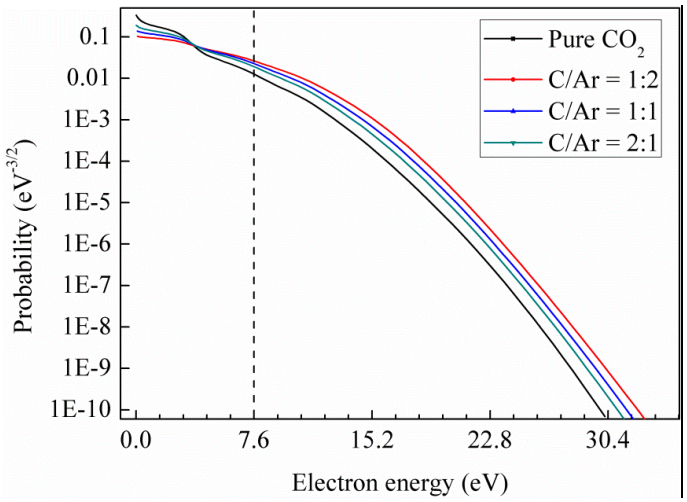

Figure 4.12 Calculated EEDFs under different ratio of CO_2: Ar.

4.6 Conclusions

In this chapter, pure CO_2 splitting in the DBD reactor was analysed by the computer simulations and experiments. The model was validated by the experiments. This work found that a higher input power enhanced the conversion rate of CO_2 slightly. The electron density played an important role in CO_2 splitting in this simulation. The entire vibrational excitation process was divided into individual level to define the main excitation state for the CO_2 splitting and find out the relationship among different excitation levels versus a changed discharge power. The excitation processes can also be very complex, if CO_2 is not in the ground state already. A more accurate model can always be obtained when the excitations from non-ground states are considered.

The generation rates of both the VT and VV modes increased with a higher discharge power, while the generation rates of the VT modes of CO_2 excitation were much higher than those of VV modes. The VT mode excitations with a lower stored energy were dominating the excitation process. Moreover, all the rate constants of deexcitations were declined by a higher

discharge power and the higher input energy helped the excited CO_2 keep the stored energy. Additionally, excited CO_2 in VT modes was much easier to be deexcited back into the ground state or a lower state by collisions of electrons/neutrals. However, instead of the ground state, more excited CO_2 in VV modes was deexcited to 0.08 eV level (1^{st} bending mode). Therefore, it concluded that VT modes were dominating the excitation process of CO_2 and 0.08 eV level (1^{st} bending) was dominating the VT modes.

For the filamentary discharge situation of DBD, the electron density has characteristics in both spatial and temporal growth. However, in order to obtain the steady-state simulations, this work calculated the electron density based on the spatial growth. The contribution of vibrational excitations for decomposition of CO_2 was calculated and from 1.38 to 18.7 % under the various electron densities from 6.57×10^{12} to 3.74×10^{14} cm^{-3}. The vibrational excitations were dramatically enhanced due to the rising electron density, but the energy efficiency declined from 9.8 to 2.3 % at the same time, caused by the deexcited processes. Therefore, vibrational excitations provided a more effective method for CO_2 splitting, but the energy consumption should be reduced by the other method, such as adding Ar as a carrier gas in the plasma gases to improve the EEDFs. With a mean electron energy provide by a better EEDF, the probability density of the electrons with high energy (> 5.5) will be increased and more CO_2 could be decomposed by either the vibrational excitations or dissociation of C=O chemical bonds, so the energy efficiency can be enhanced.

Chapter 5 Computational and experimental study on conversion of CO_2 with H_2 in a DBD reactor

In this chapter, hydrogenation process of CO_2 is investigated by simulations at atmospheric pressure and temperature of 373 K in a DBD reactor to reveal the reaction mechanism of CH_4 production. The other aim of this simulation is to investigate the effect of H_2/CO_2 ratio on the discharge behaviours, the conversion rates of the inlet gases and selectivity of the target gas – CH_4.

5.1 Applied voltage, gas voltage, total current and power description

The discharge current, gas voltage and even discharge power would be affected by the different compositions of the inlet gas, so the applied voltage and power were adjusted all the time to fix the discharge power at 30 W. The maximum applied voltage almost reached 8.2 kV with the different inlet ratios. Based on equation (3.14), a lower discharge current resulted in a higher gas voltage (**Figure 5.1**). Through the equation (3.18), the temporal dynamic discharge powers were calculated. To validate the calculations of the discharge powers, the temporal dynamic gas voltages were integrated on discharge currents in one AC cycle to obtained calculated powers which were around 33.8 W. This slight deviation may be caused by the record current signal (distortion on the oscilloscope). This procedure testified that the description of the discharge power using the novel method (described in **chapter 3**) was suitable for this work.

The electron temperature of pure H_2 under the 122 Td with the same environment can approach to 5.173 eV. The cross section of H_2 is small, so the mean free path is longer (equation 1.8). A higher concentration of H_2 raised the overall gas voltage and mean electron temperature with relative lower discharge current.

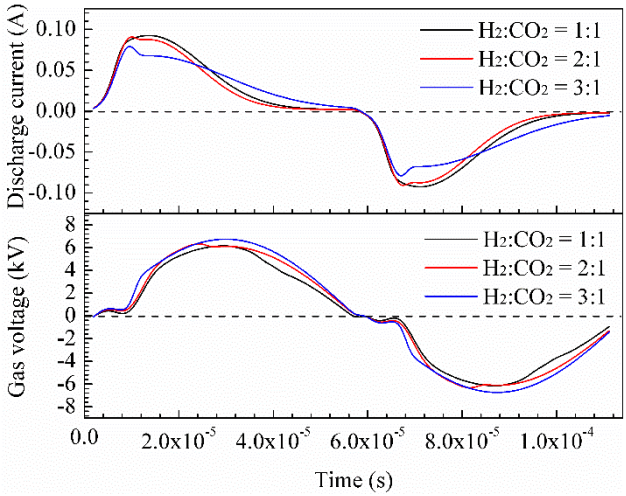

Figure 5.1 Dynamic gas voltages and total discharge currents (The discharge power was fixed at 30 W and total flow rate was 69.2 ml/min).

5.2 Results and discussions

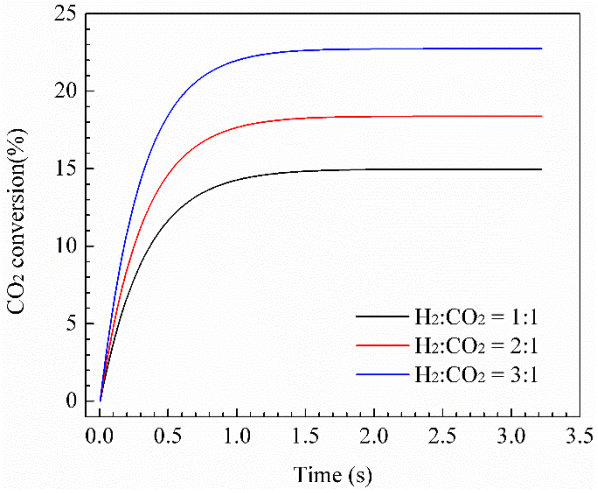

Figure 5.2 Conversion of CO_2 with different inlet ratios. (The discharge power was fixed at 30 W and total flow rate was 69.2 ml/min).

The conversion of CO_2 increased from 15.0% to 22.7% when the H_2/CO_2 ratio was increased from 1:1 to 3:1. The higher gas voltage and longer mean free paths of the injected elections increased the mean electron temperature (**Figure 5.3**). According to the results on contribution of vibrational excitations for CO_2 splitting (in **chapter 4**), most of CO_2 molecules were split by the energetic electrons directly in DBD, so higher mean electron temperature signified that more electrons (with enough energy) were able to decompose C=O bonds of CO_2.

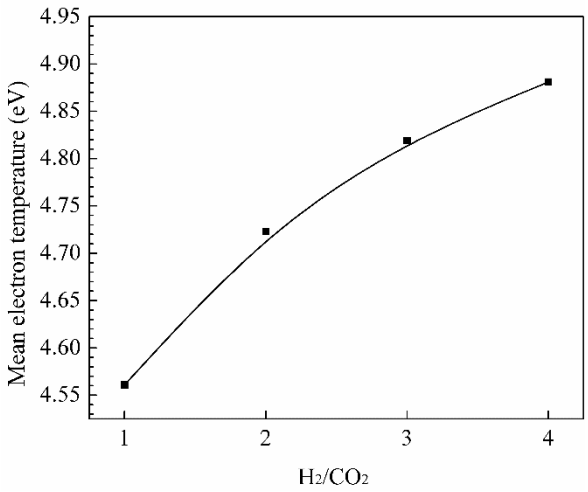

Figure 5.3 Mean electron energy with different H_2/CO_2 ratios. (The discharge power was fixed at 30 W and total flow rate was 69.2 ml/min).

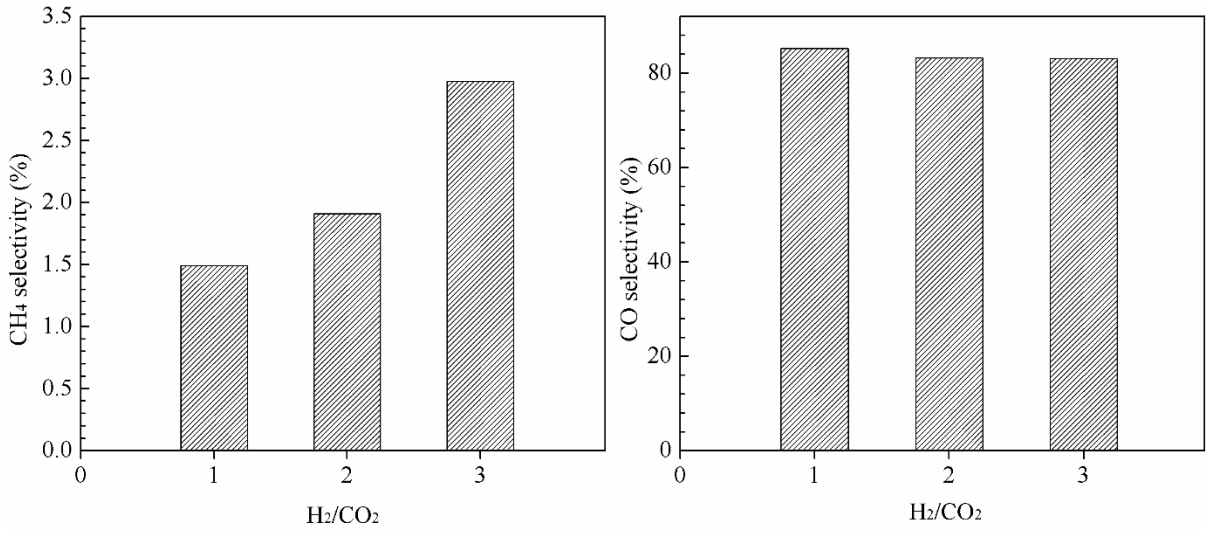

Figure 5.4 Simulation results: Effect of H_2/CO_2 ratio on selectivity of CH_4 and CO. (The discharge power was fixed at 30 W and total flow rate was 69.2 ml/min).

Figure 5.4 illustrated the influence of the H_2/CO_2 ratio on the selectivity of CH_4 and CO. The selectivity of CH_4 was very low, while the maximum selectivity was around 3% at H_2/CO_2 ratio of 3:1. CH_4 was also a relatively active particle in the plasma discharges, compared to CO_2. The dissociation energy of the first C-H bond (CH_3-H) is much lower than C=O double bond, so CH_4 was easier to be dissociate to other radical (i.e. CH_3) by collisions with energetic electrons. However, because the dihedral angle of CH_4 molecule, most electron energy could be wasted on exciting CH_4 rather than dissociating. Obviously, as shown in **Figure 5.5**, the

three of H atoms can determine the plane (1), while the 4th H atom must locate in the plane (2) with a dihedral angle θ. If an energetic electron collided with the nucleus of either H or C atom, the elastic collision would occur. Because the nucleus is much heavier than the electron. Moreover, if the injected energetic electron collided with any electrons, CH_4 could be ionised or excited. Certainly, C-H bond can also be dissociated the injected electron directly. However, if the energy of injected electron was low, the bond would only be excited, causing the rotational or vibrational excitation. Vibrational excitation can make CH_4 become to an energy-stored (reactive) particle, but rotation with a very low stored energy is useless for conversion of CH_4.

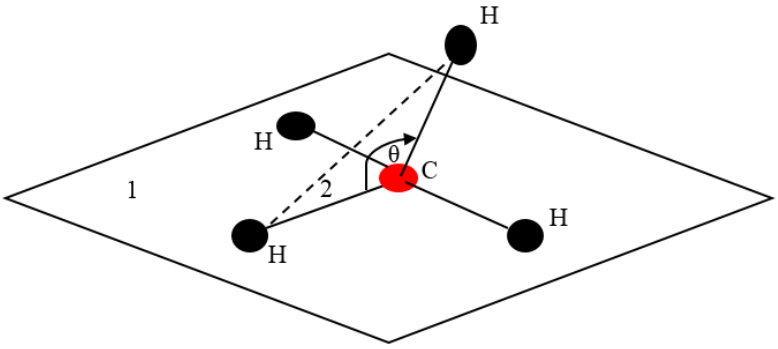

Figure 5.5 Molecular structure of CH_4: Dihedral angle [210].

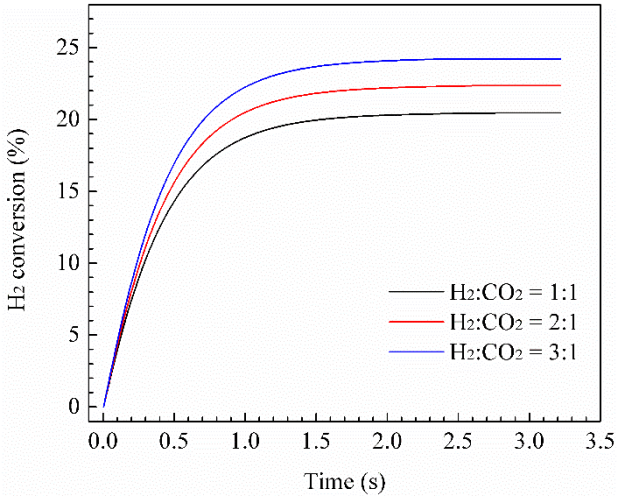

Figure 5.6 Dynamic conversion rates of H_2 with different inlet ratios. (The discharge power was fixed at 30 W and total flow rate was 69.2 ml/min).

CO selectivity decreased slightly with a lower H_2 concentration. The major pathway for generating CO was CO_2 splitting, whereas the CO selectivity reached ~82% when the inlet ratio was equal to 1. The decreasing selectivity of CO can be explained by the less inletting

amount of carbon. Moreover, lower CO_2 concentration inhibited the RWGS ($CO_2 + H_2 \rightarrow CO + H_2O$). Furthermore, oxidisation of C was the other method to produce CO, but the oxidant should be O_2. In order to achieve methanation, at least one of C=O double bonds of CO_2 must be broke. If one C=O bond was broke, CO would be formed most likely, while the other O atom would be an O (free-state) radical drifting in the plasma gas. O radical is very easy to react with H_2 to generate OH ($H_2 + O \rightarrow OH + H$, $k_{298K} = 7.02\times10^{-18}$ cm^3s^{-1}). The generation of is harder O_2 and requires a three-body reaction ($O + O + M \rightarrow O_2$, $k_{298K} = 1.05\times10^{-33}$ cm^6s^{-1}). When H_2 concentration was increased, the O radical would be fixed by excessive H_2 and the pathway of oxidisation of C by O_2 ($C + O_2 \rightarrow CO + O$, $k_{298K} = 5.22\times10^{-11}$ cm^3s^{-1}) to generate CO was obstructed, causing a lower generation of CO.

The RWGS was unavoidable reaction during the methanation, as well as the oxidisation of H/H_2. Therefore, H_2O was a necessary product and the densities were shown in **Figure 5.7**. The generation of H_2O raised with the increasing concentration of H_2. Redox reactions usually occur faster than recombination of radicals. Therefore, owing to the increment of H_2 concentration, more O element was captured by H/H_2 to generate H_2O.

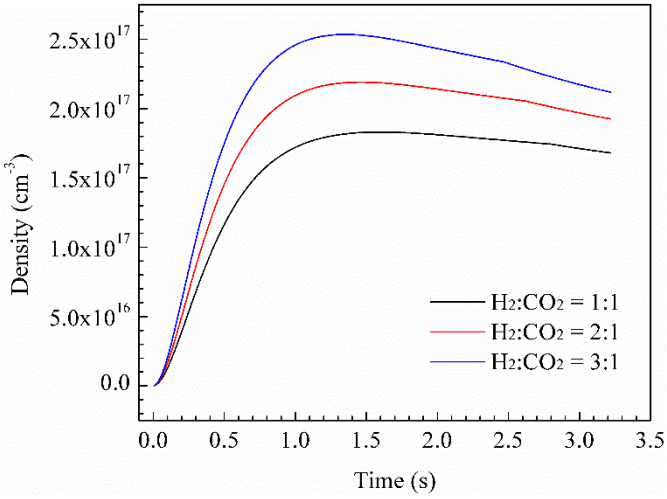

Figure 5.7 Dynamic densities of H_2O with the different H_2/CO ratios. (The discharge power was fixed at 30 W and total flow rate was 69.2 ml/min).

The desired product of this work was CH_4, so the monitoring on the behaviour of CH_4 was important. The experimental resident time of this simulation was around 3 s and this simulation set the running time of the simulation slightly over 3 s to indicate whether a particle was in equilibrium state. In **Figure 5.8**, the density of CH_4 was changing during the resident time and increasing with a higher H_2 inlet concentration, while it increased from the beginning and then stayed as a constant value.

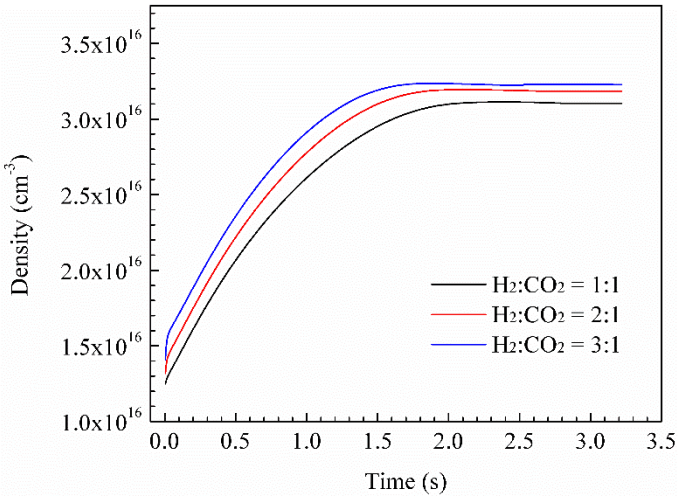

Figure 5.8 Dynamic densities of CH_4 with the different H_2/CO ratios. (The discharge power was fixed at 30 W and total flow rate was 69.2 ml/min).

When the reactants contained only H and O elements, the major products were H_2O with a small quantity of O_3 and H_2O_2. However, if carbon was involved in, the products would be diversified (i.e. hydrocarbons, alcohol, aldehydes and acids). Therefore, it was necessary to trace the carbon element in order to obtain a better understanding of the methanation. Making a general view of the simulated results, the densities of most carbon-containing products were low (less than 10^{10} cm^{-3}) due to the low conversion of CO_2. **Figure 5.9** illustrated the generations of the major hydrocarbons/carbohydrates. The densities of all other hydrocarbons/carbohydrates were too low to be illustrated. Formic acid (liquid-phase) was major carbohydrate observed in the products. On one hand, the relatively high concentrations of CO and OH resulted in a higher recombination rate for generating COOH radical (CO + OH → COOH, k_{298K} = 1.20×10^{-12} cm^3s^{-1}), whereas HCOOH can be formed by the second recombination between H and COOH radicals. On the other hand, oxidation was the other pathway to form HCOOH. For example, for the oxidic pathway, CH_2O were oxidised by OH to generate HCOOH (CH_2O + OH → H + HCOOH, k_{298K} = 5.15×10^{-13} cm^3s^{-1}). The most important pathways for generating HCOOH can be confirmed by the sensitivity analysis, which would be discussed later in this section. Moreover, formaldehyde (CH_2O) was the main carbohydrate product in gas phase. Notably, the formation of CH_2O was rapid at the beginning of the operating time and the density of it kept declining until around 0.5 s. This phenomenon was caused by the radical of HCO, which was always a very significant radical for the reactions containing C, H, and O elements. When dissociations of H_2 and CO_2 occurred, HCO was an inevitable radical with rapidly increased density of H and CO (CO + H → HCO, k_{298K} = 2.50×10^{-14} cm^3s^{-1}). CH_2O can be formed by whether hydrogen abstraction reaction with

OH/H_2O or hydrogenation by H/H_2 of HCO. However, HCO cannot stay for a long time in an environment of high concentration of H radical (H + HCO → CO + H_2, k_{298K} = 6.64×10^{-11} cm^3s^{-1}). Therefore, owing to the increasing density of H radical and oxidising reaction to form acids, the density of CH_2O stayed at a low value (10^{12} cm^{-3}) until the end of resident time.

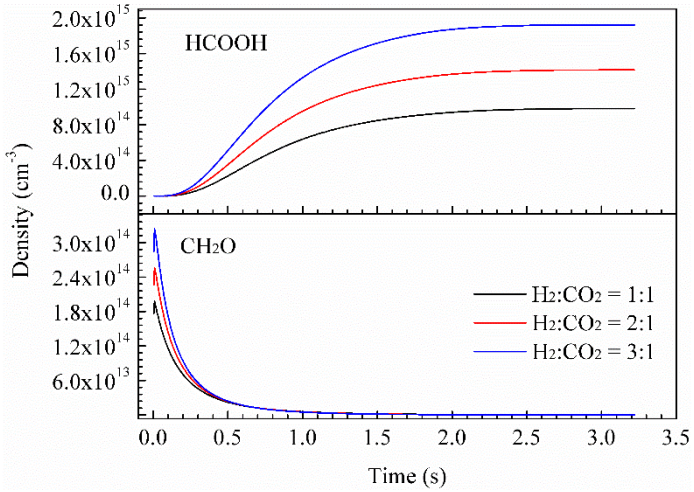

Figure 5.9 Dynamic densities of major hydrocarbons/carbohydrates with the different H_2/CO ratio. (The discharge power was fixed at 30 W and total flow rate was 69.2 ml/min).

A higher selectivity of CH_4 and conversion rates of inlet gases were observed at a higher H_2 input concentration, so it was worthy to conduct sensitivity analysis with the H_2/CO ratio of 3:1 to reveal the major mechanism of methanation process. Firstly, the overall reaction rates relate to generation/consumption of CH_4 were relatively low (less than 10^{12} $cm^{-3}s^{-1}$), shown in **Figure 5.10**. Secondly, owing to these low reaction rates, all reactions involved CH_4 were sorted out by a sub-sensitivity analysis to investigate which reactions were important for generating/consuming CH_4. Finally, according to the sub-sensitivity analysis, the generation of CH_4 was mostly based on the recombination between CH_3 and H radicals. Ions were major species for consuming the generated CH_4. Notably, the consumption rate of CH_4 by CO_2^+ was only slightly lower than the recombination rate between CH_3 and H. In other words, a lower density of CO_2^+ promoted the generation of CH_4. Moreover, CO_2^+ was mainly produced by ionisation of CO_2 and a lower CO_2 inlet concentration reduced the density of CO_2^+. This was another important reason why a higher CH_4 selectivity can be obtain with a higher H_2/CO_2 ratio. The similar generation/consumption rates also explained the reason why the densities of CH_4 stayed as a constant value until the end of resident time (**Figure 5.8**).

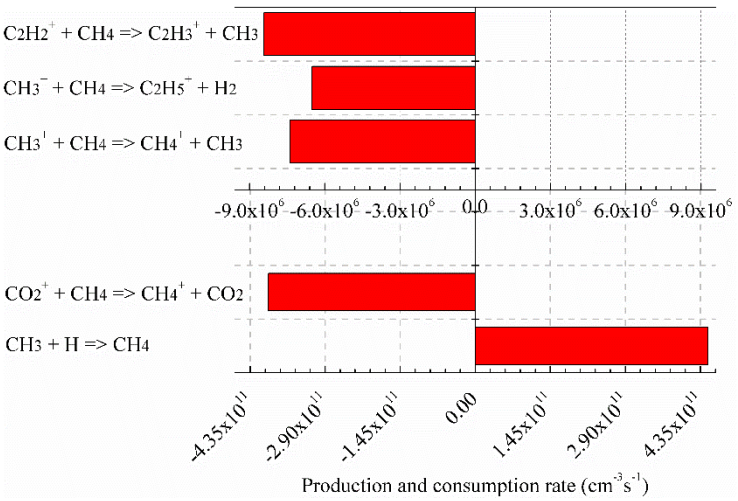

Figure 5.10 Time-average major production and consumption rates of CH_4 with H_2/CO_2 ratio of 3:1 under the discharge power of 30 W and total flow rate of 69.2 ml/min.

The reason why a sub -sensitivity analysis was conducted was that the pathways related to CH_4 may not appear in the main reaction mechanism of the methanation process. Therefore, a reliable method to investigate the pathway for generating CH_4 was reverse educing through the source radical(s). As mentioned above, CH_3 was the major source for CH_4. Therefore, the pathways of CH_3 generation should be investigated. To achieve this, it required the second sub-sensitivity analysis. In figure **5.11**, a large proportion of CH_3 was consumed by H to produce CH_4, while CH_2 was basic source for generating CH_3. Moreover, compared with the neutral-neutral reactions, the ionic reactions were much week for the CH_3 generation. Therefore, a sub-sensitivity analysis (3^{rd}) on the pathways of formation of CH_2 was the next task.

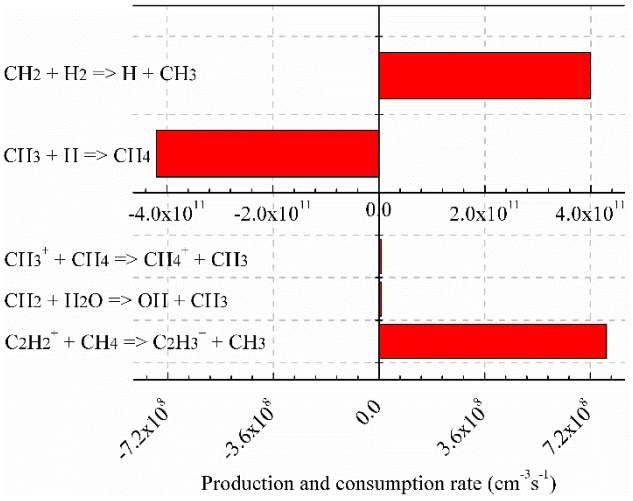

Figure 5.11 Time-average major production and consumption rates of CH_3 with H_2/CO_2 ratio of 3:1 under the discharge power of 30 W and total flow rate of 69.2 ml/min.

Figure 5.12 showed the major reactions related to CH_2, based on the 3rd sub-sensitivity analysis. Firstly, all the reaction rates became much higher and the maximum generation rate of CH_2 was greater than 6×10^{15} $cm^{-3}s^{-1}$ at ~0.6 s. Secondly, more electron-impact reactions were involved in generation/consumption of CH_2. In **Figure 5.10** and **Figure 5.11**, CH_3^+ and $C_2H_2^+$ were the major ions to consume CH_4. However, they can be the alternative sources to generate CH_2 by ionic dissociation. Thirdly, through oxygen abstraction reactions from OH and CO_2, CH_2 was a necessary radical for generating CH_2O. Finally, the generation of CH_2 was dramatically depend on the reaction between CH and H_2, while the time-average generation rate was 1000 times faster than the consumption rate of CH_2. However, after around 2 s, the generation of CH_2 was sluggish, causing the density of CH_2O staying at a very low value (**Figure 5.9**) and stagnant generation of CH_3/CH_4. Except for the inlet gas H_2, the most significant source of generation of CH_2 is CH. Therefore, one more (4th) sub-sensitivity analysis was required to investigate the generation of CH.

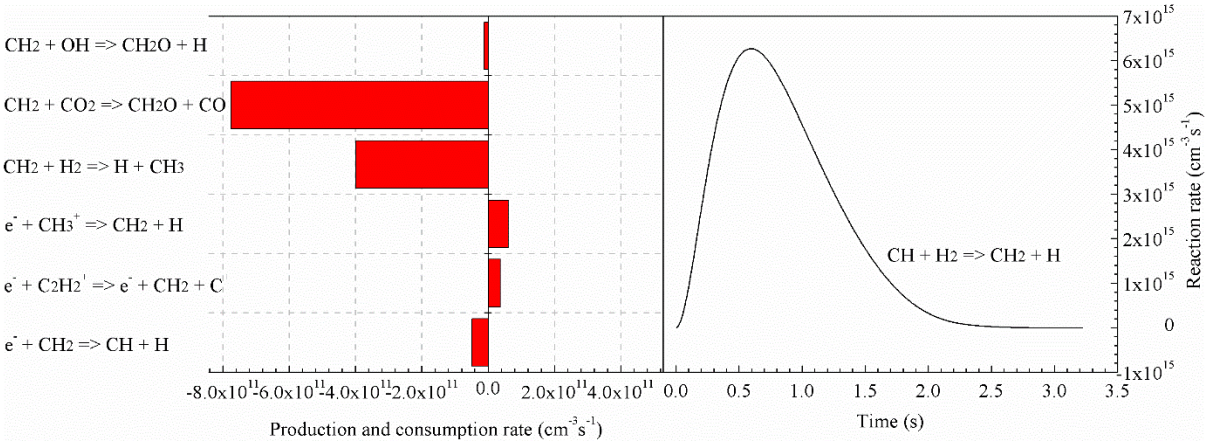

Figure 5.12 Time-average and dynamic production and consumption rates of CH_2 with H_2/CO_2 ratio of 3:1 under the discharge power of 30 W and total flow rate of 69.2 ml/min.

So far, according to the previous sub-sensitivity analysis, it seemed that CH was the primal $CH_{x,\ (x=1,2,3)}$ radical to form CH_4. Moreover, these CH_x radicals (from CH) abstracted one H atom from the other particles (i.e. H_2) step by step to reduce the number of free covalent bonds until all C-H bonds were saturated. The procedure can be described as: CH => CH_2 => CH_3 => CH_4.

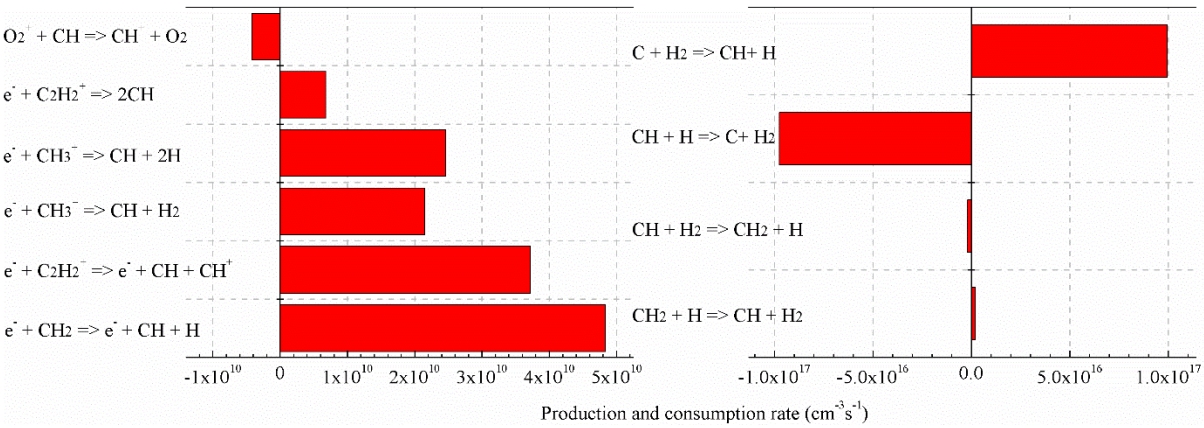

Figure 5.13 Time-average and dynamic production and consumption rates of CH with H_2/CO_2 ratio of 3:1 under the discharge power of 30 W and total flow rate of 69.2 ml/min.

In **Figure 5.13**, electron-impact dissociation of CH_2 and ions (i.e. CH_3^+ and $C_2H_2^+$) were the secondary channel to produce CH. Moreover O_2^+ consumed a small number of CH, but this reaction was not that important due to the low density of O_2. Notably, there were two pairs of reversible reactions illustrated in **Figure 5.13** (right). According to these reversible reactions, it was obvious that the major source for producing CH was C. In addition, the rates of all forward reactions (formation of CH and CH_2) were slightly larger than the ones of the reverse reactions. Therefore, the hydrogen abstraction reactions mentioned above (CH => CH_2 => CH_3 => CH_4) occurred tardily. Through these sub-sensitivity analyses and the sensitivity analysis of the entire methanation process, the mechanism of CH_4 generation can be demonstrably summarised, shown in **Figure 5.14**.

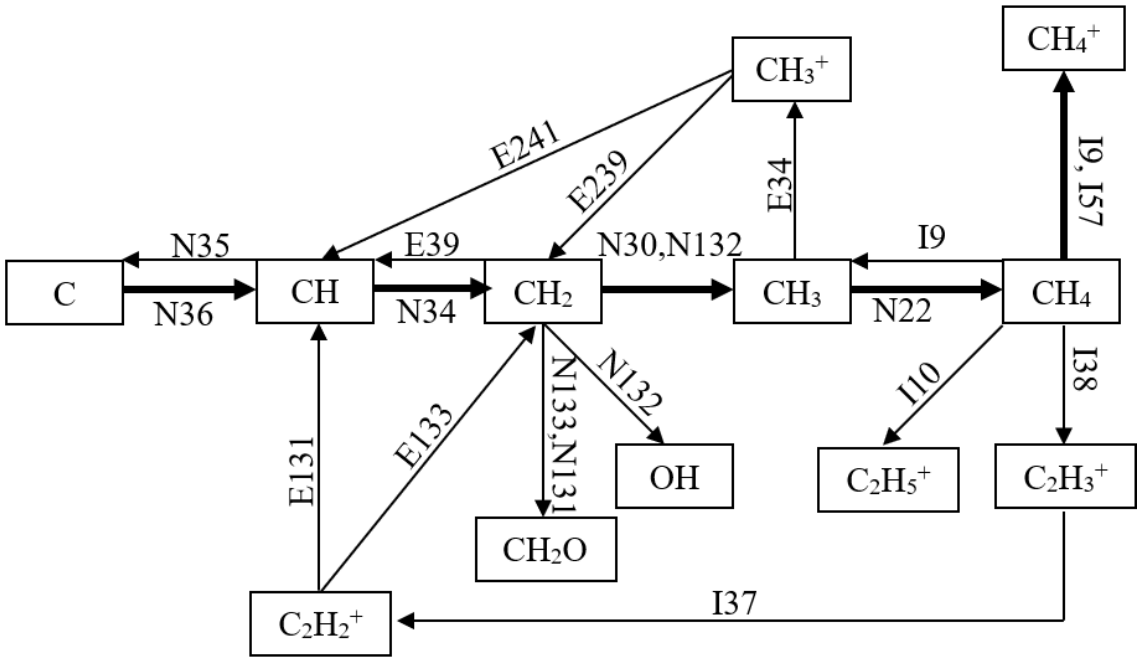

Figure 5.14 The major reaction pathways for the methanation process with H_2/CO_2 ratio of 3:1 under the discharge power of 30 W and total flow rate of 69.2 ml/min (The corresponding reactions notated with numbers can be found in **Appendix 9.2**).

The purpose of this work was to understand the mechanism of generation of CH_4, so the pathways of some common products (i.e. C, H_2O, H_2, CO, etc.) were neglected and they would be paid on more attention in the following chapters. In **Figure 5.14**, the ionic channels formed a loop to produce CH_x radicals (i.e. $C_2H_2^+ \rightarrow CH \rightarrow CH_4 \rightarrow C_2H_3^+ \rightarrow C_2H_2^+$) continuously, while this loop were considered as the secondary source for producing CH_4. The inseparable sensitivity analysis proved that the CH_4 was mainly from the C, while the CH_x radicals check and balance each other, causing the CH_4 production reaching the equilibrium ultimately.

5.3 Conclusions

The purpose of this chapter was to obtain a better understanding of the methanation process using DBD plasma. A 0D model was built using ZDplaskin to investigate the important behaviours of the major species, whereas reverse educing method via several sub-sensitivity analysis was used to investigate the mechanism of generation of CH_4. A new method was used to describe the discharge power as the essential input parameter and made our simulations available to be performed in real-time. Through the validation by the experiments, the physical and chemical models for this work were reliable and working correctly.

At the beginning of this work, the effects of inlet ratio of H_2/CO_2 (from 1:1 to 3:1) on the conversions of input gas and CH_4 selectivity was investigated. In the power description section, it found that a higher discharge can be obtained with a higher H_2 inlet concentration. The maximum conversion rate was observed of 22.7% with the H_2/CO_2 ratio of 3:1. Moreover, with increasing of inlet concertation of H_2, more H_2O would be formed, causing a higher concentration of OH. OH radical can consume CH_2 considerably to form CH_2O, resulting in a lower CH_4 selectivity. Based on a series of sub-sensitivity analysis and reverse educing method, C was found as the major/initial source radial for producing CH_4, while a loop formed by ionic reaction channel was a necessary secondary pathway of CH_4 generation. CO_2^+ was a significant ion which can consume CH_4. The mean electron temperature was increased by a higher H_2 inlet concentration, but the enhancement of CH_4 selectivity was not obvious, since more CO_2 would be ionised to form CO_2^+.

In the future work, the simulation will pay more attentions on the carbohydrate products which could be more valuable. Moreover, it will continue perfecting our simulation by changing more input parameters, such as discharge power. When the composition of inlet gas is fix, it is very difficult to change the gas voltage (mean electron energy), because of the breakdown the plasma gas. However, the increment of discharge current will raise the electron density dramatically. It is very worthy to investigate the effects of the increasing electron density, because the answer is unclear. Higher electron density will certainly improve the conversions of inlet gases due to more collisions. However, it will also produce more ions, which may break formed loop.

Chapter 6 The computational and experimental study on dry reforming of methane for producing syngas and liquid chemicals

CO_2 and CH_4 are the major contents of biogas. This chapter, therefore, is to analyse the mechanism of DRM in a DBD reactor at atmospheric pressure and ambient temperature, while the experiments conducted under the same operating conditions can validate the simulations. The collisions between electrons and ions are considered in this simulation. The simulation time are set as same as the experimental resident time to make the results more accurate.

6.1 Applied voltage, gas voltage, total current and power description

The discharge power was fixed at 10 W for this work. Different gas voltages can affect the electron-impact reactions. Therefore, the concentrations of some important radicals (i.e. CH_3) may be changed, as well as the main reaction mechanism.

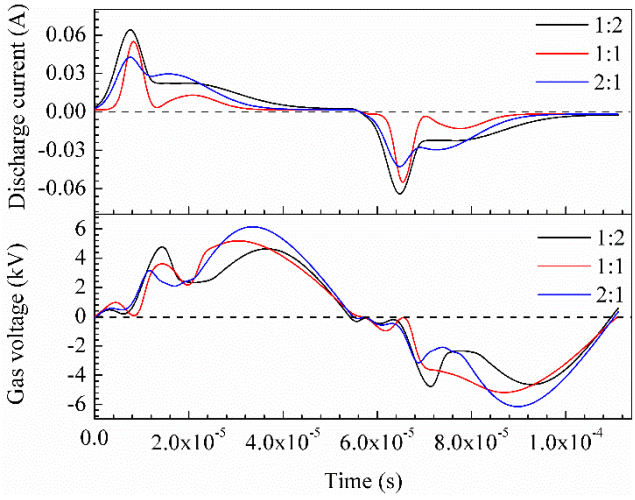

Figure 6.1 Dynamic gas voltage and total discharge current with different inlet ratios. (Total flow rate was 40 ml/min; discharge power was 10 W; CH_4: CO_2 = 1:2, 1:1, 2:1).

After obtaining the function of the current signal, the temporal dynamic gas voltage was solved, as well as the discharge power, shown in **Figure 6.1**. Furthermore, the variation of electron

temperature was dramatically depended on the gas voltage and reached maximum value of ~3.53 eV. U_g was not reduced to zero when the applied AC voltage was zero, due to memory effect of DBD, which also made reduced electric field and electron temperature nonzero. The electron temperature dropped to ~0.078 eV at the end of each half AC cycle. In terms of the discharge power, it was calculated by the temporal dynamic gas voltage multiplied by the discharge current, $I_{p,g}$.

The average experimental discharge power (10 W) was calculated by using Lissajous method, and integrate the time-evolution gas voltage on discharge current, $I_{p,g}(t)$, in one entire AC cycle. The result of the integration defined that the total calculated discharge power in one AC cycle was 10.8 W. Therefore, undoubtedly, it deemed that the calculation of temporal dynamic discharge power was correct and suitable to be used as the input parameter for the simulations.

6.2 Results and discussions

Energetic electrons in plasma could break all the chemical bonds of reactants by collisions to generate the radicals and ions (in plasma-on duration), and then new particles would be formed through recombination. The fundamental purpose of this work was to produce syngas (H_2 + CO) and valuable gas-phase chemicals (i.e. C_2H_2), so it was important to investigate the behaviours of these products, including the related radicals. The running time of the simulations was set as same as the experimental resident time (3.2 s) to compare the simulation and experimental conversion rates for validating the model.

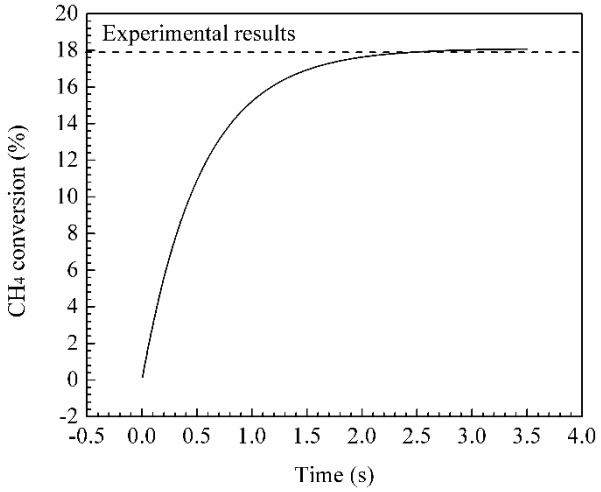

(a)

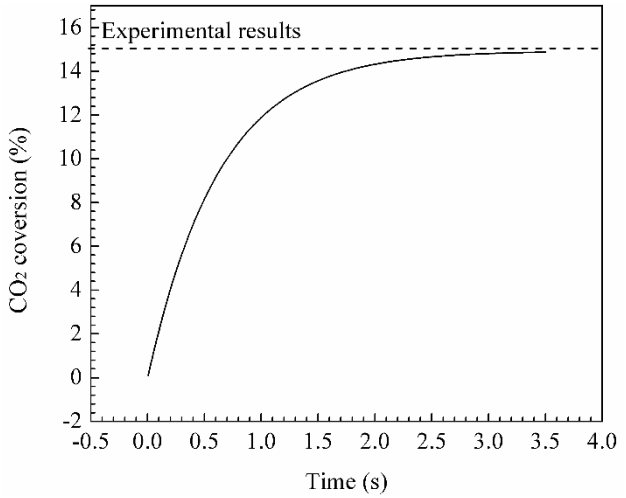

(b)

Figure 6.2 Conversion of CH_4 and CO_2. (a): Conversion of CH_4; (b): Conversion of CO_2.

The maximum experimental conversion of CH_4 and CO_2 were observed at ~17.9% and 15.1% individually (the horizontal dotted line). Moreover, for the simulations, it was clear that the CH_4 cracking and CO_2 splitting reached equilibrium during real resident time due to the reverse reactions (i.e. $CH_3 + H \rightarrow CH_4$; $CO + O \rightarrow CO_2$).

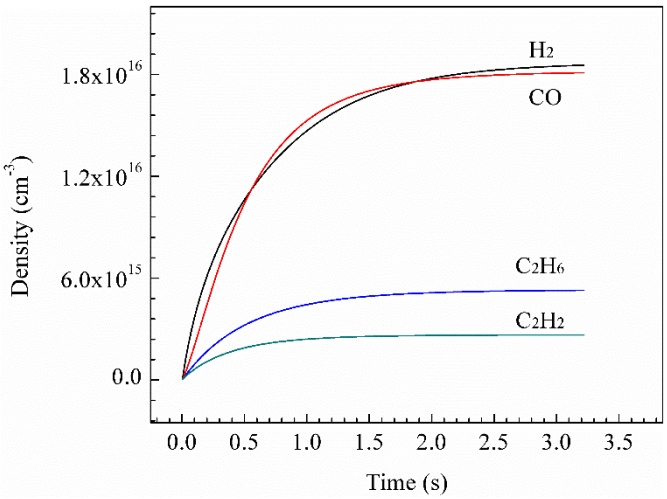

Figure 6.3 Densities of major products.

Figure 6.3 showed the calculated densities of the major products. Certainly, syngas was the most important product of the DRM process. Based on the sensitivity analysis, the generation of H_2 was mainly depended on dissociation of CH_4 and recombination of H radicals, as the reactions shown below.

$e^- + CH_4 \rightarrow CH_3 + H + e^-$ (E6, **Appendix 9.2**)

$e^- + CH_4 \rightarrow CH_2 + 2H + e^-$ (E7, **Appendix 9.2**)

$e^- + CH_4 \rightarrow CH + 3H + e^-$ (E8, **Appendix 9.2**)

$H + H + M \rightarrow H_2 + M + e^-$ (N77, **Appendix 9.2**)

CO was mainly from the splitting of CO_2. Syngas can be generated from the inlet gases directly and this was the reason why the density of it was the highest. The final state (end of resident time of 3.2 s) density of H_2 (~1.90×10^{16} cm^{-3}) was closed to the one of CO (~1.80×10^{16} cm^{-3}). In this plasma-only DRM process, the ratio of CH_4/CO_2 could not be changed dramatically, according to equation 1.7.

Hydrocarbons (i.e. C_xH_y, $_{x,y = 1\ldots n}$) were also the major gas-phase products of DRM, due to the abundant radicals. The two major hydrocarbon products, ethylene (C_2H_2) and ethane (C_2H_6), were also presented in **Figure 6.3**. Usually, it was very difficult to form C_2H_4 and the concentration of it was very low during the plasma-assisted biogas reforming for both experiments and simulations. Generations of hydrocarbons were mostly depended on two processes: recombination of C_xH_y radicals and dehydrogenation/hydrogenation processes. For the recombination, the major reactions were shown as below:

$CH + CH \rightarrow C_2H_2$ (N349, **Appendix 9.2**)

$CH_2 + CH_2 \rightarrow C_2H_4$ (N23, **Appendix 9.2**)

$CH_3 + CH_3 \rightarrow C_2H_6$ (N9, **Appendix 9.2**)

For hydrogenations, unsaturated hydrocarbons could be added with H_2/H. Nevertheless, C_2H_4 were the intermediate products of hydrogenation and very easy to react with H_2. Therefore, the hydrogenation process would not stop until C_2H_6 has been formed. Inversely, dehydrogenation process would not stop until four hydrogen atoms had been split off to form C_2H_2 [211]. It was one of reason why C_2H_6 concentration was relative higher, while the other important pathway for C_2H_6 generation was recombination of CH_3. Based on the calculations, the recombination of CH_3 took more than 70% proportion of the consumption of CH_3 and was dominating the dissociating process of CH_4. A high concentration of CH_3 provide by CH_4 cracking promoted the recombination to C_2H_6.

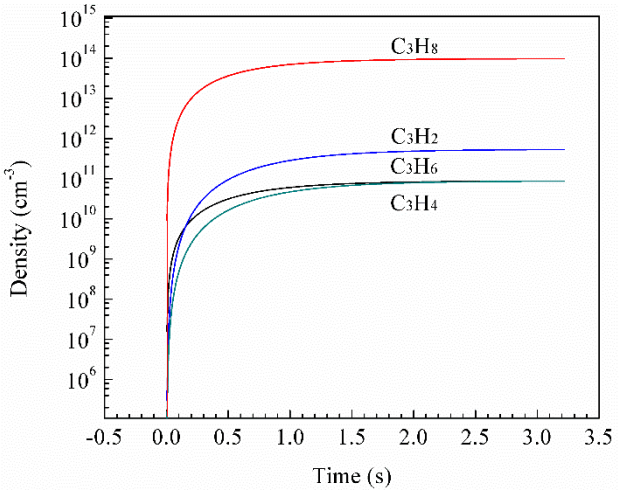

Figure 6.4 Densities of nonstaple hydrocarbons (C_3 compounds).

Figure 6.4 showed overall densities of C_3 compounds. Usually, C_3 compounds cannot be generated directly from C_1 radicals (i.e. CH_3). In other words, C_2 species were required as the intermediate products and then the C_3 compounds would be generated by recombination between C_2 species and C_1 radicals by the major reactions of:

$C_2H_3 + CH_3 \rightarrow C_3H_6$ (N16, **Appendix 9.2**)

$C_2H_6 + CH_2 \rightarrow C_3H_8$ (N40, **Appendix 9.2**)

$C_2H_5 + CH_3 \rightarrow C_3H_8$ (N12, **Appendix 9.2**)

During the generation of C_3 process, C_2 compounds also could be decomposed again via electron collisions and metastable C_2 radicals were consumed by the hydrogenation process to produce C_2 products. Therefore, the fast consumption of the C_2 species inhibited the generation of C_3 products.

The concentrations of unsaturated C_3 compounds, C_3H_4 and C_3H_6, were the lowest due to dehydrogenations/ hydrogenations and the densities of them were almost same at the end of the resident time.

The valuable hydrocarbon, butane (C_4H_{10}), was also detected in this work, shown in **Figure 6.5**. C_4H_{10} were also formed indirectly and hydrogenation of C_4H_9 was the most important pathways to form it. Obviously, the density of C_4H_{10} was much lower, compared with major products (i.e. syngas), and there was almost no generation of C_4H_{10} until 0.3 s. More recombination among C_xH_y radicals were required for generating C_4H_{10} and made the generation of C_4H_{10} slower. The major pathway for generating C_4H_{10} was shown as below:

$C_2H_5 + C_2H_4 \rightarrow C_4H_9$ (N346, **Appendix 9.2**)

$C_4H_9 + H \rightarrow C_4H_{10}$ (N348, **Appendix 9.2**)

Additionally, C_2H_5 and C_2H_4 were formed from the recombination of C_xH_y radicals mainly, Owing the competitive reactions among those C_xH_y radicals and oxidising reactions with higher reaction rates, the probability of the formation of C_4H_9 was very low.

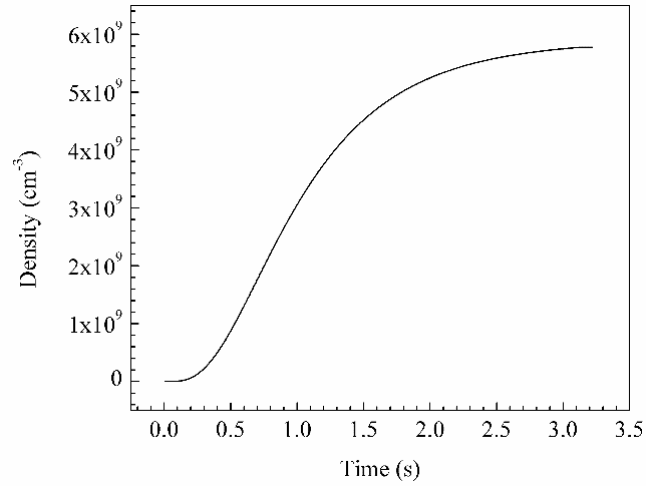

Figure 6.5 Density of C_4H_{10}.

Cracking of CH_4 and splitting of CO_2 by energetic electrons were the premier stage of the DRM to produce abundant radicals which would be consumed by the hydrogenations or oxidisations of hydrocarbons afterward to form hydrocarbons/carbohydrates. Emphatically, the different types of the reactions involved in the DRM process, including hydrogenations, oxidisation processes, recombination, decomposition, etc, could happen at the same time among radicals. Therefore, the investigations of the important radicals were necessary to understand the reaction mechanism.

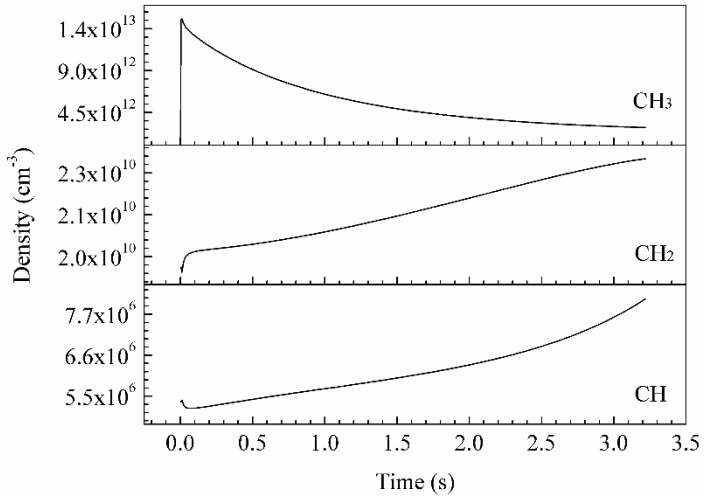

Figure 6.6 Densities of CH_3, CH_2, and CH.

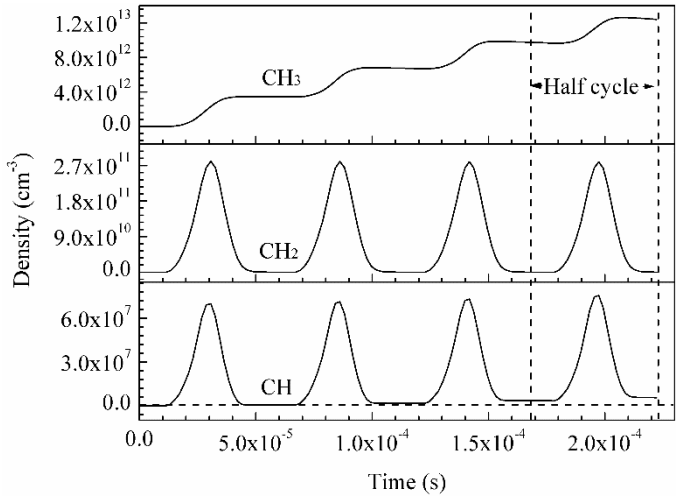

Figure 6.7 Densities of CH_3, CH_2 and CH in two AC cycles.

Figure 6.6 showed the overall change of the densities of CH_y species within the resident time and **Figure 6.7** illustrated the behaviours of these species during each half AC cycle. It was clear that the densities of the radicals, which were mainly produced from CH_4 cracking, appeared in the order of: $CH_3 > CH_2 > CH$. The energy for dissociating CH_4 molecule into CH_3 and H was the relative lower and this reaction was treated as the dominated reaction during the dissociation of CH_4, based on the calculation.

The generation and consumption of radicals happened at same time. To be specific to every AC cycle, all densities of these radicals started to increase until the peak value when the gas voltage started to increase. When the running time was reaching the termination of each half AC cycle, the mean electron energy became lower and all densities of these radicals were declining and would not recover until the running time reaching to the next half AC cycle.

Obviously, CH and CH_2 were consumed much faster than CH_3 and density of CH_3 almost stay as a constant until the end of the half cycle. The reason was that the generation of CH_3 from CH_4 cracking was still high after 1st peak of discharge power, because of the lower energy requirement. However, overall, the density of CH_3 declined to a very low value (~ 4.0×10^{12} cm^{-3}) from ~0.012 s to the end of the resident time, so the CH_3 was playing a significant role in biogas reforming and reacting with other species all the time during entire process. It seemed that the consumption rate of CH_3 increased and became larger than the generation rate at a certain simulation time.

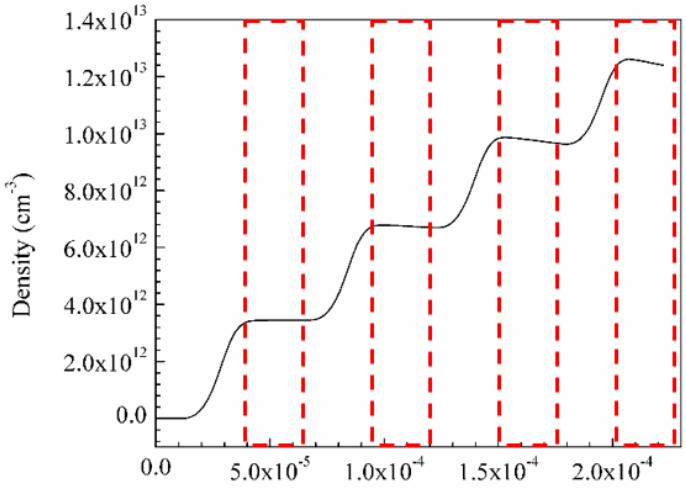

Figure 6.8 Density of CH_3 in two entire AC cycles.

Figure 6.8 clearly illustrated the density of CH_3 was rising immediately when the discharge was ignited. The four red rectangles in **Figure 6.8** defined the plasma-off durations, based on the description of the discharge power. To the 1st plasma-off duration, the generation and consumption rates of CH_3 were almost same, causing a nearly constant density of CH_3. However, the density of CH_3 started to decrease in the 2nd plasma-off duration. The consumption rate was rising in the plasma-off durations with the increasing of the running time. Based on the overall change of density of CH_3 shown in **Figure 6.6**, the generation and consumption of CH_3 reached the equilibrium at density of 1.46×10^{13} cm^{-3} at around 0.012 s, while the density of CH_3 started to decrease. With the increasing of simulation time, more radicals, which can enhance recombination and oxidisation process, were generated to consume CH_3. The consumption of CH_3 was often accompanied by generation of CH_2 (i.e. $CH_3 + OH \rightarrow H_2O + CH_2$, $k = 1.13\times10^{-12}$ cm^3/s), while consumption of CH_2 was often accompanied by generation of CH (i.e. $CH_2 + H \rightarrow H_2 + CH$, $k = 2.01\times10^{-10}$ cm^3/s). As a result, the densities of CH_2 and CH appeared an increasing trend until the end of resident time.

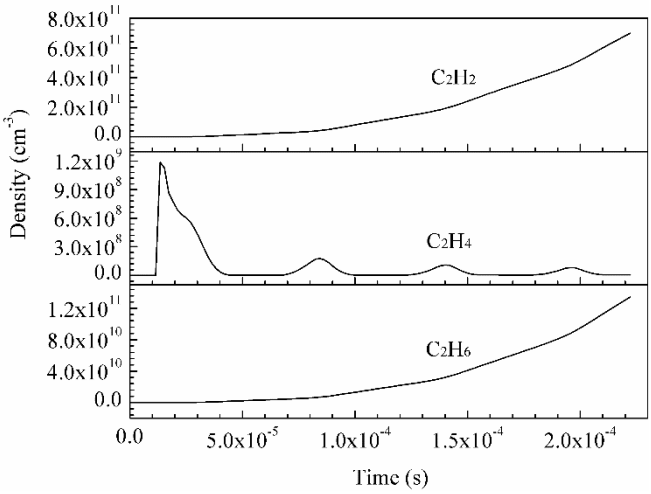

Figure 6.9 Densities of major C_2 products in two entire AC cycles.

In order to have a better understanding of the mechanism, it was necessary to investigate the generations of C_2 products during every half AC cycle. In **Figure 6.9**, the curves of C_2H_2 and C_2H_6 increased continuously and explained why the density of C_2H_2 and C_2H_6 were higher among the C_2 compounds. However, the odd curve of C_2H_4 showed a remarkable response to the discharge, and it kept descending with every half cycle. It was not difficult to explain this phenomenon by the electron-impact reaction ($e^- + C_2H_4 \rightarrow C_2H_3 + H + e^-$) and was worthy to investigate the densities of C_2 radicals.

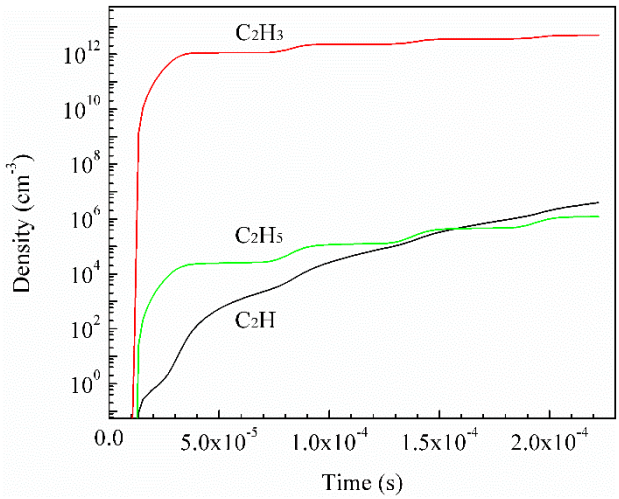

Figure 6.10 Densities of major C_2 radicals in two entire AC cycles.

Figure 6.10 explicitly defined that C_2H_4 was much easier to be decomposed into C_2H_3, causing a high density of C_2H_3. Combined with the density of C_2H_4 shown in **Figure 6.9**, it indicated that the low generation of C_2H_4 was also due to the dissociation by electrons, while the high

density of C_2H_3 promoted the generation of C_2H_2 (i.e. $C_2H_3 + C_2H_3 \rightarrow C_2H_4 + C_2H_2$ or $C_2H_3 + OH \rightarrow H_2O + C_2H_2$).

Through the investigation on the behaviours of C_xH_y, it was clear that the oxidising reactions of the C_xH_y, whose products of them often contained H_2O and OH, were important. There was no O_2 being detected in the experiments and the simulation densities of O_2 and O were also very low ~ 10^4 cm^{-3}, shown in **Figure 6.11**. C_xH_y were very difficult to react with CO_2 directly under room temperature, so CO_2 must be split into CO and O ($e^- + CO_2 \rightarrow CO + O$) for further reactions. Therefore, it implied that the major oxidant of DRM was OH.

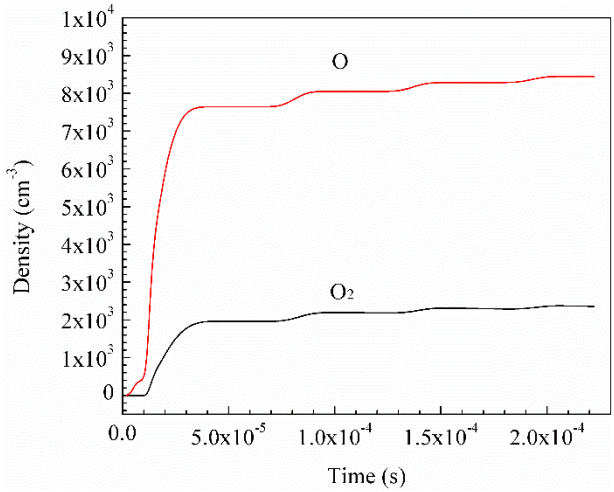

Figure 6.11 Densities of O and O_2 in two entire AC cycles.

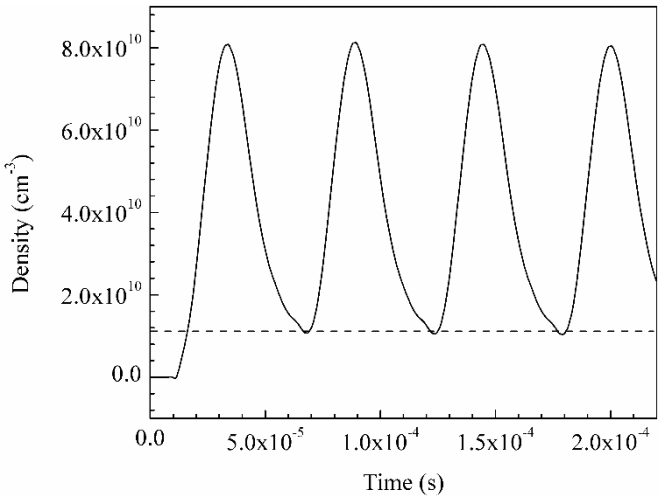

Figure 6.12 Density of OH in two AC entire cycles.

The radical OH was an important radical for the alcohol products (i.e. $CH_3 + OH \rightarrow CH_3OH$). **Figure 6.12** indicated that the generation of OH was also depended on the discharges and the density was decreasing with the increasing of the simulation time. Moreover, the density of OH raised at the beginning of every half cycle, because more CO_2 were split into O and CO under a higher discharge power, promoting the oxidisation of H_2/H to produce OH. However, when the discharge power was decreasing, CO_2 cannot provide the enough amount of O or O_2. The radicals OH were consumed very fast, because of either H/H_2 or C_xH_y radicals. Therefore, the density of OH were very low at the end of half AC cycle.

A rough understanding of the pathways for generating the important species can be obtained by the investigation on the corresponding densities. However, there were too many species involved in this simulation and it was impossible to show all the behaviours/densities of these species. Therefore, sensitivity analysis was very necessary to define a more accurate reaction pathway.

The reaction rates related to DRM process have been reported very clearly and most of the reaction rates they presented were at ultimate steady or in average values. However, for the DBD plasma-assisted reaction, the reaction rates were changing, so it is worthy to study on the temporal dynamic reaction rates of DRM. The investigation started from the conversions of the inlet gases, shown in **Figure 6.13**.

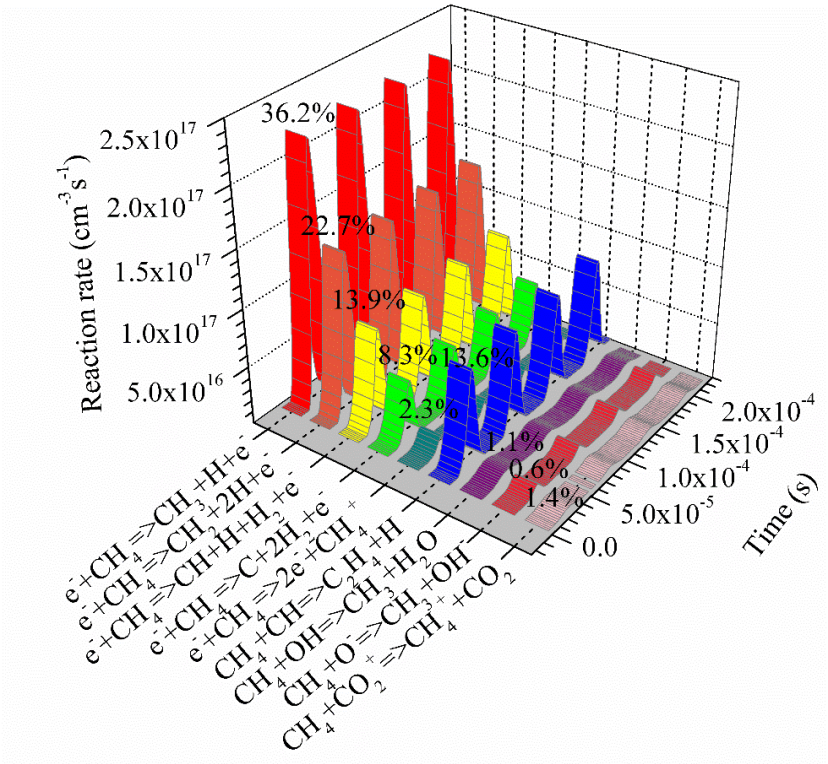

Figure 6.13 Dynamic reaction rates of the major reactions for consumption of CH_4.

The proportions of contribution to consume CH_4 of every reaction was summarised within the whole resident time. The first stage of CH_4 cracking was the dominated reaction of CH_4 conversion, occupying 36.2% and it can explain why the density of CH_3 radical was that high. All illustrated reaction rates appeared the similar fluctuation. Absolutely, the electron-impact reactions were intensified dramatically during the plasma-on duration, while the reaction rates of them dropped to a very low value when the plasma was extinguished. Normally, electrons would not affect neutral-neutral reactions directly, but the neutral reaction would be influenced by the concentrations of each reactant. Taking the example of the reaction between CH_4 and CH, CH radicals were from the third stage of electron-impact CH_4 cracking mainly, so the concentration of it defined the reaction rate of this reaction. However, the reaction rates of neutral-neutral reactions did not fall back to zero, because of the survivals of involved species. The reaction rates of the neutral-neutral reactions declined to a very low level at the end of half AC cycle and they would not recover until next half AC cycle with "fresh" radicals generated by plasma. Moreover, except for the electron-impact reactions, CH_4 can be converted by CH, OH, O^- and CO_2^+. Notably, CH was an efficient radical to consume CH_4, taking up to 13.6 %, through the replacement reaction occurring between CH and H.

However, the conversion of CO_2 was different, more than 90% converted CO_2 molecules were caused by electron-impact reaction (i.e. $e^- + CO_2 \Rightarrow CO + O + e^-$), because of the stability of CO_2.

Additionally, plasma-assisted reactions can be complex, because the electron-impact reactions and chemical reactions can occur concurrently, including the competitive reactions such as recombination (for hydrocarbons) and oxidising reactions (for carbohydrates) can also happen in the same time. Therefore, the investigations of the behaviours of the important radicals, such as CH_x, were also necessary and helpful for the analysis of the reaction mechanism.

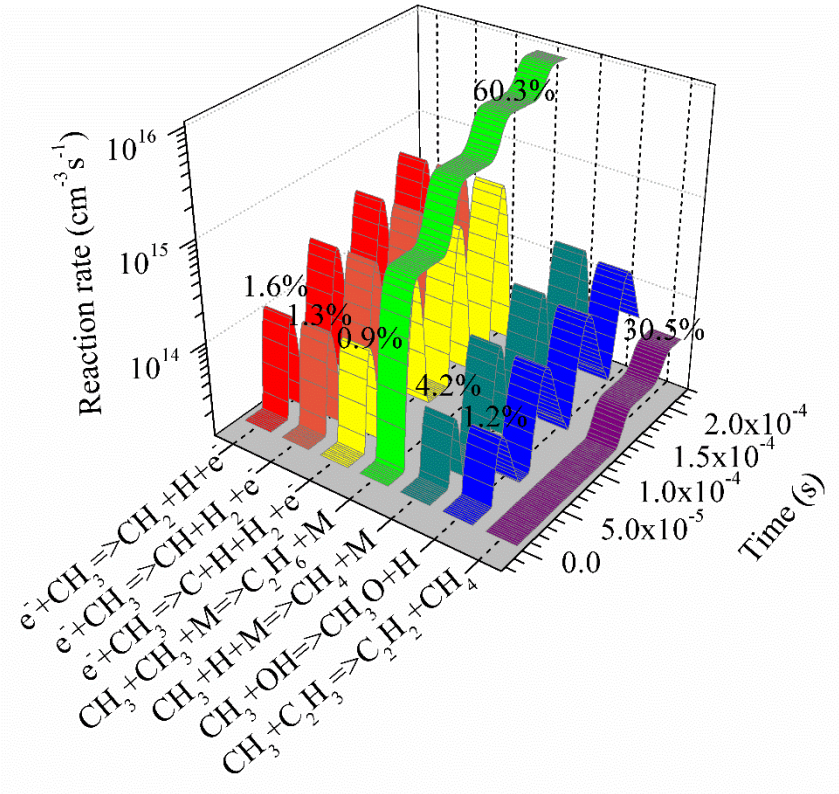

Figure 6.14 Dynamic reaction rates of the major reactions for consumption of CH_3.

Figure 6.14 clearly showed that recombination of CH_3 to produce C_2H_6 was dominating the consumption of CH_3 and it explained the reason why the selectivity of C_2H_6 was the highest, except for syngas. The electron-impact of CH_3 appeared much weaker (less than 4%). Obviously, the growth rate of recombination of CH_3 decreased when the competitive reaction became significant. In the beginning of the DRM, the concentration of C_2H_3 was low, but its rising concentration (in **Figure 6.10**) strengthened the reaction between CH_3 and C_2H_3 and it were responsible for 30.5% for the overall CH_3 consumption. However, the oxidising process of CH_3 can be almost neglected and only very small amount of CH_3 were oxidised by OH.

For CH_2 radical, it presented a very different process, shown in **Figure 6.15**. The process of recombination of CH_2 to produce C_2H_4 was very weak, as well as the other neutral-neutral reactions. Oppositely, the oxidising process became more important to consume CH_2. It was a prime explanation of the low concentration of C_2H_4. Therefore, CH_2 can be considered as the necessary radical for the generation of carbohydrates.

So far, this simulation had investigated the behaviours of the major species in plasma gas and the reaction rates of the major reactions, which would be combined with the results from the

sensitivity analysis to define the major reaction pathway of the gas-phase products, shown in **Figure 6.16**.

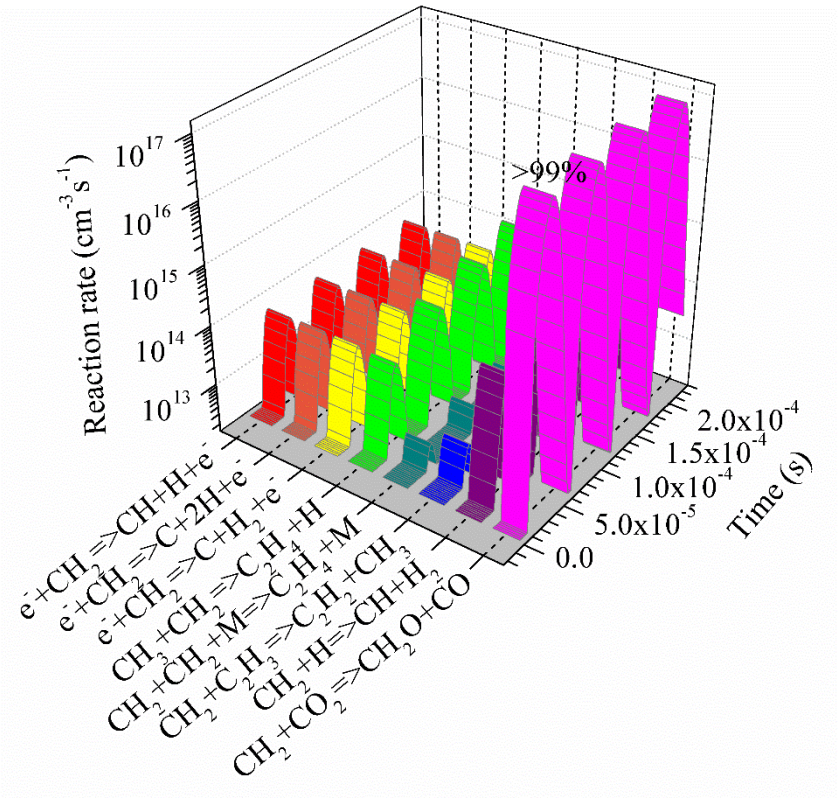

Figure 6.15 Dynamic reaction rates of the major reactions for consumption of CH_2.

The recombination of H radicals, which were mainly produced by the CH_4 cracking through the electron-impact reactions, was the major pathway for generating H_2. Moreover, H_2 was often generated with the recombination reactions, providing an alternative channel to produce H_2. CO was generated by the electron-impact dissociation of CO_2 mainly and HCO was also the necessary source for CO generation, except for CO_2 splitting. In DBD plasma-assisted DRM, the formation of O_2 was difficult, because, instead of producing O_2, most of O radicals were consumed by H_2 to generated OH.

Clearly, CH_3 can be considered as the most active radical for the DRM process and the recombination for C_xH_y products. C_2H_4 was generated as an intermediate product and consumed rapidly by either electrons or H radical to produce C_2H_3 which was the major source for generation of C_2H_2. CH_2O was formed and consumed by H and OH radicals fast to generate HCO, so it was not detected in the output gas.

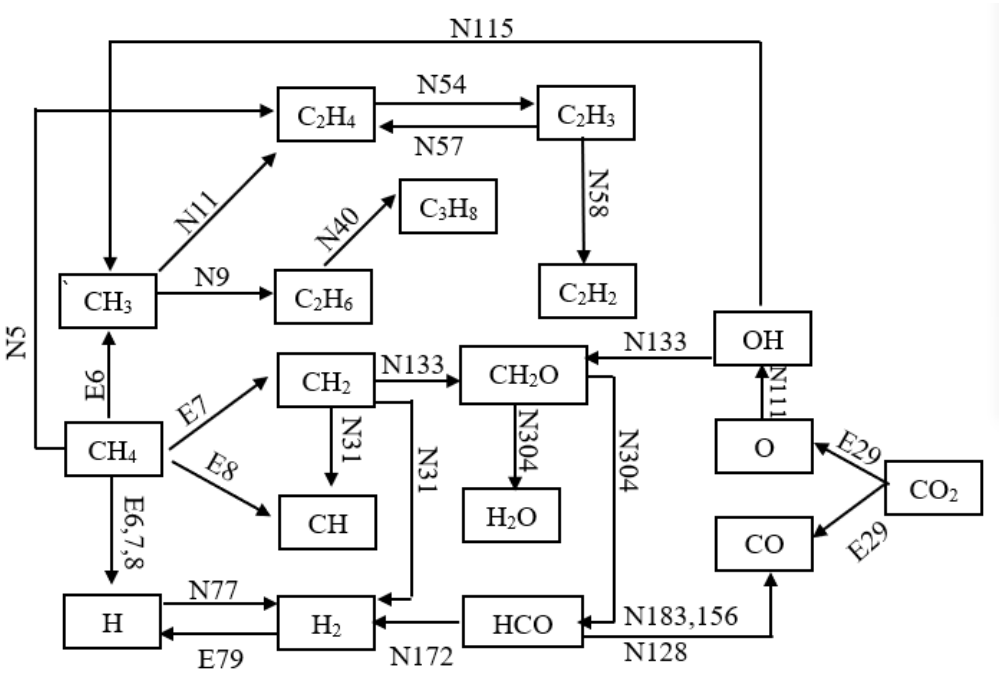

Figure 6.16. Major reaction pathway for biogas reforming to produce gas-phase products. (The corresponding reactions notated with numbers can be found in **Appendix 9.2**).

6.6 Conclusions

This chapter investigated the DBD plasma-assisted DRM (biogas reforming) to produce the syngas and valued chemicals through experiments and simulations. All densities of the species involved in DRM had been investigated within the simulation time or in every AC cycle. In every AC cycle, all important species, such as C_xH_y radicals and OH showed a clear periodic behaviour. The syngas was depended mainly by the electron-impact decompositions of the inlet gases. Except for syngas, C_2H_2 and C_2H_6 were the major gas-products and almost no C_2H_4 was detected for the experiments and simulations. CH_3 radical was the most active radical among the radicals to produce hydrocarbons during the DRM process. Moreover, 60.3% of CH_3 radicals were consumed by the recombining process to produce C_2H_6, while recombination of CH_2 to produce C_2H_4 can be almost neglected and more than 99% of CH_2 radicals were consumed by the oxidising process (by OH) to generate aldehydes. However, aldehydes have not been detected in our experiments. Based on the reaction mechanism, aldehydes must exist in the plasma gas with a very short lifetime and then were the very important sources for the generation of syngas.

This simulation work provided a better understanding of the DRM process and still can be improved. Syngas was not the unique product of aldehydes. Therefore, the project will pay more attention on the liquid products in the next chapter.

Chapter 7 Computational study on DBD plasma steam reforming of methane by stable isotope analysis

In this chapter, a simulation of SMR process had been carried out under atmospheric pressure and temperature of 373 K in a DBD reactor to investigate the reaction mechanism of H_2 production. In order to determine pathways for H_2 generation, the reactant H_2O is replaced by D_2O for the simulation work, based on the extreme similar physical/chemical characteristics and electron-impact cross sections [212], while the compound-specific isotope analysis (CISA) technique is used to calculate the different contributions of the inlet reactants (steam/methane) for producing H_2 and to trace the deuterium of steam flowing into hydrocarbons or carbohydrates. Additionally, the new-built comprehensive computational model for this work is validated by the experimental results, including conversion rate of CH_4 and selectivity of major products (i.e. H_2, CO, hydrocarbons in the form of C_xH_y…), under the same operating conditions.

7.1 Investigation of the effects of discharge power

This work started from the investigation with the effects on power (from 10 - 30 W) of the discharge behaviours, shown in the **Figure 7.1**. For this low steam concentration, the maximum applied voltage was observed at 7.4 kV. The differences among the gas voltages under the various discharge power were slight. Obviously, not only amplitudes of total current signal were magnified but also the corresponding duration was broadened when the discharge power was increased. The peak of current appeared earlier with a higher input voltage. The inlet gases were broken down and the gas voltage reached to the breakdown voltage more quickly, with a faster increasing of applied voltage. The calculated powers were 10.2 W, 19.7 W and 30.8 W, respectively. A higher discharge power can provide a longer plasma-on time, which can enhance the effects of electron-impact reactions.

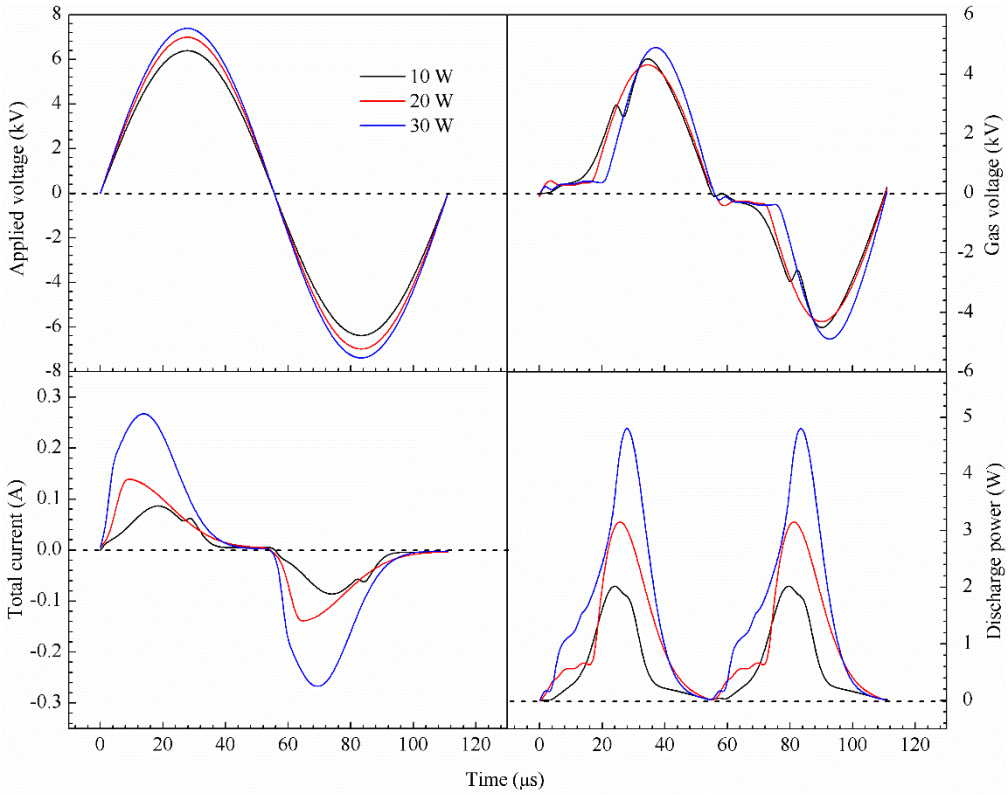

Figure 7.1 Dynamic applied voltage, gas voltage, total discharge current and discharge power. (The steam concentration was 2.5 % and total flow rate was 40 ml/min).

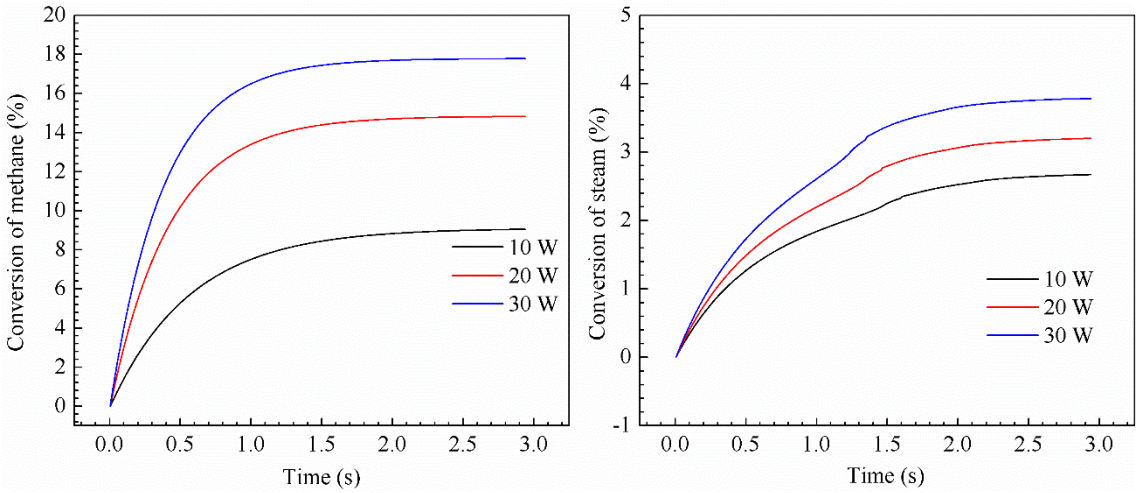

(a)

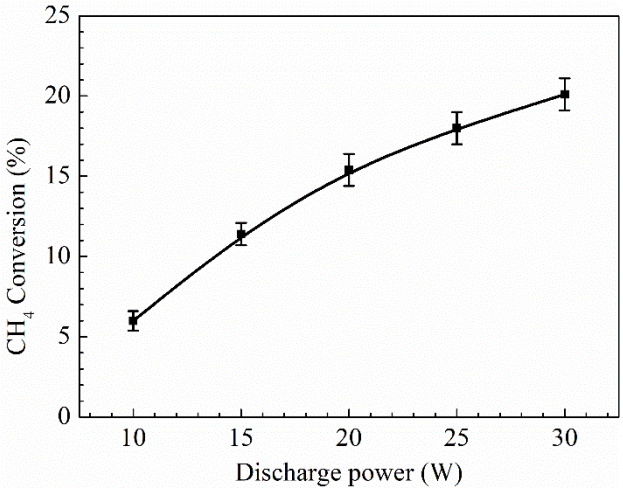

(b)

Figure 7.2 Dynamic conversion rates of inlet gases under different discharge powers with the steam concentration was 2.5 % and total flow rate was 40 ml/min. (a): simulation results. (b): experimental results.

The increasing discharge power promoted the conversion CH_4 (up to 18%), while less than 4% of D_2O was converted at a discharge power of 30 W. Hydrogen can be produced by the conversion of either methane or steam, while higher conversion of methane increased the densities C_xH_y of radicals and the probability of the generation of hydrocarbons through recombination.

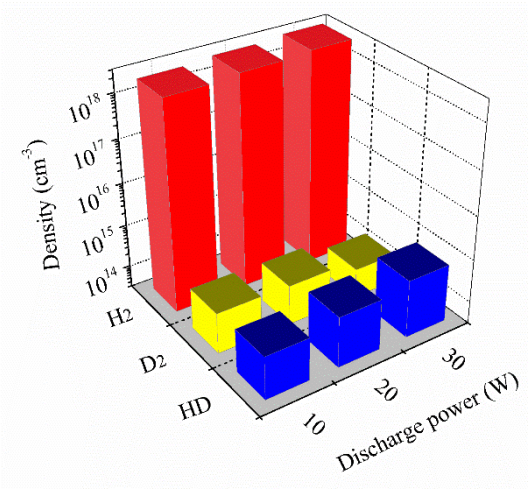

(a)

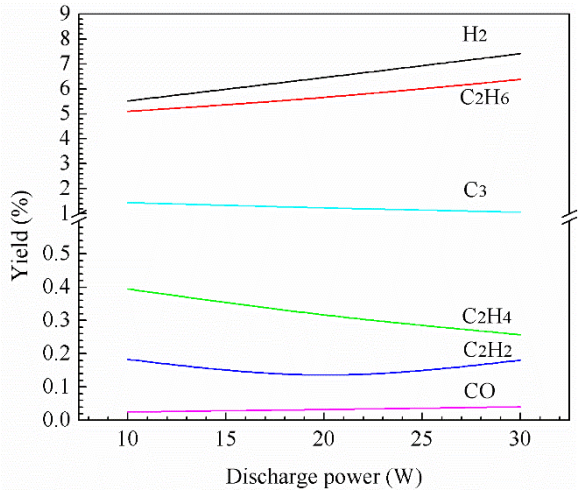

(b)

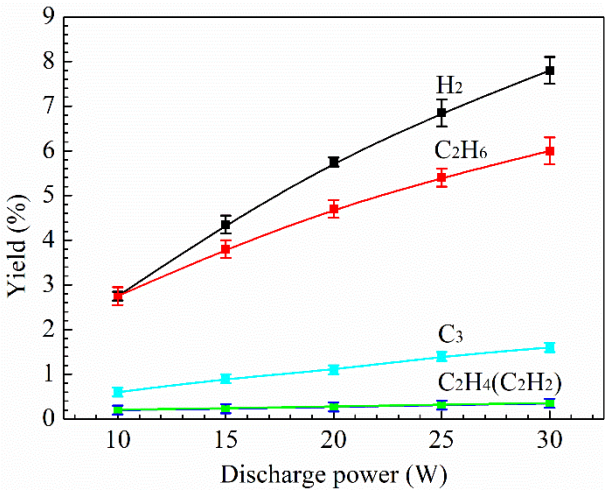

(c)

Figure 7.3 The important gas-phase products under different discharge powers with steam concentration of 2.5%. (a): Simulation results of different distributions of hydrogen product

generated from methane and steam. (b): Simulation results of the individual yield of the major gas-phase products. Here, C_3 consisted of $C_3H_{y,y=2,4,6,8}$. (c): Experimental results of the individual yield of the major gas-phase products.

As shown in **Figure 7.3**, the generation of hydrogen was enhanced by an increasing power. Additionally, hydrogen was generated from methane and steam, but more than 99% of H_2 was produced by cracking of methane under this low steam concentration. The maximum yield of H_2 was observed of 7.4%, while the generation of CO was almost negligible. In this case, the amount of CO was dramatically depended on the converted steam, which provided O element. The low density of CO was beneficial to prevent poisoning of catalyst. Beside syngas, hydrocarbons can be considered as the major products of SMR, while the yield of C_2H_6 was the highest and up to ~6.4%. So far, the simulated results had shown a very good agreement with the experimental results.

In this simulation, all heterogeneous isotope carriers were considered for calculating the yields of hydrocarbons (i.e. $C_2H_xD_{y,\ x=0,1,2,3,4,5\ \&\ y=5,4,3,2,1,0}$). However, D_2 and D were produced by the dissociation of D_2O and they would make contribution on the generation of hydrocarbons. Therefore, it was significant to trace the deuterium element to understand the reaction mechanism. One mole of D_2O provides two moles of D atoms (D also can exist in the form of OD radical), so the total proportion, *x*, of compounds (hydrocarbons or carbohydrates) containing D element should be in the relationship of:

$$x(\%) = \frac{2 \times n_{D_2O(converted)} - 2 \times n_{D_2} - n_{HD} - n_{HDO} - x \times n_{CD_xH_y}}{2 \times n_{D_2O(converted)}} \tag{7.1}$$

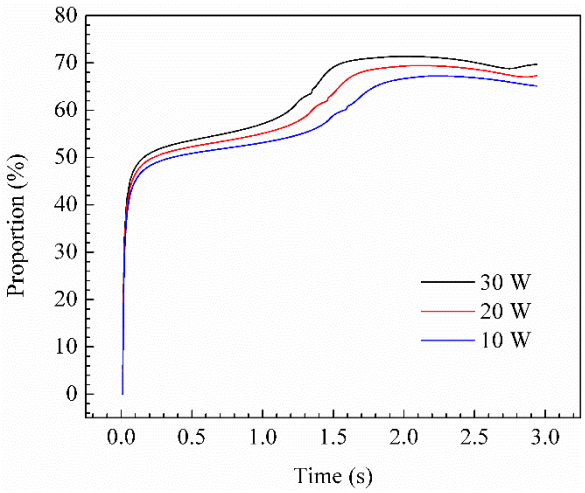

Figure 7.4 Calculated proportion of deuterium element contributed on the generation of hydrocarbons and carbohydrates with steam concentration of 2.5%.

At the resident time of 3 s, more than 70% of deuterium were consumed to produce hydrocarbons and carbohydrates and it revealed that the generation of hydrogen from steam was restricted when the steam concentration was low. An increased discharge power reduced the generations of hydrocarbons and carbohydrates. With the increasing the density of H_2, more D radicals were consumed to produce HD, shown in **Figure 7.3**. Although this displacement reaction would not affect the H_2 production, contribution of steam on hydrogen production was changed.

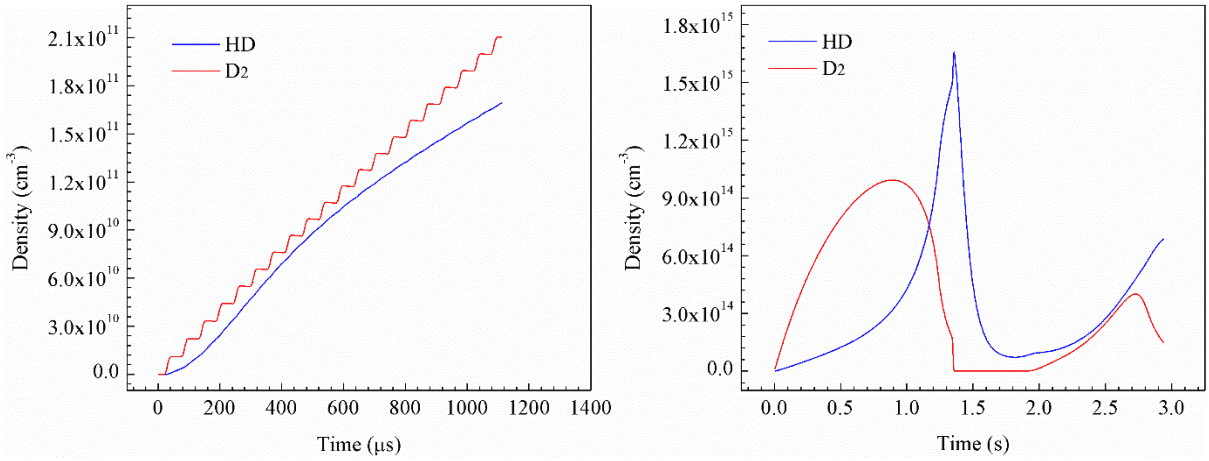

Figure 7.5 Hydrogen production consisting of D_2 and HD with the discharge powers of 30 W and steam concentration of 2.5%. (a): Generations of D_2 and HD within 10 AC cycles (~1111 μs). (b) Generations of D_2 and HD during the entire resident time (3 s).

Based on the dynamic simulation, the generation of D_2 was dramatically depended on the electron-impact dissociation of D_2O ($e^- + D_2O \rightarrow D_2 + O + e^-$, ε = 13 eV). The required energy was very high (13 eV), so the maximum density of D_2 was only ~9.7×10^{14} cm^{-3} at the resident time of around 0.8 s. At the beginning of the reaction, the density of HD grows tardily compared with that of D_2, because of the larger amount of D atoms provided by D_2O ($e^- + D_2O \rightarrow D + OD + e^-$, 7 eV), leading to the displacement reaction ($HD + D \rightarrow D_2 + H$). Moreover, the density of HD approached 1.7×10^{15} cm^{-3} at the resident time of around 1.4 s, resulting in the lower increasing rate of the proportion of deuterium element contributed on the generation of hydrocarbons and carbohydrates before around 1.5 s, as shown in **Figure 7.5**.

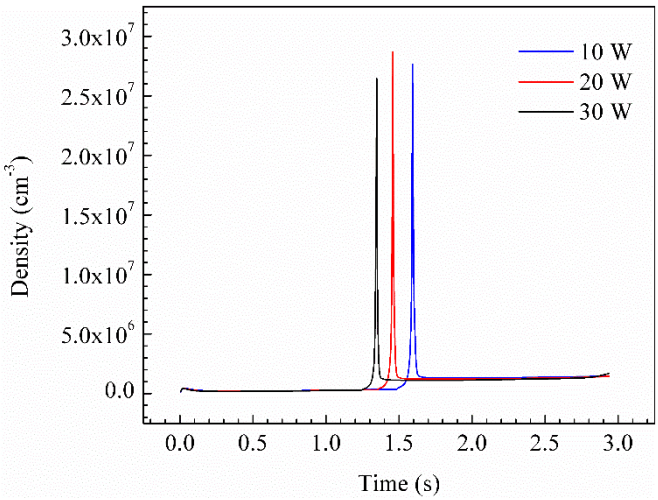

Figure 7.6 Generation of O_2 under different discharge powers from 10 W to 30 W with steam concentration of 2.5%.

As illustrated in **Figure 7.6**, the density of O_2 were almost same, but the sequent peaks appear at 1.3 s, 1.45 s and 1.6 s under discharge power from 10 W to 30 W. Notably, the highest density of O_2, which would reduce the yield H_2, was obtained at the discharge power of 20 W, corresponding to the specific energy input (SEI) of 30 J/cm^{-3}.

The peaks of O_2 must be formed by the reactions among the related radicals, such as OD. In **Figure 7.6 and Figure 7.7**, the consistency on time of the appearances of the peaks was observed between O_2 and OD under different discharge powers, so it suggested that the peaks of O_2 were caused by the rapid generation of OD. Moreover, the sharp declined density of D_2 (in **Figure 7.5**) and O, observed at the same position (on resident time) as the appearances of O_2 and OD peaks, can be explained by the reaction: $D_2 + O \rightarrow D + OD$. Similarly, the reaction ($OD + OD \rightarrow DO_2 + D$) was enhanced by the relative higher concentration of OD, leading to the simultaneous peak of DO_2 (in **Figure 7.7**). Additionally, the metastable radical DO_2 can react with OD promptly and this process result in the peak of O_2 ($DO_2 + OD \rightarrow O_2 + D_2O$, k_{373K} = of 3.8×10^{-11} cm^{3}s^{-1}).

It was obvious that the duration of the peak (at 1.5 s) of DO_2 was wider. On one hand, DO_2 was consumed by OD and the spontaneous recombination ($DO_2 + DO_2 \rightarrow D_2O_2 + O_2$, k_{373K} = 2.70×10^{-13} cm^{3}s^{-1}). The recombination with a relative lower reaction rate constant would become more significant when the concentration of OD decreased, resulting a slower decrement of the density of DO_2. On the other hand, a part of generated O_2 was recombined with D atoms to regenerate DO_2 ($D + O_2 \rightarrow DO_2$, k_{373K} = 2.42×10^{-11} cm^{3}s^{-1}), reducing the consumption rate of DO_2. Moreover, because the density of O_2 almost stayed as a constant

value after the peak, it implied that the rates of DO_2 recombination and regeneration were almost the same. Even the rate constant of recombination was much lower than the one of regeneration, the low density of O_2 and high density of DO_2 made the density of O_2 at equilibrium.

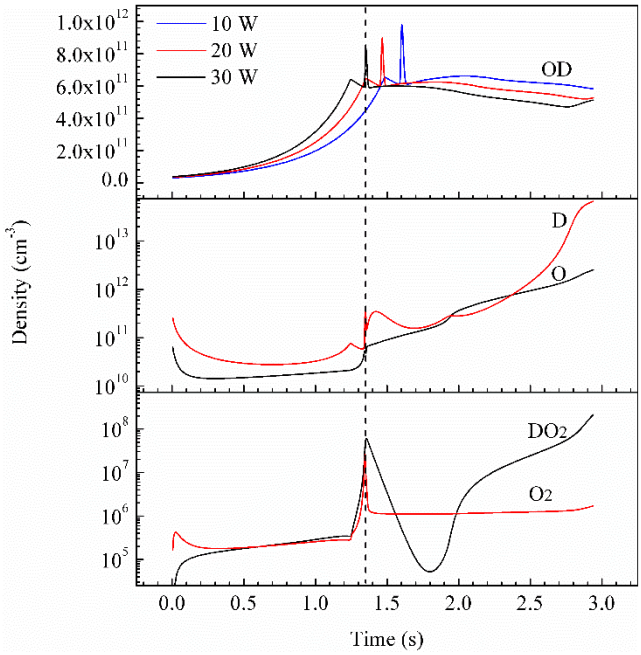

Figure 7.7 Dynamic densities of the important species related to the splitting of D_2O with the steam concentration of 2.5%. (The 1st picture shows the density of OD under different discharge power and discharge powers of the 2nd and 3rd pictures were fixed at 30 W).

As mentioned above, the displacement reactions were inevitable during the SRM process. They were acceptable and would not reduce the yield of hydrogen, if the displacements only occurred between hydrogen products (i.e. $H_2 + D \rightarrow HD + H$). However, if they occurred among abundant radicals (i.e. $CH_3 + D \rightarrow CH_2D + H$), it would then dramatically reduce the hydrogen yield, especially for the hydrogen yield from steam. Moreover, if the deuterium element was consumed by the recombination among those radicals (i.e. $CH_2 + D \rightarrow CH_2D$), it would make the ultimate products swerve to hydrocarbons instead of H_2.

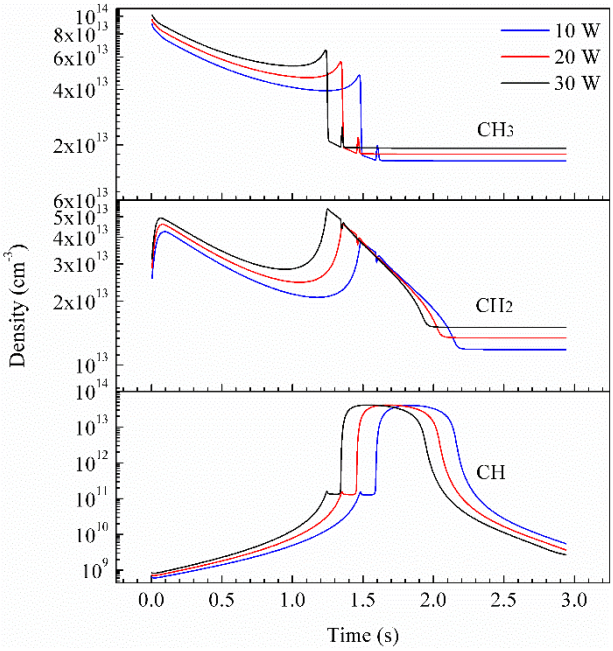

Figure 7.8 Dynamic densities of $CH_{x,(x=1,2,3)}$ radicals under different discharge powers with the steam concentration of 2.5%.

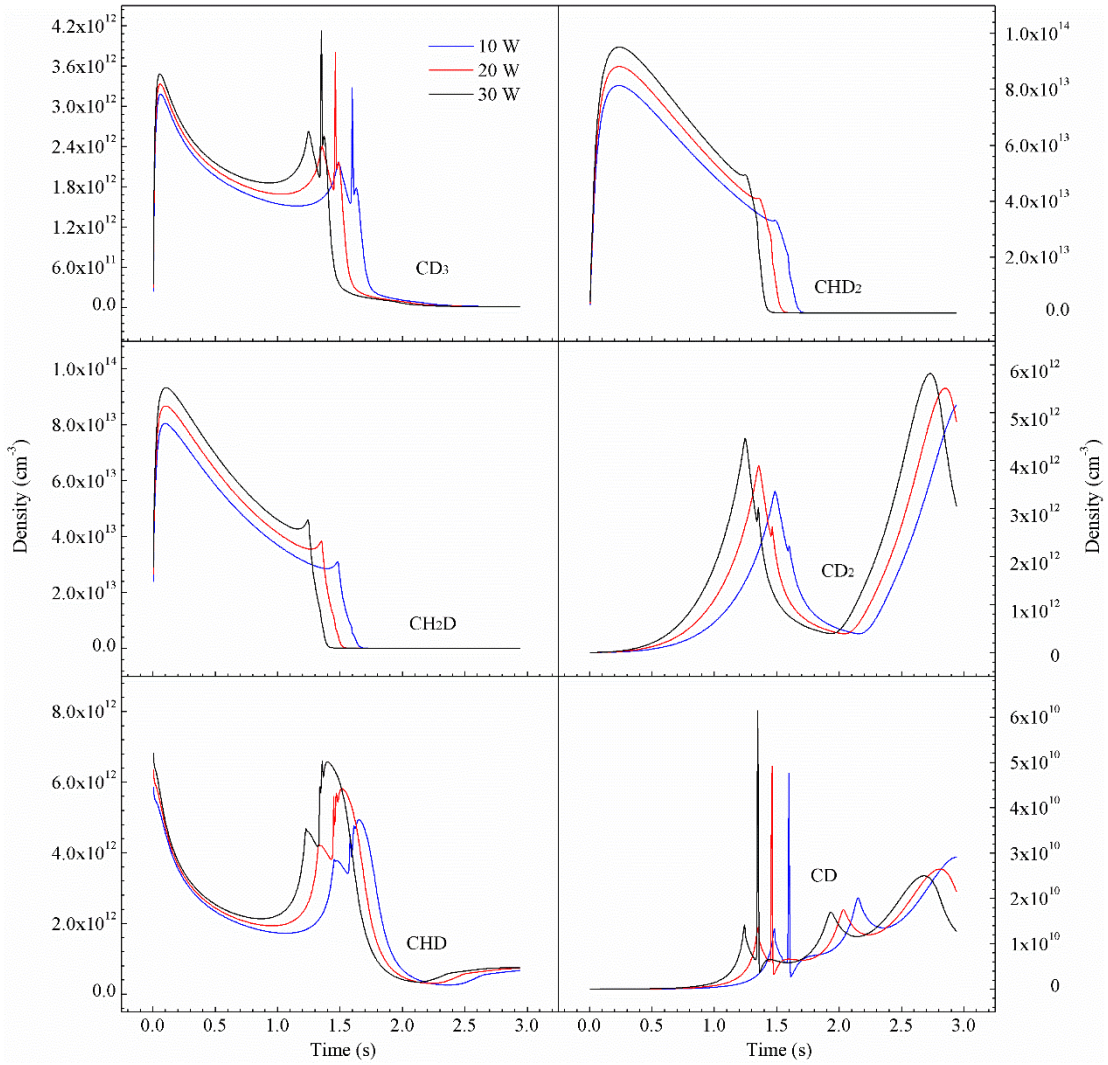

Figure 7.9 Dynamic densities of $CH_xD_{y(x=0,1,2\ \&\ y=1,2,3)}$ radicals under different discharge powers with the steam concentration of 2.5%.

$CH_xD_{y(x=0,1,2\ and\ y=1,2,3)}$ radicals were the major source particles for the hydrocarbons containing D element and they can be formed immediately through the cracking of CH_4, as shown in **Figure 7.8** and **Figure 7.9**. The profiles of CH_2D and CHD_2 density were very similar to the ones of CH_3 before the 3rd peak of CD_3 (where the O_2 peaks were observed), so the displacement reactions ($CH_3 + D \rightarrow CH_2D + H$ & $CH_3 + 2D \rightarrow CHD_2 + 2H$) occurred synchronously with the generation of CH_3. Moreover, the densities of CH_3, CH_2D and CHD_2 were almost same, so it indicated that the D radicals flew into these CH_xD_y radicals immediately and the hydrogen yield was limited by the displacement reactions. The density of CD_3 were much lower compared with other heterogeneous isotope carriers of CH_3 radical. All heterogeneous isotope carriers showed the slight peaks at around 1.25 s and these peaks were caused by the increasing density of CH_3 (in **Figure 7.8**). However, CH_3 radicals were involved

in many reactions and the sensitivity analyse was used to investigate what exactly happened to these radicals at the resident time of 1.35 s. In terms of the density of CH_2, about 10% of CH_2 was involved in the displacement reaction to generate CHD, within the resident time of 3 s ($CH_2 + D \rightarrow CHD + H$ & $CHD + D \leftrightarrow CD_2 + H$). In addition, CD/CH radicals had the negligible effect in SRM process due to the low densities of them. However, among all competitive reactions, most of D radicals have been consumed by other radicals with much higher density (i.e. CH_3), so the residual D atoms cannot maintain the generation of CD, causing a rapid drop of CD.

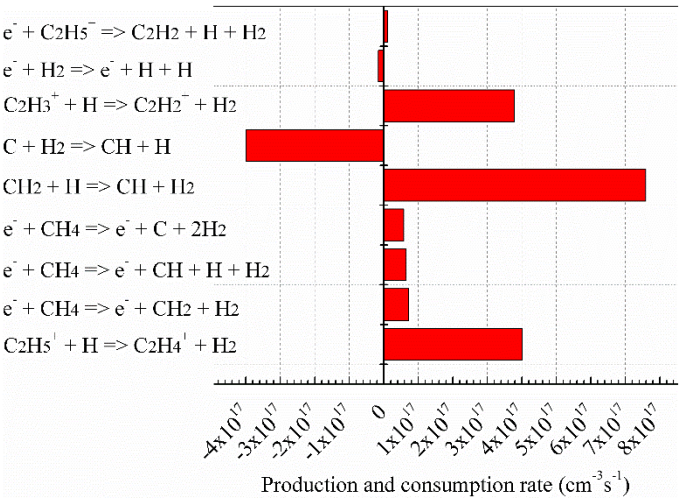

Figure 7.10 Major production and consumption rates of generation of hydrogen under the discharge power of 30 W with the steam concentration of 2.5%.

Owing to the large amount of the species involved in this simulation, it was impossible to summarise the major pathways or dominant reactions in SMR process from only the investigation of the temporal dynamic densities of the important radicals. Therefore, the sensitivity analysis was conduct starting from the investigation on production and consumption rates of hydrogen, as shown in **Figure 7.10**. Clearly, CH_4 cracking was the prominent source of the hydrogen production, since no reaction was related to deuterium. Moreover, CH_2, $C_2H_5^+$ and $C_2H_3^+$ were the essential channels of the hydrogen production, while C was the major pathway for the consumption of hydrogen. CH_2 as the most important radical to produce H_2 can be generated from cracking of CH_4 directly. Based on the sensitivity analysis $C_2H_5^+$ and $C_2H_3^+$ ions were mainly produced by the following steps:

$e^- + CH_4 \rightarrow CH_4^+ + 2e^-$ (E9, **Appendix 9.3**)

$CH_4^+ + C_2H_4 \rightarrow C_2H_4^+ + CH_4$ (I3, **Appendix 9.3**)

$C_2H_4^+ + C_2H_3 \rightarrow C_2H_3^+ + C_2H_4$ (I30, **Appendix 9.3**)

$C_2H_3^+ + C_2H_6 \rightarrow C_2H_5^+ + C_2H_4$ (I33, **Appendix 9.3**)

or

$CH_4^+ + C_2H_2 \rightarrow C_2H_3^+ + CH_3$ (I4, **Appendix 9.3**)

$C_2H_3^+ + C_2H_6 \rightarrow C_2H_5^+ + C_2H_4$ (I33, **Appendix 9.3**)

The mechanism of the entire SMR process was summarised in the **Figure 7.11**. The mechanism was dominated by the cracking of CH_4, because of the lower concentration of steam. Although the pathway of D_2O to D_2 were illustrated in **Figure 7.11**, the reaction rate related to D element was only 2.45×10^{15} $cm^{-3}s^{-1}$. The ionisation of CH_4 to generate CH_4^+ can be considered as a trigger for all ionic reactions, providing $C_2H_3^+$ and $C_2H_4^+$ which were the basic resources for $C_2H_2^+$ and $C_2H_5^+$ generation. Moreover, lots of radicals, including C_2H_2 and H_2, can be generated from $C_2H_5^+$. Most of H atoms have been consumed by the recombination reactions to produce hydrocarbons (i.e. C_2H_6) rather than H_2. Additionally, most of D atoms have been involved in the displacement reactions to produce the CH_2D, causing a low hydrogen yield from steam.

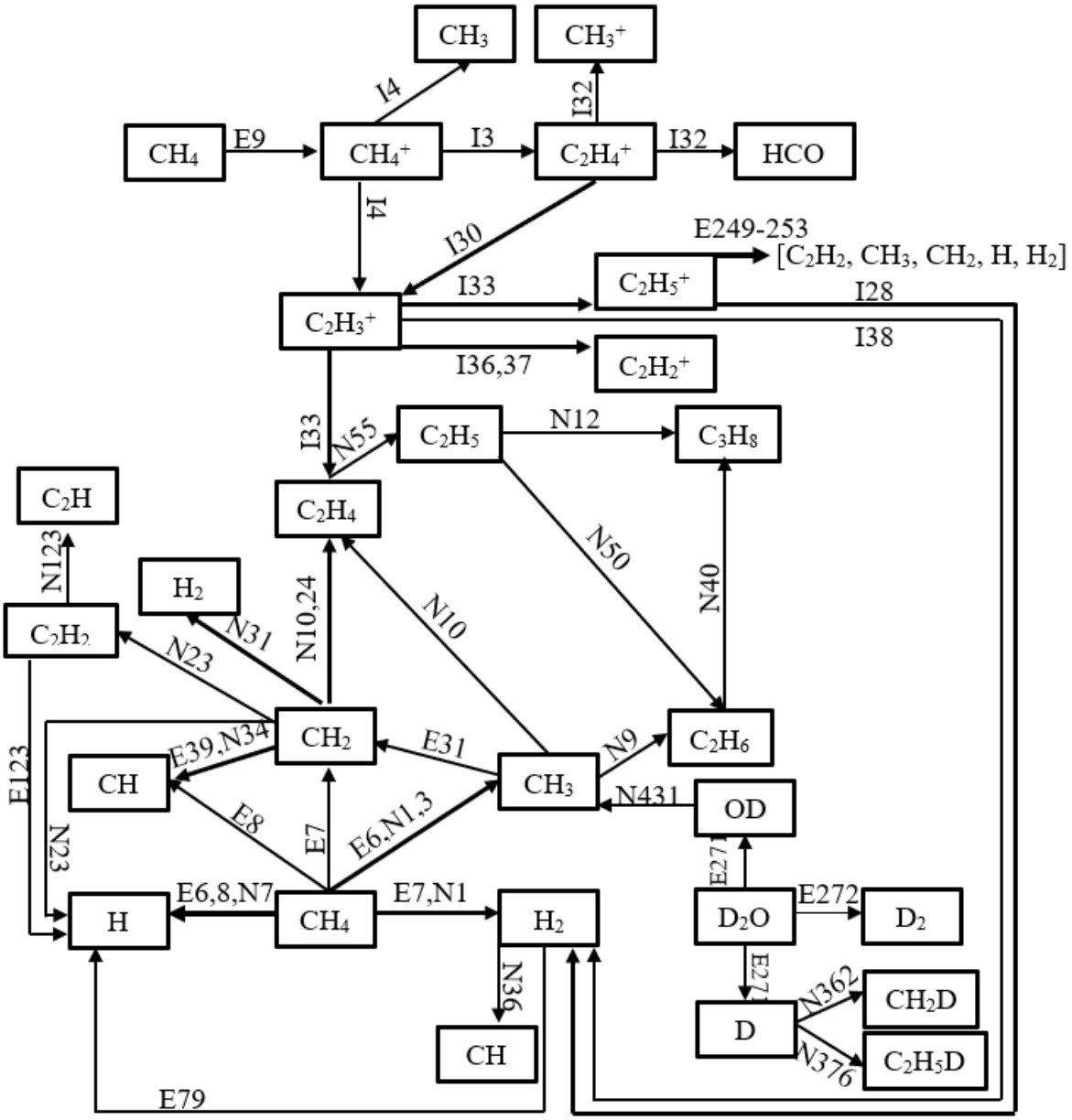

Figure 7.11 Overview of the major reaction pathways for the SMR process under the discharge power 30 W with steam concentration of 2.5%. The thickness of the arrows was corresponded with the reaction rate (rates of 10^{16} cm^3s^{-1} were displayed in 0.5 pt line; rates of 10^{17} were displayed 1.0 pt line; rates of 10^{18} were displayed 1.5 pt line) and can be superposed. For example, the rate of the reaction between CH_4 and CH was in the magnitude of 10^{18} cm^3s^{-1}, while the rate of the reaction between CH_4 and electrons was in the magnitude of 10^{17} cm^3s^{-1}. Therefore, the thickness of CH_4 to H was 2.5 pt (1 pt + 1.5 pt). (The corresponding reactions notated with numbers can be found in **Appendix 9.3**).

The sensitivity analysis was a very useful method to define the mechanism of SMR and the purposes of this work was to enhance the hydrogen production and understand the role of steam in the SMR process. Therefore, a sub-sensitivity analysis was condunted containing deuterium.

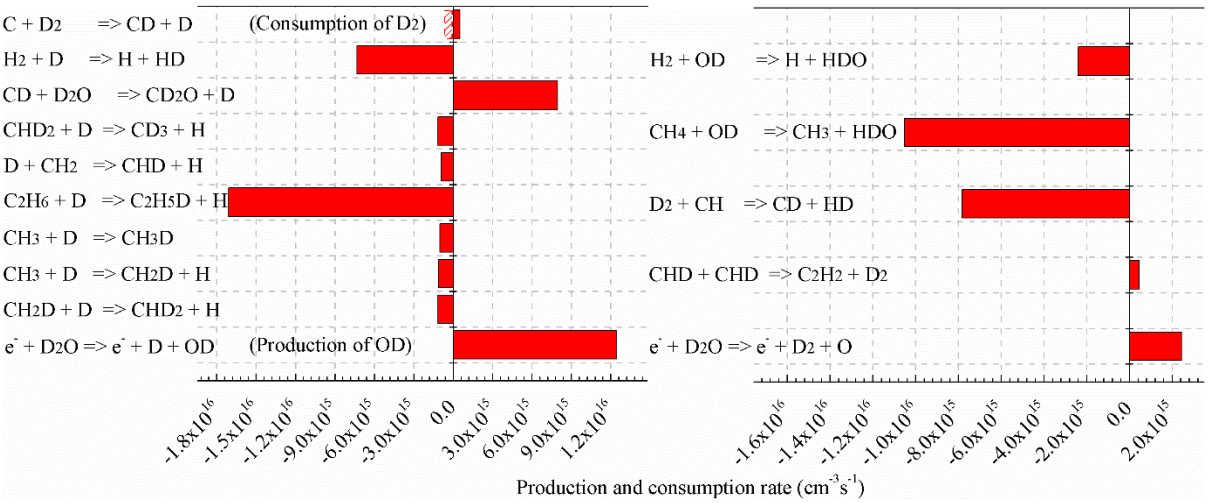

Figure 7.12 Major production and consumption rates of D, D_2 and OD under the discharge power of 30 W with the steam concentration of 2.5%.

The rates of the reactions involving deuterium were much lower compared with the ones of the entire SMR process. Based on the sub-sensitivity analysis, most of the D and OD radicals were generated by the electron-impact decomposition of steam. CD can also be oxidised by steam to generate D and CD_2O. Moreover, at the end of the resident time, the density of CD_2O (with the heterogeneous isotope carrier of CHDO) and CH_2O were ~1.3×10^{12} cm^{-3} and ~1.1×10^{7} cm^{-3}, respectively at a discharge power of 30 W. It implied that steam made more contributions on the generation of aldehydes. However, aldehydes were not the final product and they are major sources for the generation of carbohydrates (i.e. alcohol) via hydrogenations. Additionally, owing to the high concentration of C_2H_6, the displacement reaction to generate C_2H_5D was the most important channel for the consumption of D atoms. The major pathway of the generation of D_2 was the electron-impact decomposition of steam, but D_2 was very easy to react with CH to produce HD. Absolutely, there was no effect on hydrogen yield, if more HD was generated, but higher density of CD would promote the formation of CD_2O, promoting the generation of carbohydrates.

According to the sub-sensitivity analysis, this simulation defined which reactions can affect the hydrogen yield from steam, after the decomposition of steam. In **Figure 7.13**, the displacement reaction between CHD_2 and D was the most important reaction to generate CD_3 and the major reason why the curves of the density of CD_3 appeared peaks at the same

simulation time (**Figure 7.9**). Moreover, according to the investigation of the behaviours of species as described above, a series of appearances of peaks observed on O_2 and DO_2 were caused by the sharp peaks of OD. **Figure 7.14** defined the two reactions which can cause those peaks, while the reaction between OH and D_2O was more essential.

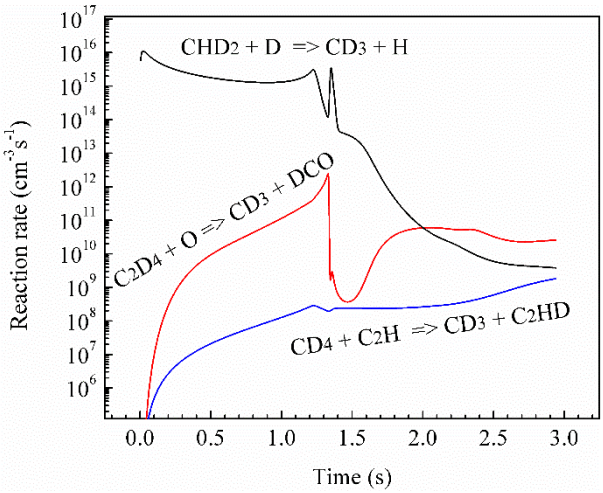

Figure 7.13 Dynamic reaction rate for producing CD_3 under the discharge power of 30 W with the steam concentration of 2.5%.

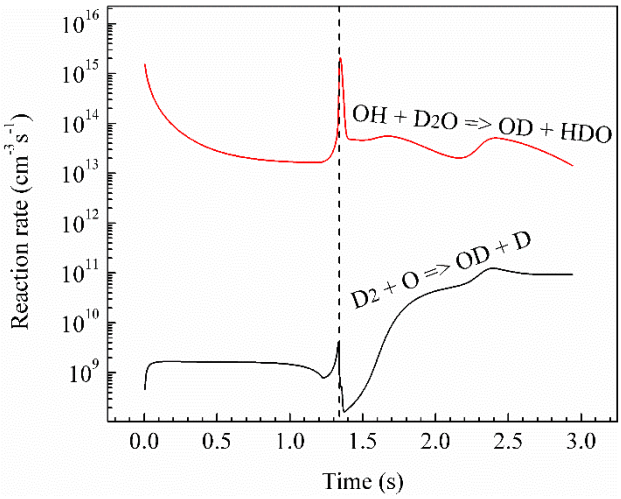

Figure 7.14 Dynamic reaction rate for producing OD under the discharge power of 30 W with the steam concentration of 2.5%.

In order to obtain a better understanding of the role of steam in SMR process, an individual mechanism only based on the deuterium element was illustrated in **Figure 7.15**. It was not difficult to perceive that most of D atoms were consumed by the displacement reaction with C_xH_y radicals (i.e. CH_3, CH_2 ...) and H_2, while each displacement reaction produced H atom with the corresponding heterogeneous isotope carrier. These heterogeneous isotope carriers

were the important resources for the formation of the corresponding hydrocarbons. According to the temporal dynamic density study, two reactions were enhanced at 1.45 s, as shown within the red circle in **Figure 7.15**. However, the reaction rates illustrated in figure 7.15 were 10 times less than the ones list in the overview mechanism of SMR (**Figure 7.11**). Therefore, a higher inlet steam concentration was required to investigate the further impact of steam.

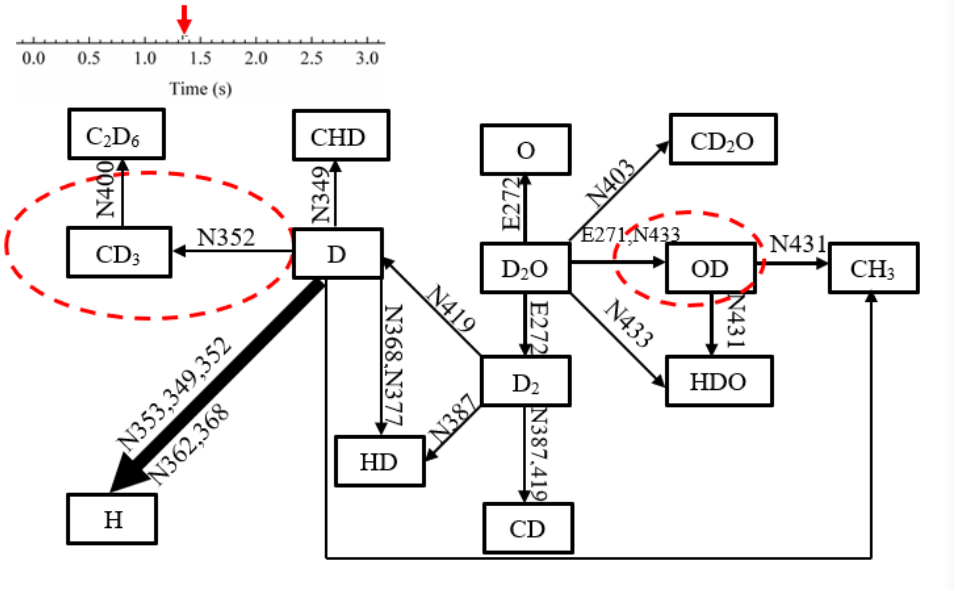

Figure 7.15 Major reaction pathways conclude from the sub-sensitivity analysis under the discharge power 30 W with steam concentration of 2.5%. The thickness of the arrows is corresponded with the reaction rate (rates of 10^{15} cm^3s^{-1} were displayed in 0.5 pt line; rates of 10^{16} were displayed 1.0 pt line; rates of 10^{17} were displayed 1.5 pt line) and can be superposed. The red arrow pointed to the time when the reactions in the red circle were enhanced. (The corresponding reactions notated with numbers can be found in **Appendix 9.3**).

7.2 Investigation of the effects of steam concentration

The effects of discharge power on the SMR process had been investigated at a lower steam concentration. However, in industry, excess steam ($CH_4/H_2O < 1$) would be inlet to the reacting chamber to guarantee the maximum H_2 yield. As a result, in this section, the steam concentration was increased to obtain a better understanding of the role of steam in the SMR process.

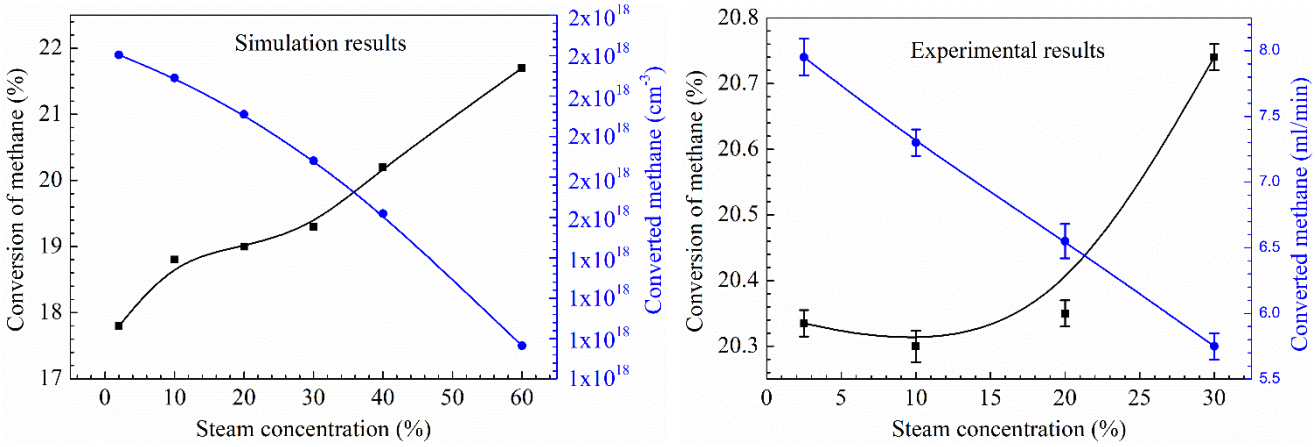

Figure 7.16 Simulation/experimental conversion rates and amount of converted methane with different steam concentrations under the discharge power of 30 W and total flow rate of 40 ml/min.

For the experiments, the concentration of steam was increased up to 30% by rising the temperature of the water bath, but the increment was restricted by the saturated vapour pressure. For the simulations, the steam concentration was increased to 60% with a much easier process by adjusting the ratio of the inlet gas. The different compositions of the inlet gas changed the discharge behaviour. However, the changes of gas voltage and discharge current were not obvious with an increasing steam concentration under the same discharge power of 30 W, resulting in a limited effect on the reduced electrical field. Moreover, because the cross sections of the targeted species in the plasma gas were changed, the EEDFs and mean electron energy were influenced.

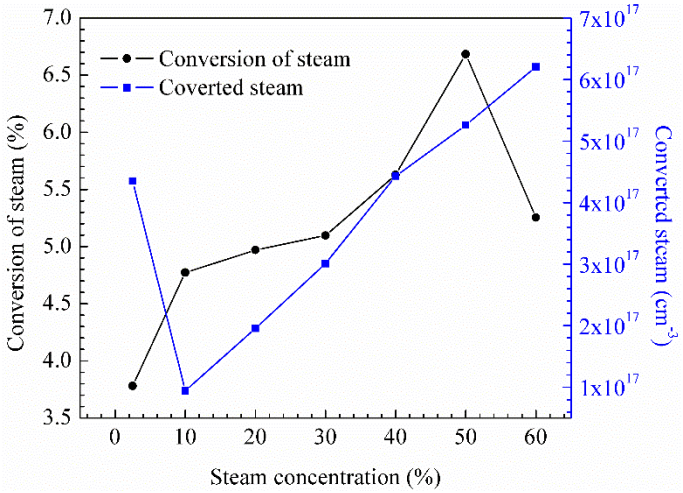

Figure 7.17 Simulation conversion rates and amount of converted steam with different concentrations of steam under the discharge power of 30 W and total flow rate of 40 ml/min.

The experiments revealed that concentration of steam made a negligible effect in the methane conversion and the simulations agreed well with this result, especially when the steam concentration was increased from 10% to 30%. However, the total amount of converted methane declined when the steam concentration was increased in experiments and simulations. The maximum conversions of methane were obtained with a low methane concentration of 21.1%.

Figure 7.17 illustrated that the fluctuant curves of conversion rate and converted amount of steam. Generally, the amount of converted steam appeared an increasing trend. The conversion of steam reached the peak of ~6.7% at the steam concentration of 50%. Higher conversion of steam can provide higher concentrations of radicals involved D element (i.e. D and OD) and then these radicals would be an effective channel to convert CH_4.

The yields of all gas phase products would be changed by the increasing steam concentration. With the increasing of steam concentration, more hydrogen was produced by steam. As defined in **Figure 7.18(a)**, at a low steam concentration of 2.5%, more than 99% of hydrogen yield was from CH_4 cracking, but the proportion reduced to 95% when the steam concentration was increased to 60%. For comparison, the yields of C_2H_6, C_2H_4, C_2H_2, C_3 compounds and CO were illustrated in **Figure 7.18(b)** and **Figure 7.18(c)** and the simulation model was well validated by the experimental results via the distributions and variation trends of yield of these gas-phase products. For the simulations and experiments, hydrogen was the major product, when the steam concentration was lower than 30%. However, instead of H_2, C_2H_6 became to the main compound of the outlet gas when the steam concentration was increased further. This interesting phenomenon could be caused by the increasing densities of O and OD radicals generated by the decomposition of D_2O, causing a increasing density of CH_3 ($CH_4 + O \rightarrow CH_3 + OH$ or $CH_4 + OD \rightarrow CH_3 + HDO$). The yield of C_3 compounds almost remained as a constant and the yields of the unsaturated hydrocarbons was less than 1%. Notably in this work, the density of CO was too low to be the GC. Therefore, the yield of CO was not shown in figure **7.18(c)**.

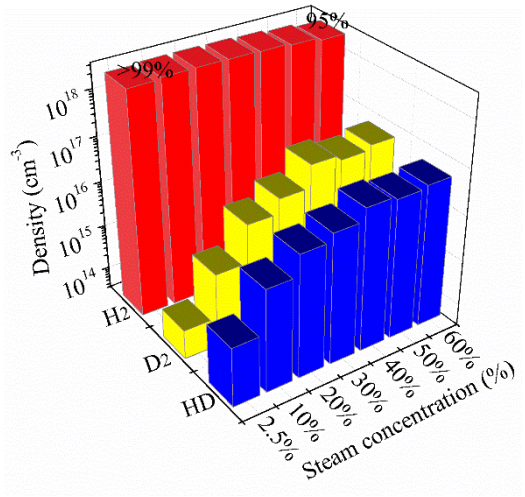

(a)

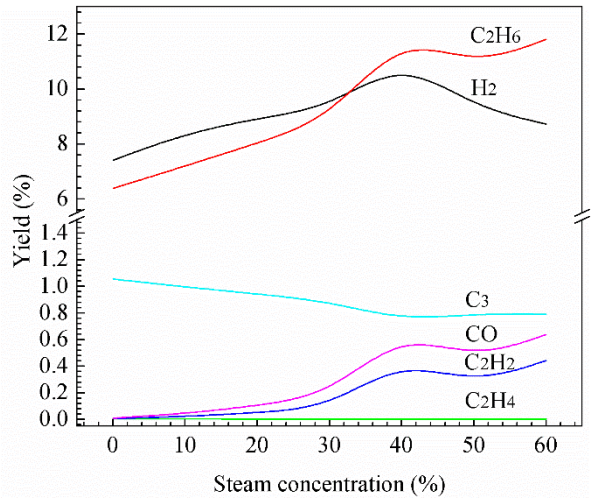

(b)

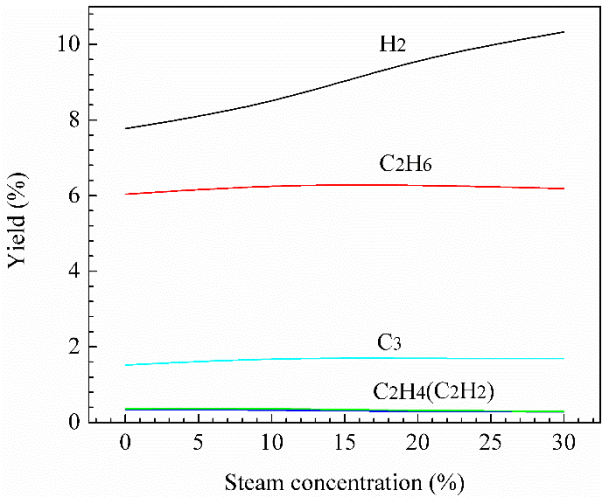

(c)

Figure 7.18 The important gas-phase products under the discharge powers 30W with the different steam concentrations. (a): Different distributions of hydrogen product generated from

methane and steam. (b): Simulation results of individual yield. Here, C_3 consists of $C_3H_{y,y=2,4,6,8}$. (c): Experimental individual yield.

Equation (7.1) clearly defined the proportion of deuterium element on the generation of hydrocarbons and carbohydrates. More than 40% of steam was converted to the hydrogen production with the steam concentration 60% and it was not difficult to be explained by the decreasing inlet carbon content. Therefore, combined with the investigations on the effects of discharge power on SMR, more converted steam would contribute on the hydrogen production when the steam concentration or the discharge power was higher.

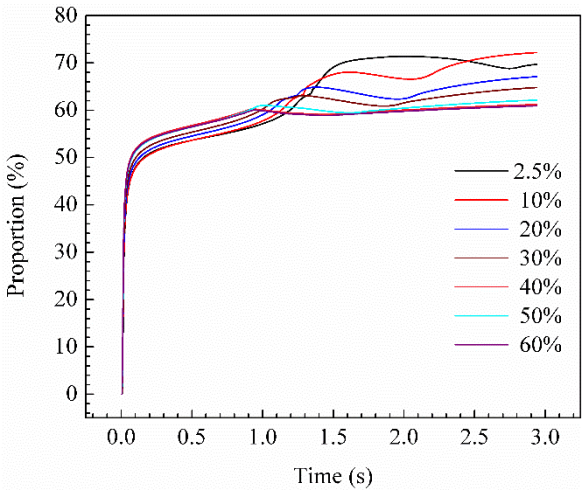

Figure 7.19 Proportion of deuterium element contributed on the generation of hydrocarbons and carbohydrates under the discharge power of 30 W with different steam concentrations.

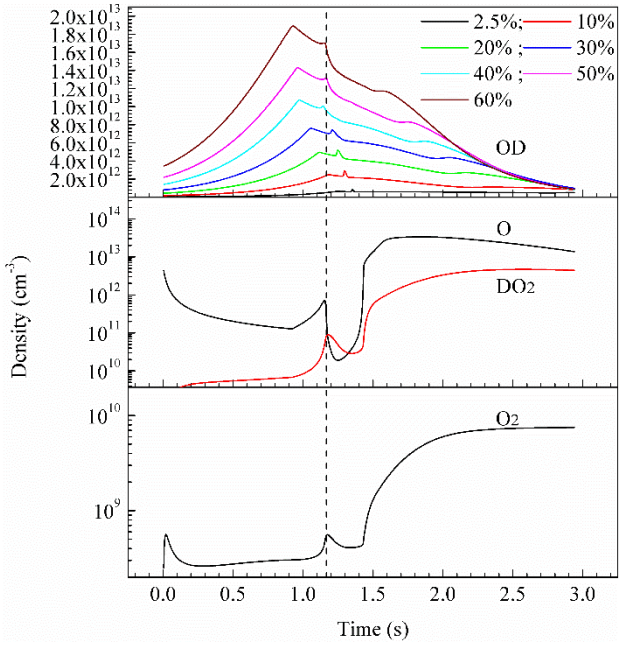

Figure 7.20 Dynamic densities of the important species related to the splitting of D_2O under the discharge power 30W. (The 1st picture showed the density of OD under different concentrations of steam and the concentrations of steam of the 2nd and 3rd pictures were fixed at 60%).

The peaks still can be observed on the profiles of the essential species, such as OD, O_2, etc. The OD radical was generated steadily via the decomposition of steam at the beginning of the reaction. Moreover, when the more steam was converted, the generation rate of OD radicals was slower than the consumption rate of OD, causing the decreasing of OD density. At a higher steam concentration, the 1st peak (maximum density of OD) appears earlier and OD radical was also consumed faster. For the appearance of the 2nd peak, as discussed above, it still can be considered as an essential pathway for producing O_2, as well as the carbohydrates. Avoiding the repetition, simply, OD can promote the generation of DO_2, which was the important source for the generation of O_2. Compared with other species, the density of O_2 was still much lower, so it was not detected by the GC.

Obviously, the rising of the density of OD would affect the behaviors of the other reactive radicals, especially for the hydrocarbon radicals (CH_xD_y) which can react with OD directly. The CH_x radicals were always the major source for the existence of CH_xD_y. In **figure 7.21**, the density of the CH_x became lower and it can be explained by the lower inlet concentration of CH_4 and the enhancement of the displacement reactions which was caused by the higher density of the radicals from the decomposition of steam. Moreover, for the CH_3 radical, the

obvious decrement was observed. Based on the mechanism concluded at the low steam concentration, formations of C_2H_4 and C_2H_6 ($CH_3 + CH_2 \rightarrow C_2H_4 + H$ and $CH_3 + CH_3 \rightarrow C_2H_6$) were the two major channels to consume CH_3. Therefore, the steady decrease was caused by the generation of C_2H_6 which was occurring all the time during the SMR process, while the sharp decrement was caused by the rapid increasing of density of CH_2. The next smaller peaks of on the CH_3 curve were related to the rapid increasing of density of OD ($CH_4 + OD \rightarrow CH_3 + HDO$). For the CH_2, the density of it became much lower when the steam concentration is raised to 60%. Based on the simulation of DRM in **Chapter 6**, CH_2 was very easy to be oxidised, so the density of it was difficult to stay at a high value when the densities of oxidants, including O, OD, and DO_2, were increased with a higher inlet concentration of steam. Moreover, CH_4 was oxidised faster by the OD radical to produce CH_3 and HDO and it was the basic source for generating CH_2, so these were the major reasons why the density of CH_2 was reduced.

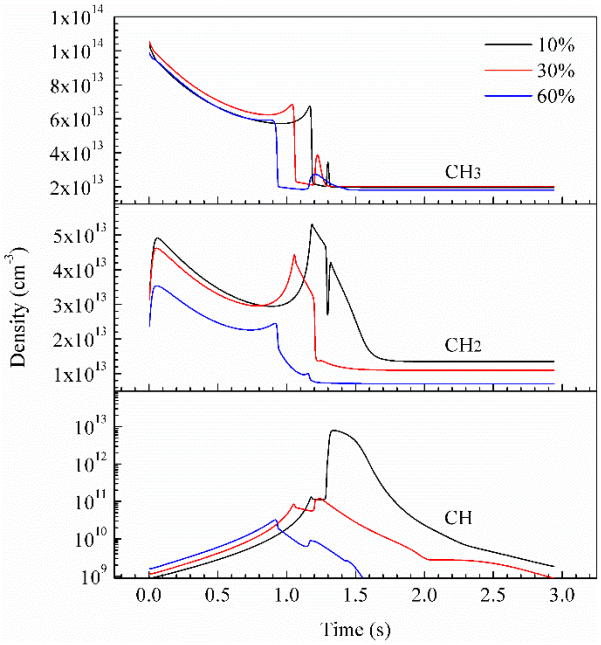

Figure 7.21 Dynamic densities of $CH_{x,(x=1,2,3)}$ radicals under the discharge power of 30 W with different concentrations of steam.

The relevant heterogeneous isotope carriers of CH_x radicals would also be affected by the increasing steam concentration. In **Figure 7.22**, more CD_3 radicals were generated during the SMR process. Most of CD_3 radicals were formed by the displacement reaction between D and CHD_2 as defined in **Figure 7.13**. The of peaks of CD_3 and CHD_2 appeared at the same simulation time with the same amplitudes and the sharp peaks of CD_3 disappeared when the

concentration of steam was increased. It implied that the CHD_2 affect more on the generation of CD and the effect of the radicals (i.e. O), causing the sharp peaks of CD_3 in **Figure 7.9**, was weakened due to the relative low density of O. The profiles of CH_2D curve was exactly similar to that of CHD_2, so the displacement reactions for generating CH_2D and CHD_2 from CH_3 were occurring at the same time with the almost same reaction rate. Moreover, the similar densities of all heterogeneous isotope carriers of CH_3 radicals and CH_2 implied that the displacement reactions of CH_3 were very easy to happen. The density of CD_2 became much higher when the steam concentration was increased to 60%. Moreover, the density of CD_2 was higher that CHD and the general tendencies of CD_2 become non-regular. Therefore, except for the displacement reactions, CD_2 must be involved into other reactions. Similarly, the densities of CH and CD were still very low. CD and CH radicals would not affect the reaction mechanism dramatically, due the low densities of them.

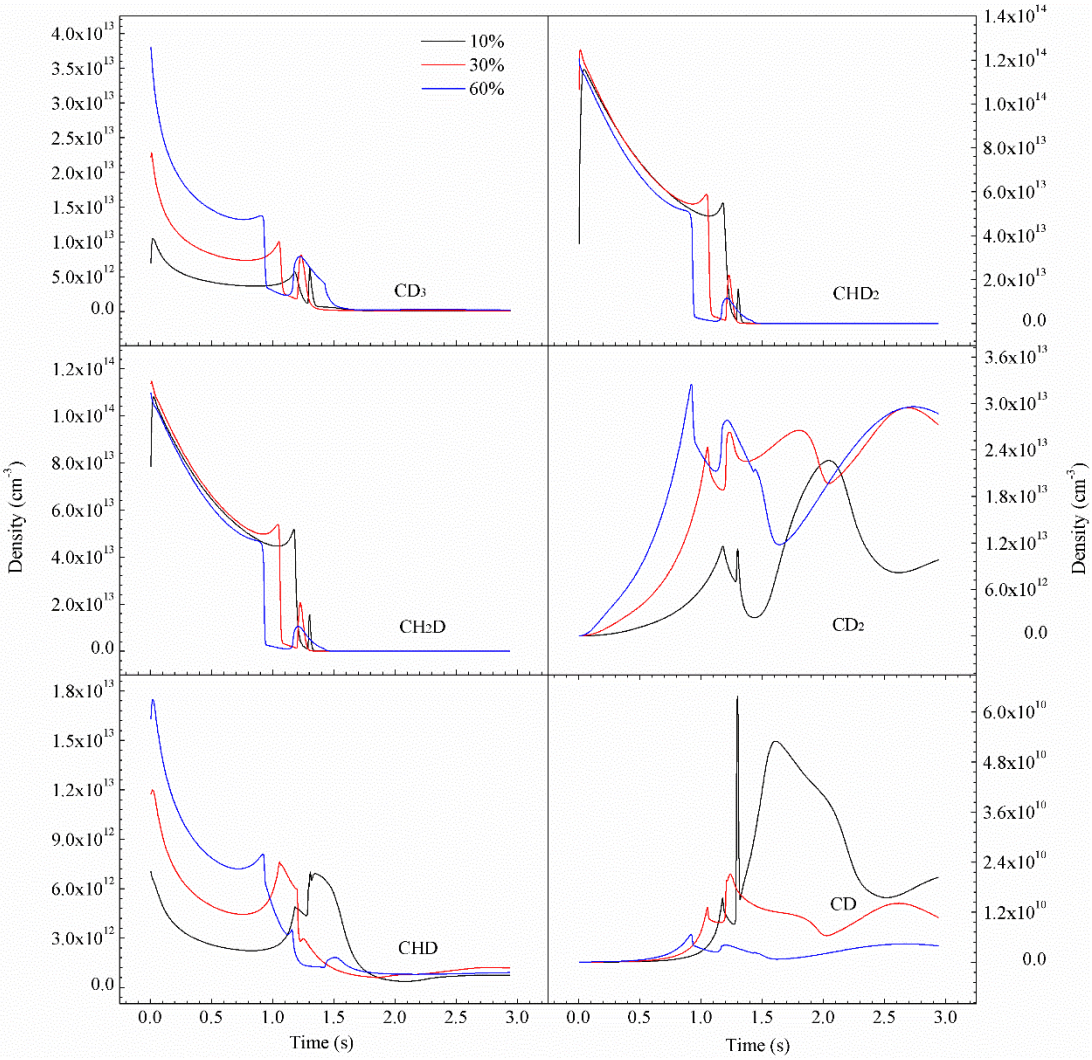

Figure 7.22 Dynamic densities of $CH_xD_{y(x=0,1,2\ \&\ y=1,2,3)}$ radicals under the discharge power of 30 W with different steam concentrations.

Based on **Figure 7.16** and **Figure 7.17**, the ratio of converted CH_4 and D_2O was ~ 1.6, but steam made much less contribution on the hydrogen yield (less than 5% with a steam concentration of 60%). It revealed that most of the deuterium was consumed for generating the hydrocarbons or carbohydrates. As a result, the sensitivity analysis was conducted again to understand to the mechanism of SMR process with a higher steam concentration.

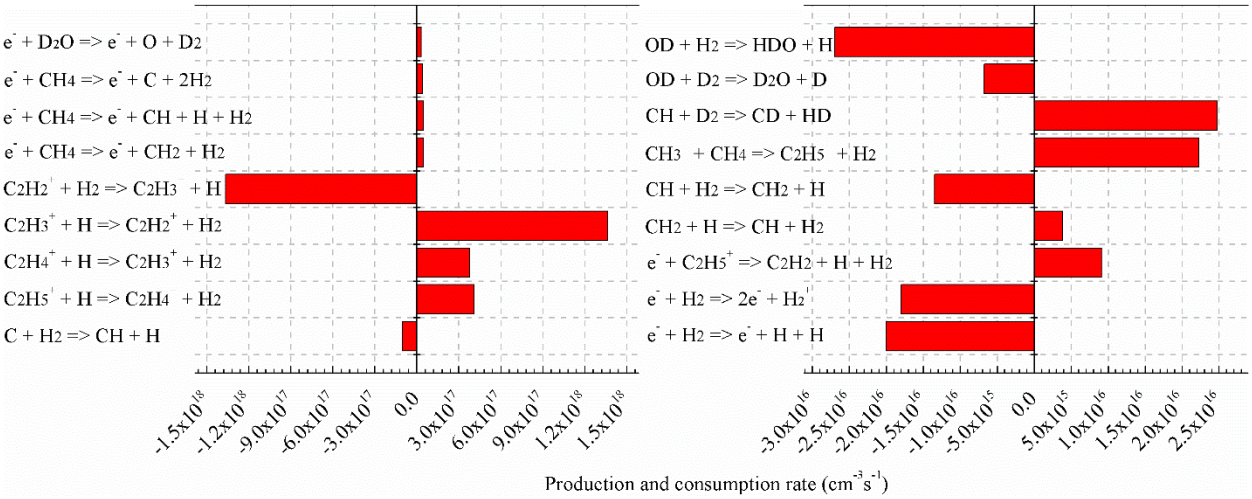

Figure 7.23 Major production and consumption rates of H_2 production under the discharge power of 30 W with the steam concentration of 60%.

Figure 7.23 illustrated that the pathway of the generation of hydrogen was changed when the steam concentration was increased. Firstly, the overall hydrogen generation rate was much lower (only half, compared the rates in **Figure 7.10**) when CH_4 concentration was reduced to 40%. Even if the concentration of steam was increased remarkably, the major sources for the hydrogen yield were still CH_4 and the cracked radicals from CH_4. Therefore, there was no doubt that a lower CH_4 concentration inhibited the generation rate of the hydrogen production. Secondly, for the generation of H_2 (from CH_4 cracking), $C_2H_5^+$ was still the important channel for the generation of H_2, while CH_3^+ and $C_2H_4^+$ became the alternative channels for producing H_2. As the procedure defined above, $C_2H_3^+$ can be generated from $C_2H_4^+$ or CH_4^+ (single step). Nevertheless, for this single step process ($CH_4^+ + C_2H_2 \rightarrow C_2H_3^+ + CH_3$), the generation of $C_2H_3^+$ was limited by the low concentration of C_2H_2, since the density of C_2H_2 (with the relative lowest yield among the C_2 hydrocarbons shown in **Figure 7.3 and Figure 7.18**) became much lower when the steam concentration was increased. Moreover, the reverse reaction ($C_2H_2^+ + H_2 \rightarrow C_2H_3^+ + H$) consumed H_2 with a similar rate, offsetting the generation of H_2 from $C_2H_3^+$ channel. Furthermore, CH_2 cannot be considered as the major channel for H_2 production again and was suffering from a worse situation when the steam concentration was higher. The reverse

reaction ($CH + H_2 \rightarrow CH_2 + H$) consumed H_2 much faster than generation. H must be involved to other more important reactions with a higher steam concentration, so CH_2 lost the priority to generate H_2. Finally, the deuterium-containing reactions appeared in the major pathways of the generation of hydrogen. D_2 was mainly produced by the electron-impact of D_2O directly, while it can also generate HD via displacement reaction with CH. Certainly, the displacement reactions always occurred among H_2, HD and D_2, but they would not affect the total hydrogen yield. In addition, with the increasing density of OD, the total hydrogen yield was reduced and the reverse reactions were enhanced ($OD + H_2 \rightarrow HDO + H$ or $OD + D_2 \rightarrow D_2O + D$). It was easy to conclude the overall deuterium-containing mechanism, through the sensitivity analysis and the investigation on the behaviours of the most important radicals, to investigate the role of steam during the SMR process.

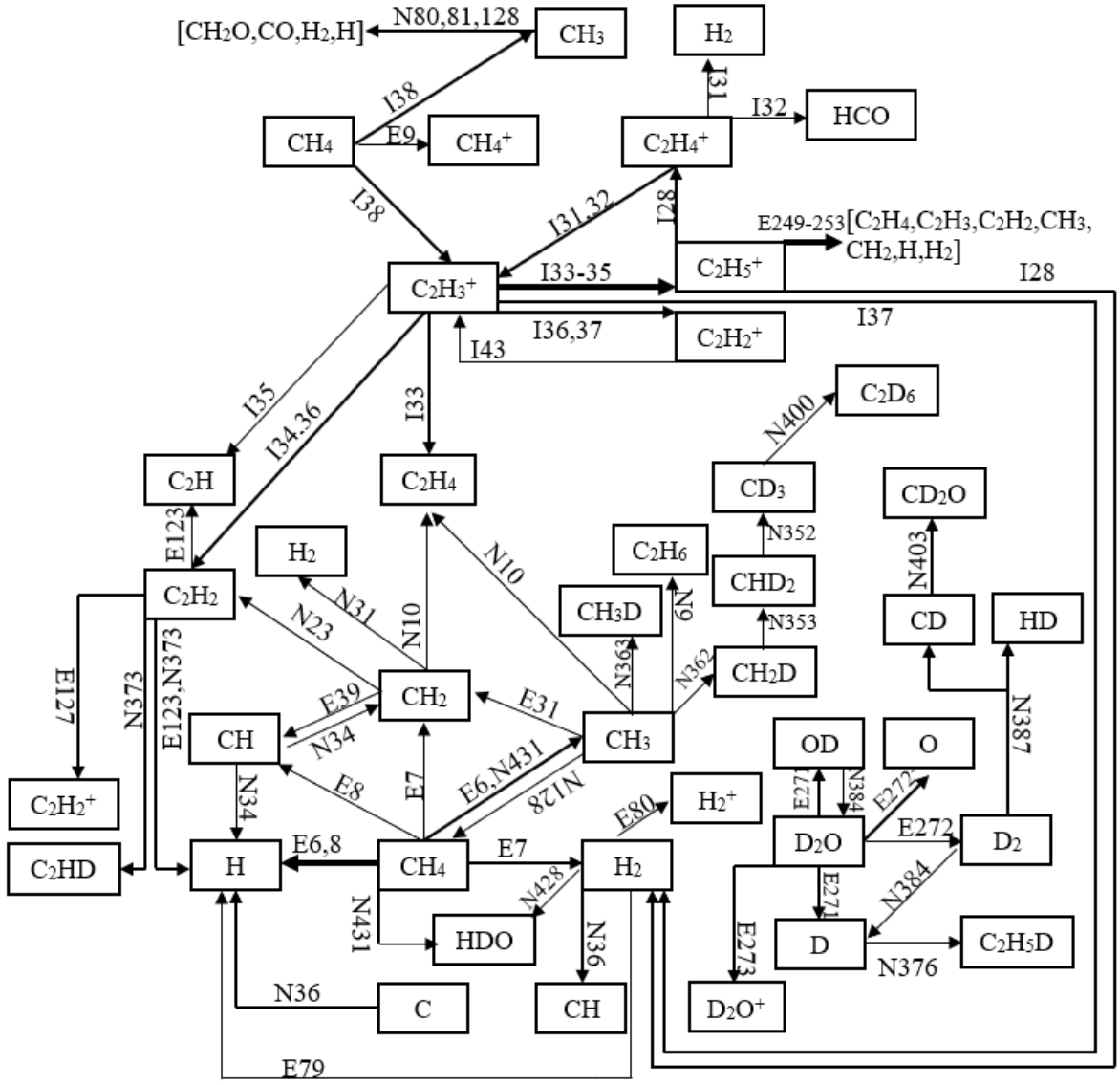

Figure 7.24 Overview of the major reaction pathways for the SMR process, including deuterium element, under the discharge power 30 W with steam concentration of 60%. The thickness of the arrows was corresponded with the reaction rate (rates of 10^{16} cm^3s^{-1} were displayed in 0.5 pt line; rates of 10^{17} were displayed 1.0 pt line) and can be superposed. (The corresponding reactions notated with numbers can be found in **Appendix 9.3**).

Generally, all the reaction rates in **Figure 7.24** were slower than the ones with a very low steam concentration, while, in other words, the entire reacting system became sluggish. The channels of H_2 generation became more heterogeneous, with the increasing of the inlet steam. Basically, the hydrogen can be produced by the electron-impact reactions from the inlet source and ionic reactions. It was obvious that most of deuterium did not form the expected product, hydrogen. CH_3 radical generated by CH_4 cracking can be considered as a "bridge" shifting the final products towards the hydrocarbons and carbohydrates. For example, OD can oxidise CH_4 to

CH_3 directly and then the displacement reactions would convert CH_3 into $CH_xD_{y(x=0,1,2\ \&\ y=1,2,3)}$ radicals and these CH_xD_y radicals would be major source for the heterogeneous isotope carriers of hydrocarbons (i.e. C_2D_6).

Additionally, after displacing with some radicals, the generated radical (i.e. CD) can continue reacting with oxidant (i.e. steam) to produce carbohydrates (i.e. CD_2O). The generation of CD_2O was not low and the peak density of it approached to ~1.8×10^{16} cm^{-3}. However, aldehydes would not last for long in the SMR process and they would be oxidised or hydrogenated to form liquid products (i.e. alcohol and acid), which was not the concern for this work.

Furthermore, the reserve reactions which can restrict the conversion of inlet gas were also enhanced with an in increasing steam concentration. For an example, H_2 was oxidised by OD to form HDO, while CH_3 can also be recombined with D to generate CH_3D.

Particularly, ionic reactions were an alternative channel for generating radicals in the plasm. The pathway for the ionic reactions were also changed by a higher steam concentration. In **Figure 7.24**, $C_2H_2^+$ can be treated as a "trigger" for all ionic reactions. It explained the reason why the final observed density of C_2H_2 was low. $C_2H_2^+$ can be produce by the electron-impact reaction directly and then it would react with the inlet gas CH_4 immediately to generate $C_2H_3^+$. A loop among $C_2H_3^+$, $C_2H_4^+$ and $C_2H_5^+$ would be formed after the generation of $C_2H_2^+$, whereas all these ions, including CH_3^+ produced from $C_2H_4^+$, were the sources for the hydrogen production. In addition, the ionic reactions can also produce HCO, which was the very important intermediate radical for the carbohydrates.

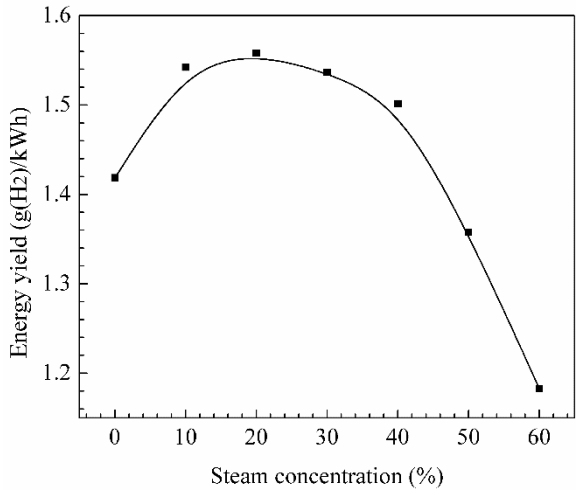

Figure 7.25 The calculated energy yield under the discharge of 30W with different steam concentrations.

In **Figure 7.25**, The maximum energy yield of this work can reach 1.56 g(H_2)/kWh, while the one of the published work using the similar operating conditions was around 0.5 g(H_2)/kWh [147]. However, the highest energy yield was observed at the steam concentration of 20%, while it dropped remarkably with a dramatic increasing of steam concentration. Obviously, much more input energy was consumed by the higher inlet of steam, since the radicals such as D and OD generated by steam made more contribution on the generation of the hydrocarbons and carbohydrates, instead of hydrogen production.

7.3. Conclusions

The purpose of this simulation was to obtain a better understanding of the process DBD plasma-assisted steam reforming of methane (SMR). To achieve that goal, a 0D model using ZDplaskin was built to investigate the behaviours of the major species. Combined with isotopic study by using D_2O as the inlet gas, it was much easier to understand the role of steam SMR process. Based on the isotopic study, the pathway was revealed easily and the destinations of the hydrogen element from steam were identified during the SMR process. Through the validation by the experiments, there was no doubt that the physical and chemical models used in this simulation were working correctly.

Primarily, the effects of discharge power (from 10 to 30 W) and steam concentration (from 2.5% to 60%) on hydrogen yield and mechanism of the SMR process were investigated. In terms of the power discharge section, it found that the applied voltage increased slightly with a higher discharge power, but the discharge power would not affect the gas voltage considerably. However, the amplitude and duration of the discharge current were increased dramatically by the increasing discharge power, so the plasma-on duration was also broadened. Additionally, a higher discharge power or steam concentration can rise the conversion rate of CH_4 and the maximum conversion was observed of around 21% under the discharge power of 30 W with the steam concentration of 60%, corresponding to the lowest energy yield of 1.18 g(H_2)/kWh. This work also studied on the proportion of steam contributed on the hydrogen yield and it revealed that steam would make more contribution on the hydrogen yield under a lower discharge power and higher steam concentration. C_2H_6 was the major hydrocarbon product of the SMR and a non-negligible proportion of it was formed from steam.

Based on the study on the behaviours of the important species, it was clear that OD radical was significant, during the SMR process, and it can always be an initial source for all oxygen-containing reactions. Moreover, with the increasing of the density of OD, it also provided an essential channel to convert methane. Except for the study on the behaviours of the important species, this work also conducted the sensitivity analysis to obtain the more accurate mechanisms. No matter how high the steam concertation was, methane was always the major source for generating hydrogen. Additionally, ionic reaction was the particular channel to produce hydrogen, compared with the traditional SMR process, whereas the pathways were different when the steam concentration was increased remarkably. $C_2H_2^+$ can be treated as a "trigger" for the ionic channel to generate hydrogen. However, a higher steam concentration can also promote the displacement reactions, which occurred at any time. Unfortunately, the displacement reactions occurred more likely among the CH_x radicals, so it restricted the final hydrogen yield, causing a lower energy yield for hydrogen. In the future work, this new model should also consider about the generations of liquid products such as alcohol and acid, so the carbohydrate products, which could be more valuable, would be paid more attentions on. Therefore, the chemical model should be perfected further by adding more isotopic reactions to obtain the more accurate results for the liquid products.

Chapter 8 Conclusions and recommendations for future researches

Conclusions

This project had investigated the DBD plasma-assisted reforming of biogas through simulations using a novel power description and experiments. Clear mechanisms of the reactions related to biogas reforming had been defined by the simulations which had been validated by the experiments.

The size of a 0D model can be large, this project simulated the densities of all species involved in reactions. CH_4 and CO_2 were the major contents of biogas and important reactants for this project. The thermal catalytic conversions of CH_4 and CO_2 were not efficient, while, in this study, DBD plasmas provided a higher conversion of biogas. In **Chapter 3**, the maximum conversion of CO_2 reached 26% under the discharge power of 90 W for the simulation results, while maximum efficiency (9.8 %) was obtained with a lowest discharge power (10 W). A higher input power can only enhance the CO_2 conversion slightly, because it strengthened deexcitations due to the significantly increased electron density. All vibrational excitations processes were investigated to define the major excitation states for the CO_2 splitting and the relationship among different excitation levels. The generation rates of VT modes were much higher than the ones of VV modes. The VT modes were dominating the excitation process of CO_2 and 0.08 eV level (1^{st} bending) was dominating the VT modes. For excited CO_2, an increasing discharge power was helpful to keep the stored energy. The contribution of vibrational excitations for CO_2 decomposition was increased from 1.38 to 18.7 % (10 - 90 W). The vibrational excitations were dramatically enhanced by the rising electron density, but the energy efficiency declined very quickly caused by the deexcitation processes, from 9.8 to 2.3 %. Therefore, vibrational excitations can provide an effective method for CO_2 splitting, but it also resulted in a higher energy consumption, because of the redundant electron collisions. Instead of discharge/input power, EEDFs, which can be affected by gas composition, should be optimised to enhance the DBD plasma-assisted conversion of CO_2.

For CO_2 hydrogenation, the H_2/CO_2 ratio was increased from 1 to 3. A higher discharge voltage was observed with a higher H_2 inlet concentration. The maximum conversion rate was observed of 22.7% with the H_2/CO_2 ratio of 3:1. The concentration of OH was increased with a higher

H_2/CO_2 ratio. OH was an important racial to consume CH_2, resulting a lower yield of CH_4 indirectly. C was defined as the major/initial source radical for producing CH_4, while a loop formed by ionic reaction channel was a necessary secondary pathway of CH_4 generation.

More attention was paid on DRM with CH_4/CO_2 ratio of 1. In every AC cycle, the important species, such as C_xH_y radicals and OH, showed a clear periodic behaviour. H/C ratio of the major product syngas was slightly greater than one. Except for syngas, C_2H_2 and C_2H_6 were the major gas-products. CH_3 took the highest proportion among the radicals, but the density of it kept decreasing until the end of resident time. On the other hand, 60.3% of CH_3 radicals are consumed by the recombination process to produce C_2H_6 and more than 99% of CH_2 radicals were consumed by the oxidising process to generate aldehydes, which was a very important source for the generation of syngas and liquid products.

For the SMR, primarily, the effects of discharge power (from 10 to 30 W) and steam concentration (from 2.5% to 60%) on H_2 yield and mechanism of the SMR process were investigated. The applied voltage increased slightly with a higher discharge power and the plasma-on duration was also extended. Additionally, either a higher discharge power or a higher steam concentration raised the conversion rate of CH_4. The maximum conversion rate was observed of around 21% under the discharge power of 30 W with the steam concentration of 60%, but the energy yield reached the lowest value of 1.18 g(H_2)/kWh. The steam made more contribution to the hydrogen production under a lower discharge power and higher steam concentration. Ethane was the major hydrocarbon product of the SMR and was formed from steam. OD was an important radical to ignite reactions for all oxygen-containing reactions. Methane was always the major source for generating hydrogen. Additionally, ionic reaction was the particular channel to produce hydrogen, compared with the traditional SMR process. $C_2H_2^+$ can be treated as a “trigger” for the ionic channel to generate hydrogen. A higher steam concentration promoted the displacement reactions, which occur at any time. Unfortunately, the displacement reactions more likely occur among the CH_x radicals, causing a lower yield of H_2.

Recommendations for future researches

Reforming of biogas has been widely used in industry through the traditional thermal catalytic method. On one hand, this process can remit the issue of energy crisis of fossil fuels by

providing an energy source such as syngas. On the other hand, it can also be considered as treatment for the climate change caused by GHGs. However, high operating temperature (power consumption) and deactivation of catalysts caused by carbon deposition are the major challenges. Plasma successfully reduces the operating temperature to around ambient temperature. As defined in this project, almost all reactions can be initiated under ~300 K.

However, the drawbacks of 0D simulations and plasma-assisted reactions cannot be ignored. Firstly, for every simulation, assumptions should be made in advance. Only the suitable assumptions can provide the relative reliable results and save the computational time. Secondly, for simulating the plasma-driven reactions, the surface reactions are required to be neglected. Finally, it is difficult to simulate the electron-impact reactions of the lager particles (i.e. acids), because of the lack of the cross-section data.

Plasma could break any chemical bond and the chemical equilibrium. Therefore, for some reactions, the conversion could be enhanced. However, the scattered radicals cannot guarantee the selectivity of the desired products. Consequently, catalysts are necessary to improve the yield of target products so that the energy efficiency can be enhanced.

In order to keep up with the trends of the development of biogas reforming, more attempts should be focused on the simulations on plasma-catalytic reactions. A hierarchical and heterogeneous model, containing the various models (i.e. DFT and classical MD) together, should be considered in the first place. DFT/MD calculations give insight into the specific surface reactions in detail. The selection of these specific surface reactions can be based on the chemical model beforehand, while the most important reactions for generating the target species can then be fed back to the DFT/MD calculations to obtain a suitable adjustment of the chemical parameters, such as rate constant. The simulations will be performed again with the new adjusted parameters to obtain the more accurate results. However, number of reactions in a chemical model could be more than thousands, so the workload is very high. Additionally, the computation time of either MD or DFT is very short (in picosecond), so the entire hierarchical model is needed to be split into many scales in ~100 ps. Typically, the duration of one filament (streamer) of DBD is in nanoseconds (1-30 ns). Therefore, ten of DFT/MD calculations are required to constitute an integrated calculation during one filament of DBD. Subsequently, the results of one filament can be the input data for the next filament. By this iteration, the calculations in atomistic scale model (in picosecond) can form a mesoscale simulation (in nanosecond) and the mesoscale simulation will finally perform the macroscale

scale model (in millisecond or seconds). However, the number of the filaments of DBD cannot be defined, so a suitable assumption on the quantity of streamers should be made. If a hundred filaments of DBD are sampled, a thousand of DFT/MD calculations are required. Obviously, the workload is incredible. Finally, whichever the method is used for placing catalysts in the reactor, the reduced electric field must be affected, such as the enhancement due to the presence of pellets in a packed bed reactor. The parameters of plasma in the duration of every filament will also be influenced. Therefore, these problems must be solved for simulating plasma-catalytic reactions.

References

1. Tasnim, F., S.A. Iqbal, and A.R. Chowdhury, *Biogas production from anaerobic co-digestion of cow manure with kitchen waste and Water Hyacinth.* Renewable Energy, 2017. **109**: p. 434-439.
2. Chandra, R., H. Takeuchi, and T. Hasegawa, *Methane production from lignocellulosic agricultural crop wastes: A review in context to second generation of biofuel production.* Renewable & Sustainable Energy Reviews, 2012. **16**(3): p. 1462-1476.
3. Xu, F.Q., et al., *Anaerobic digestion of food waste - Challenges and opportunities.* Bioresource Technology, 2018. **247**: p. 1047-1058.
4. Vita, A., et al., *Methanol synthesis from biogas: A thermodynamic analysis.* Renewable Energy, 2018. **118**: p. 673-684.
5. Aguilera, P.G. and F.J.G. Ortiz, *Techno-economic assessment of biogas plant upgrading by adsorption of hydrogen sulfide on treated sewage-sludge.* Energy Conversion and Management, 2016. **126**: p. 411-420.
6. Akunna, J.C. and A. Hierholtzer, *Co-digestion of terrestrial plant biomass with marine macro-algae for biogas production.* Biomass & Bioenergy, 2016. **93**: p. 137-143.
7. Boldrin, A., et al., *Optimised biogas production from the co-digestion of sugar beet with pig slurry: Integrating energy, GHG and economic accounting.* Energy, 2016. **112**: p. 606-617.
8. Khan, E.U. and A.R. Martin, *Review of biogas digester technology in rural Bangladesh.* Renewable & Sustainable Energy Reviews, 2016. **62**: p. 247-259.
9. Arbag, H., et al., *Enhancement of catalytic performance of Ni based mesoporous alumina by Co incorporation in conversion of biogas to synthesis gas.* Applied Catalysis B-Environmental, 2016. **198**: p. 254-265.
10. Rathod, V.P., J. Shete, and P.V. Bhale, *Experimental investigation on biogas reforming to hydrogen rich syngas production using solar energy.* International Journal of Hydrogen Energy, 2016. **41**(1): p. 132-138.
11. Verma, P. and S.K. Samanta, *Overview of Biogas Reforming Technologies for Hydrogen Production: Advantages and Challenges*, in *Proceedings of the First International Conference on Recent Advances in Bioenergy Research*, S. Kumar, S.K. Khanal, and Y.K. Yadav, Editors. 2016. p. 227-243.
12. Bong, C.P.C., et al., *The characterisation and treatment of food waste for improvement of biogas production during anaerobic digestion - A review.* Journal of Cleaner Production, 2018. **172**: p. 1545-1558.
13. Bruhn, A., et al., *Bioenergy potential of Ulva lactuca: Biomass yield, methane production and combustion.* Bioresource Technology, 2011. **102**(3): p. 2595-2604.
14. Yadvika, et al., *Enhancement of biogas production from solid substrates using different techniques - a review.* Bioresource Technology, 2004. **95**(1): p. 1-10.
15. Gedebjerg, A., et al., *Prediction of mortality in patients with chronic obstructive pulmonary disease with the new Global Initiative for Chronic Obstructive Lung Disease 2017 classification: a cohort study.* Lancet Respiratory Medicine, 2018. **6**(3): p. 204-212.
16. Rosenthal, J., et al., *Clean cooking and the SDGs: Integrated analytical approaches to guide energy interventions for health and environment goals.* Energy for Sustainable Development, 2018. **42**: p. 152-159.
17. Angelidaki, I., et al., *Biogas upgrading and utilization: Current status and perspectives.* Biotechnology Advances, 2018. **36**(2): p. 452-466.

18. Park, J.H., et al., *Direct interspecies electron transfer via conductive materials: A perspective for anaerobic digestion applications.* Bioresource Technology, 2018. **254**: p. 300-311.
19. dos Santos, I.F.S., et al., *Assessment of potential biogas production from multiple organic wastes in Brazil: Impact on energy generation, use, and emissions abatement.* Resources Conservation and Recycling, 2018. **131**: p. 54-63.
20. Braguglia, C.M., et al., *Anaerobic bioconversion of food waste into energy: A critical review.* Bioresource Technology, 2018. **248**: p. 37-56.
21. Fay, A.R. and G.A. McKinley, *Global trends in surface ocean pCO(2) from in situ data.* Global Biogeochemical Cycles, 2013. **27**(2): p. 541-557.
22. Obst, M., L. Pavlovic, and K.H. Hopmann, *Carbon-carbon bonds with CO2: Insights from computational studies.* Journal of Organometallic Chemistry, 2018. **864**: p. 115-127.
23. Artz, J., et al., *Sustainable Conversion of Carbon Dioxide: An Integrated Review of Catalysis and Life Cycle Assessment.* Chemical Reviews, 2018. **118**(2): p. 434-504.
24. Indarto, A., et al., *Conversion of CO2 by gliding arc plasma.* Environmental Engineering Science, 2006. **23**(6): p. 1033-1043.
25. Aerts, R., T. Martens, and A. Bogaerts, *Influence of Vibrational States on CO2 Splitting by Dielectric Barrier Discharges.* Journal of Physical Chemistry C, 2012. **116**(44): p. 23257-23273.
26. Zhu, A., et al., *Conversion of CO2 by non-equilibrium plasma at atmospheric pressure.* Huanjing Kexue, 1998. **19**(2): p. 20-23.
27. Tsujii, M., et al., *Decomposition of CO2 into CO and O in a microwave-excited discharge flow of CO2/He or CO2/Ar mixtures.* Chemistry Letters, 2001.
28. Li, R.X., et al., *Plasma catalysis for CO2 decomposition by using different dielectric materials.* Fuel Processing Technology, 2006. **87**(7): p. 617-622.
29. Kraus, M., et al., *CO2 reforming of methane by the combination of dielectric-barrier discharges and catalysis.* Physical Chemistry Chemical Physics, 2001. **3**(3): p. 294-300.
30. Wang, Q., Y. Cheng, and Y. Jin, *Dry reforming of methane in an atmospheric pressure plasma fluidized bed with Ni/gamma-Al2O3 catalyst.* Catalysis Today, 2009. **148**(3-4): p. 275-282.
31. Li, R.X., et al., *Dense and strong plasma initiated by Ca0.7Sr0.3TiO3 ceramic.* Physics of Plasmas, 2004. **11**(8): p. 3715-3720.
32. Andreev, S.N., et al., *Plasma-chemical CO2 decomposition in a non-self-sustained discharge with a controlled electronic component of plasma.* Spectrochimica Acta Part a-Molecular and Biomolecular Spectroscopy, 2004. **60**(14): p. 3361-3369.
33. Yamasue, E., et al., *Carbon dioxide reduction into carbon by mechanically milled wustite.* Journal of Materials Science, 2007. **42**(13): p. 5196-5202.
34. Jin, W.Q., et al., *Efficient catalytic decomposition of CO2 to CO and O-2 over Pd/mixed-conducting oxide catalyst in an oxygen-permeable membrane reactor.* Environmental Science & Technology, 2008. **42**(8): p. 3064-3068.
35. Eremin, A.V., V.S. Ziborov, and V.V. Shumova, *Kinetics of CO2 dissociation at multimodal vibrational nonequilibrium.* Chemical Physics Reports, 1997. **16**(9): p. 1507-1520.
36. Tu, X. and J.C. Whitehead, *Plasma dry reforming of methane in an atmospheric pressure AC gliding arc discharge: Co-generation of syngas and carbon nanomaterials.* International Journal of Hydrogen Energy, 2014. **39**(18): p. 9658-9669.
37. Mahammadunnisa, S., et al., *CO2 reduction to syngas and carbon nanofibres by plasma-assisted in situ decomposition of water.* International Journal of Greenhouse Gas Control, 2013. **16**: p. 361-363.

38. Gallon, H.J., X. Tu, and J.C. Whitehead, *Effects of Reactor Packing Materials on H2 Production by CO2 Reforming of CH4 in a Dielectric Barrier Discharge.* Plasma Processes and Polymers, 2012. **9**(1): p. 90-97.
39. Yang, H.B., et al., *Atomically dispersed Ni(i) as the active site for electrochemical CO2 reduction.* Nature Energy, 2018. **3**(2): p. 140-147.
40. Aerts, R., T. Martens, and A. Bogaerts, *Influence of Vibrational States on CO2 Splitting by Dielectric Barrier Discharges (vol 116, pg 23257, 2012).* Journal of Physical Chemistry C, 2014. **118**(48): p. 28330-28330.
41. Paulussen, S., et al., *Conversion of carbon dioxide to value-added chemicals in atmospheric pressure dielectric barrier discharges.* Plasma Sources Science & Technology, 2010. **19**(3).
42. Kozak, T. and A. Bogaerts, *Splitting of CO2 by vibrational excitation in non-equilibrium plasmas: a reaction kinetics model.* Plasma Sources Science & Technology, 2014. **23**(4).
43. Yu, Q.Q., et al., *Non-thermal plasma assisted CO2 reforming of propane over Ni/gamma-Al2O3 catalyst.* Catalysis Communications, 2011. **12**(14): p. 1318-1322.
44. Luo, M., et al., *Review of hydrogen production using chemical-looping technology.* Renewable & Sustainable Energy Reviews, 2018. **81**: p. 3186-3214.
45. Alvarez, A., et al., *Challenges in the Greener Production of Formates/Formic Acid, Methanol, and DME by Heterogeneously Catalyzed CO2 Hydrogenation Processes.* Chemical Reviews, 2017. **117**(14): p. 9804-9838.
46. Kattel, S., et al., *CATALYSIS Active sites for CO2 hydrogenation to methanol on Cu/ZnO catalysts.* Science, 2017. **355**(6331): p. 1296-+.
47. Larmier, K., et al., *CO2-to-Methanol Hydrogenation on Zirconia-Supported Copper Nanoparticles: Reaction Intermediates and the Role of the Metal-Support Interface.* Angewandte Chemie-International Edition, 2017. **56**(9): p. 2318-2323.
48. Goguet, A., et al., *Study of the origin of the deactivation of a Pt/CeO2 catalyst during reverse water gas shift (RWGS) reaction.* Journal of Catalysis, 2004. **226**(2): p. 382-392.
49. Shirazi, M., E.C. Neyts, and A. Bogaerts, *DFT study of Ni-catalyzed plasma dry reforming of methane.* Applied Catalysis B-Environmental, 2017. **205**: p. 605-614.
50. Skoulidas, A.I. and D.S. Sholl, *Self-diffusion and transport diffusion of light gases in metal-organic framework materials assessed using molecular dynamics simulations.* Journal of Physical Chemistry B, 2005. **109**(33): p. 15760-15768.
51. Hirsch, D. and A. Steinfeld, *Solar hydrogen production by thermal decomposition of natural gas using a vortex-flow reactor.* International Journal of Hydrogen Energy, 2004. **29**(1): p. 47-55.
52. Li, W.Z., et al., *Syngas Production via Steam-CO2 Dual Reforming of Methane over LA-Ni/ZrO2 Catalyst Prepared by L-Arginine Ligand-Assisted Strategy: Enhanced Activity and Stability.* Acs Sustainable Chemistry & Engineering, 2015. **3**(12): p. 3461-3476.
53. Cormier, J.M. and I. Rusu, *Syngas production via methane steam reforming with oxygen: plasma reactors versus chemical reactors.* Journal of Physics D-Applied Physics, 2001. **34**(18): p. 2798-2803.
54. Watanabe, F., et al., *Influence of nitrogen impurity for steam methane reforming over noble metal catalysts.* Fuel Processing Technology, 2016. **152**: p. 15-21.
55. Rostrup-Nielsen, J.R. and T. Rostrup-Nielsen, *Large-scale hydrogen production.* Cattech, 2002. **6**(4): p. 150-159.
56. Bengaard, H.S., et al., *Steam reforming and graphite formation on Ni catalysts.* Journal of Catalysis, 2002. **209**(2): p. 365-384.

57. Katheria, S., et al., *Effect of calcination temperature on stability and activity of Ni/MgAl2O4 catalyst for steam reforming of methane at high pressure condition.* International Journal of Hydrogen Energy, 2016. **41**(32): p. 14123-14132.
58. Kyriakides, A.S., et al., *Optimization of an experimental membrane reactor for low-temperature methane steam reforming.* Clean Technologies and Environmental Policy, 2016. **18**(7): p. 2065-2075.
59. Abu El Hawa, H.W., et al., *Steam methane reforming in a Pd-Au membrane reactor: Long-term assessment.* International Journal of Hydrogen Energy, 2016. **41**(24): p. 10193-10201.
60. Iulianelli, A., et al., *Advances on methane steam reforming to produce hydrogen through membrane reactors technology: A review.* Catalysis Reviews-Science and Engineering, 2016. **58**(1): p. 1-35.
61. Barelli, L., et al., *Hydrogen production through sorption-enhanced steam methane reforming and membrane technology: A review.* Energy, 2008. **33**(4): p. 554-570.
62. Habibi, N., H. Arandiyan, and M. Rezaei, *Mesoporous MgO center dot Al2O3 nanopowder-supported meso-macroporous nickel catalysts: a new path to high-performance biogas reforming for syngas.* Rsc Advances, 2016. **6**(35): p. 29576-29585.
63. Benito, M., et al., *Ni-Co bimetallic catalyst for hydrogen production in sewage treatment plants: Biogas reforming and tars removal.* International Journal of Hydrogen Energy, 2015. **40**(42): p. 14456-14468.
64. Bereketidou, O.A. and M.A. Goula, *Biogas reforming for syngas production over nickel supported on ceria-alumina catalysts.* Catalysis Today, 2012. **195**(1): p. 93-100.
65. Pawar, V., et al., *Study of Short-Term Catalyst Deactivation Due to Carbon Deposition during Biogas Dry Reforming on Supported Ni Catalyst.* Energy & Fuels, 2015. **29**(12): p. 8047-8052.
66. Ay, H. and D. Uner, *Dry reforming of methane over CeO2 supported Ni, Co and Ni-Co catalysts.* Applied Catalysis B-Environmental, 2015. **179**: p. 128-138.
67. Zhang, J.S. and F.X. Li, *Coke-resistant Ni@SiO2 catalyst for dry reforming of methane.* Applied Catalysis B-Environmental, 2015. **176**: p. 513-521.
68. Luisetto, I., et al., *Ni/CeO2-Al2O3 catalysts for the dry reforming of methane: The effect of CeAlO3 content and nickel crystallite size on catalytic activity and coke resistance.* Applied Catalysis a-General, 2015. **500**: p. 12-22.
69. Multani, R.S., T. Feldmann, and G.P. Demopoulos, *Antimony in the metallurgical industry: A review of its chemistry and environmental stabilization options.* Hydrometallurgy, 2016. **164**: p. 141-153.
70. Afif, A., et al., *Ammonia-fed fuel cells: a comprehensive review.* Renewable & Sustainable Energy Reviews, 2016. **60**: p. 822-835.
71. Saadatjou, N., A. Jafari, and S. Sahebdelfar, *Ruthenium Nanocatalysts for Ammonia Synthesis: A Review.* Chemical Engineering Communications, 2015. **202**(4): p. 420-448.
72. Behling, N., *Making Fuel Cells Work.* Issues in Science and Technology, 2013. **29**(3): p. 83-90.
73. Hibbitts, D.D., et al., *Mechanistic Role of Water on the Rate and Selectivity of Fischer-Tropsch Synthesis on Ruthenium Catalysts.* Angewandte Chemie-International Edition, 2013. **52**(47): p. 12273-12278.
74. Bhatelia, T., et al., *Chain length dependent olefin re-adsorption model for Fischer-Tropsch synthesis over Co-Al2O3 catalyst.* Fuel Processing Technology, 2014. **125**: p. 277-289.
75. Brown, T.R., *A techno-economic review of thermochemical cellulosic biofuel pathways.* Bioresource Technology, 2015. **178**: p. 166-176.

76. Chernyak, S.A., et al., *New hybrid CNT-alumina supports for Co-based Fischer-Tropsch catalysts.* Fuel Processing Technology, 2015. **140**: p. 267-275.
77. Bukur, D.B., B. Todic, and N. Elbashir, *Role of water-gas-shift reaction in Fischer-Tropsch synthesis on iron catalysts: A review.* Catalysis Today, 2016. **275**: p. 66-75.
78. Ail, S.S. and S. Dasappa, *Biomass to liquid transportation fuel via Fischer Tropsch synthesis - Technology review and current scenario.* Renewable & Sustainable Energy Reviews, 2016. **58**: p. 267-286.
79. Floudas, C.A., J.A. Elia, and R.C. Baliban, *Hybrid and single feedstock energy processes for liquid transportation fuels: A critical review.* Computers & Chemical Engineering, 2012. **41**: p. 24-51.
80. Uddin, W., et al., *Biogas potential for electric power generation in Pakistan: A survey.* Renewable & Sustainable Energy Reviews, 2016. **54**: p. 25-33.
81. Goeppert, A., et al., *Recycling of carbon dioxide to methanol and derived products - closing the loop.* Chemical Society Reviews, 2014. **43**(23): p. 7995-8048.
82. Tonks, L. and I. Langmuir, *A general theory of the plasma of an arc.* Physical Review, 1929. **34**(6): p. 0876-0922.
83. Fridman, A., *Plasma Chemistry*. Plasma Chemistry. 2008. 1-978.
84. Hammer, T., T. Kappes, and M. Baldauf, *Plasma catalytic hybrid processes: gas discharge initiation and plasma activation of catalytic processes.* Catalysis Today, 2004. **89**(1-2): p. 5-14.
85. Gomez, E., et al., *Thermal plasma technology for the treatment of wastes: A critical review.* Journal of Hazardous Materials, 2009. **161**(2-3): p. 614-626.
86. Konjevic, N., I.R. Videnovic, and M.M. Kuraica, *Emission spectroscopy of the cathode fall region of an analytical glow discharge.* Journal De Physique Iv, 1997. **7**(C4): p. 247-258.
87. Di Piazza, A., et al., *Extremely high-intensity laser interactions with fundamental quantum systems.* Reviews of Modern Physics, 2012. **84**(3): p. 1177-1228.
88. Chang, J.S., P.A. Lawless, and T. Yamamoto, *CORONA DISCHARGE PROCESSES.* Ieee Transactions on Plasma Science, 1991. **19**(6): p. 1152-1166.
89. Vandenbroucke, A.M., et al., *Non-thermal plasmas for non-catalytic and catalytic VOC abatement.* Journal of Hazardous Materials, 2011. **195**: p. 30-54.
90. Xu, C. and X. Tu, *Plasma-assisted methane conversion in an atmospheric pressure dielectric barrier discharge reactor.* Journal of Energy Chemistry, 2013. **22**(3): p. 420-425.
91. Istadi and N.A.S. Amin, *Co-generation of synthesis gas and C2+ hydrocarbons from methane and carbon dioxide in a hybrid catalytic-plasma reactor: A review.* Fuel, 2006. **85**(5-6): p. 577-592.
92. Kogelschatz, U., *Dielectric-barrier discharges: Their history, discharge physics, and industrial applications.* Plasma Chemistry and Plasma Processing, 2003. **23**(1): p. 1-46.
93. Laroussi, M., *Nonthermal decontamination of biological media by atmospheric-pressure plasmas: Review, analysis, and prospects.* Ieee Transactions on Plasma Science, 2002. **30**(4): p. 1409-1415.
94. Liu, S.H. and M. Neiger, *Electrical modelling of homogeneous dielectric barrier discharges under an arbitrary excitation voltage.* Journal of Physics D-Applied Physics, 2003. **36**(24): p. 3144-3150.
95. Fridman, A., A. Chirokov, and A. Gutsol, *Non-thermal atmospheric pressure discharges.* Journal of Physics D-Applied Physics, 2005. **38**(2): p. R1-R24.
96. Mutaf-Yardimci, O., et al., *Thermal and nonthermal regimes of gliding arc discharge in air flow.* Journal of Applied Physics, 2000. **87**(4): p. 1632-1641.

97. Czernichowski, A., *GLIDING ARC - APPLICATIONS TO ENGINEERING AND ENVIRONMENT CONTROL.* Pure and Applied Chemistry, 1994. **66**(6): p. 1301-1310.
98. Fridman, A., et al., *Gliding arc gas discharge.* Progress in Energy and Combustion Science, 1999. **25**(2): p. 211-231.
99. Tsuji, M., et al., *Decomposition of CO2 into CO and O in a microwave-excited discharge flow of CO2/He or CO2/Ar mixtures.* Chemistry Letters, 2001(1): p. 22-23.
100. Sakurai, T. and A. Yokoyama, *Decompositions of carbon dioxide, carbon monoxide and gaseous water by microwave discharge.* Journal of Nuclear Science and Technology, 2000. **37**(9): p. 814-820.
101. Whitehead, J.C., *Plasma catalysis: A solution for environmental problems.* Pure and Applied Chemistry, 2010. **82**(6): p. 1329-1336.
102. Van Durme, J., et al., *Combining non-thermal plasma with heterogeneous catalysis in waste gas treatment: A review.* Applied Catalysis B-Environmental, 2008. **78**(3-4): p. 324-333.
103. Tu, X. and J.C. Whitehead, *Plasma-catalytic dry reforming of methane in an atmospheric dielectric barrier discharge: Understanding the synergistic effect at low temperature.* Applied Catalysis B-Environmental, 2012. **125**: p. 439-448.
104. Chen, H.L., et al., *Review of plasma catalysis on hydrocarbon reforming for hydrogen production-Interaction, integration, and prospects.* Applied Catalysis B-Environmental, 2008. **85**(1-2): p. 1-9.
105. Chen, H.L., et al., *Removal of Volatile Organic Compounds by Single-Stage and Two-Stage Plasma Catalysis Systems: A Review of the Performance Enhancement Mechanisms, Current Status, and Suitable Applications.* Environmental Science & Technology, 2009. **43**(7): p. 2216-2227.
106. Yu, Q.Q., et al., *Characteristics of the Decomposition of CO2 in a Dielectric Packed-Bed Plasma Reactor.* Plasma Chemistry and Plasma Processing, 2012. **32**(1): p. 153-163.
107. Chen, H.L., et al., *Review of packed-bed plasma reactor for ozone generation and air pollution control.* Industrial & Engineering Chemistry Research, 2008. **47**(7): p. 2122-2130.
108. Neyts, E.C., et al., *Plasma Catalysis: Synergistic Effects at the Nanoscale.* Chemical Reviews, 2015. **115**(24): p. 13408-13446.
109. Zhang, A.J., et al., *Conversion of greenhouse gases into syngas via combined effects of discharge activation and catalysis.* Chemical Engineering Journal, 2010. **156**(3): p. 601-606.
110. Van Laer, K. and A. Bogaerts, *Fluid modelling of a packed bed dielectric barrier discharge plasma reactor.* Plasma Sources Science & Technology, 2016. **25**(1).
111. Zhang, Y.R., et al., *Can plasma be formed in catalyst pores? A modeling investigation.* Applied Catalysis B-Environmental, 2016. **185**: p. 56-67.
112. Lino, A.V.P., E.M. Assaf, and J.M. Assaf, *Hydrotalcites derived catalysts for syngas production from biogas reforming: Effect of nickel and cerium load.* Catalysis Today, 2017. **289**: p. 78-88.
113. Vita, A., et al., *Biogas as renewable raw material for syngas production by tri-reforming process over NiCeO2 catalysts: Optimal operative condition and effect of nickel content.* Fuel Processing Technology, 2014. **127**: p. 47-58.
114. Luneau, M., et al., *Deactivation mechanism of Ni supported on Mg-Al spinel during autothermal reforming of model biogas.* Applied Catalysis B-Environmental, 2017. **203**: p. 289-299.

115. Izquierdo, U., et al., *Tri-reforming: A new biogas process for synthesis gas and hydrogen production.* International Journal of Hydrogen Energy, 2013. **38**(18): p. 7623-7631.
116. Araki, S., et al., *Reforming Reactions of Model Biogas over Honeycomb Supported Ni Catalysts.* Journal of the Japan Petroleum Institute, 2009. **52**(3): p. 120-127.
117. Araki, S., et al., *Autothermal reforming of biogas over a monolithic catalyst.* Journal of Natural Gas Chemistry, 2010. **19**(5): p. 477-481.
118. Angeli, S.D., et al., *Catalyst development for steam reforming of methane and model biogas at low temperature.* Applied Catalysis B-Environmental, 2016. **181**: p. 34-46.
119. Chang, A.C.C. and K.Y. Lee, *Biogas reforming by the honeycomb reactor for hydrogen production.* International Journal of Hydrogen Energy, 2016. **41**(7): p. 4358-4365.
120. Chiodo, V., et al., *Effect of pollutants on biogas steam reforming.* International Journal of Hydrogen Energy, 2017. **42**(3): p. 1622-1628.
121. Roy, P.S., et al., *Steam-biogas reforming over a metal-foam-coated (Pd-Rh)/(CeZrO2-Al2O3) catalyst compared with pellet type alumina-supported Ru and Ni catalysts.* Journal of Co2 Utilization, 2015. **12**: p. 12-20.
122. Ahmed, S., S.H.D. Lee, and M.S. Ferrandon, *Catalytic steam reforming of biogas - Effects of feed composition and operating conditions.* International Journal of Hydrogen Energy, 2015. **40**(2): p. 1005-1015.
123. Lin, K.H., H.F. Chang, and A.C.C. Chang, *Biogas reforming for hydrogen production over mesoporous Ni2xCe1-xO2 catalysts.* International Journal of Hydrogen Energy, 2012. **37**(20): p. 15696-15703.
124. Cipiti, F., et al., *Design of a biogas steam reforming reactor: A modelling and experimental approach.* International Journal of Hydrogen Energy, 2016. **41**(27): p. 11577-11583.
125. Effendi, A., et al., *Steam reforming of a clean model biogas over Ni/Al2O3 in fluidized- and fixed-bed reactors.* Catalysis Today, 2002. **77**(3): p. 181-189.
126. Izquierdo, U., et al., *Biogas steam and oxidative reforming processes for synthesis gas and hydrogen production in conventional and microreactor reaction systems.* International Journal of Hydrogen Energy, 2012. **37**(18): p. 13829-13842.
127. Nahar, G., D. Mote, and V. Dupont, *Hydrogen production from reforming of biogas: Review of technological advances and an Indian perspective.* Renewable & Sustainable Energy Reviews, 2017. **76**: p. 1032-1052.
128. Laosiripojana, N., et al., *Role and advantages of H2S in catalytic steam reforming over nanoscale CeO2-based catalysts.* Journal of Catalysis, 2010. **276**(1): p. 6-15.
129. Appari, S., et al., *Deactivation and regeneration of Ni catalyst during steam reforming of model biogas: An experimental investigation.* International Journal of Hydrogen Energy, 2014. **39**(1): p. 297-304.
130. Ashrafi, M., et al., *Experimental Study of Model Biogas Catalytic Steam Reforming: 2. Impact of Sulfur on the Deactivation and Regeneration of Ni-Based Catalysts.* Energy & Fuels, 2008. **22**(6): p. 4190-4195.
131. Sengupta, S., K. Ray, and G. Deo, *Effects of modifying Ni/Al2O3 catalyst with cobalt on the reforming of CH4 with CO2 and cracking of CH4 reactions.* International Journal of Hydrogen Energy, 2014. **39**(22): p. 11462-11472.
132. Saha, B., et al., *Evaluating the performance of non-precious metal based catalysts for sulfur-tolerance during the dry reforming of biogas.* Fuel, 2014. **120**: p. 202-217.
133. Asencios, Y.J.O., J.D.A. Bellido, and E.M. Assaf, *Synthesis of NiO-MgO-ZrO2 catalysts and their performance in reforming of model biogas.* Applied Catalysis a-General, 2011. **397**(1-2): p. 138-144.

134. Li, X.Y., et al., *Dry reforming of methane over Ni/La2O3 nanorod catalysts with stabilized Ni nanoparticles.* Applied Catalysis B-Environmental, 2017. **202**: p. 683-694.
135. Xu, J.K., et al., *Biogas reforming for hydrogen production over nickel and cobalt bimetallic catalysts.* International Journal of Hydrogen Energy, 2009. **34**(16): p. 6646-6654.
136. Zimicz, M.G., B.A. Reznik, and S.A. Larrondo, *Conversion of biogas to synthesis gas over NiO/CeO2-Sm2O3 catalysts.* Fuel, 2015. **149**: p. 95-99.
137. Pino, L., et al., *Hydrogen from biogas: Catalytic tri-reforming process with Ni/La-Ce-O mixed oxides.* Applied Catalysis B-Environmental, 2014. **148**: p. 91-105.
138. Xu, J.K., et al., *Biogas reforming for hydrogen production over a Ni-Co bimetallic catalyst: Effect of operating conditions.* International Journal of Hydrogen Energy, 2010. **35**(23): p. 13013-13020.
139. Juan-Juan, J., M.C. Roman-Martinez, and M.J. Illan-Gomez, *Effect of potassium content in the activity of K-promoted Ni/Al2O3 catalysts for the dry reforming of methane.* Applied Catalysis a-General, 2006. **301**(1): p. 9-15.
140. Charisiou, N.D., et al., *Syngas production via the biogas dry reforming reaction over nickel supported on modified with CeO2 and/or La2O3 alumina catalysts.* Journal of Natural Gas Science and Engineering, 2016. **31**: p. 164-183.
141. Zhao, J., W. Zhou, and J.X. Ma, *Pretreatment as the crucial step for biogas reforming over Ni-Co bimetallic catalyst - A mechanistic study of CO2 pretreatment.* International Journal of Hydrogen Energy, 2014. **39**(25): p. 13429-13436.
142. Goula, M.A., et al., *Nickel on alumina catalysts for the production of hydrogen rich mixtures via the biogas dry reforming reaction: Influence of the synthesis method.* International Journal of Hydrogen Energy, 2015. **40**(30): p. 9183-9200.
143. Kameshima, S., et al., *Pulsed dry methane reforming in plasma-enhanced catalytic reaction.* Catalysis Today, 2015. **256**: p. 67-75.
144. Zeng, Y.X., et al., *Plasma-catalytic dry reforming of methane over gamma-Al2O3 supported metal catalysts.* Catalysis Today, 2015. **256**: p. 80-87.
145. Choi, D.H., et al., *Production of hydrogen-rich syngas from methane reforming by steam microwave plasma.* Journal of Industrial and Engineering Chemistry, 2016. **34**: p. 286-291.
146. Randolph, K., in *Annual merit review and peer evaluation Meeting, May 16, 2013 (2013)*,*https://www.hydrogen.energy.gov/pdfs/review13/pd000_randolph_2013_o.pdf*. 2013: U.S. DOE. Hydrogen production.
147. Czylkowski, D., et al., *Microwave plasma-based method of hydrogen production via combined steam reforming of methane.* Energy, 2016. **113**: p. 653-661.
148. Goujard, V., J.M. Tatibouet, and C. Batiot-Dupeyrat, *Use of a non-thermal plasma for the production of synthesis gas from biogas.* Applied Catalysis a-General, 2009. **353**(2): p. 228-235.
149. Martini, L.M., et al., *Oxidation of CH4 by CO2 in a dielectric barrier discharge.* Chemical Physics Letters, 2014. **593**: p. 55-60.
150. Rico, V.J., et al., *Evaluation of Different Dielectric Barrier Discharge Plasma Configurations As an Alternative Technology for Green C-1 Chemistry in the Carbon Dioxide Reforming of Methane and the Direct Decomposition of Methanol.* Journal of Physical Chemistry A, 2010. **114**(11): p. 4009-4016.
151. Mei, D.H., et al., *Optimization of CO2 Conversion in a Cylindrical Dielectric Barrier Discharge Reactor Using Design of Experiments.* Plasma Processes and Polymers, 2016. **13**(5): p. 544-556.
152. Dai, B., et al., *Study on the hydrogenation coupling of methane.* Science in China Series B-Chemistry, 2001. **44**(2): p. 191-195.

153. Li, M.W., et al., *Carbon dioxide reforming of methane using DC corona discharge plasma reaction.* Journal of Physical Chemistry A, 2004. **108**(10): p. 1687-1693.
154. Li, M.W., Y.L. Tian, and G.H. Xu, *Characteristics of carbon dioxide reforming of methane via alternating current (AC) corona plasma reactions.* Energy & Fuels, 2007. **21**(4): p. 2335-2339.
155. Aziznia, A., et al., *Comparison of dry reforming of methane in low temperature hybrid plasma-catalytic corona with thermal catalytic reactor over Ni/gamma-Al2O3.* Journal of Natural Gas Chemistry, 2012. **21**(4): p. 466-475.
156. Zhang, X.L., et al., *The simultaneous activation of methane and carbon dioxide to C-2 hydrocarbons under pulse corona plasma over La2O3/gamma-Al2O3 catalyst.* Catalysis Today, 2002. **72**(3-4): p. 223-227.
157. Eliasson, B., C.J. Liu, and U. Kogelschatz, *Direct conversion of methane and carbon dioxide to higher hydrocarbons using catalytic dielectric-barrier discharges with zeolites.* Industrial & Engineering Chemistry Research, 2000. **39**(5): p. 1221-1227.
158. Zhang, K., U. Kogelschatz, and B. Eliasson, *Conversion of greenhouse gases to synthesis gas and higher hydrocarbons.* Energy & Fuels, 2001. **15**(2): p. 395-402.
159. Jiang, T., et al., *Plasma methane conversion using dielectric-barrier discharges with zeolite A.* Catalysis Today, 2002. **72**(3-4): p. 229-235.
160. Song, H.K., et al., *Synthesis gas production via dielectric barrier discharge over Ni/gamma-Al2O3 catalyst.* Catalysis Today, 2004. **89**(1-2): p. 27-33.
161. Wang, Q., et al., *Dry Reforming of Methane in a Dielectric Barrier Discharge Reactor with Ni/Al(2)O(3) Catalyst: Interaction of Catalyst and Plasma.* Energy & Fuels, 2009. **23**(8): p. 4196-4201.
162. Zeng, Y.X., et al., *Plasma-Catalytic Dry Reforming of Methane over Al2O3 Supported Metal Catalysts*. 2015 42nd Ieee International Conference on Plasma Sciences. 2015.
163. Lee, H., H.K. Song, and B.R. Min, *Heating effect of plasma catalytic reaction on the CH4 reforming of CO2 over Ni/gamma-Al2O3 catalyst in dielectric-barrier discharge reactor.* Chemistry Letters, 2006. **35**(6): p. 646-647.
164. Li, Y., et al., *Co-generation of syngas and higher hydrocarbons from CO2 and CH4 using dielectric-barrier discharge: Effect of electrode materials.* Energy & Fuels, 2001. **15**(2): p. 299-302.
165. Bo, Z., et al., *Plasma assisted dry methane reforming using gliding arc gas discharge: Effect of feed gases proportion.* International Journal of Hydrogen Energy, 2008. **33**(20): p. 5545-5553.
166. Indarto, A., et al., *Effect of additive gases on methane conversion using gliding arc discharge.* Energy, 2006. **31**(14): p. 2986-2995.
167. Zheng, C.H., et al., *Quantitative assessment of industrial VOC emissions in China: Historical trend, spatial distribution, uncertainties, and projection.* Atmospheric Environment, 2017. **150**: p. 116-125.
168. Zhu, X.B., et al., *Plasma-catalytic removal of formaldehyde over Cu-Ce catalysts in a dielectric barrier discharge reactor.* Applied Catalysis B-Environmental, 2015. **170**: p. 293-300.
169. Zhu, X.B., et al., *Catalyst screening for acetone removal in a single-stage plasma-catalysis system.* Catalysis Today, 2015. **256**: p. 108-114.
170. Zhu, X.B., et al., *Investigation of hybrid plasma-catalytic removal of acetone over CuO/gamma-Al2O3 catalysts using response surface method.* Chemosphere, 2016. **155**: p. 9-17.
171. De Bie, C., et al., *Dielectric barrier discharges used for the conversion of greenhouse gases: modeling the plasma chemistry by fluid simulations.* Plasma Sources Science & Technology, 2011. **20**(2).

172. Yang, Y., *Direct non-oxidative methane conversion by non-thermal plasma: Experimental study.* Plasma Chemistry and Plasma Processing, 2003. **23**(2): p. 283-296.
173. Agiral, A., et al., *Propane conversion at ambient temperatures C-C and C-H bond activation using cold plasma in a microreactor.* Chemical Engineering & Technology, 2008. **31**(8): p. 1116-1123.
174. De Bie, C., et al., *Fluid Modeling of the Conversion of Methane into Higher Hydrocarbons in an Atmospheric Pressure Dielectric Barrier Discharge.* Plasma Processes and Polymers, 2011. **8**(11): p. 1033-1058.
175. Tsolas, N., et al., *Plasma flow reactor studies of H-2/O-2/Ar kinetics.* Combustion and Flame, 2016. **165**: p. 144-153.
176. De Bie, C., J. van Dijk, and A. Bogaerts, *CO2 Hydrogenation in a Dielectric Barrier Discharge Plasma Revealed.* Journal of Physical Chemistry C, 2016. **120**(44): p. 25210-25224.
177. Verma, C., et al., *Molecular dynamics and Monte Carlo simulations as powerful tools for study of interfacial adsorption behavior of corrosion inhibitors in aqueous phase: A review.* Journal of Molecular Liquids, 2018. **260**: p. 99-120.
178. Neyts, E.C. and A. Bogaerts, *Understanding plasma catalysis through modelling and simulation-a review.* Journal of Physics D-Applied Physics, 2014. **47**(22).
179. Liu, N.Y., et al., *Density functional theory study of water-gas shift reaction on TM@Cu-12 core-shell nanoclusters.* Protection of Metals and Physical Chemistry of Surfaces, 2016. **52**(3): p. 387-398.
180. Liu, C., T.R. Cundari, and A.K. Wilson, *CO2 Reduction on Transition Metal (Fe, Co, Ni, and Cu) Surfaces: In Comparison with Homogeneous Catalysis.* Journal of Physical Chemistry C, 2012. **116**(9): p. 5681-5688.
181. Goddard, W.A., et al., *Development of the ReaxFF reactive force field for mechanistic studies of catalytic selective oxidation processes on BiMoOx.* Topics in Catalysis, 2006. **38**(1-3): p. 93-103.
182. Somers, W., et al., *Interactions of plasma species on nickel catalysts: A reactive molecular dynamics study on the influence of temperature and surface structure.* Applied Catalysis B-Environmental, 2014. **154**: p. 1-8.
183. Somers, W., et al., *Plasma Species Interacting with Nickel Surfaces: Toward an Atomic Scale Understanding of Plasma-Catalysis.* Journal of Physical Chemistry C, 2012. **116**(39): p. 20958-20965.
184. Somers, W., et al., *Temperature influence on the reactivity of plasma species on a nickel catalyst surface: An atomic scale study.* Catalysis Today, 2013. **211**: p. 131-136.
185. S. Pancheshnyi, B.E., G.J.M. Hagelaar, L.C. Pitchford,. *Computer code ZDPlasKin*. 2008; Available from: http://www.zdplaskin.laplace.univ-tlse.fr.
186. Hagelaar, G.J.M. and L.C. Pitchford, *Solving the Boltzmann equation to obtain electron transport coefficients and rate coefficients for fluid models.* Plasma Sources Science & Technology, 2005. **14**(4): p. 722-733.
187. Shi, S., *Advances in modeling hydrocarbon cracking kinetic predictions by quantum chemical theory: A review.* International Journal of Energy Research, 2018. **42**(10): p. 3164-3181.
188. Laidler, K.J., *Chemical Kinetics*. 1964.
189. Janev, R.K. and D. Reiter, *Collision processes of CHy and CHy+ hydrocarbons with plasma electrons and protons.* Physics of Plasmas, 2002. **9**(9): p. 4071-4081.
190. Janev, R.K. and D. Reiter, *Collision processes of C2,3Hy and C2,3Hy+ hydrocarbons with electrons and protons.* Physics of Plasmas, 2004. **11**(2): p. 780-829.
191. *Puech database, private communication*. 2018; Available from: www.lxcat.net.
192. *Morgan database, private communication*. 2018; Available from: www.lxcat.net.

193. NIST. *Chemical Kinetics Database, Standard Reference Database 17, Version 7.0 (Web Version),* . 2015; Available from: https://kinetics.nist.gov/kinetics/index.jsp.
194. Ferranti, F., et al., *Partial Element Equivalent Circuit Models in the Solution of the Electric Field Integral Equation*. 2012 International Conference on Electromagnetics in Advanced Applications. 2012. 329-332.
195. Chen, B. and S. Lampe, *The use of MATLAB as a computer tool for teaching control systems*, in *1996 International Conference on Simulation and Multimedia in Engineering Education*, M.F. Iskander, et al., Editors. 1996. p. 181-184.
196. Mohorek, M. and T.P. Webb, *Establishing a Conceptual Framework for Handoffs Using Communication Theory*. Journal of Surgical Education, 2015. **72**(3): p. 402-409.
197. Sorokina, M., et al., *Shannon Capacity of Nonlinear Communication Channels*, in *2016 Conference on Lasers and Electro-Optics*. 2016.
198. Manley, T., *The electric characteristics of the ozonator discharge.* Trasnsactions of the electrochemical society, 1943. **84**: p. 83-96.
199. Snoeckx, R., et al., *Plasma-based dry reforming: improving the conversion and energy efficiency in a dielectric barrier discharge.* Rsc Advances, 2015. **5**(38): p. 29799-29808.
200. Zeng, Y.X. and X. Tu, *Plasma-catalytic hydrogenation of CO2 for the cogeneration of CO and CH4 in a dielectric barrier discharge reactor: effect of argon addition.* Journal of Physics D-Applied Physics, 2017. **50**(18).
201. R. Celiberto, A.L., M. Capitelli, R.K. Janev, J.M. Wadehra and D.E. Atems, *Cross Section Data for Electron-Impact Inelastic Processes of Vibrationally Excited Hydrogen Molecules and Their Isotopes.* INTERNATIONAL NUCLEAR DATA COMMITTEE, 1999.
202. Zhang, K., B. Eliasson, and U. Kogelschatz, *Direct conversion of greenhouse gases to synthesis gas and C-4 hydrocarbons over zeolite HY promoted by a dielectric-barrier discharge.* Industrial & Engineering Chemistry Research, 2002. **41**(6): p. 1462-1468.
203. Yao, S.L., et al., *Plasma reforming and coupling of methane with carbon dioxide.* Energy & Fuels, 2001. **15**(5): p. 1295-1299.
204. Indarto, A., et al., *Decomposition of greenhouse gases by plasma.* Environmental Chemistry Letters, 2008. **6**(4): p. 215-222.
205. Matsumoto, H., et al., *Profiles of carbon dioxide decomposition in a dielectric-barrier discharge-plasma system.* Bulletin of the Chemical Society of Japan, 1999. **72**(11): p. 2567-2571.
206. Zhou, L.M., et al., *Nonequilibrium plasma reforming of greenhouse gases to synthesis gas.* Energy & Fuels, 1998. **12**(6): p. 1191-1199.
207. Parajulee, S., S. Ikezawa, and M. Hayakawa, *Decomposition of CO2 by large flow atmospheric microwave plasma (LAMP).* Abstracts of Papers of the American Chemical Society, 2010. **240**.
208. Zheng, G.Y., et al., *The mutual conversion of CO2 and CO in dielectric barrier discharge (DBD).* Plasma Chemistry and Plasma Processing, 2003. **23**(1): p. 59-68.
209. Wang, S., et al., *Enhancement of CO2 conversion rate and conversion efficiency by homogeneous discharges.* Plasma Chemistry and Plasma Processing, 2012. **32**: p. 979-989.
210. Ma, Y., et al., *Molecular dynamics simulation of hydrocarbon molecule adsorption on kaolinite (001) surface.* Fuel, 2019. **237**: p. 989-1002.
211. Wang, L., et al., *Direct conversion of methanol to n-C4H10 and H-2 in a dielectric barrier discharge reactor.* Green Chemistry, 2016. **18**(20): p. 5658-5666.
212. Nishimura, H. and K. Yano, *Total Electron-Scattering Cross-Sections for Ar, N2, H2o and D2o.* Journal of the Physical Society of Japan, 1988. **57**(6): p. 1951-1956.

213. Post, D.E., *A REVIEW OF RECENT DEVELOPMENTS IN ATOMIC PROCESSES FOR DIVERTORS AND EDGE PLASMAS.* Journal of Nuclear Materials, 1995. **220**: p. 143-157.
214. Reiter, D., *Modeling of fusion edge plasmas: Atomic and molecular data issues*, in *Nuclear Fusion Research: UNDERSTANDING PLASMA-SURFACE INTERACTIONS*, R.E.H. Clark and D.H. Reiter, Editors. 2005. p. 29-60.
215. Reiter, D., et al., *The role of atomic and molecular processes in magnetic fusion plasmas*, in *Atomic and Molecular Data and Their Applications*, T. Kato, H. Funaba, and D. Kato, Editors. 2005. p. 3-12.

9 Appendixes

9.1 CO_2 splitting

Table 9.1 Neutral Reactions Included in the Model [193].

No.	Reaction	Rate constant
N1	$CO_2 + M \Rightarrow CO + O + M$	$3.91\times10^{-10}\exp(-49430/T_g)$
N2	$CO_2 + O \Rightarrow CO + O_2$	$2.80\times10^{-11}\exp(-26500/T_g)$
N3	$O + CO + M \Rightarrow CO_2 + M$	$8.20\times10^{-34}\exp(-1510/T_g)$
N4	$O_2 + CO \Rightarrow CO_2 + O$	$4.20\times10^{-12}\exp(-24000/T_g)$
N5	$O_3 + CO \Rightarrow CO_2 + O_2$	4.00×10^{-25}
N6	$O + C2O \Rightarrow CO + CO$	5.00×10^{-11}
N7	$O_2 + C2O \Rightarrow CO_2 + CO$	3.30×10^{-13}
N8	$O + O_3 \Rightarrow O_2 + O_2$	$3.\ 10\times10^{-14}T_g^{0.75}\exp(-1575/T_g)$
N9	$O_3 + M \Rightarrow O_2 + O + M$	$4.12\times10^{-10}\exp(-11430/T_g)$
N10	$O + O_2 + M \Rightarrow O_3 + M$	$6.11\times10^{-34}T_g^{-2.6}$
N11	$O + O + M \Rightarrow O_2 + M$	$1.27\times10^{-32}T_g^{-1}\exp(-170/T_g)$

Table 9.2 Electron Attachment and Electron-ion Recombination Reactions Included in the Model [213-215].

No.	Reaction	Rate constant
A1	$e^- + CO_2 \Rightarrow O^- + CO$	$5.00\times10^{-13}T_g^{-1.5}$
A2	$e^- + O_2 \Rightarrow O^- + O$	$3.\ 00\times10^{-12}T_g^{-1.5}$
A3	$e^- + O_3 \Rightarrow O^- + O_2$	$8.90\times10^{-12}T_g^{1.5}$
A4	$e^- + O_2 + M \Rightarrow O_2^- + M$	$2.20\times10^{-14}\exp(-600/T_g)$
A5	$e^- + O + M \Rightarrow O^- + M$	$1.00\times10^{-31}\exp(-600/T_g)$
A6	$e^- + CO_2^+ \Rightarrow CO + O$	$2.00\times10^{-5}T_g^{-0.5}$
A7	$e^- + C_2O_4^+ \Rightarrow CO_2 + CO_2$	$2.00\times10^{-5}T_g^{-0.5}$
A8	$e^- + O_2^+ + M \Rightarrow O_2 + M$	1.00×10^{-26}
A9	$e^- + O_2^+ \Rightarrow O + O$	$6.00\times10^{-07}T_g^{-0.5}$
A10	$e^- + O^+ + M \Rightarrow O + M$	1.00×10^{-26}

Table 9.3 Electron Impact Reactions Included in the Model [186, 191, 192].

No.	Reaction	Rate constant
E1	$e^- + CO_2 \Rightarrow CO_2\_0.0 + e^-$	*f(σ)*
E2	$e^- + CO_2 \Rightarrow CO_2\_0.08 + e^-$	*f(σ)*
E3	$e^- + CO_2 \Rightarrow CO_2\_0.17 + e^-$	*f(σ)*
E4	$e^- + CO_2 \Rightarrow CO_2\_0.25 + e^-$	*f(σ)*
E5	$e^- + CO_2 \Rightarrow CO_2\_0.29 + e^-$	*f(σ)*
E6	$e^- + CO_2 \Rightarrow CO_2\_0.34 + e^-$	*f(σ)*
E7	$e^- + CO_2 \Rightarrow CO_2\_0.42 + e^-$	*f(σ)*
E8	$e^- + CO_2 \Rightarrow CO_2\_0.51 + e^-$	*f(σ)*
E9	$e^- + CO_2 \Rightarrow CO_2\_2.5 + e^-$	*f(σ)*
E10	$e^- + CO_2 \Rightarrow CO_2\_5.5 + e^-$	*f(σ)*
E11	$e^- + CO_2 \Rightarrow CO_2\_7 + e^-$	*f(σ)*
E12	$e^- + CO_2\_0.08 \Rightarrow CO_2 + e^-$	*f(σ)*
E13	$e^- + CO_2\_0.17 \Rightarrow CO_2\_0.08 + e^-$	*f(σ)*
E14	$e^- + CO_2\_0.17 \Rightarrow CO_2 + e^-$	*f(σ)*
E15	$e^- + CO_2\_0.25 \Rightarrow CO_2\_0.17 + e^-$	*f(σ)*
E16	$e^- + CO_2\_0.25 \Rightarrow CO_2\_0.08 + e^-$	*f(σ)*
E17	$e^- + CO_2\_0.25 \Rightarrow CO_2 + e^-$	*f(σ)*
E18	$e^- + CO_2\_0.29 \Rightarrow CO_2\_0.25 + e^-$	*f(σ)*
E19	$e^- + CO_2\_0.29 \Rightarrow CO_2\_0.17 + e^-$	*f(σ)*
E20	$e^- + CO_2\_0.29 \Rightarrow CO_2\_0.08 + e^-$	*f(σ)*
E21	$e^- + CO_2\_0.29 \Rightarrow CO_2 + e^-$	*f(σ)*
E22	$e^- + CO_2\_0.34 \Rightarrow CO_2\_0.29 + e^-$	*f(σ)*
E23	$e^- + CO_2\_0.34 \Rightarrow CO_2\_0.25 + e^-$	*f(σ)*
E24	$e^- + CO_2\_0.34 \Rightarrow CO_2\_0.17 + e^-$	*f(σ)*
E25	$e^- + CO_2\_0.34 \Rightarrow CO_2\_0.08 + e^-$	*f(σ)*
E26	$e^- + CO_2\_0.34 \Rightarrow CO_2 + e^-$	*f(σ)*
E27	$e^- + CO_2\_0.4 \Rightarrow CO_2\_0.34 + e^-$	*f(σ)*
E28	$e^- + CO_2\_0.4 \Rightarrow CO_2\_0.29 + e^-$	*f(σ)*
E29	$e^- + CO_2\_0.4 \Rightarrow CO_2\_0.25 + e^-$	*f(σ)*
E30	$e^- + CO_2\_0.4 \Rightarrow CO_2\_0.17 + e^-$	*f(σ)*

E31	$e^- + CO_2\_0.4 \Rightarrow CO_2\_0.08 + e^-$	$f(\sigma)$
E32	$e^- + CO_2\_0.4 \Rightarrow CO_2 + e^-$	$f(\sigma)$
E33	$e^- + CO_2\_0.5 \Rightarrow CO_2\_0.4 + e^-$	$f(\sigma)$
E34	$e^- + CO_2\_0.5 \Rightarrow CO_2\_0.34 + e^-$	$f(\sigma)$
E35	$e^- + CO_2\_0.5 \Rightarrow CO_2\_0.29 + e^-$	$f(\sigma)$
E36	$e^- + CO_2\_0.5 \Rightarrow CO_2\_0.25 + e^-$	$f(\sigma)$
E37	$e^- + CO_2\_0.5 \Rightarrow CO_2\_0.17 + e^-$	$f(\sigma)$
E38	$e^- + CO_2\_0.5 \Rightarrow CO_2\_0.08 + e^-$	$f(\sigma)$
E39	$e^- + CO_2\_0.5 \Rightarrow CO_2 + e^-$	$f(\sigma)$
E40	$e^- + CO_2\_2.5 \Rightarrow CO_2\_0.34 + e^-$	$f(\sigma)$
E41	$e^- + CO_2\_2.5 \Rightarrow CO_2\_0.29 + e^-$	$f(\sigma)$
E42	$e^- + CO_2\_2.5 \Rightarrow CO_2\_0.08 + e^-$	$f(\sigma)$
E43	$e^- + CO_2\_2.5 \Rightarrow CO_2 + e^-$	$f(\sigma)$
E44	$e^- + CO_2\_5.0 \Rightarrow CO_2\_0.34 + e^-$	$f(\sigma)$
E45	$e^- + CO_2\_5.0 \Rightarrow CO_2\_0.29 + e^-$	$f(\sigma)$
E46	$e^- + CO_2\_5.0 \Rightarrow CO_2\_0.08 + e^-$	$f(\sigma)$
E47	$e^- + CO_2\_5.0 \Rightarrow CO_2 + e^-$	$f(\sigma)$
E48	$e^- + CO_2\_7.0 \Rightarrow CO_2\_0.34 + e^-$	$f(\sigma)$
E49	$e^- + CO_2\_7.0 \Rightarrow CO_2\_0.29 + e^-$	$f(\sigma)$
E50	$e^- + CO_2\_7.0 \Rightarrow CO_2\_0.08 + e^-$	$f(\sigma)$
E51	$e^- + CO_2\_7.0 \Rightarrow CO_2\_0. + e^-$	$f(\sigma)$
E52	$e^- + CO_2 \Rightarrow CO + O + e^-$	1.600×10^{-11}
E53	$e^- + O_2 \Rightarrow O + O + e^-$	$4.500 \times 10^{-11} T_g^{0.5} \exp(-70000/T_g)$
E54	$e^- + O_3 \Rightarrow O_2 + O + e^-$	9.000×10^{-10}
E55	$e^- + CO \Rightarrow CO^+ + e^- + e^-$	$0.980 \times 10^{-11} T_g^{0.5} \exp(-150000/T_g)$
E56	$e^- + CO_2 \Rightarrow CO_2^+ + e^- + e^-$	$0.910 \times 10^{-11} T_g^{0.5} \exp(-150000/T_g)$
E57	$e^- + CO_2 \Rightarrow CO^+ + O + e^- + e^-$	$0.910 \times 10^{-12} T_g^{0.5} \exp(-150000/T_g)$
E58	$e^- + CO_2 \Rightarrow O^+ + CO + e^- + e^-$	$0.910 \times 10^{-12} T_g^{0.5} \exp(-150000/T_g)$
E59	$e^- + O \Rightarrow O^+ + e^- + e^-$	$4.100 \times 10^{-11} T_g^{0.5} \exp(-150000/T_g)$
E60	$e^- + O_2 \Rightarrow O_2^+ + e^- + e^-$	$1.100 \times 10^{-11} T_g^{0.5} \exp(-140000/T_g)$
E61	$e^- + O_2 \Rightarrow O^+ + O + e^- + e^-$	$0.825 \times 10^{-11} T_g^{0.5} \exp(-140000/T_g)$
E62	$e^- + O_3 \Rightarrow O_2^+ + O + e^- + e^-$	$3.200 \times 10^{-11} T_g^{0.5} \exp(-150000/T_g)$
E63	$e^- + O_3 \Rightarrow O^+ + O^- + O + e^-$	$8.400 \times 10^{-12} T_g^{0.5} \exp(-210000/T_g)$

Table 9.4 Ion-neutral and ion-ion Reactions Included in the Model [213-215].

No.	Reaction	Rate constant
I1	$O^+ + CO_2 \rightarrow O2^+ + CO$	9.4×10^{-10}
I2	$O^+ + CO_2 \rightarrow O + CO_2^+$	4.5×10^{-10}
I3	$CO^+ + CO_2 \rightarrow CO_2^+ + CO$	1.0×10^{-9}
I4	$O^- + CO_2 + M \rightarrow CO_3^- + M$	9.0×10^{-29}
I5	$O_2^- + CO_2 + M \rightarrow CO_4^- + M$	1.0×10^{-29}
I6	$O^+ + CO \rightarrow O + CO^+$	$4.9 \times 10^{-12} Tg^{0.5} \exp(-4580/Tg)$
I7	$O^- + CO \rightarrow CO_2 + e^-$	5.5×10^{-10}
I8	$CO_3^- + CO \rightarrow 2CO_2 + e^-$	5.0×10^{-13}
I9	$C^+ + CO \rightarrow C + CO^+$	5.0×10^{-11}
I10	$CO^+ + C \rightarrow CO + C^+$	1.1×10^{-10}
I11	$O_2^+ + C \rightarrow CO^+ + O$	5.2×10^{-11}
I12	$O_2^+ + C \rightarrow C^+ + O_2$	5.2×10^{-11}
I13	$CO_2^- + CO_2^+ \rightarrow CO + O_2 + O$	6.0×10^{-7}
I14	$CO^+ + O \rightarrow CO + O^+$	1.4×10^{-10}
I15	$CO^+ + O_2 \rightarrow CO + O_2^+$	1.2×10^{-10}
I16	$C_2O_4^+ + M \rightarrow CO_2^+ + CO_2 + M$	1.0×10^{-14}
I17	$C_2O_4^+ + CO_3^- \rightarrow 3CO_2 + O$	5.0×10^{-7}
I18	$C_2O_4^+ + O_2^- \rightarrow 2CO_2 + O_2$	6.0×10^{-7}
I19	$O_2^+ + CO_3^- \rightarrow CO_2 + O_2 + O$	3.0×10^{-7}
I20	$CO_3^- + O \rightarrow CO_2 + O^-$	8.0×10^{-11}
I21	$C^+ + O_2 \rightarrow CO + O^+$	6.2×10^{-10}
I22	$C^+ + O_2 \rightarrow CO^+ + O$	3.8×10^{-10}
I23	$O^+ + O_2 \rightarrow O + O_2^+$	$1.9 \times 10^{-11} Tg^{-0.5}$
I24	$O_2^+ + O_2 + M \rightarrow O_4^+ + M$	2.4×10^{-30}
I25	$O_2^- + O_2 + M \rightarrow O_4^- + M$	3.5×10^{-31}
I26	$O^- + O_2 \rightarrow O_3 + e^-$	1.0×10^{-12}
I27	$O^- + O_2 + M \rightarrow O_3^- + M$	$3.0 \times 10^{-28} Tg^{-1}$
I28	$O^- + O3 \rightarrow O + O3^-$	8.0×10^{-10}
I29	$O^- + O_3 \rightarrow 2O_2 + e^-$	3.0×10^{-10}

No.	Reaction	Rate constant
I30	$O_2^- + O_3 \rightarrow O_2 + O_3^-$	4.0×10^{-10}
I31	$O_3^- + O_3 \rightarrow 3O_2 + e^-$	3.0×10^{-10}
I32	$O^+ + O_3 \rightarrow O_2^+ + O_2$	1.0×10^{-10}
I33	$O^+ + O + M \rightarrow O_2^+ + M$	1.0×10^{-29}
I34	$O^- + O \rightarrow O_2 + e^-$	2.3×10^{-10}
I35	$O_2^- + O \rightarrow O_2 + O^-$	3.3×10^{-10}
I36	$O_2^- + O \rightarrow O_3 + e^-$	3.3×10^{-10}
I37	$O_3^- + O \rightarrow O_3 + O^-$	1.0×10^{-13}
I38	$O_3^- + O \rightarrow O_2 + O_2 + e^-$	1.0×10^{-13}
I39	$O_3^- + O \rightarrow O_2^- + O_2$	2.5×10^{-10}
I40	$O_4^- + O \rightarrow O_3^- + O_2$	4.0×10^{-10}
I41	$O_4^- + O \rightarrow O^- + 2O_2$	3.0×10^{-10}
I42	$O_4^+ + O \rightarrow O_2^+ + O_3$	3.0×10^{-10}
I43	$O_2^- + O^+ + M \rightarrow O_3 + M$	2.0×10^{-25}
I44	$O_2^- + O^+ \rightarrow O + O_2$	2.7×10^{-7}
I45	$O_2^- + O_2^+ \rightarrow 2O_2$	2.0×10^{-7}
I46	$O_2^- + O_2^+ \rightarrow O_2 + 2O$	4.2×10^{-7}
I47	$O_2^- + O_2^+ + M \rightarrow 2O_2 + M$	2.0×10^{-25}
I48	$O_2^- + O_2 \rightarrow 2O_2 + e^-$	2.18×10^{-18}
I49	$O_2^- + M \rightarrow O_2 + M + e^-$	$2.7 \times 10^{-10} Tg^{0.5} \exp(-5590/Tg)$
I50	$O_3^- + O_2^+ \rightarrow O_2 + O_3$	2.0×10^{-7}
I51	$O_3^- + O_2^+ \rightarrow O_3 + 2O$	1.0×10^{-7}
I52	$O_3^- + O^+ \rightarrow O_3 + O$	1.0×10^{-7}
I53	$O_3^- + O_2 \rightarrow O_2 + O_3 + e^-$	2.3×10^{-11}
I54	$O_3^- + M \rightarrow O_3 + e^-$	2.3×10^{-11}
I55	$O^- + O^+ \rightarrow 2O$	4.0×10^{-8}
I56	$O^- + O^+ + M \rightarrow O_2 + M$	2.0×10^{-25}
I57	$O^- + O_2^+ \rightarrow O_2 + O$	1.0×10^{-7}
I58	$O^- + O_2^+ \rightarrow 3O$	2.6×10^{-8}

9.2 Hydrogenation and biogas reforming

Table 9.5 Neutral-neutral reactions simulated in this model, with the corresponding rate constants adopted from NIST database [193]. The group M for the three-body collision is made up of the background gas.

No.	Reaction	Rate constant (cm^3s^{-1})
N1	$CH_4 + H \Rightarrow CH_3 + H_2$	8.43×10^{-19}
N2	$CH_4 + CH \Rightarrow C_2H_4 + H$	9.74×10^{-11}
N3	$CH_4 + CH_2 \Rightarrow CH_3 + CH_3$	2.78×10^{-19}
N4	$CH_4 + C_2H \Rightarrow C_2H_2 + CH_3$	1.31×10^{-12}
N5	$CH_4 + C_2H_3 \Rightarrow C_2H_4 + CH_3$	2.28×10^{-18}
N6	$CH_4 + C_2H_5 \Rightarrow C_2H_6 + CH_3$	1.83×10^{-24}
N7	$CH_4 + C_3H_7 \Rightarrow C_3H_8 + CH_3$	4.38×10^{-24}
N8	$CH_3 + CH_3 \Rightarrow C_2H_5 + H$	2.71×10^{-19}
N9	$CH_3 + CH_3 + M \Rightarrow C_2H_6 + M$	1.56×10^{-26} (cm^6s^{-1})
N10	$CH_3 + CH_2 \Rightarrow C_2H_4 + H$	7.01×10^{-11}
N11	$CH_3 + C_2H_5 \Rightarrow C_2H_4 + CH_4$	1.91×10^{-12}
N12	$CH_3 + C_2H_5 + M \Rightarrow C_3H_8 + M$	1.93×10^{-23} (cm^6s^{-1})
N13	$CH_3 + C_2H_6 \Rightarrow C_2H_5 + CH_4$	7.21×10^{-21}
N14	$CH_3 + C_2H_4 \Rightarrow C_2H_3 + CH_4$	1.94×10^{-21}
N15	$CH_3 + C_2H_3 \Rightarrow C_2H_2 + CH_4$	6.51×10^{-13}
N16	$CH_3 + C_2H_3 + M \Rightarrow C_3H_6 + M$	4.91×10^{-30} (cm^6s^{-1})
N17	$CH_3 + C_2H_2 \Rightarrow C_2H + CH_4$	7.65×10^{-26}
N18	$CH_3 + C_3H_8 \Rightarrow C_3H_7 + CH_4$	1.02×10^{-20}
N19	$CH_3 + C_3H_7 \Rightarrow C_3H_6 + CH_4$	3.07×10^{-12}
N20	$CH_3 + H_2 \Rightarrow H + CH_4$	9.90×10^{-21}
N21	CH3 + H => CH2 + H2	9.96×10^{-22}
N22	$CH_3 + H + M \Rightarrow CH_4 + M$	2.97×10^{-28} (cm^6s^{-1})
N23	$CH_2 + CH_2 \Rightarrow C_2H_2 + 2H$	5.27×10^{-11}
N24	$CH_2 + C_2H_5 \Rightarrow C_2H_4 + CH_3$	3.01×10^{-11}
N25	$CH_2 + C_2H_3 \Rightarrow C_2H_2 + CH_3$	3.01×10^{-11}
N26	$CH_2 + C_2H \Rightarrow C_2H_2 + CH$	3.01×10^{-11}

N27	$CH_2 + C_3H_8 \Rightarrow C_3H_7 + CH_3$	1.02×10^{-20}
N28	$CH_2 + C_3H_7 \Rightarrow C_2H_4 + C_2H_5$	3.01×10^{-11}
N29	$CH_2 + C_3H_7 \Rightarrow C_3H_6 + CH_3$	3.01×10^{-12}
N30	$CH_2 + H_2 \Rightarrow CH_3 + H$	5.00×10^{-15}
N31	$CH_2 + H \Rightarrow CH + H_2$	2.01×10^{-10}
N32	$CH + C_2H_6 + M \Rightarrow C_3H_7 + M$	1.14×10^{-29} (cm^6s^{-1})
N33	$CH + C_2H_6 \Rightarrow C_3H_6 + H$	3.00×10^{-11}
N34	$CH + H_2 \Rightarrow CH_2 + H$	6.80×10^{-13}
N35	$CH + H \Rightarrow C + H_2$	1.00×10^{-10}
N36	$C + H_2 \Rightarrow CH + H$	1.50×10^{-10}
N37	$C_2H_6 + C_2H_3 \Rightarrow C_2H_5 + C_2H_4$	3.39×10^{-21}
N38	$C_2H_6 + C_2H \Rightarrow C_2H_2 + C_2H_5$	5.99×10^{-12}
N39	$C_2H_6 + C_3H_7 \Rightarrow C_3H_8 + C_2H_5$	3.16×10^{-22}
N40	$C_2H_6 + CH_2 \Rightarrow C_3H_8$	4.80×10^{-12}
N41	$C_2H_6 + H \Rightarrow C_2H_5 + H_2$	4.96×10^{-17}
N42	$C_2H_5 + C_2H_5 \Rightarrow C_2H_6 + C_2H_4$	2.41×10^{-12}
N43	$C_2H_5 + C_2H \Rightarrow C_2H_2 + C_2H_4$	3.01×10^{-12}
N44	$C_2H_5 + C_3H_8 \Rightarrow C_2H_6 + C_3H_7$	3.62×10^{-22}
N45	$C_2H_5 + C_3H_7 \Rightarrow C_2H_4 + C_3H_8$	1.91×10^{-12}
N46	$C_2H_5 + C_3H_7 \Rightarrow C_2H_6 + C_3H_6$	2.41×10^{-12}
N47	$C_2H_5 + H_2 \Rightarrow C_2H_6 + H$	2.91×10^{-21}
N48	$C_2H_5 + H \Rightarrow CH_3 + CH_3$	5.99×10^{-11}
N49	$C_2H_5 + H \Rightarrow C_2H_4 + H_2$	3.01×10^{-12}
N50	$C_2H_5 + H \Rightarrow C_2H_6$	5.99×10^{-11}
N51	$C_2H_5 + C_2H_4 \Rightarrow C_3H_6 + CH_3$	3.82×10^{-17}
N52	$C_2H_4 \Rightarrow C_2H_2 + H_2$	1.40×10^{-27}
N53	$C_2H_4 + C_2H \Rightarrow C_2H_2 + C_2H_3$	1.40×10^{-10}
N54	$C_2H_4 + H \Rightarrow C_2H_3 + H_2$	6.70×10^{-05}
N55	$C_2H_4 + H \Rightarrow C_2H_5$	1.30×10^{-12}
N56	$C_2H_4 + H_2 + M \Rightarrow C_2H_6 + M$	6.86×10^{-36} (cm^6s^{-1})
N57	$C_2H_3 + C_2H_3 \Rightarrow C_2H_4 + H_2$	1.90×10^{-12}
N58	$C_2H_3 + C_2H \Rightarrow C_2H_2 + C_2H_2$	1.90×10^{-12}
N59	$C_2H_3 + C_3H_8 \Rightarrow C_2H_4 + C_3H_7$	3.40×10^{-20}

N60	$C_2H_3 + C_3H_7 => C_3H_8 + C_2H_2$	2.01×10^{-12}
N61	$C_2H_3 + C_3H_7 => C_3H_6 + C_2H_4$	2.01×10^{-12}
N62	$C_2H_3 + H_2 => C_2H_4 + H$	9.78×10^{-20}
N63	$C_2H_3 + H => C_2H_2 + H_2$	2.01×10^{-11}
N64	$C_2H_3 + H + M => C_2H_4 + M$	8.26×10^{-30} (cm^6s^{-1})
N65	$C_2H_2 + H => C_2H + H_2$	6.12×10^{-27}
N66	$C_2H_2 + H + M => C_2H_3 + M$	2.81×10^{-31} (cm^6s^{-1})
N67	$C_2H + C_3H_8 => C_2H_2 + C_3H_7$	5.99×10^{-12}
N68	$C_2H + C_3H_7 => C_3H_6 + C_2H_2$	1.00×10^{-11}
N69	$C_2H + H_2 => C_2H_2 + H$	1.52×10^{-13}
N70	$C_2H + H + M => C_2H_2 + M$	9.44×10^{-30} (cm^6s^{-1})
N71	$C_3H_8 + H => C_3H_7 + H_2$	5.15×10^{-17}
N72	$C_3H_7 + C_3H_7 => C_3H_6 + C_3H_8$	2.81×10^{-12}
N73	$C_3H_7 + H_2 => C_3H_8 + H$	7.12×10^{-21}
N74	$C_3H_7 + H => C_3H_6 + H_2$	3.01×10^{-12}
N75	C3H7 + H => C3H8	9.68×10^{-11}
N76	$C_3H_6 + H + M => C_3H_7 + M$	3.79×10^{-33} (cm^6s^{-1})
N77	$H + H + M => H_2 + M$	6.00×10^{-33} (cm^6s^{-1})
N78	$O + O + M => O_2 + M$	7.19×10^{-33} (cm^6s^{-1})
N79	$CH_4 + O => CH_3 + OH$	5.54×10^{-18}
N80	$CH_3 + O => CH_2O + H$	1.12×10^{-10}
N81	$CH_3 + O => CO + H_2 + H$	2.80×10^{-11}
N82	$CH_2 + O => CO + H_2$	5.53×10^{-11}
N83	$CH_2 + O => CO + 2H$	8.29×10^{-11}
N84	$CH_2 + O_2 => CO_2 + H_2$	1.42×10^{-12}
N85	$CH_2 + O_2 => CO + H_2O$	1.42×10^{-12}
N86	$CH_2 + O_2 => CH_2O + O$	5.39×10^{-13}
N87	$CH + O => CO + H$	6.90×10^{-11}
N88	$CH + O_2 => CO_2 + H$	1.20×10^{-11}
N89	$CH + O_2 => CO + OH$	8.00×10^{-12}
N90	$CH + O_2 => HCO + O$	8.00×10^{-12}
N91	$CH + O_2 => CO + H + O$	1.20×10^{-11}
N92	$C + O_2 => CO + O$	2.45×10^{-13}

N93	$C_2H_6 + O \Rightarrow C_2H_5 + OH$	5.11×10^{-16}
N94	$C_2H_5 + O \Rightarrow CH_3HCO + H$	8.80×10^{-11}
N95	$C_2H_5 + O \Rightarrow CH_2O + CH_3$	6.90×10^{-11}
N96	$C_2H_5 + O \Rightarrow C_2H_4 + OH$	4.40×10^{-11}
N97	$C_2H_5 + O_2 \Rightarrow C_2H_4 + HO_2$	3.80×10^{-15}
N98	$C_2H_4 + O \Rightarrow CH_2HCO + H$	2.63×10^{-13}
N99	$C_2H_4 + O \Rightarrow HCO + CH_3$	4.51×10^{-13}
N100	$C_2H_3 + O \Rightarrow C_2H_2 + OH$	1.25×10^{-11}
N101	$C_2H_3 + O \Rightarrow CO + CH_3$	1.25×10^{-11}
N102	$C_2H_3 + O \Rightarrow HCO + CH_2$	1.25×10^{-11}
N103	$C_2H_3 + O \Rightarrow CH_2CO + H$	1.25×10^{-11}
N104	$C_2H_3 + O_2 \Rightarrow CH_2O + HCO$	9.00×10^{-11}
N105	$C_2H_2 + O \Rightarrow CH_2 + CO$	6.75×10^{-14}
N106	$C_2H_2 + O \Rightarrow C_2HO + H$	6.75×10^{-14}
N107	$C_2H + O \Rightarrow CH + CO$	1.70×10^{-11}
N108	$C_2H + O_2 \Rightarrow HCO + CO$	3.00×10^{-11}
N109	$C_2H + O_2 \Rightarrow C_2HO + O$	1.00×10^{-12}
N110	$C_3H_8 + O \Rightarrow C_3H_7 + OH$	2.73×10^{-15}
N111	$H_2 + O \Rightarrow OH + H$	9.32×10^{-18}
N112	$H + O + CH_4 \Rightarrow OH + CH_4$	4.33×10^{-32} (cm^6s^{-1})
N113	$H + O_2 \Rightarrow OH + O$	1.87×10^{-22}
N114	$H + O_2 + CH_4 \Rightarrow HO_2 + CH_4$	5.40×10^{-32} (cm^6s^{-1})
N115	$CH_4 + OH \Rightarrow CH_3 + H_2O$	6.62×10^{-15}
N116	$CH_4 + HO_2 \Rightarrow CH_3 + H_2O_2$	8.76×10^{-27}
N117	$CH_4 + HCO \Rightarrow CH_3 + CH_2O$	6.07×10^{-30}
N118	$CH_4 + CH_3O \Rightarrow CH_3OH + CH_3$	9.42×10^{-20}
N119	$CH_3 + CO + CH_4 \Rightarrow CH_3CO + CH_4$	4.19×10^{-36} (cm^6s^{-1})
N120	$CH_3 + H_2O \Rightarrow CH_4 + OH$	1.82×10^{-25}
N121	$CH_3 + OH \Rightarrow CH_2 + H_2O$	1.13×10^{-12}
N122	$CH_3 + OH \Rightarrow CH_2OH + H$	1.32×10^{-11}
N123	$CH_3 + OH \Rightarrow CH_3O + H$	1.90×10^{-10}
N124	$CH_3 + OH \Rightarrow CH_3OH$	2.30×10^{-27}
N125	$CH_3 + HO_2 \Rightarrow CH_3O + OH$	3.00×10^{-11}

N126	$CH_3 + HO_2 => CH_4 + O_2$	5.99×10^{-12}
N127	$CH_3 + CH_2O => CH_4 + HCO$	6.14×10^{-18}
N128	$CH_3 + HCO => CH_4 + CO$	2.00×10^{-10}
N129	$CH_3 + CH_3O => CH_4 + CH_2O$	4.00×10^{-11}
N130	$CH_3 + CH_3CHO => CH_4 + CH_3CO$	4.95×10^{-18}
N131	$CH_2 + CO_2 => CH_2O + CO$	3.90×10^{-14}
N132	$CH_2 + H_2O => CH_3 + OH$	1.90×10^{-16}
N133	$CH_2 + OH => CH_2O + H$	3.00×10^{-11}
N134	$CH_2 + HO_2 => CH_2O + OH$	3.00×10^{-11}
N135	$CH_2 + CH_2O => CH_3 + HCO$	1.00×10^{-14}
N136	$CH_2 + HCO => CH_3 + CO$	3.00×10^{-11}
N137	$CH_2 + CH_3O => CH_3 + CH_2O$	3.00×10^{-11}
N138	$CH + CO_2 => 2CO + H$	9.68×10^{-13}
N139	$CH + CO_2 => HCO + CO$	9.68×10^{-13}
N140	$CH + CO => C_2HO$	4.04×10^{-30}
N141	$C_2H_6 + OH => C_2H_5 + H_2O$	2.46×10^{-13}
N142	$C_2H_6 + HO_2 => C_2H_5 + H_2O_2$	6.36×10^{-24}
N143	$C_2H_6 + HCO => C_2H_5 + CH_2O$	2.19×10^{-26}
N144	$C_2H_6 + CH_3O => C_2H_5 + CH_3OH$	2.72×10^{-18}
N145	$C_2H_5 + OH => C_2H_4 + H_2O$	4.00×10^{-11}
N146	$C_2H_5 + HO_2 => C_2H_6 + O_2$	5.00×10^{-13}
N147	$C_2H_5 + HO_2 => C_2H_4 + H_2O_2$	5.00×10^{-13}
N148	$C_2H_5 + CH_2O => C_2H_6 + HCO$	4.47×10^{-18}
N149	$C_2H_5 + HCO => C_2H_6 + CO$	2.00×10^{-10}
N150	$C_2H_5 + CH_3O => C_2H_6 + CH_2O$	4.00×10^{-11}
N151	$C_2H_4 + OH => C_2H_3 + H_2O$	1.54×10^{-16}
N152	$C_2H_4 + HO_2 => CH_3CHO + OH$	1.62×10^{-20}
N153	$C_2H_3 + H_2O => C_2H_4 + OH$	1.82×10^{-25}
N154	$C_2H_3 + OH => C_2H_2 + H_2O$	5.00×10^{-11}
N155	$C_2H_3 + CH_2O => C_2H_4 + HCO$	4.41×10^{-18}
N156	$C_2H_3 + HCO => C_2H_4 + CO$	1.50×10^{-10}
N157	$C_2H_3 + CH_3O => C_2H_4 + CH_2O$	4.00×10^{-11}
N158	$C_2H_2 + OH => C_2H + H_2O$	1.77×10^{-22}

N159	$C_2H_2 + HO_2 => CH_2CO + OH$	1.62×10^{-20}
N160	$C_2H + OH => CH_2 + CO$	3.00×10^{-11}
N161	$C_2H + OH => C_2H_2 + O$	3.00×10^{-11}
N162	$C_2H + HO_2 => C_2H_2 + O_2$	3.00×10^{-11}
N163	$C_2H + HO_2 => C_2HO + OH$	3.00×10^{-11}
N164	$C_2H + HCO => C_2H_2 + CO$	1.00×10^{-10}
N165	$C_2H + CH_3O => C_2H_2 + CH_2O$	4.00×10^{-11}
N166	$C_3H_8 + OH => C_3H_7 + H_2O$	3.76×10^{-15}
N167	$C_3H_8 + CH_3O => C_3H_7 + CH_3OH$	1.42×10^{-17}
N168	$C_3H_7 + CH_2O => C_3H_8 + HCO$	4.10×10^{-18}
N169	$C_3H_7 + HCO => C_3H_8 + CO$	1.00×10^{-10}
N170	$C_3H_7 + CH_3O => C_3H_8 + CH_2O$	4.00×10^{-11}
N171	$H_2 + OH => H + H_2O$	7.02×10^{-15}
N172	$H_2 + HCO => H + CH_2O$	2.78×10^{-26}
N173	$H + CO_2 => CO + OH$	1.40×10^{-29}
N174	$H + CO + M => HCO + M$	1.54×10^{-34}
N175	$H + H_2O => H_2 + OH$	5.86×10^{-26}
N176	$H + OH => H_2 + O$	1.05×10^{-16}
N177	$H + OH + M => H_2O + M$	4.33×10^{-30}
N178	$H + HO_2 => H_2 + O_2$	5.90×10^{-12}
N179	$H + HO_2 => H_2O + O$	2.40×10^{-12}
N180	$H + HO_2 => OH + OH$	7.20×10^{-11}
N181	$H + CH_2O => H_2 + HCO$	5.72×10^{-14}
N182	$H + CH_2O => H_2 + HCO$	3.86×10^{-14}
N183	$H + HCO => H_2 + CO$	1.50×10^{-10}
N184	$H + CH_3O => H_2 + CH_2O$	2.32×10^{-11}
N185	$H + CH_3O => CH_3 + OH$	9.93×10^{-12}
N186	$H + CH_3CHO => H_2 + CH_3CO$	8.98×10^{-14}
N187	$H + CH_2CO => CH_3 + CO$	1.04×10^{-13}
N188	$H + C_2HO => CH_2 + CO$	2.50×10^{-10}
N189	$CO + O + M => CO_2 + M$	1.11×10^{-35}
N190	$O + H_2O => OH + OH$	4.48×10^{-24}
N191	$O + OH => H + O_2$	3.46×10^{-11}

N192	$O + HO_2 => O_2 + OH$	5.70×10^{-11}
N193	$O + CH_2O => OH + HCO$	1.73×10^{-13}
N194	$O + HCO => CO + OH$	5.00×10^{-11}
N195	$O + HCO => H + CO_2$	5.00×10^{-11}
N196	$O + CH_3O => CH_3 + O_2$	2.20×10^{-11}
N197	$O + CH_3O => OH + CH_2O$	3.00×10^{-12}
N198	$O + CH_3CHO => OH + CH_3CO$	4.68×10^{-13}
N199	$O + CH_2CO => CH_2 + CO_2$	2.29×10^{-13}
N200	$O + CH_2CO => CH_2O + CO$	7.88×10^{-14}
N201	$O + CH_2CO => HCO + CO + H$	4.33×10^{-14}
N202	$O + CH_2CO => 2HCO$	4.33×10^{-14}
N203	$O + C_2HO => 2CO + H$	1.90×10^{-10}
N204	$O_2 + HCO => CO + HO_2$	5.10×10^{-12}
N205	$O_2 + CH_3O => CH_2O + HO_2$	1.97×10^{-15}
N206	$O_2 + CH_2CHO => CH_2O + CO + OH$	3.00×10^{-14}
N207	$O_2 + C_2HO => 2CO + OH$	6.46×10^{-13}
N208	$CO + OH => CO_2 + H$	1.25×10^{-13}
N209	$CO + CH_3O => CO_2 + CH_3$	6.56×10^{-20}
N210	$H_2O + CH_3O => CH_3OH + OH$	1.67×10^{-14}
N211	$OH + OH => H_2O + O$	1.47×10^{-12}
N212	$OH + OH + M => H_2O_2 + M$	6.86×10^{-31}
N213	$OH + HO_2 => O_2 + H_2O$	1.10×10^{-10}
N214	$OH + CH_2O => H_2O + HCO$	8.47×10^{-12}
N215	$OH + HCO => CO + H_2O$	1.70×10^{-10}
N216	$OH + CH_3O => CH_2O + H_2O$	3.00×10^{-11}
N217	$OH + CH_3CHO => CH_3CO + H_2O$	1.49×10^{-11}
N218	$OH + CH_2CO => CO + CH_2OH$	1.14×10^{-11}
N219	$2HO_2 => H_2O_2 + O_2$	1.63×10^{-12}
N220	$HO_2 + CH_2O => H_2O_2 + HCO$	1.05×10^{-20}
N221	$HO_2 + HCO => OH + H + CO_2$	5.00×10^{-11}
N222	$HO_2 + CH_3O => CH_2O + H_2O_2$	5.00×10^{-13}
N223	$CH_2O + CH_3O => CH_3OH + HCO$	1.14×10^{-15}
N224	$2HCO => CH_2O + CO$	5.00×10^{-11}

N225	$2CH_3O \Rightarrow CH_2O + CH_3OH$	1.00×10^{-10}
N226	$CH_4 + CH_3CO \Rightarrow CH_3CHO + CH_3$	1.14×10^{-29}
N227	$CH_4 + CH_2OH \Rightarrow CH_3OH + CH_3$	2.55×10^{-27}
N228	$CH_3 + H_2O_2 \Rightarrow CH_4 + HO_2$	5.46×10^{-14}
N229	$CH_3 + CH_3OH \Rightarrow CH_4 + CH_3O$	1.01×10^{-20}
N230	$CH_3 + CH_3OH \Rightarrow CH_4 + CH_2OH$	2.66×10^{-20}
N231	$CH_3 + CH_2OH \Rightarrow CH_4 + CH_2O$	4.00×10^{-12}
N232	$CH_2 + H_2O_2 \Rightarrow CH_3 + HO_2$	1.00×10^{-14}
N233	$CH_2 + CH_3CO \Rightarrow CH_2CO + CH_3$	3.00×10^{-11}
N234	$CH_2 + CH_3OH \Rightarrow CH_3O + CH_3$	1.01×10^{-20}
N235	$CH_2 + CH_3OH \Rightarrow CH_2OH + CH_3$	2.66×10^{-20}
N236	$CH_2 + CH_2OH \Rightarrow CH_2O + CH_3$	2.00×10^{-12}
N237	$CH_2 + CH_2OH \Rightarrow C_2H_4 + OH$	4.00×10^{-11}
N238	$C_2H_5 + H_2O_2 \Rightarrow C_2H_6 + HO_2$	2.83×10^{-15}
N239	$C_2H_5 + CH_3OH \Rightarrow C_2H_6 + CH_3O$	3.50×10^{-22}
N240	$C_2H_5 + CH_3OH \Rightarrow C_2H_6 + CH_2OH$	9.49×10^{-22}
N241	$C_2H_5 + CH_2OH \Rightarrow C_2H_6 + CH_2O$	4.00×10^{-12}
N242	$C_2H_5 + CH_2OH \Rightarrow CH_3OH + C_2H_4$	4.00×10^{-12}
N243	$C_2H_3 + H_2O_2 \Rightarrow C_2H_4 + HO_2$	5.46×10^{-14}
N244	$C_2H_3 + CH_3OH \Rightarrow C_2H_4 + CH_3O$	1.01×10^{-20}
N245	$C_2H_3 + CH_3OH \Rightarrow C_2H_4 + CH_2OH$	2.66×10^{-20}
N246	$C_2H_3 + CH_2OH \Rightarrow C_2H_4 + CH_2O$	5.00×10^{-11}
N247	$C_2H_2 + CH_2OH \Rightarrow C_2H_3 + CH_2O$	3.32×10^{-19}
N248	$C_2H + CH_3OH \Rightarrow C_2H_2 + CH_3O$	2.00×10^{-12}
N249	$C_2H + CH_3OH \Rightarrow C_2H_2 + CH_2OH$	1.00×10^{-11}
N250	$C_2H + CH_2OH \Rightarrow C_2H_2 + CH_2O$	5.99×10^{-11}
N251	$C_3H_7 + OH \Rightarrow C_3H_6 + H_2O$	4.00×10^{-11}
N252	$C_3H_7 + H_2O_2 \Rightarrow C_3H_8 + HO_2$	7.08×10^{-17}
N253	$C_3H_7 + CH_3OH \Rightarrow C_3H_8 + CH_3O$	3.51×10^{-22}
N254	$C_3H_7 + CH_3OH \Rightarrow C_3H_8 + CH_2OH$	8.45×10^{-22}
N255	$C_3H_7 + CH_2OH \Rightarrow C_3H_8 + CH_2O$	1.90×10^{-12}
N256	$C_3H_7 + CH_2OH \Rightarrow C_3H_6 + CH_3OH$	8.00×10^{-13}
N257	$H + H_2O_2 \Rightarrow H_2O + OH$	4.20×10^{-14}

N258	$H + H_2O_2 => H_2 + HO_2$	5.15×10^{-15}
N259	$H + CH_3OH => CH_2OH + H_2$	1.27×10^{-15}
N260	$H + CH_3OH => CH_3O + H_2$	3.18×10^{-16}
N261	$H + CH_2OH => CH_2O + H_2$	1.00×10^{-11}
N262	$H + CH_2OH => CH_3 + OH$	1.90×10^{-10}
N263	$H + CH_2OH + M => CH_3OH + M$	1.18×10^{-29}
N264	$O + H_2O_2 => HO_2 + OH$	8.91×10^{-16}
N265	$O + H_2O_2 => O_2 + H_2O$	8.91×10^{-16}
N266	$O + CH_3CO => OH + CH_2CO$	8.75×10^{-11}
N267	$O + CH_3CO => CO_2 + CH_3$	2.63×10^{-10}
N268	$O + CH_3OH => OH + CH_2OH$	1.12×10^{-14}
N269	$O + CH_3OH => OH + CH_3O$	1.68×10^{-15}
N270	$O + CH_2OH => CH_2O + OH$	7.00×10^{-11}
N271	$O_2 + CH_2OH => CH_2O + HO_2$	9.70×10^{-12}
N272	$OH + H_2O_2 => HO2 + H_2O$	1.70×10^{-12}
N273	$OH + CH_3CO => CH_2CO + H_2O$	2.00×10^{-11}
N274	$OH + CH_3CO => CH_3 + CO + OH$	5.00×10^{-11}
N275	$OH + CH_3OH => H_2O + CH_2OH$	7.67×10^{-13}
N276	$OH + CH_3OH => H_2O + CH_3O$	1.35×10^{-13}
N277	$OH + CH_2OH => CH_2O + H_2O$	4.00×10^{-11}
N278	$HO_2 + CH_3CO => CH_3 + CO_2 + OH$	5.00×10^{-11}
N279	$HO_2 + CH_3OH => CH_2OH + H_2O_2$	1.10×10^{-22}
N280	$HO_2 + CH_2OH => CH_2O + H_2O_2$	2.00×10^{-11}
N281	$CH_2O + CH_3CO => CH_3CHO + HCO$	1.17×10^{-22}
N282	$CH_2O + CH_2OH => CH_3OH + HCO$	4.22×10^{-18}
N283	$HCO + H_2O_2 => CH_2O + HO_2$	1.50×10^{-18}
N284	$HCO + CH_3CO => CH_3CHO + CO$	1.50×10^{-11}
N285	$HCO + CH_3OH => CH_2O + CH_2OH$	6.85×10^{-23}
N286	$HCO + CH_2OH => 2CH_2O$	3.00×10^{-10}
N287	HCO + CH2OH => CH3OH + CO	2.00×10^{-10}
N288	$CH_3O + CH_3CO => CH_3OH + CH_2CO$	1.00×10^{-11}
N289	$CH_3O + CH_2OH => CH_2O + CH_3OH$	4.00×10^{-11}
N290	$H_2O_2 + CH_3CO => CH_3CHO + HO_2$	3.05×10^{-19}

N291	$H_2O_2 + CH_2OH => CH_3OH + HO_2$	6.56×10^{-17}
N292	$CH_3CO + CH_3OH => CH_3CHO + CH_2OH$	2.22×10^{-22}
N293	$2CH_2OH => CH_2O + CH_3OH$	8.00×10^{-12}
N294	$C_3H_5 + O_2 => CH_3CHO + HCO$	7.21×10^{-12}
N295	$HCO + CH_3CO => CH_3CHO + CO$	1.50×10^{-11}
N296	$CH_3CHOH + O => CH_3CHO + OH$	1.50×10^{-10}
N297	$CH_3CHOH + O_2 => CH_3CHO + HO_2$	1.90×10^{-11}
N298	$CH_3 + HCO => CH_3CHO$	4.42×10^{-11}
N299	$CH + O_2 => HCO + O$	1.45×10^{-10}
N300	$C_2H_3 + O_2 => CH_2O + HCO$	2.62×10^{-12}
N301	$C_2H + O_2 => CO + HCO$	4.00×10^{-12}
N302	$CH_2O + O => HCO + OH$	1.67×10^{-13}
N303	$CH_2O + H => H_2 + HCO$	5.52×10^{-14}
N304	$CH_2O + OH => HCO + H_2O$	9.38×10^{-12}
N305	$CH_2O + HO_2 => HCO + H_2O_2$	2.52×10^{-18}
N306	$CH_2O + CH_3 => HCO + CH_4$	6.14×10^{-18}
N307	$HCO + CH_2 => CO + CH_3$	3.01×10^{-11}
N308	$HCO + O => CO + OH$	5.00×10^{-11}
N309	$HCO + O => CO_2 + H$	5.00×10^{-11}
N310	$HCO + H => CO + H2$	1.13×10^{-10}
N311	$HCO + O_2 => CO + HO_2$	5.20×10^{-12}
N312	$HCO + OH => CO + H_2O$	1.83×10^{-10}
N313	$HCO => CO + H$	3.35×10^{-22}
N314	$HCO + CH_3 => CO + CH_4$	4.00×10^{-11}
N315	$CH_3 + O_2 => CH_3O_2$	2.21×10^{-12}
N316	$CH_4 + O_2 => CH_3O_2 + H$	3.80×10^{-76}
N317	$CH_3CO + O_2 => CH_3COOO$	5.00×10^{-12}
N318	$C_2H_5 + O_2 => C_2H_5OO$	1.50×10^{-28}
N319	$CH_3CHO + O_2 => CH_3COOOH$	5.16×10^{-23}
N320	$CH_3CHO + CH_3COOO => CH_3COOOH + CH_3CO$	1.34×10^{-17}
N321	$CH_3CHO + OH => CH_3COOH + H$	2.00×10^{-21}
N322	$CH_3O_2 + CH_3COOO => CH_3COOH + CH_2O + O_2$	5.50×10^{-12}
N323	$CH_3COOOH + C_3H_6 => CH_3COOH + C_3H_6O$	3.85×10^{-14}

N324	$CO + OH \Rightarrow COOH$	1.20×10^{-12}
N325	$CH_3 + COOH \Rightarrow CH_3COOH$	5.81×10^{-10}
N326	$CH_3CO + O \Rightarrow CH3COO$	1.99×10^{-10}
N327	$CH_3COO + H \Rightarrow CH_3COOH$	3.79×10^{-11}
N328	$C_2H_5 + OH \Rightarrow C_2H_5OH$	1.28×10^{-10}
N329	$2C_2H_5OO \Rightarrow C_2H_5OH + CH_3CHO + O_2$	2.34×10^{-14}
N330	$CH_3CHOH + H \Rightarrow C_2H_5OH$	8.30×10^{-11}
N331	$CH_2O + OH \Rightarrow HCOOH + H$	2.01×10^{-13}
N332	$CH_3CHO + H \Rightarrow CH_3CHOH$	2.49×10^{-18}
N333	$C_2H_5OH + O \Rightarrow CH_3CHOH + OH$	1.03×10^{-13}
N334	$C_2H_5OH + OH \Rightarrow CH_3CHOH + H_2O$	5.00×10^{-13}
N335	$C_2H_5OH + CH_3 \Rightarrow CH_4 + CH_3CHOH$	2.79×10^{-56}
N336	$CH_3 + CH_3CO \Rightarrow CH_3COCH_3$	6.97×10^{-20}
N337	$CH_3COCH_3 + O \Rightarrow CH_3COCH_2 + OH$	1.13×10^{-15}
N338	$CH_3COCH_3 + OH \Rightarrow CH_3COCH_2 + H_2O$	2.20×10^{-13}
N339	$CH_3COCH_3 + H \Rightarrow CH_3COCH_2 + H_2$	6.70×10^{-16}
N340	$CH_3COCH_3 + HO_2 \Rightarrow CH_3COCH_2 + H_2O_2$	3.49×10^{-16}
N341	$CH_3COCH_3 + CH_3 \Rightarrow CH_3COCH_2 + CH_4$	5.56×10^{-20}
N342	$C_3H_7 + CH_3 \Rightarrow C_4H_{10}$	7.02×10^{-21}
N343	$CH_3OH + C_4H_9 \Rightarrow C_4H_{10} + CH_2OH$	7.98×10^{-22}
N344	$CH_4 + C_4H_9 \Rightarrow C_4H_{10} + CH_3$	8.82×10^{-23}
N345	$CH_2O + C_4H_9 \Rightarrow C_4H_{10} + HCO$	9.23×10^{-18}
N346	$C_2H_4 + C_2H_5 \Rightarrow C_4H_9$	9.58×10^{-19}
N347	$C_2H_5 + C_2H_5 \Rightarrow C_4H_{10}$	1.66×10^{-11}
N348	$C_4H_9 + H \Rightarrow C_4H_{10}$	4.26×10^{-11}

Table 9.6 Electron-impact reactions simulated in the model. All the reaction rates for these reactions are depend on the cross section of each particle and instantaneous electron temperature [186, 191, 192].

No.	Reaction		Rate constant
E1	$e^- + CH_4 \Rightarrow CH_3 + H^-$	Dissociative Attachment	$f(\sigma)$, ε
E2	$e^- + CH_4 \Rightarrow CH_2^- + H_2$	Dissociative Attachment	$f(\sigma)$, ε
E3	$e^- + CH_4 \Rightarrow e^- + CH_4$	Momentum Transfer	$f(\sigma)$, ε
E4	$e^- + CH_4 \Rightarrow e^- + CH_{4(V24)}$	Vibrational Excitation	$f(\sigma)$, ε
E5	$e^- + CH_4 \Rightarrow e^- + CH_{4(V13)}$	Vibrational Excitation	$f(\sigma)$, ε
E6	$e^- + CH_4 \Rightarrow e^- + CH_3 + H$	Dissociative Excitation	$f(\sigma)$, ε
E7	$e^- + CH_4 \Rightarrow e^- + CH_2 + 2H$	Dissociative Excitation	$f(\sigma)$, ε
E8	$e^- + CH_4 \Rightarrow e^- + CH + 3H$	Dissociative Excitation	$f(\sigma)$, ε
E9	$e^- + CH_4 \Rightarrow 2e^- + CH_4^+$	Ionisation	$f(\sigma)$, ε
E10	$e^- + CO_2 \Rightarrow CO + O^-$	Dissociative Attachment	$f(\sigma)$, ε
E11	$e^- + CO_2 \Rightarrow e^- + CO_2^*$	Momentum Transfer	$f(\sigma)$, ε
E12-19	$e^- + CO_2 \Rightarrow e^- + CO_{2(V1-8)}$	Vibrational Excitation	$f(\sigma)$, ε
E20-27	$e^- + CO_2 \Rightarrow e^- + CO_{2(E1-8)}$	Electronic Excitation	$f(\sigma)$, ε
E28	$e^- + CO_2 \Rightarrow 2e^- + CO_2^+$	Ionisation	$f(\sigma)$, ε
E29	$e^- + CO_2 \Rightarrow e^- + CO + O$	Dissociative Excitation	$f(\sigma)$, ε
E30	$e^- + CH_3 \Rightarrow e^- + CH_{3(P)}$	Excitation	$f(\sigma)$, ε
E31	$e^- + CH_3 \Rightarrow e^- + CH_2 + H$	Dissociative Excitation	$f(\sigma)$, ε
E32	$e^- + CH_3 \Rightarrow e^- + CH + H_2$	Dissociative Excitation	$f(\sigma)$, ε
E33	$e^- + CH_3 \Rightarrow e^- + H + C + H_2$	Dissociative Excitation	$f(\sigma)$, ε
E34	$e^- + CH_3 \Rightarrow 2e^- + CH_3^+$	Ionisation	$f(\sigma)$, ε
E35	$e^- + CH_3 \Rightarrow 2e^- + H + CH_2^+$	Dissociative Ionisation	$f(\sigma)$, ε
E36	$e^- + CH_3^+ \Rightarrow 2e^- + H + H^+ + CH^+$	Dissociative Ionisation	$f(\sigma)$, ε
E37	$e^- + CH_3^+ \Rightarrow 2e^- + H_2 + H^+ + C^+$	Dissociative Ionisation	$f(\sigma)$, ε
E38	$e^- + CH_2 \Rightarrow e^- + CH_2^*$	Excitation	$f(\sigma)$, ε
E39	$e^- + CH_2 \Rightarrow e^- + CH + H$	Dissociative Excitation	$f(\sigma)$, ε
E40	$e^- + CH_2 \Rightarrow e^- + C + H_2$	Dissociative Excitation	$f(\sigma)$, ε
E41	$e^- + CH_2 \Rightarrow e^- + C + 2H$	Dissociative Excitation	$f(\sigma)$, ε
E42	$e^- + CH_2 \Rightarrow 2e^- + CH_2^+$	Ionisation	$f(\sigma)$, ε

E43	$e^- + CH_2 \Rightarrow 2e^- + H + CH^+$	Dissociative Ionisation	$f(\sigma)$, ε
E44	$e^- + CH_2^+ \Rightarrow 2e^- + H + H^+ + C^+$	Dissociative Ionisation	$f(\sigma)$, ε
E45	$e^- + C \Rightarrow e^- + C$	Momentum Transfer	$f(\sigma)$, ε
E46	$e^- + C \Rightarrow e^- + C_{(1D)}$	Excitation	$f(\sigma)$, ε
E47	$e^- + C \Rightarrow e^- + C_{(1S)}$	Excitation	$f(\sigma)$, ε
E48	$e^- + C \Rightarrow 2e^- + C^+$	Ionisation	$f(\sigma)$, ε
E49	$e^- + CO \Rightarrow e^- + CO$	Momentum Transfer	$f(\sigma)$, ε
E50-59	$e^- + CO \Rightarrow e^- + CO_{(V1-10)}$	Vibrational Excitation	$f(\sigma)$, ε
E60-64	$e^- + CO \Rightarrow e^- + CO_{(E1-5)}$	Electronic Excitation	$f(\sigma)$, ε
E65	$e^- + CO \Rightarrow e^- + C + O$	Dissociative Excitation	$f(\sigma)$, ε
E66	$e^- + CO \Rightarrow 2e^- + CO^+$	Ionisation	$f(\sigma)$, ε
E67	$e^- + H_2 \Rightarrow H + H^-$	Dissociative Attachment	$f(\sigma)$, ε
E68	$e^- + H_2 \Rightarrow e^- + H_{2(j0\text{-}2,\ j1\text{-}3)}$	Rotational Excitation	$f(\sigma)$, ε
E69-71	$e^- + H_2 \Rightarrow e^- + H_{2(V1\text{-}3)}$	Vibrational Excitation	$f(\sigma)$, ε
E72	$e^- + H_2 \Rightarrow e^- + H_2(B^1\Sigma_u^+)$	Electronic Excitation	$f(\sigma)$, ε
E73	$e^- + H_2 \Rightarrow e^- + H_2(c^3\Pi_u)$	Electronic Excitation	$f(\sigma)$, ε
E74	$e^- + H_2 \Rightarrow e^- + H_2(a^3\Sigma_g^+)$	Electronic Excitation	$f(\sigma)$, ε
E75	$e^- + H_2 \Rightarrow e^- + H_2(C^1\Pi_u)$	Electronic Excitation	$f(\sigma)$, ε
E76	$e^- + H_2 \Rightarrow e^- + H_2(^1\Sigma_g^+)$	Electronic Excitation	$f(\sigma)$, ε
E77	$e^- + H_2 \Rightarrow e^- + H_2(D^3\Pi_u)$	Electronic Excitation	$f(\sigma)$, ε
E78	$e^- + H_2 \Rightarrow e^- + H_{2(E1\text{-}2)}$	Electronic Excitation	$f(\sigma)$, ε
E79	$e^- + H_2 \Rightarrow e^- + H_{2(Rydberg)}$	Rydberg Excitation	$f(\sigma)$, ε
E80	$e^- + H_2 \Rightarrow 2e^- + H_2^+$	Ionisation	$f(\sigma)$, ε
E81	$e^- + H \Rightarrow e^- + H$	Momentum Transfer	$f(\sigma)$, ε
E82	$e^- + H \Rightarrow e^- + H_{(2p)}$	Excitation	$f(\sigma)$, ε
E83	$e^- + H \Rightarrow e^- + H_{(2s)}$	Excitation	$f(\sigma)$, ε
E84	$e^- + H \Rightarrow 2e^- + H^+$	Ionisation	$f(\sigma)$, ε
E85	$e^- + O_2 \Rightarrow O_2^-$	Attachment	$f(\sigma)$, ε
E86	$e^- + O_2 \Rightarrow e^- + O_2$	Momentum Transfer	$f(\sigma)$, ε
E87-89	$e^- + O_2 \Rightarrow e^- + O_{2(R1\text{-}3)}$	Rotational Excitation	$f(\sigma)$, ε
E90-93	$e^- + O_2 \Rightarrow e^- + O_{2(V1\text{-}4)}$	Vibrational Excitation	$f(\sigma)$, ε
E94	$e^- + O_2 \Rightarrow e^- + O_2(b^1\Sigma^+)$	Electronic Excitation	$f(\sigma)$, ε
E95	$e^- + O_2 \Rightarrow e^- + O_2(a^1\delta^+)$	Electronic Excitation	$f(\sigma)$, ε

E96-101	$e^- + O_2 \Rightarrow e^- + O + O$	Dissociative Excitation	$f(\sigma)$, ε
E102	$e^- + O_2 \Rightarrow 2e^- + O_2^+$	Ionisation	$f(\sigma)$, ε
E103	$e^- + O \Rightarrow e^- + O$	Momentum Transfer	$f(\sigma)$, ε
E104	$e^- + O \Rightarrow e^- + O_{(1D)}$	Excitation	$f(\sigma)$, ε
E105	$e^- + O \Rightarrow e^- + O_{(1S)}$	Excitation	$f(\sigma)$, ε
E106	$e^- + O \Rightarrow 2e^- + O^+$	Ionisation	$f(\sigma)$, ε
E107	$e^- + H_2O \Rightarrow H_2 + O^-$	Dissociative Attachment	$f(\sigma)$, ε
E108	$e^- + H_2O \Rightarrow OH + H^-$	Dissociative Attachment	$f(\sigma)$, ε
E109	$e^- + H_2O \Rightarrow H + OH^-$	Dissociative Attachment	$f(\sigma)$, ε
E110	$e^- + H_2O \Rightarrow e^- + H_2O$	Momentum Transfer	$f(\sigma)$, ε
E111-113	$e^- + H_2O \Rightarrow e^- + H_2O_{(V1\text{-}3)}$	Vibrational Excitation	$f(\sigma)$, ε
E114	$e^- + H_2O \Rightarrow e^- + H + OH$	Dissociative Excitation	$f(\sigma)$, ε
E115	$e^- + H_2O \Rightarrow e^- + H_2 + O$	Dissociative Excitation	$f(\sigma)$, ε
E116	$e^- + H_2O \Rightarrow 2e^- + H_2O^+$	Ionisation	$f(\sigma)$, ε
E117	$e^- + C_2H_2 \Rightarrow e^- + C_2H_2$	Momentum Transfer	$f(\sigma)$, ε
E118-120	$e^- + C_2H_2 \Rightarrow e^- + C_2H_{2(V2,5\ \&31)}$	Vibrational Excitation	$f(\sigma)$, ε
E121-122	$e^- + C_2H_2 \Rightarrow e^- + C_2H_{2(E1\ \&2)}$	Electronic Excitation	$f(\sigma)$, ε
E123	$e^- + C_2H_2 \Rightarrow e^- + H + C_2H$	Dissociative Excitation	$f(\sigma)$, ε
E124	$e^- + C_2H_2 \Rightarrow e^- + 2H + C_2$	Dissociative Excitation	$f(\sigma)$, ε
E125	$e^- + C_2H_2 \Rightarrow e^- + CH + CH$	Dissociative Excitation	$f(\sigma)$, ε
E126	$e^- + C_2H_2 \Rightarrow e^- + C + CH_2$	Dissociative Excitation	$f(\sigma)$, ε
E127	$e^- + C_2H_2 \Rightarrow 2e^- + C_2H_2^+$	Ionisation	$f(\sigma)$, ε
E128	$e^- + C_2H_2^+ \Rightarrow e^- + C_2H^+ + H$	Dissociation of Ion	$f(\sigma)$, ε
E129	$e^- + C_2H_2^+ \Rightarrow e^- + C_2H + H^+$	Dissociation of Ion	$f(\sigma)$, ε
E130	$e^- + C_2H_2^+ \Rightarrow e^- + H_2 + C_2^+$	Dissociation of Ion	$f(\sigma)$, ε
E131	$e^- + C_2H_2^+ \Rightarrow e^- + CH + CH^+$	Dissociation of Ion	$f(\sigma)$, ε
E132	$e^- + C_2H_2^+ \Rightarrow e^- + C + CH_2^+$	Dissociation of Ion	$f(\sigma)$, ε
E133	$e^- + C_2H_2^+ \Rightarrow e^- + C^+ + CH_2$	Dissociation of Ion	$f(\sigma)$, ε
E134	$e^- + C_2H_2^+ \Rightarrow 2e^- + C_2H^+ + H^+$	Dissociative Ionisation	$f(\sigma)$, ε
E135	$e^- + C_2H_2^+ \Rightarrow 2e^- + C_2^+ + H_2^+$	Dissociative Ionisation	$f(\sigma)$, ε
E136	$e^- + C_2H_2^+ \Rightarrow 2e^- + C_2^+ + H + H^+$	Dissociative Ionisation	$f(\sigma)$, ε
E137	$e^- + C_2H_2^+ \Rightarrow 2e^- + CH^+ + CH^+$	Dissociative Ionisation	$f(\sigma)$, ε
E138	$e^- + C_2H_2^+ \Rightarrow 2e^- + C^+ + H + CH^+$	Dissociative Ionisation	$f(\sigma)$, ε

E139	$e^- + C_2H_2^+ \Rightarrow 2e^- + CH_2^+ + C^+$	Dissociative Ionisation	$f(\sigma)$, ε
E140	$e^- + C_2H_4 \Rightarrow e^- + C_2H_4$	Momentum Transfer	$f(\sigma)$, ε
E141-142	$e^- + C_2H_4 \Rightarrow e^- + C_2H_{4(V1\ \&\ 2)}$	Vibrational Excitation	$f(\sigma)$, ε
E143-144	$e^- + C_2H_4 \Rightarrow e^- + C_2H_{4(E1\ \&\ 2)}$	Electronic Excitation	$f(\sigma)$, ε
E145	$e^- + C_2H_4 \Rightarrow e^- + C_2H_3 + H$	Dissociative Excitation	$f(\sigma)$, ε
E146	$e^- + C_2H_4 \Rightarrow e^- + C_2H_2 + H_2$	Dissociative Excitation	$f(\sigma)$, ε
E147	$e^- + C_2H_4 \Rightarrow e^- + C_2H_2 + 2H$	Dissociative Excitation	$f(\sigma)$, ε
E148	$e^- + C_2H_4 \Rightarrow e^- + C_2H + H_2 + H$	Dissociative Excitation	$f(\sigma)$, ε
E149	$e^- + C_2H_4 \Rightarrow e^- + CH_3 + CH$	Dissociative Excitation	$f(\sigma)$, ε
E150	$e^- + C_2H_4 \Rightarrow e^- + CH_2 + CH_2$	Dissociative Excitation	$f(\sigma)$, ε
E151	$e^- + C_2H_4 \Rightarrow e^- + C + CH_4$	Dissociative Excitation	$f(\sigma)$, ε
E152	$e^- + C_2H_4 \Rightarrow 2e^- + C_2H_4^+$	Ionisation	$f(\sigma)$, ε
E153	$e^- + C_2H_4^+ \Rightarrow e^- + H + C_2H_3^+$	Dissociation of Ion	$f(\sigma)$, ε
E154	$e^- + C_2H_4^+ \Rightarrow e^- + H_2 + C_2H_2^+$	Dissociation of Ion	$f(\sigma)$, ε
E155	$e^- + C_2H_4^+ \Rightarrow e^- + H_2^+ + C_2H_2$	Dissociation of Ion	$f(\sigma)$, ε
E156	$e^- + C_2H_4^+ \Rightarrow e^- + CH_3^+ + CH$	Dissociation of Ion	$f(\sigma)$, ε
E157	$e^- + C_2H_4^+ \Rightarrow e^- + CH_3 + CH^+$	Dissociation of Ion	$f(\sigma)$, ε
E158	$e^- + C_2H_4^+ \Rightarrow e^- + CH_2 + CH_2^+$	Dissociation of Ion	$f(\sigma)$, ε
E159	$e^- + C_2H_4^+ \Rightarrow e^- + CH_4 + C^+$	Dissociation of Ion	$f(\sigma)$, ε
E160	$e^- + C_2H_4^+ \Rightarrow 2e^- + C_2H_3^+ + H^+$	Dissociative Ionisation	$f(\sigma)$, ε
E161	$e^- + C_2H_4^+ \Rightarrow 2e^- + C_2H_2^+ + H_2^+$	Dissociative Ionisation	$f(\sigma)$, ε
E162	$e^- + C_2H_4^+ \Rightarrow 2e^- + C_2H_2^+ + H + H^+$	Dissociative Ionisation	$f(\sigma)$, ε
E163	$e^- + C_2H_4^+ \Rightarrow 2e^- + CH_3^+ + CH^+$	Dissociative Ionisation	$f(\sigma)$, ε
E164	$e^- + C_2H_4^+ \Rightarrow 2e^- + CH_2^+ + CH_2^+$	Dissociative Ionisation	$f(\sigma)$, ε
E165	$e^- + C_2H_4^+ \Rightarrow 2e^- + CH_4^+ + C^+$	Dissociative Ionisation	$f(\sigma)$, ε
E166	$e^- + C_2H_6 \Rightarrow C_2H_6^-$	Attachment	$f(\sigma)$, ε
E167	$e^- + C_2H_6 \Rightarrow e^- + C_2H_6$	Momentum Transfer	$f(\sigma)$, ε
E168-169	$e^- + C_2H_6 \Rightarrow e^- + C_2H_{6(V13\ \&\ 24)}$	Vibrational Excitation	$f(\sigma)$, ε
E170	$e^- + C_2H_6 \Rightarrow e^- + C_2H_5 + H$	Dissociative Excitation	$f(\sigma)$, ε
E171	$e^- + C_2H_6 \Rightarrow e^- + C_2H_4 + H_2$	Dissociative Excitation	$f(\sigma)$, ε
E172	$e^- + C_2H_6 \Rightarrow e^- + C_2H_3 + H + H_2$	Dissociative Excitation	$f(\sigma)$, ε
E173	$e^- + C_2H_6 \Rightarrow e^- + C_2H_2 + 2H_2$	Dissociative Excitation	$f(\sigma)$, ε
E174	$e^- + C_2H_6 \Rightarrow e^- + CH_4 + CH_2$	Dissociative Excitation	$f(\sigma)$, ε

E175	$e^- + C_2H_6 \Rightarrow e^- + CH_3 + CH_3$	Dissociative Excitation	$f(\sigma)$, ε
E176	$e^- + C_2H_6 \Rightarrow 2e^- + C_2H_6^+$	Ionisation	$f(\sigma)$, ε
E177	$e^- + C_2H_6^+ \Rightarrow e^- + C_2H_5^+ + H$	Dissociation of Ion	$f(\sigma)$, ε
E178	$e^- + C_2H_6^+ \Rightarrow e^- + C_2H_4^+ + H_2$	Dissociation of Ion	$f(\sigma)$, ε
E179	$e^- + C_2H_6^+ \Rightarrow e^- + CH_3^+ + CH_3$	Dissociation of Ion	$f(\sigma)$, ε
E180	$e^- + C_2H_6^+ \Rightarrow 2e^- + C_2H_5^+ + H^+$	Dissociative Ionisation	$f(\sigma)$, ε
E181	$e^- + C_2H_6^+ \Rightarrow 2e^- + C_2H_4^+ + H_2^+$	Dissociative Ionisation	$f(\sigma)$, ε
E182	$e^- + C_2H_6^+ \Rightarrow 2e^- + C_2H_4^+ + H + H^+$	Dissociative Ionisation	$f(\sigma)$, ε
E183	$e^- + C_2H_6^+ \Rightarrow 2e^- + C_2H_3^+ + H_2 + H^+$	Dissociative Ionisation	$f(\sigma)$, ε
E184	$e^- + C_2H_6^+ \Rightarrow 2e^- + C_2H_2^+ + H_2 + H_2^+$	Dissociative Ionisation	$f(\sigma)$, ε
E185	$e^- + C_2H_6^+ \Rightarrow 2e^- + CH_4^+ + CH_2^+$	Dissociative Ionisation	$f(\sigma)$, ε
E186	$e^- + C_2H_6^+ \Rightarrow 2e^- + CH_3^+ + CH_3^+$	Dissociative Ionisation	$f(\sigma)$, ε
E187	$e^- + C_3H_6 \Rightarrow C_3H_6^-$	Attachment	$f(\sigma)$, ε
E188	$e^- + C_3H_6 \Rightarrow e^- + C_3H_6$	Momentum Transfer	$f(\sigma)$, ε
E189	$e^- + C_3H_6 \Rightarrow e^- + C_3H_{6(V)}$	Vibrational Excitation	$f(\sigma)$, ε
E190	$e^- + C_3H_6 \Rightarrow e^- + C_3H_5 + H$	Dissociative Excitation	$f(\sigma)$, ε
E191	$e^- + C_3H_6 \Rightarrow e^- + C_3H_4 + H_2$	Dissociative Excitation	$f(\sigma)$, ε
E192	$e^- + C_3H_6 \Rightarrow e^- + C_3H_3 + H + H_2$	Dissociative Excitation	$f(\sigma)$, ε
E193	$e^- + C_3H_6 \Rightarrow e^- + C_3H_2 + 2H_2$	Dissociative Excitation	$f(\sigma)$, ε
E194	$e^- + C_3H_6 \Rightarrow e^- + C_2H_4 + CH_2$	Dissociative Excitation	$f(\sigma)$, ε
E195	$e^- + C_3H_6 \Rightarrow e^- + C_2H_3 + CH_3$	Dissociative Excitation	$f(\sigma)$, ε
E196	$e^- + C_3H_6 \Rightarrow e^- + C_2H_2 + CH_4$	Dissociative Excitation	$f(\sigma)$, ε
E197	$e^- + C_3H_6 \Rightarrow 2e^- + C_3H_6^+$	Ionisation	$f(\sigma)$, ε
E198	$e^- + C_3H_6^+ \Rightarrow e^- + C_2H_5^+ + CH$	Dissociation of Ion	$f(\sigma)$, ε
E199	$e^- + C_3H_6^+ \Rightarrow e^- + C_2H_4^+ + CH_2$	Dissociation of Ion	$f(\sigma)$, ε
E200	$e^- + C_3H_6^+ \Rightarrow e^- + C_2H_3^+ + CH_3$	Dissociation of Ion	$f(\sigma)$, ε
E201	$e^- + C_3H_6^+ \Rightarrow e^- + C_2H_2^+ + CH_4$	Dissociation of Ion	$f(\sigma)$, ε
E202	$e^- + C_3H_6^+ \Rightarrow e^- + CH_4^+ + C_2H_2$	Dissociation of Ion	$f(\sigma)$, ε
E203	$e^- + C_3H_6^+ \Rightarrow e^- + CH_3^+ + C_2H_3$	Dissociation of Ion	$f(\sigma)$, ε
E204	$e^- + C_3H_6^+ \Rightarrow e^- + CH_2^+ + C_2H_4$	Dissociation of Ion	$f(\sigma)$, ε
E205	$e^- + C_3H_6^+ \Rightarrow 2e^- + C_2H_6^+ + C^+$	Dissociative Ionisation	$f(\sigma)$, ε
E206	$e^- + C_3H_6^+ \Rightarrow 2e^- + C_2H_5^+ + CH^+$	Dissociative Ionisation	$f(\sigma)$, ε
E207	$e^- + C_3H_6^+ \Rightarrow 2e^- + C_2H_4^+ + CH_2^+$	Dissociative Ionisation	$f(\sigma)$, ε

E208	$e^- + C_3H_6^+ \Rightarrow 2e^- + C_2H_3^+ + CH_3^+$	Dissociative Ionisation	*f(σ), ε*
E209	$e^- + C_3H_6^+ \Rightarrow 2e^- + C_2H_2^+ + CH_4^+$	Dissociative Ionisation	*f(σ), ε*
E210	$e^- + C_3H_6^+ \Rightarrow 2e^- + C_2H^+ + H + CH_4^+$	Dissociative Ionisation	*f(σ), ε*
E211	$e^- + C_3H_6^+ \Rightarrow 2e^- + C_2H^+ + H^+ + CH_4$	Dissociative Ionisation	*f(σ), ε*
E212	$e^- + C_3H_6^+ \Rightarrow 2e^- + C_2^+ + CH_4^+ + H_2$	Dissociative Ionisation	*f(σ), ε*
E213	$e^- + C_3H_8 \Rightarrow C_3H_8^-$	Attachment	*f(σ), ε*
E214	$e^- + C_3H_8 \Rightarrow e^- + C_3H_8$	Momentum Transfer	*f(σ), ε*
E215-216	$e^- + C_3H_8 \Rightarrow e^- + C_3H_{8(V1\ \&\ 2)}$	Vibrational Excitation	*f(σ), ε*
E217	$e^- + C_3H_8 \Rightarrow e^- + C_3H_{8(E)}$	Electronic Excitation	*f(σ), ε*
E218	$e^- + C_3H_8 \Rightarrow e^- + C_3H_7 + H$	Dissociative Excitation	*f(σ), ε*
E219	$e^- + C_3H_8 \Rightarrow e^- + C_3H_6 + H_2$	Dissociative Excitation	*f(σ), ε*
E220	$e^- + C_3H_8 \Rightarrow e^- + C_3H_4 + 2H_2$	Dissociative Excitation	*f(σ), ε*
E221	$e^- + C_3H_8 \Rightarrow e^- + C_2H_6 + CH_2$	Dissociative Excitation	*f(σ), ε*
E222	$e^- + C_3H_8 \Rightarrow e^- + C_2H_5 + CH_3$	Dissociative Excitation	*f(σ), ε*
E223	$e^- + C_3H_8 \Rightarrow e^- + C_2H_4 + CH_4$	Dissociative Excitation	*f(σ), ε*
E224	$e^- + C_3H_8 \Rightarrow 2e^- + C_3H_8^+$	Ionisation	*f(σ), ε*
E225	$e^- + C_3H_8^+ \Rightarrow e^- + C_2H_5^+ + CH_3$	Dissociation of Ion	*f(σ), ε*
E226	$e^- + C_3H_8^+ \Rightarrow e^- + C_2H_4^+ + CH_4$	Dissociation of Ion	*f(σ), ε*
E227	$e^- + C_3H_8^+ \Rightarrow 2e^- + C_2H_6^+ + CH_2^+$	Dissociative Ionisation	*f(σ), ε*
E228	$e^- + C_3H_8^+ \Rightarrow 2e^- + C_2H_5^+ + CH_3^+$	Dissociative Ionisation	*f(σ), ε*
E229	$e^- + C_3H_8^+ \Rightarrow 2e^- + C_2H_4^+ + CH_4^+$	Dissociative Ionisation	*f(σ), ε*
E230	$e^- + C_3H_8^+ \Rightarrow 2e^- + C_2H_3^+ + CH_4 + H^+$	Dissociative Ionisation	*f(σ), ε*
E231	$e^- + C_3H_8^+ \Rightarrow 2e^- + C_2H_3^+ + H + CH_4^+$	Dissociative Ionisation	*f(σ), ε*
E232	$e^- + C_3H_8^+ \Rightarrow 2e^- + C_2H_3^+ + H_2 + CH_3^+$	Dissociative Ionisation	*f(σ), ε*
E233	$e^- + C_3H_8^+ \Rightarrow 2e^- + C_2H_3^+ + H_2^+ + CH_3$	Dissociative Ionisation	*f(σ), ε*
E234	$e^- + C_3H_8^+ \Rightarrow 2e^- + C_2H_2^+ + CH_4^+ + H_2$	Dissociative Ionisation	*f(σ), ε*
E235	$e^- + C_3H_8^+ \Rightarrow 2e^- + C_2H_2^+ + CH_4 + H_2^+$	Dissociative Ionisation	*f(σ), ε*
E236	$e^- + CH_4^+ \Rightarrow CH_3 + H$	Recombination	[20]
E237	$e^- + CH_4^+ \Rightarrow CH_2 + 2H$	Recombination	[20]
E238	$e^- + CH_4^+ \Rightarrow CH + H_2 + H$	Recombination	[20]
E239	$e^- + CH_3^+ \Rightarrow CH_2 + H$	Recombination	[20]
E240	$e^- + CH_3^+ \Rightarrow CH + H_2$	Recombination	[20]
E241	$e^- + CH_3^+ \Rightarrow CH + 2H$	Recombination	[20]

E242	$e^- + CH_3^+ \Rightarrow C + H + H_2$	Recombination	[20]
E243	$e^- + CH_2^+ \Rightarrow CH + H$	Recombination	[20]
E244	$e^- + CH_2^+ \Rightarrow C + H_2$	Recombination	[20]
E245	$e^- + CH_2^+ \Rightarrow C + 2H$	Recombination	[20]
E246	$e^- + CH^+ \Rightarrow C + H$	Recombination	[20]
E247	$e^- + C_2H_6^+ \Rightarrow C_2H_5 + H$	Recombination	[20]
E248	$e^- + C_2H_6^+ \Rightarrow C_2H_4 + 2H$	Recombination	[20]
E249	$e^- + C_2H_5^+ \Rightarrow C_2H_4 + H$	Recombination	[20]
E250	$e^- + C_2H_5^+ \Rightarrow C_2H_3 + 2H$	Recombination	[20]
E251	$e^- + C_2H_5^+ \Rightarrow C_2H_2 + H + H_2$	Recombination	[20]
E252	$e^- + C_2H_5^+ \Rightarrow C_2H_2 + 3H$	Recombination	[20]
E253	$e^- + C_2H_5^+ \Rightarrow CH_3 + CH_2$	Recombination	[20]
E254	$e^- + C_2H_4^+ \Rightarrow C_2H_3 + H$	Recombination	[20]
E255	$e^- + C_2H_4^+ \Rightarrow C_2H_2 + 2H$	Recombination	[20]
E256	$e^- + C_2H_4^+ \Rightarrow C_2H + H_2 + H$	Recombination	[20]
E257	$e^- + C_2H_3^+ \Rightarrow C_2H_2 + H$	Recombination	[20]
E258	$e^- + C_2H_3^+ \Rightarrow C_2H + 2H$	Recombination	[20]
E259	$e^- + C_2H_2^+ \Rightarrow C_2H + H$	Recombination	[20]
E260	$e^- + C_2H_2^+ \Rightarrow CH + CH$	Recombination	[20]
E261	$e^- + O_2^+ + O_2 \Rightarrow O_2 + O_2$	Recombination	[20]
E262	$e^- + O_2^+ \Rightarrow O + O$	Recombination	[20]
E263	$e^- + CO_2^+ \Rightarrow CO + O$	Recombination	[20]

Table 9.7 Ion-neutral/ions involved in this model, and the corresponding reaction rate constant are adopted from the literature [213-215].

No.	**Reaction**	**Rate constant (cm^3s^{-1})**
I1	$CH_4^+ + C_2H_6 \Rightarrow C_2H_4^+ + CH_4 + H_2$	1.91×10^{-9}
I2	$CH_4^+ + C_2H_4 \Rightarrow C_2H_5^+ + CH_3$	4.23×10^{-10}
I3	$CH_4^+ + C_2H_4 \Rightarrow C_2H_4^+ + CH_4$	1.38×10^{-9}
I4	$CH_4^+ + C_2H_2 \Rightarrow C_2H_3^+ + CH_3$	1.23×10^{-9}
I5	$CH_4^+ + C_2H_2 \Rightarrow C_2H_2^+ + CH_4$	1.13×10^{-9}

I6	$CH_4^+ + H \Rightarrow CH_3^+ + H_2$	1.00×10^{-11}
I7	$CH_4^+ + O \Rightarrow CH_3^+ + OH$	1.00×10^{-9}
I8	$CH_4^+ + O_2 \Rightarrow CH_4 + O_2^+$	3.90×10^{-10}
I9	$CH_3^+ + CH_4 \Rightarrow CH_4^+ + CH_3$	1.36×10^{-10}
I10	$CH_3^+ + CH_4 \Rightarrow C_2H_5^+ + H_2$	1.20×10^{-9}
I11	$CH_3^+ + CH_2 \Rightarrow C_2H_3^+ + H_2$	9.90×10^{-10}
I12	$CH_3^+ + CH \Rightarrow C_2H_2^+ + H_2$	7.10×10^{-10}
I13	$CH_3^+ + C_2H_6 \Rightarrow C_2H_5^+ + CH_4$	1.48×10^{-9}
I14	$CH_3^+ + C_2H_4 \Rightarrow C_2H_3^+ + CH_4$	3.50×10^{-10}
I15	$CH_3^+ + C_2H_3 \Rightarrow C_2H_3^+ + CH_3$	3.00×10^{-10}
I16	$CH_2^+ + CH_4 \Rightarrow CH_3^+ + CH_3$	1.38×10^{-10}
I17	$CH_2^+ + CH_4 \Rightarrow C_2H_5^+ + H$	3.90×10^{-10}
I18	$CH_2^+ + CH_4 \Rightarrow C_2H_4^+ + H_2$	8.40×10^{-10}
I19	$CH_2^+ + CH_4 \Rightarrow C_2H_3^+ + H_2 + H$	2.31×10^{-10}
I20	$CH_2^+ + CH_4 \Rightarrow C_2H_3^+ + 2H_2$	3.97×10^{-10}
I21	$CH^+ + CH_4 \Rightarrow C_2H_4^+ + H$	6.50×10^{-11}
I22	$CH^+ + CH_4 \Rightarrow C_2H_3^+ + H_2$	1.09×10^{-9}
I23	$CH^+ + CH_4 \Rightarrow C_2H_2^+ + H + H_2$	1.43×10^{-10}
I24	$CH^+ + H_2 \Rightarrow CH_2^+ + H$	1.20×10^{-9}
I25	$C_2H_6^+ + C_2H_4 \Rightarrow C_2H_4^+ + C_2H_6$	1.15×10^{-9}
I26	$C_2H_6^+ + C_2H_2 \Rightarrow C_2H_5^+ + C_2H_3$	2.47×10^{-10}
I27	$C_2H_6^+ + H \Rightarrow C_2H_5^+ + H_2$	1.00×10^{-10}
I28	$C_2H_5^+ + H \Rightarrow C_2H_4^+ + H_2$	1.00×10^{-11}
I29	$C_2H_4^+ + C_2H_3 \Rightarrow C_2H_5^+ + C_2H_2$	5.00×10^{-10}
I30	$C_2H_4^+ + C_2H_3 \Rightarrow C_2H_3^+ + C_2H_4$	5.00×10^{-10}
I31	$C_2H_4^+ + H \Rightarrow C_2H_3^+ + H_2$	3.00×10^{-10}
I32	$C_2H_4^+ + O \Rightarrow C_2H_3^+ + HCO$	1.08×10^{-10}
I33	$C_2H_3^+ + C_2H_6 \Rightarrow C_2H_5^+ + C_2H_4$	2.91×10^{-10}
I34	$C_2H_3^+ + C_2H_4 \Rightarrow C_2H_5^+ + C_2H_2$	8.90×10^{-10}
I35	$C_2H_3^+ + C_2H_3 \Rightarrow C_2H_5^+ + C_2H$	5.00×10^{-10}
I36	$C_2H_3^+ + C_2H \Rightarrow C_2H_2^+ + C_2H_2$	3.30×10^{-10}
I37	$C_2H_3^+ + H \Rightarrow C_2H_2^+ + H_2$	6.80×10^{-11}
I38	$C_2H_2^+ + CH_4 \Rightarrow C_2H_3^+ + CH_3$	4.10×10^{-9}

I39	$C_2H_2^+ + C_2H_6 \Rightarrow C_2H_5^+ + C_2H_3$	1.31×10^{-10}
I40	$C_2H_2^+ + C_2H_6 \Rightarrow C_2H_4^+ + C_2H_4$	2.48×10^{-10}
I41	$C_2H_2^+ + C_2H_4 \Rightarrow C_2H_4^+ + C_2H_2$	4.14×10^{-10}
I42	$C_2H_2^+ + C_2H_3 \Rightarrow C_2H_3^+ + C_2H_2$	3.30×10^{-10}
I43	$C_2H_2^+ + H_2 \Rightarrow C_2H_3^+ + H$	1.00×10^{-11}
I44	$O_2^+ + CH_2 \Rightarrow CH_2^+ + O_2$	4.30×10^{-10}
I45	$O_2^+ + CH \Rightarrow CH^+ + O_2$	3.10×10^{-10}
I46	$O_2^+ + C_2H_4 \Rightarrow C_2H_4^+ + O_2$	6.80×10^{-10}
I47	$O_2^+ + C_2H_2 \Rightarrow C_2H_2^+ + O_2$	1.11×10^{-9}
I48	$O_2^+ + O^- \Rightarrow O + O_2$	2.90×10^{-8}
I49	$O_2^+ + O^- \Rightarrow 3O$	2.90×10^{-8}
I50	$O^- + CH_4 \Rightarrow OH^- + CH_3$	1.00×10^{-10}
I51	$O^- + C \Rightarrow e^- + CO$	5.00×10^{-10}
I52	$O^- + H_2 \Rightarrow e^- + H_2O$	7.00×10^{-10}
I53	$O^- + H_2 \Rightarrow OH^- + H$	3.00×10^{-11}
I54	$O^- + H \Rightarrow e^- + OH$	5.00×10^{-10}
I55	$O^- + O \Rightarrow e^- + O_2$	2.30×10^{-11}
I56	$O^- + CO \Rightarrow e^- + CO_2$	6.50×10^{-10}
I57	$CO_2^+ + CH_4 \Rightarrow CH_4^+ + CO_2$	5.50×10^{-10}
I58	$CO_2^+ + C_2H_4 \Rightarrow C_2H_4^+ + CO_2$	1.50×10^{-10}
I59	$CO_2^+ + C_2H_2 \Rightarrow C_2H_2^+ + CO_2$	7.30×10^{-10}
I60	$CO_2^+ + O_2 \Rightarrow O_2^+ + CO_2$	5.30×10^{-11}
I61	$CO_2^+ + O \Rightarrow O_2^+ + CO$	1.64×10^{-10}
I62	$OH^- + CH_3 \Rightarrow e^- + CH_3OH$	1.00×10^{-9}
I63	$OH^- + CH \Rightarrow e^- + CH_2O$	5.00×10^{-10}
I64	$OH^- + C \Rightarrow e^- + HCO$	5.00×10^{-10}
I65	$OH^- + H \Rightarrow e^- + H_2O$	1.40×10^{-9}

9.3 Steam reforming of methane

Table 9.8 Neutral-neutral reactions simulated in this model at 373 K, with the corresponding rate constants adopted from NIST database. The group M for the three-body collision is made up of the background gas [193].

No.	Reaction	Rate constant (cm^3s^{-1})
N1	$CH_4 + H \Rightarrow CH_3 + H_2$	8.43×10^{-19}
N2	$CH_4 + CH \Rightarrow C_2H_4 + H$	9.74×10^{-11}
N3	$CH_4 + CH_2 \Rightarrow CH_3 + CH_3$	2.78×10^{-19}
N4	$CH_4 + C_2H \Rightarrow C_2H_2 + CH_3$	1.31×10^{-12}
N5	$CH_4 + C_2H_3 \Rightarrow C_2H_4 + CH_3$	2.28×10^{-18}
N6	$CH_4 + C_2H_5 \Rightarrow C_2H_6 + CH_3$	1.83×10^{-24}
N7	$CH_4 + C_3H_7 \Rightarrow C_3H_8 + CH_3$	4.38×10^{-24}
N8	$CH_3 + CH_3 \Rightarrow C_2H_5 + H$	2.71×10^{-19}
N9	$CH_3 + CH_3 + M \Rightarrow C_2H_6 + M$	1.56×10^{-26} (cm^6s^{-1})
N10	$CH_3 + CH_2 \Rightarrow C_2H_4 + H$	7.01×10^{-11}
N11	$CH_3 + C_2H_5 \Rightarrow C_2H_4 + CH_4$	1.91×10^{-12}
N12	$CH_3 + C_2H_5 + M \Rightarrow C_3H_8 + M$	1.93×10^{-23} (cm^6s^{-1})
N13	$CH_3 + C_2H_6 \Rightarrow C_2H_5 + CH_4$	7.21×10^{-21}
N14	$CH_3 + C_2H_4 \Rightarrow C_2H_3 + CH_4$	1.94×10^{-21}
N15	$CH_3 + C_2H_3 \Rightarrow C_2H_2 + CH_4$	6.51×10^{-13}
N16	$CH_3 + C_2H_3 + M \Rightarrow C_3H_6 + M$	4.91×10^{-30} (cm^6s^{-1})
N17	$CH_3 + C_2H_2 \Rightarrow C_2H + CH_4$	7.65×10^{-26}
N18	$CH_3 + C_3H_8 \Rightarrow C_3H_7 + CH_4$	1.02×10^{-20}
N19	$CH_3 + C_3H_7 \Rightarrow C_3H_6 + CH_4$	3.07×10^{-12}
N20	$CH_3 + H_2 \Rightarrow H + CH_4$	9.90×10^{-21}
N21	CH3 + H => CH2 + H2	9.96×10^{-22}
N22	$CH_3 + H + M \Rightarrow CH_4 + M$	2.97×10^{-28} (cm^6s^{-1})
N23	$CH_2 + CH_2 \Rightarrow C_2H_2 + 2H$	5.27×10^{-11}
N24	$CH_2 + C_2H_5 \Rightarrow C_2H_4 + CH_3$	3.01×10^{-11}
N25	$CH_2 + C_2H_3 \Rightarrow C_2H_2 + CH_3$	3.01×10^{-11}
N26	$CH_2 + C_2H \Rightarrow C_2H_2 + CH$	3.01×10^{-11}

N27	$CH_2 + C_3H_8 \Rightarrow C_3H_7 + CH_3$	1.02×10^{-20}
N28	$CH_2 + C_3H_7 \Rightarrow C_2H_4 + C_2H_5$	3.01×10^{-11}
N29	$CH_2 + C_3H_7 \Rightarrow C_3H_6 + CH_3$	3.01×10^{-12}
N30	$CH_2 + H_2 \Rightarrow CH_3 + H$	5.00×10^{-15}
N31	$CH_2 + H \Rightarrow CH + H_2$	2.01×10^{-10}
N32	$CH + C_2H_6 + M \Rightarrow C_3H_7 + M$	1.14×10^{-29} (cm^6s^{-1})
N33	$CH + C_2H_6 \Rightarrow C_3H_6 + H$	3.00×10^{-11}
N34	$CH + H_2 \Rightarrow CH_2 + H$	6.80×10^{-13}
N35	$CH + H \Rightarrow C + H_2$	1.00×10^{-10}
N36	$C + H_2 \Rightarrow CH + H$	1.50×10^{-10}
N37	$C_2H_6 + C_2H_3 \Rightarrow C_2H_5 + C_2H_4$	3.39×10^{-21}
N38	$C_2H_6 + C_2H \Rightarrow C_2H_2 + C_2H_5$	5.99×10^{-12}
N39	$C_2H_6 + C_3H_7 \Rightarrow C_3H_8 + C_2H_5$	3.16×10^{-22}
N40	$C_2H_6 + CH_2 \Rightarrow C_3H_8$	4.80×10^{-12}
N41	$C_2H_6 + H \Rightarrow C_2H_5 + H_2$	4.96×10^{-17}
N42	$C_2H_5 + C_2H_5 \Rightarrow C_2H_6 + C_2H_4$	2.41×10^{-12}
N43	$C_2H_5 + C_2H \Rightarrow C_2H_2 + C_2H_4$	3.01×10^{-12}
N44	$C_2H_5 + C_3H_8 \Rightarrow C_2H_6 + C_3H_7$	3.62×10^{-22}
N45	$C_2H_5 + C_3H_7 \Rightarrow C_2H_4 + C_3H_8$	1.91×10^{-12}
N46	$C_2H_5 + C_3H_7 \Rightarrow C_2H_6 + C_3H_6$	2.41×10^{-12}
N47	$C_2H_5 + H_2 \Rightarrow C_2H_6 + H$	2.91×10^{-21}
N48	$C_2H_5 + H \Rightarrow CH_3 + CH_3$	5.99×10^{-11}
N49	$C_2H_5 + H \Rightarrow C_2H_4 + H_2$	3.01×10^{-12}
N50	$C_2H_5 + H \Rightarrow C_2H_6$	5.99×10^{-11}
N51	$C_2H_5 + C_2H_4 \Rightarrow C_3H_6 + CH_3$	3.82×10^{-17}
N52	$C_2H_4 \Rightarrow C_2H_2 + H_2$	1.40×10^{-27}
N53	$C_2H_4 + C_2H \Rightarrow C_2H_2 + C_2H_3$	1.40×10^{-10}
N54	$C_2H_4 + H \Rightarrow C_2H_3 + H_2$	6.70×10^{-05}
N55	$C_2H_4 + H \Rightarrow C_2H_5$	1.30×10^{-12}
N56	$C_2H_4 + H_2 + M \Rightarrow C_2H_6 + M$	6.86×10^{-36} (cm^6s^{-1})
N57	$C_2H_3 + C_2H_3 \Rightarrow C_2H_4 + H_2$	1.90×10^{-12}
N58	$C_2H_3 + C_2H \Rightarrow C_2H_2 + C_2H_2$	1.90×10^{-12}
N59	$C_2H_3 + C_3H_8 \Rightarrow C_2H_4 + C_3H_7$	3.40×10^{-20}

N60	$C_2H_3 + C_3H_7 => C_3H_8 + C_2H_2$	2.01×10^{-12}
N61	$C_2H_3 + C_3H_7 => C_3H_6 + C_2H_4$	2.01×10^{-12}
N62	$C_2H_3 + H_2 => C_2H_4 + H$	9.78×10^{-20}
N63	$C_2H_3 + H => C_2H_2 + H_2$	2.01×10^{-11}
N64	$C_2H_3 + H + M => C_2H_4 + M$	8.26×10^{-30} (cm^6s^{-1})
N65	$C_2H_2 + H => C_2H + H_2$	6.12×10^{-27}
N66	$C_2H_2 + H + M => C_2H_3 + M$	2.81×10^{-31} (cm^6s^{-1})
N67	$C_2H + C_3H_8 => C_2H_2 + C_3H_7$	5.99×10^{-12}
N68	$C_2H + C_3H_7 => C_3H_6 + C_2H_2$	1.00×10^{-11}
N69	$C_2H + H_2 => C_2H_2 + H$	1.52×10^{-13}
N70	$C_2H + H + M => C_2H_2 + M$	9.44×10^{-30} (cm^6s^{-1})
N71	$C_3H_8 + H => C_3H_7 + H_2$	5.15×10^{-17}
N72	$C_3H_7 + C_3H_7 => C_3H_6 + C_3H_8$	2.81×10^{-12}
N73	$C_3H_7 + H_2 => C_3H_8 + H$	7.12×10^{-21}
N74	$C_3H_7 + H => C_3H_6 + H_2$	3.01×10^{-12}
N75	C3H7 + H => C3H8	9.68×10^{-11}
N76	$C_3H_6 + H + M => C_3H_7 + M$	3.79×10^{-33} (cm^6s^{-1})
N77	$H + H + M => H_2 + M$	6.00×10^{-33} (cm^6s^{-1})
N78	$O + O + M => O_2 + M$	7.19×10^{-33} (cm^6s^{-1})
N79	$CH_4 + O => CH_3 + OH$	5.54×10^{-18}
N80	$CH_3 + O => CH_2O + H$	1.12×10^{-10}
N81	$CH_3 + O => CO + H_2 + H$	2.80×10^{-11}
N82	$CH_2 + O => CO + H_2$	5.53×10^{-11}
N83	$CH_2 + O => CO + 2H$	8.29×10^{-11}
N84	$CH_2 + O_2 => CO_2 + H_2$	1.42×10^{-12}
N85	$CH_2 + O_2 => CO + H_2O$	1.42×10^{-12}
N86	$CH_2 + O_2 => CH_2O + O$	5.39×10^{-13}
N87	$CH + O => CO + H$	6.90×10^{-11}
N88	$CH + O_2 => CO_2 + H$	1.20×10^{-11}
N89	$CH + O_2 => CO + OH$	8.00×10^{-12}
N90	$CH + O_2 => HCO + O$	8.00×10^{-12}
N91	$CH + O_2 => CO + H + O$	1.20×10^{-11}
N92	$C + O_2 => CO + O$	2.45×10^{-13}

N93	$C_2H_6 + O \Rightarrow C_2H_5 + OH$	5.11×10^{-16}
N94	$C_2H_5 + O \Rightarrow CH_3HCO + H$	8.80×10^{-11}
N95	$C_2H_5 + O \Rightarrow CH_2O + CH_3$	6.90×10^{-11}
N96	$C_2H_5 + O \Rightarrow C_2H_4 + OH$	4.40×10^{-11}
N97	$C_2H_5 + O_2 \Rightarrow C_2H_4 + HO_2$	3.80×10^{-15}
N98	$C_2H_4 + O \Rightarrow CH_2HCO + H$	2.63×10^{-13}
N99	$C_2H_4 + O \Rightarrow HCO + CH_3$	4.51×10^{-13}
N100	$C_2H_3 + O \Rightarrow C_2H_2 + OH$	1.25×10^{-11}
N101	$C_2H_3 + O \Rightarrow CO + CH_3$	1.25×10^{-11}
N102	$C_2H_3 + O \Rightarrow HCO + CH_2$	1.25×10^{-11}
N103	$C_2H_3 + O \Rightarrow CH_2CO + H$	1.25×10^{-11}
N104	$C_2H_3 + O_2 \Rightarrow CH_2O + HCO$	9.00×10^{-11}
N105	$C_2H_2 + O \Rightarrow CH_2 + CO$	6.75×10^{-14}
N106	$C_2H_2 + O \Rightarrow C_2HO + H$	6.75×10^{-14}
N107	$C_2H + O \Rightarrow CH + CO$	1.70×10^{-11}
N108	$C_2H + O_2 \Rightarrow HCO + CO$	3.00×10^{-11}
N109	$C_2H + O_2 \Rightarrow C_2HO + O$	1.00×10^{-12}
N110	$C_3H_8 + O \Rightarrow C_3H_7 + OH$	2.73×10^{-15}
N111	$H_2 + O \Rightarrow OH + H$	9.32×10^{-18}
N112	$H + O + CH_4 \Rightarrow OH + CH_4$	4.33×10^{-32} (cm^6s^{-1})
N113	$H + O_2 \Rightarrow OH + O$	1.87×10^{-22}
N114	$H + O_2 + CH_4 \Rightarrow HO_2 + CH_4$	5.40×10^{-32} (cm^6s^{-1})
N115	$CH_4 + OH \Rightarrow CH_3 + H_2O$	6.62×10^{-15}
N116	$CH_4 + HO_2 \Rightarrow CH_3 + H_2O_2$	8.76×10^{-27}
N117	$CH_4 + HCO \Rightarrow CH_3 + CH_2O$	6.07×10^{-30}
N118	$CH_4 + CH_3O \Rightarrow CH_3OH + CH_3$	9.42×10^{-20}
N119	$CH_3 + CO + CH_4 \Rightarrow CH_3CO + CH_4$	4.19×10^{-36} (cm^6s^{-1})
N120	$CH_3 + H_2O \Rightarrow CH_4 + OH$	1.82×10^{-25}
N121	$CH_3 + OH \Rightarrow CH_2 + H_2O$	1.13×10^{-12}
N122	$CH_3 + OH \Rightarrow CH_2OH + H$	1.32×10^{-11}
N123	$CH_3 + OH \Rightarrow CH_3O + H$	1.90×10^{-10}
N124	$CH_3 + OH \Rightarrow CH_3OH$	2.30×10^{-27}
N125	$CH_3 + HO_2 \Rightarrow CH_3O + OH$	3.00×10^{-11}

N126	$CH_3 + HO_2 => CH_4 + O_2$	5.99×10^{-12}
N127	$CH_3 + CH_2O => CH_4 + HCO$	6.14×10^{-18}
N128	$CH_3 + HCO => CH_4 + CO$	2.00×10^{-10}
N129	$CH_3 + CH_3O => CH_4 + CH_2O$	4.00×10^{-11}
N130	$CH_3 + CH_3CHO => CH_4 + CH_3CO$	4.95×10^{-18}
N131	$CH_2 + CO_2 => CH_2O + CO$	3.90×10^{-14}
N132	$CH_2 + H_2O => CH_3 + OH$	1.90×10^{-16}
N133	$CH_2 + OH => CH_2O + H$	3.00×10^{-11}
N134	$CH_2 + HO_2 => CH_2O + OH$	3.00×10^{-11}
N135	$CH_2 + CH_2O => CH_3 + HCO$	1.00×10^{-14}
N136	$CH_2 + HCO => CH_3 + CO$	3.00×10^{-11}
N137	$CH_2 + CH_3O => CH_3 + CH_2O$	3.00×10^{-11}
N138	$CH + CO_2 => 2CO + H$	9.68×10^{-13}
N139	$CH + CO_2 => HCO + CO$	9.68×10^{-13}
N140	$CH + CO => C_2HO$	4.04×10^{-30}
N141	$C_2H_6 + OH => C_2H_5 + H_2O$	2.46×10^{-13}
N142	$C_2H_6 + HO_2 => C_2H_5 + H_2O_2$	6.36×10^{-24}
N143	$C_2H_6 + HCO => C_2H_5 + CH_2O$	2.19×10^{-26}
N144	$C_2H_6 + CH_3O => C_2H_5 + CH_3OH$	2.72×10^{-18}
N145	$C_2H_5 + OH => C_2H_4 + H_2O$	4.00×10^{-11}
N146	$C_2H_5 + HO_2 => C_2H_6 + O_2$	5.00×10^{-13}
N147	$C_2H_5 + HO_2 => C_2H_4 + H_2O_2$	5.00×10^{-13}
N148	$C_2H_5 + CH_2O => C_2H_6 + HCO$	4.47×10^{-18}
N149	$C_2H_5 + HCO => C_2H_6 + CO$	2.00×10^{-10}
N150	$C_2H_5 + CH_3O => C_2H_6 + CH_2O$	4.00×10^{-11}
N151	$C_2H_4 + OH => C_2H_3 + H_2O$	1.54×10^{-16}
N152	$C_2H_4 + HO_2 => CH_3CHO + OH$	1.62×10^{-20}
N153	$C_2H_3 + H_2O => C_2H_4 + OH$	1.82×10^{-25}
N154	$C_2H_3 + OH => C_2H_2 + H_2O$	5.00×10^{-11}
N155	$C_2H_3 + CH_2O => C_2H_4 + HCO$	4.41×10^{-18}
N156	$C_2H_3 + HCO => C_2H_4 + CO$	1.50×10^{-10}
N157	$C_2H_3 + CH_3O => C_2H_4 + CH_2O$	4.00×10^{-11}
N158	$C_2H_2 + OH => C_2H + H_2O$	1.77×10^{-22}

N159	$C_2H_2 + HO_2 => CH_2CO + OH$	1.62×10^{-20}
N160	$C_2H + OH => CH_2 + CO$	3.00×10^{-11}
N161	$C_2H + OH => C_2H_2 + O$	3.00×10^{-11}
N162	$C_2H + HO_2 => C_2H_2 + O_2$	3.00×10^{-11}
N163	$C_2H + HO_2 => C_2HO + OH$	3.00×10^{-11}
N164	$C_2H + HCO => C_2H_2 + CO$	1.00×10^{-10}
N165	$C_2H + CH_3O => C_2H_2 + CH_2O$	4.00×10^{-11}
N166	$C_3H_8 + OH => C_3H_7 + H_2O$	3.76×10^{-15}
N167	$C_3H_8 + CH_3O => C_3H_7 + CH_3OH$	1.42×10^{-17}
N168	$C_3H_7 + CH_2O => C_3H_8 + HCO$	4.10×10^{-18}
N169	$C_3H_7 + HCO => C_3H_8 + CO$	1.00×10^{-10}
N170	$C_3H_7 + CH_3O => C_3H_8 + CH_2O$	4.00×10^{-11}
N171	$H_2 + OH => H + H_2O$	7.02×10^{-15}
N172	$H_2 + HCO => H + CH_2O$	2.78×10^{-26}
N173	$H + CO_2 => CO + OH$	1.40×10^{-29}
N174	$H + CO + M => HCO + M$	1.54×10^{-34}
N175	$H + H_2O => H_2 + OH$	5.86×10^{-26}
N176	$H + OH => H_2 + O$	1.05×10^{-16}
N177	$H + OH + M => H_2O + M$	4.33×10^{-30}
N178	$H + HO_2 => H_2 + O_2$	5.90×10^{-12}
N179	$H + HO_2 => H_2O + O$	2.40×10^{-12}
N180	$H + HO_2 => OH + OH$	7.20×10^{-11}
N181	$H + CH_2O => H_2 + HCO$	5.72×10^{-14}
N182	$H + CH_2O => H_2 + HCO$	3.86×10^{-14}
N183	$H + HCO => H_2 + CO$	1.50×10^{-10}
N184	$H + CH_3O => H_2 + CH_2O$	2.32×10^{-11}
N185	$H + CH_3O => CH_3 + OH$	9.93×10^{-12}
N186	$H + CH_3CHO => H_2 + CH_3CO$	8.98×10^{-14}
N187	$H + CH_2CO => CH_3 + CO$	1.04×10^{-13}
N188	$H + C_2HO => CH_2 + CO$	2.50×10^{-10}
N189	$CO + O + M => CO_2 + M$	1.11×10^{-35}
N190	$O + H_2O => OH + OH$	4.48×10^{-24}
N191	$O + OH => H + O_2$	3.46×10^{-11}

N192	$O + HO_2 => O_2 + OH$	5.70×10^{-11}
N193	$O + CH_2O => OH + HCO$	1.73×10^{-13}
N194	$O + HCO => CO + OH$	5.00×10^{-11}
N195	$O + HCO => H + CO_2$	5.00×10^{-11}
N196	$O + CH_3O => CH_3 + O_2$	2.20×10^{-11}
N197	$O + CH_3O => OH + CH_2O$	3.00×10^{-12}
N198	$O + CH_3CHO => OH + CH_3CO$	4.68×10^{-13}
N199	$O + CH_2CO => CH_2 + CO_2$	2.29×10^{-13}
N200	$O + CH_2CO => CH_2O + CO$	7.88×10^{-14}
N201	$O + CH_2CO => HCO + CO + H$	4.33×10^{-14}
N202	$O + CH_2CO => 2HCO$	4.33×10^{-14}
N203	$O + C_2HO => 2CO + H$	1.90×10^{-10}
N204	$O_2 + HCO => CO + HO_2$	5.10×10^{-12}
N205	$O_2 + CH_3O => CH_2O + HO_2$	1.97×10^{-15}
N206	$O_2 + CH_2CHO => CH_2O + CO + OH$	3.00×10^{-14}
N207	$O_2 + C_2HO => 2CO + OH$	6.46×10^{-13}
N208	$CO + OH => CO_2 + H$	1.25×10^{-13}
N209	$CO + CH_3O => CO_2 + CH_3$	6.56×10^{-20}
N210	$H_2O + CH_3O => CH_3OH + OH$	1.67×10^{-14}
N211	$OH + OH => H_2O + O$	1.47×10^{-12}
N212	$OH + OH + M => H_2O_2 + M$	6.86×10^{-31}
N213	$OH + HO_2 => O_2 + H_2O$	1.10×10^{-10}
N214	$OH + CH_2O => H_2O + HCO$	8.47×10^{-12}
N215	$OH + HCO => CO + H_2O$	1.70×10^{-10}
N216	$OH + CH_3O => CH_2O + H_2O$	3.00×10^{-11}
N217	$OH + CH_3CHO => CH_3CO + H_2O$	1.49×10^{-11}
N218	$OH + CH_2CO => CO + CH_2OH$	1.14×10^{-11}
N219	$2HO_2 => H_2O_2 + O_2$	1.63×10^{-12}
N220	$HO_2 + CH_2O => H_2O_2 + HCO$	1.05×10^{-20}
N221	$HO_2 + HCO => OH + H + CO_2$	5.00×10^{-11}
N222	$HO_2 + CH_3O => CH_2O + H_2O_2$	5.00×10^{-13}
N223	$CH_2O + CH_3O => CH_3OH + HCO$	1.14×10^{-15}
N224	$2HCO => CH_2O + CO$	5.00×10^{-11}

N225	$2CH_3O \Rightarrow CH_2O + CH_3OH$	1.00×10^{-10}
N226	$CH_4 + CH_3CO \Rightarrow CH_3CHO + CH_3$	1.14×10^{-29}
N227	$CH_4 + CH_2OH \Rightarrow CH_3OH + CH_3$	2.55×10^{-27}
N228	$CH_3 + H_2O_2 \Rightarrow CH_4 + HO_2$	5.46×10^{-14}
N229	$CH_3 + CH_3OH \Rightarrow CH_4 + CH_3O$	1.01×10^{-20}
N230	$CH_3 + CH_3OH \Rightarrow CH_4 + CH_2OH$	2.66×10^{-20}
N231	$CH_3 + CH_2OH \Rightarrow CH_4 + CH_2O$	4.00×10^{-12}
N232	$CH_2 + H_2O_2 \Rightarrow CH_3 + HO_2$	1.00×10^{-14}
N233	$CH_2 + CH_3CO \Rightarrow CH_2CO + CH_3$	3.00×10^{-11}
N234	$CH_2 + CH_3OH \Rightarrow CH_3O + CH_3$	1.01×10^{-20}
N235	$CH_2 + CH_3OH \Rightarrow CH_2OH + CH_3$	2.66×10^{-20}
N236	$CH_2 + CH_2OH \Rightarrow CH_2O + CH_3$	2.00×10^{-12}
N237	$CH_2 + CH_2OH \Rightarrow C_2H_4 + OH$	4.00×10^{-11}
N238	$C_2H_5 + H_2O_2 \Rightarrow C_2H_6 + HO_2$	2.83×10^{-15}
N239	$C_2H_5 + CH_3OH \Rightarrow C_2H_6 + CH_3O$	3.50×10^{-22}
N240	$C_2H_5 + CH_3OH \Rightarrow C_2H_6 + CH_2OH$	9.49×10^{-22}
N241	$C_2H_5 + CH_2OH \Rightarrow C_2H_6 + CH_2O$	4.00×10^{-12}
N242	$C_2H_5 + CH_2OH \Rightarrow CH_3OH + C_2H_4$	4.00×10^{-12}
N243	$C_2H_3 + H_2O_2 \Rightarrow C_2H_4 + HO_2$	5.46×10^{-14}
N244	$C_2H_3 + CH_3OH \Rightarrow C_2H_4 + CH_3O$	1.01×10^{-20}
N245	$C_2H_3 + CH_3OH \Rightarrow C_2H_4 + CH_2OH$	2.66×10^{-20}
N246	$C_2H_3 + CH_2OH \Rightarrow C_2H_4 + CH_2O$	5.00×10^{-11}
N247	$C_2H_2 + CH_2OH \Rightarrow C_2H_3 + CH_2O$	3.32×10^{-19}
N248	$C_2H + CH_3OH \Rightarrow C_2H_2 + CH_3O$	2.00×10^{-12}
N249	$C_2H + CH_3OH \Rightarrow C_2H_2 + CH_2OH$	1.00×10^{-11}
N250	$C_2H + CH_2OH \Rightarrow C_2H_2 + CH_2O$	5.99×10^{-11}
N251	$C_3H_7 + OH \Rightarrow C_3H_6 + H_2O$	4.00×10^{-11}
N252	$C_3H_7 + H_2O_2 \Rightarrow C_3H_8 + HO_2$	7.08×10^{-17}
N253	$C_3H_7 + CH_3OH \Rightarrow C_3H_8 + CH_3O$	3.51×10^{-22}
N254	$C_3H_7 + CH_3OH \Rightarrow C_3H_8 + CH_2OH$	8.45×10^{-22}
N255	$C_3H_7 + CH_2OH \Rightarrow C_3H_8 + CH_2O$	1.90×10^{-12}
N256	$C_3H_7 + CH_2OH \Rightarrow C_3H_6 + CH_3OH$	8.00×10^{-13}
N257	$H + H_2O_2 \Rightarrow H_2O + OH$	4.20×10^{-14}

N258	$H + H_2O_2 => H_2 + HO_2$	5.15×10^{-15}
N259	$H + CH_3OH => CH_2OH + H_2$	1.27×10^{-15}
N260	$H + CH_3OH => CH_3O + H_2$	3.18×10^{-16}
N261	$H + CH_2OH => CH_2O + H_2$	1.00×10^{-11}
N262	$H + CH_2OH => CH_3 + OH$	1.90×10^{-10}
N263	$H + CH_2OH + M => CH_3OH + M$	1.18×10^{-29}
N264	$O + H_2O_2 => HO_2 + OH$	8.91×10^{-16}
N265	$O + H_2O_2 => O_2 + H_2O$	8.91×10^{-16}
N266	$O + CH_3CO => OH + CH_2CO$	8.75×10^{-11}
N267	$O + CH_3CO => CO_2 + CH_3$	2.63×10^{-10}
N268	$O + CH_3OH => OH + CH_2OH$	1.12×10^{-14}
N269	$O + CH_3OH => OH + CH_3O$	1.68×10^{-15}
N270	$O + CH_2OH => CH_2O + OH$	7.00×10^{-11}
N271	$O_2 + CH_2OH => CH_2O + HO_2$	9.70×10^{-12}
N272	$OH + H_2O_2 => HO2 + H_2O$	1.70×10^{-12}
N273	$OH + CH_3CO => CH_2CO + H_2O$	2.00×10^{-11}
N274	$OH + CH_3CO => CH_3 + CO + OH$	5.00×10^{-11}
N275	$OH + CH_3OH => H_2O + CH_2OH$	7.67×10^{-13}
N276	$OH + CH_3OH => H_2O + CH_3O$	1.35×10^{-13}
N277	$OH + CH_2OH => CH_2O + H_2O$	4.00×10^{-11}
N278	$HO_2 + CH_3CO => CH_3 + CO_2 + OH$	5.00×10^{-11}
N279	$HO_2 + CH_3OH => CH_2OH + H_2O_2$	1.10×10^{-22}
N280	$HO_2 + CH_2OH => CH_2O + H_2O_2$	2.00×10^{-11}
N281	$CH_2O + CH_3CO => CH_3CHO + HCO$	1.17×10^{-22}
N282	$CH_2O + CH_2OH => CH_3OH + HCO$	4.22×10^{-18}
N283	$HCO + H_2O_2 => CH_2O + HO_2$	1.50×10^{-18}
N284	$HCO + CH_3CO => CH_3CHO + CO$	1.50×10^{-11}
N285	$HCO + CH_3OH => CH_2O + CH_2OH$	6.85×10^{-23}
N286	$HCO + CH_2OH => 2CH_2O$	3.00×10^{-10}
N287	HCO + CH2OH => CH3OH + CO	2.00×10^{-10}
N288	$CH_3O + CH_3CO => CH_3OH + CH_2CO$	1.00×10^{-11}
N289	$CH_3O + CH_2OH => CH_2O + CH_3OH$	4.00×10^{-11}
N290	$H_2O_2 + CH_3CO => CH_3CHO + HO_2$	3.05×10^{-19}

N291	$H_2O_2 + CH_2OH => CH_3OH + HO_2$	6.56×10^{-17}
N292	$CH_3CO + CH_3OH => CH_3CHO + CH_2OH$	2.22×10^{-22}
N293	$2CH_2OH => CH_2O + CH_3OH$	8.00×10^{-12}
N294	$C_3H_5 + O_2 => CH_3CHO + HCO$	7.21×10^{-12}
N295	$HCO + CH_3CO => CH_3CHO + CO$	1.50×10^{-11}
N296	$CH_3CHOH + O => CH_3CHO + OH$	1.50×10^{-10}
N297	$CH_3CHOH + O_2 => CH_3CHO + HO_2$	1.90×10^{-11}
N298	$CH_3 + HCO => CH_3CHO$	4.42×10^{-11}
N299	$CH + O_2 => HCO + O$	1.45×10^{-10}
N300	$C_2H_3 + O_2 => CH_2O + HCO$	2.62×10^{-12}
N301	$C_2H + O_2 => CO + HCO$	4.00×10^{-12}
N302	$CH_2O + O => HCO + OH$	1.67×10^{-13}
N303	$CH_2O + H => H_2 + HCO$	5.52×10^{-14}
N304	$CH_2O + OH => HCO + H_2O$	9.38×10^{-12}
N305	$CH_2O + HO_2 => HCO + H_2O_2$	2.52×10^{-18}
N306	$CH_2O + CH_3 => HCO + CH_4$	6.14×10^{-18}
N307	$HCO + CH_2 => CO + CH_3$	3.01×10^{-11}
N308	$HCO + O => CO + OH$	5.00×10^{-11}
N309	$HCO + O => CO_2 + H$	5.00×10^{-11}
N310	$HCO + H => CO + H2$	1.13×10^{-10}
N311	$HCO + O_2 => CO + HO_2$	5.20×10^{-12}
N312	$HCO + OH => CO + H_2O$	1.83×10^{-10}
N313	$HCO => CO + H$	3.35×10^{-22}
N314	$HCO + CH_3 => CO + CH_4$	4.00×10^{-11}
N315	$CH_3 + O_2 => CH_3O_2$	2.21×10^{-12}
N316	$CH_4 + O_2 => CH_3O_2 + H$	3.80×10^{-76}
N317	$CH_3CO + O_2 => CH_3COOO$	5.00×10^{-12}
N318	$C_2H_5 + O_2 => C_2H_5OO$	1.50×10^{-28}
N319	$CH_3CHO + O_2 => CH_3COOOH$	5.16×10^{-23}
N320	$CH_3CHO + CH_3COOO => CH_3COOOH + CH_3CO$	1.34×10^{-17}
N321	$CH_3CHO + OH => CH_3COOH + H$	2.00×10^{-21}
N322	$CH_3O_2 + CH_3COOO => CH_3COOH + CH_2O + O_2$	5.50×10^{-12}
N323	$CH_3COOOH + C_3H_6 => CH_3COOH + C_3H_6O$	3.85×10^{-14}

N324	$CO + OH \Rightarrow COOH$	1.20×10^{-12}
N325	$CH_3 + COOH \Rightarrow CH_3COOH$	5.81×10^{-10}
N326	$CH_3CO + O \Rightarrow CH3COO$	1.99×10^{-10}
N327	$CH_3COO + H \Rightarrow CH_3COOH$	3.79×10^{-11}
N328	$C_2H_5 + OH \Rightarrow C_2H_5OH$	1.28×10^{-10}
N329	$2C_2H_5OO \Rightarrow C_2H_5OH + CH_3CHO + O_2$	2.34×10^{-14}
N330	$CH_3CHOH + H \Rightarrow C_2H_5OH$	8.30×10^{-11}
N331	$CH_2O + OH \Rightarrow HCOOH + H$	2.01×10^{-13}
N332	$CH_3CHO + H \Rightarrow CH_3CHOH$	2.49×10^{-18}
N333	$C_2H_5OH + O \Rightarrow CH_3CHOH + OH$	1.03×10^{-13}
N334	$C_2H_5OH + OH \Rightarrow CH_3CHOH + H_2O$	5.00×10^{-13}
N335	$C_2H_5OH + CH_3 \Rightarrow CH_4 + CH_3CHOH$	2.79×10^{-56}
N336	$CH_3 + CH_3CO \Rightarrow CH_3COCH_3$	6.97×10^{-20}
N337	$CH_3COCH_3 + O \Rightarrow CH_3COCH_2 + OH$	1.13×10^{-15}
N338	$CH_3COCH_3 + OH \Rightarrow CH_3COCH_2 + H_2O$	2.20×10^{-13}
N339	$CH_3COCH_3 + H \Rightarrow CH_3COCH_2 + H_2$	6.70×10^{-16}
N340	$CH_3COCH_3 + HO_2 \Rightarrow CH_3COCH_2 + H_2O_2$	3.49×10^{-16}
N341	$CH_3COCH_3 + CH_3 \Rightarrow CH_3COCH_2 + CH_4$	5.56×10^{-20}
N342	$C_3H_7 + CH_3 \Rightarrow C_4H_{10}$	7.02×10^{-21}
N343	$CH_3OH + C_4H_9 \Rightarrow C_4H_{10} + CH_2OH$	7.98×10^{-22}
N344	$CH_4 + C_4H_9 \Rightarrow C_4H_{10} + CH_3$	8.82×10^{-23}
N345	$CH_2O + C_4H_9 \Rightarrow C_4H_{10} + HCO$	9.23×10^{-18}
N346	$C_2H_4 + C_2H_5 \Rightarrow C_4H_9$	9.58×10^{-19}
N347	$C_2H_5 + C_2H_5 \Rightarrow C_4H_{10}$	1.66×10^{-11}
N348	$C_4H_9 + H \Rightarrow C_4H_{10}$	4.26×10^{-11}
N349	$D + CH_2 \Rightarrow CHD + H$	1.83×10^{-10}
N350	$HD + D \Rightarrow HD + D$	6.80×10^{-16}
N351	$HD + D \Rightarrow D_2 + H$	3.66×10^{-15}
N352	$CHD_2 + D \Rightarrow CD_3 + H$	1.91×10^{-10}
N353	$CH_2D + D \Rightarrow CHD_2 + H$	2.09×10^{-10}
N354	$O_2 + D \Rightarrow DO_2$	2.42×10^{-11}
N355	$O_2 + D \Rightarrow OD + O$	1.06×10^{-18}
N356	$D_2 + D \Rightarrow D_2 + D$	1.83×10^{-16}

N357	$COD_3 + D => CD_2O + D_2$	3.16×10^{-11}
N358	$CD_2OD + D => COD_3 + D$	7.97×10^{-11}
N359	$OH + D => H + OD$	4.54×10^{-11}
N360	$C_2H_3D + D => C_2H_2D_2 + H$	1.90×10^{-12}
N361	$HCO + D => HD + CO$	1.38×10^{-10}
N362	$CH_3 + D => CH_2D + H$	2.31×10^{-10}
N363	$CH_3 + D => CH_3D$	2.10×10^{-10}
N364	$CH_3O + D => CH_2O + HD$	3.65×10^{-11}
N365	$CD_2O + D => D_2 + DCO$	2.46×10^{-12}
N366	$C_2D_6 + D => D_2 + C_2D_5$	1.61×10^{-19}
N367	$CD_3CDO + D => D_2 + COD_3C$	3.20×10^{-14}
N368	$H_2 + D => H + HD$	5.04×10^{-15}
N369	$C_2D_2 + D => C_2D_3$	8.03×10^{-13}
N370	$C_2D_4 + D => C_2D_5$	2.16×10^{-12}
N371	$CH_3CHO + D => C_2H_4OD$	4.93×10^{-17}
N372	$CH_3CHO + D => HD + CH_3CO$	2.39×10^{-13}
N373	$C_2H_2 + D => C_2HD + H$	8.34×10^{-13}
N374	$C_2H_2 + D => C_2H + HD$	5.06×10^{-20}
N375	$C_2H_4 + D => C_2H_4D$	2.27×10^{-12}
N376	$C_2H_6 + D => C_2H_5 + HD$	3.13×10^{-16}
N377	$CH_4 + D => CH_3 + HD$	2.51×10^{-17}
N378	$CH_3OH + D => HD + CH_2OH$	1.94×10^{-15}
N379	$CH_2O + D => HCO + HD$	1.72×10^{-13}
N380	$CH_2O + D => CHDO + H$	8.78×10^{-14}
N381	$D_2 + O => OD + D$	2.99×10^{-17}
N382	$D + D => D_2$	5.00×10^{-16}
N383	$D_2 + CD => CD_2 + D$	1.39×10^{-11}
N384	$D_2 + OD => D_2O + D$	1.19×10^{-14}
N385	$D_2 + H => HD + D$	7.25×10^{-16}
N386	$D_2 + OH => HDO + D$	8.97×10^{-15}
N387	$D_2 + CH => CD + HD$	9.18×10^{-11}
N388	$D_2 + CH_3 => CH_3D + D$	2.09×10^{-19}
N389	$D_2 + C_2H => C_2HD + D$	5.35×10^{-13}

N390	$D_2 + C_2H_5 \Rightarrow C_2H_5D + D$	1.82×10^{-20}
N391	$CH_3D + OH \Rightarrow CH_2D + H_2O$	2.09×10^{-14}
N392	$CH_3D + CD_3 \Rightarrow CD_4 + CH_3$	2.47×10^{-21}
N393	$CH_2D_2 + OH \Rightarrow CHD_2 + H_2O$	1.04×10^{-14}
N394	$CHD_3 + OH \Rightarrow CD_3 + H_2O$	1.95×10^{-15}
N395	$CD_4 + O \Rightarrow CD_3 + OD$	1.69×10^{-17}
N396	$CD_4 + OH \Rightarrow CD_3 + HDO$	8.63×10^{-16}
N397	$CD_4 + C_2H \Rightarrow CD_3 + C_2HD$	1.82×10^{-12}
N398	$CD_3 + COD_3C \Rightarrow CO + C_2D_6$	8.63×10^{-11}
N399	$CD_3 + HD \Rightarrow CD_4 + H$	6.71×10^{-18}
N400	$CD_3 + CD_3 \Rightarrow C_2D_6$	5.25×10^{-11}
N401	$COD_3H + CD_3 \Rightarrow CHD_3 + COD_3$	5.59×10^{-19}
N402	$CD_2 + CD_2 \Rightarrow C_2D_4$	2.01×10^{-12}
N403	$CD + D_2O \Rightarrow CD_2O + D$	1.71×10^{-11}
N404	$CD + O_2 \Rightarrow CO + OD$	3.60×10^{-11}
N405	$CD + O_2 \Rightarrow CO_2 + D$	3.60×10^{-11}
N406	$CD + H_2O \Rightarrow CHDO + H$	1.47×10^{-11}
N407	$CD + H_2O \Rightarrow CH_2O + D$	1.38×10^{-11}
N408	$C_2D_6 + C_2H \Rightarrow C_2HD + C_2D_5$	3.11×10^{-12}
N409	$C_2D_5 + C_2D_5 \Rightarrow C_2D_4 + C_2D_6$	2.08×10^{-12}
N410	$C_2D_4 + O \Rightarrow CD_3 + DCO$	1.26×10^{-12}
N411	$C_2D_4 + H \Rightarrow C_2HD_4$	2.50×10^{-12}
N412	$C_2D_2 + O \Rightarrow CO + CD_2$	1.43×10^{-13}
N413	$C_2D_2 + H \Rightarrow C_2HD_2$	9.14×10^{-13}
N414	$C_2D_2 + OH \Rightarrow C_2D + HDO$	1.30×10^{-13}
N415	$C_2D + H_2 \Rightarrow C_2HD + H$	7.02×10^{-13}
N416	$C_2D + O_2 \Rightarrow DCO + CO$	2.94×10^{-11}
N417	$C_2H + HD \Rightarrow C_2HD + H$	1.89×10^{-13}
N418	$C_2D_6 + OH \Rightarrow HDO + C_2D_5$	1.61×10^{-13}
N419	$C + D_2 \Rightarrow CD + D$	1.13×10^{-10}
N420	$COD_3 + O_2 \Rightarrow CD_2O + DO_2$	7.97×10^{-18}
N421	$OD + OD \Rightarrow D_2O + O$	4.01×10^{-13}
N422	$OD + DO_2 \Rightarrow O_2 + D_2O$	3.80×10^{-11}

N423	$H_2O + OD \Rightarrow OH + HDO$	1.33×10^{-14}
N424	$H_2O_2 + OD \Rightarrow OH + HDO_2$	2.01×10^{-15}
N425	$H_2O_2 + OD \Rightarrow HO_2 + HDO$	1.79×10^{-12}
N426	$D_2O_2 + OD \Rightarrow D_2O + DO_2$	7.43×10^{-13}
N427	$OH + OD \Rightarrow HDO + O$	1.50×10^{-12}
N428	$H_2 + OD \Rightarrow H + HDO$	6.14×10^{-15}
N429	$CO + OD \Rightarrow CO_2 + D$	1.15×10^{-13}
N430	$C_2H_6 + OD \Rightarrow C_2H_5 + HDO$	2.74×10^{-13}
N431	$CH_4 + OD \Rightarrow CH_3 + HDO$	2.52×10^{-14}
N432	$HD + O \Rightarrow H + OD$	1.35×10^{-17}
N433	$OH + D_2O \Rightarrow OD + HDO$	4.70×10^{-10}
N434	$O_2 + DCO \Rightarrow CO + DO_2$	5.11×10^{-12}
N435	$OH + HD \Rightarrow H + HDO$	7.00×10^{-15}
N436	$OH + D_2O_2 \Rightarrow DO_2 + HDO$	5.30×10^{-13}
N437	$DO_2 + DO_2 \Rightarrow D_2O_2 + O_2$	4.68×10^{-13}
N438	$HD + O \Rightarrow OH + D$	3.63×10^{-17}
N439	$H + HD \Rightarrow H_2 + D$	5.76×10^{-16}
N440	$OH + HD \Rightarrow H_2O + D$	1.65×10^{-14}
N441	$CH_3 + HD \Rightarrow CH_4 + D$	1.01×10^{-17}
N442	$C_2H + HD \Rightarrow C_2H_2 + D$	3.03×10^{-13}

Table 9.9 Electron-impact reactions simulated in the model. All the reaction rates for these reactions are depend on the cross section of each particle and instantaneous electron temperature [186,191,192].

No.	**Reaction**		**Rate constant**
E1	$e^- + CH_4 \Rightarrow CH_3 + H^-$	Dissociative Attachment	$f(\sigma), \varepsilon$
E2	$e^- + CH_4 \Rightarrow CH_2^- + H_2$	Dissociative Attachment	$f(\sigma), \varepsilon$
E3	$e^- + CH_4 \Rightarrow e^- + CH_4$	Momentum Transfer	$f(\sigma), \varepsilon$
E4	$e^- + CH_4 \Rightarrow e^- + CH_{4(V24)}$	Vibrational Excitation	$f(\sigma), \varepsilon$
E5	$e^- + CH_4 \Rightarrow e^- + CH_{4(V13)}$	Vibrational Excitation	$f(\sigma), \varepsilon$
E6	$e^- + CH_4 \Rightarrow e^- + CH_3 + H$	Dissociative Excitation	$f(\sigma), \varepsilon$
E7	$e^- + CH_4 \Rightarrow e^- + CH_2 + 2H$	Dissociative Excitation	$f(\sigma), \varepsilon$

E8	$e^- + CH_4 \Rightarrow e^- + CH + 3H$	Dissociative Excitation	$f(\sigma)$, ε
E9	$e^- + CH_4 \Rightarrow 2e^- + CH_4^+$	Ionisation	$f(\sigma)$, ε
E10	$e^- + CO_2 \Rightarrow CO + O^-$	Dissociative Attachment	$f(\sigma)$, ε
E11	$e^- + CO_2 \Rightarrow e^- + CO_2^*$	Momentum Transfer	$f(\sigma)$, ε
E12-19	$e^- + CO_2 \Rightarrow e^- + CO_{2(V1-8)}$	Vibrational Excitation	$f(\sigma)$, ε
E20-27	$e^- + CO_2 \Rightarrow e^- + CO_{2(E1-8)}$	Electronic Excitation	$f(\sigma)$, ε
E28	$e^- + CO_2 \Rightarrow 2e^- + CO_2^+$	Ionisation	$f(\sigma)$, ε
E29	$e^- + CO_2 \Rightarrow e^- + CO + O$	Dissociative Excitation	$f(\sigma)$, ε
E30	$e^- + CH_3 \Rightarrow e^- + CH_{3(P)}$	Excitation	$f(\sigma)$, ε
E31	$e^- + CH_3 \Rightarrow e^- + CH_2 + H$	Dissociative Excitation	$f(\sigma)$, ε
E32	$e^- + CH_3 \Rightarrow e^- + CH + H_2$	Dissociative Excitation	$f(\sigma)$, ε
E33	$e^- + CH_3 \Rightarrow e^- + H + C + H_2$	Dissociative Excitation	$f(\sigma)$, ε
E34	$e^- + CH_3 \Rightarrow 2e^- + CH_3^+$	Ionisation	$f(\sigma)$, ε
E35	$e^- + CH_3 \Rightarrow 2e^- + H + CH_2^+$	Dissociative Ionisation	$f(\sigma)$, ε
E36	$e^- + CH_3^+ \Rightarrow 2e^- + H + H^+ + CH^+$	Dissociative Ionisation	$f(\sigma)$, ε
E37	$e^- + CH_3^+ \Rightarrow 2e^- + H_2 + H^+ + C^+$	Dissociative Ionisation	$f(\sigma)$, ε
E38	$e^- + CH_2 \Rightarrow e^- + CH_2^*$	Excitation	$f(\sigma)$, ε
E39	$e^- + CH_2 \Rightarrow e^- + CH + H$	Dissociative Excitation	$f(\sigma)$, ε
E40	$e^- + CH_2 \Rightarrow e^- + C + H_2$	Dissociative Excitation	$f(\sigma)$, ε
E41	$e^- + CH_2 \Rightarrow e^- + C + 2H$	Dissociative Excitation	$f(\sigma)$, ε
E42	$e^- + CH_2 \Rightarrow 2e^- + CH_2^+$	Ionisation	$f(\sigma)$, ε
E43	$e^- + CH_2 \Rightarrow 2e^- + H + CH^+$	Dissociative Ionisation	$f(\sigma)$, ε
E44	$e^- + CH_2^+ \Rightarrow 2e^- + H + H^+ + C^+$	Dissociative Ionisation	$f(\sigma)$, ε
E45	$e^- + C \Rightarrow e^- + C$	Momentum Transfer	$f(\sigma)$, ε
E46	$e^- + C \Rightarrow e^- + C_{(1D)}$	Excitation	$f(\sigma)$, ε
E47	$e^- + C \Rightarrow e^- + C_{(1S)}$	Excitation	$f(\sigma)$, ε
E48	$e^- + C \Rightarrow 2e^- + C^+$	Ionisation	$f(\sigma)$, ε
E49	$e^- + CO \Rightarrow e^- + CO$	Momentum Transfer	$f(\sigma)$, ε
E50-59	$e^- + CO \Rightarrow e^- + CO_{(V1-10)}$	Vibrational Excitation	$f(\sigma)$, ε
E60-64	$e^- + CO \Rightarrow e^- + CO_{(E1-5)}$	Electronic Excitation	$f(\sigma)$, ε
E65	$e^- + CO \Rightarrow e^- + C + O$	Dissociative Excitation	$f(\sigma)$, ε
E66	$e^- + CO \Rightarrow 2e^- + CO^+$	Ionisation	$f(\sigma)$, ε
E67	$e^- + H_2 \Rightarrow H + H^-$	Dissociative Attachment	$f(\sigma)$, ε

E68	$e^- + H_2 \Rightarrow e^- + H_{2(j0\text{-}2,\ j1\text{-}3)}$	Rotational Excitation	$f(\sigma)$, ε
E69-71	$e^- + H_2 \Rightarrow e^- + H_{2(V1\text{-}3)}$	Vibrational Excitation	$f(\sigma)$, ε
E72	$e^- + H_2 \Rightarrow e^- + H_2(B^1\Sigma_u^+)$	Electronic Excitation	$f(\sigma)$, ε
E73	$e^- + H_2 \Rightarrow e^- + H_2(c^3\Pi_u)$	Electronic Excitation	$f(\sigma)$, ε
E74	$e^- + H_2 \Rightarrow e^- + H_2(a^3\Sigma_g^+)$	Electronic Excitation	$f(\sigma)$, ε
E75	$e^- + H_2 \Rightarrow e^- + H_2(C^1\Pi_u)$	Electronic Excitation	$f(\sigma)$, ε
E76	$e^- + H_2 \Rightarrow e^- + H_2(^1\Sigma_g^+)$	Electronic Excitation	$f(\sigma)$, ε
E77	$e^- + H_2 \Rightarrow e^- + H_2(D^3\Pi_u)$	Electronic Excitation	$f(\sigma)$, ε
E78	$e^- + H_2 \Rightarrow e^- + H_{2(E1\text{-}2)}$	Electronic Excitation	$f(\sigma)$, ε
E79	$e^- + H_2 \Rightarrow e^- + H + H$	Rydberg Excitation	$f(\sigma)$, ε
E80	$e^- + H_2 \Rightarrow 2e^- + H_2^+$	Ionisation	$f(\sigma)$, ε
E81	$e^- + H \Rightarrow e^- + H$	Momentum Transfer	$f(\sigma)$, ε
E82	$e^- + H \Rightarrow e^- + H_{(2p)}$	Excitation	$f(\sigma)$, ε
E83	$e^- + H \Rightarrow e^- + H_{(2s)}$	Excitation	$f(\sigma)$, ε
E84	$e^- + H \Rightarrow 2e^- + H^+$	Ionisation	$f(\sigma)$, ε
E85	$e^- + O_2 \Rightarrow O_2^-$	Attachment	$f(\sigma)$, ε
E86	$e^- + O_2 \Rightarrow e^- + O_2$	Momentum Transfer	$f(\sigma)$, ε
E87-89	$e^- + O_2 \Rightarrow e^- + O_{2(R1\text{-}3)}$	Rotational Excitation	$f(\sigma)$, ε
E90-93	$e^- + O_2 \Rightarrow e^- + O_{2(V1\text{-}4)}$	Vibrational Excitation	$f(\sigma)$, ε
E94	$e^- + O_2 \Rightarrow e^- + O_2(b^1\Sigma^+)$	Electronic Excitation	$f(\sigma)$, ε
E95	$e^- + O_2 \Rightarrow e^- + O_2(a^1\delta^+)$	Electronic Excitation	$f(\sigma)$, ε
E96-101	$e^- + O_2 \Rightarrow e^- + O + O$	Dissociative Excitation	$f(\sigma)$, ε
E102	$e^- + O_2 \Rightarrow 2e^- + O_2^+$	Ionisation	$f(\sigma)$, ε
E103	$e^- + O \Rightarrow e^- + O$	Momentum Transfer	$f(\sigma)$, ε
E104	$e^- + O \Rightarrow e^- + O_{(1D)}$	Excitation	$f(\sigma)$, ε
E105	$e^- + O \Rightarrow e^- + O_{(1S)}$	Excitation	$f(\sigma)$, ε
E106	$e^- + O \Rightarrow 2e^- + O^+$	Ionisation	$f(\sigma)$, ε
E107	$e^- + H_2O \Rightarrow H_2 + O^-$	Dissociative Attachment	$f(\sigma)$, ε
E108	$e^- + H_2O \Rightarrow OH + H^-$	Dissociative Attachment	$f(\sigma)$, ε
E109	$e^- + H_2O \Rightarrow H + OH^-$	Dissociative Attachment	$f(\sigma)$, ε
E110	$e^- + H_2O \Rightarrow e^- + H_2O$	Momentum Transfer	$f(\sigma)$, ε
E111-113	$e^- + H_2O \Rightarrow e^- + H_2O_{(V1\text{-}3)}$	Vibrational Excitation	$f(\sigma)$, ε
E114	$e^- + H_2O \Rightarrow e^- + H + OH$	Dissociative Excitation	$f(\sigma)$, ε

E115	$e^- + H_2O \Rightarrow e^- + H_2 + O$	Dissociative Excitation	$f(\sigma)$, ε
E116	$e^- + H_2O \Rightarrow 2e^- + H_2O^+$	Ionisation	$f(\sigma)$, ε
E117	$e^- + C_2H_2 \Rightarrow e^- + C_2H_2$	Momentum Transfer	$f(\sigma)$, ε
E118-120	$e^- + C_2H_2 \Rightarrow e^- + C_2H_{2(V2,5\ \&31)}$	Vibrational Excitation	$f(\sigma)$, ε
E121-122	$e^- + C_2H_2 \Rightarrow e^- + C_2H_{2(E1\ \&2)}$	Electronic Excitation	$f(\sigma)$, ε
E123	$e^- + C_2H_2 \Rightarrow e^- + H + C_2H$	Dissociative Excitation	$f(\sigma)$, ε
E124	$e^- + C_2H_2 \Rightarrow e^- + 2H + C_2$	Dissociative Excitation	$f(\sigma)$, ε
E125	$e^- + C_2H_2 \Rightarrow e^- + CH + CH$	Dissociative Excitation	$f(\sigma)$, ε
E126	$e^- + C_2H_2 \Rightarrow e^- + C + CH_2$	Dissociative Excitation	$f(\sigma)$, ε
E127	$e^- + C_2H_2 \Rightarrow 2e^- + C_2H_2^+$	Ionisation	$f(\sigma)$, ε
E128	$e^- + C_2H_2^+ \Rightarrow e^- + C_2H^+ + H$	Dissociation of Ion	$f(\sigma)$, ε
E129	$e^- + C_2H_2^+ \Rightarrow e^- + C_2H + H^+$	Dissociation of Ion	$f(\sigma)$, ε
E130	$e^- + C_2H_2^+ \Rightarrow e^- + H_2 + C_2^+$	Dissociation of Ion	$f(\sigma)$, ε
E131	$e^- + C_2H_2^+ \Rightarrow e^- + CH + CH^+$	Dissociation of Ion	$f(\sigma)$, ε
E132	$e^- + C_2H_2^+ \Rightarrow e^- + C + CH_2^+$	Dissociation of Ion	$f(\sigma)$, ε
E133	$e^- + C_2H_2^+ \Rightarrow e^- + C^+ + CH_2$	Dissociation of Ion	$f(\sigma)$, ε
E134	$e^- + C_2H_2^+ \Rightarrow 2e^- + C_2H^+ + H^+$	Dissociative Ionisation	$f(\sigma)$, ε
E135	$e^- + C_2H_2^+ \Rightarrow 2e^- + C_2^+ + H_2^+$	Dissociative Ionisation	$f(\sigma)$, ε
E136	$e^- + C_2H_2^+ \Rightarrow 2e^- + C_2^+ + H + H^+$	Dissociative Ionisation	$f(\sigma)$, ε
E137	$e^- + C_2H_2^+ \Rightarrow 2e^- + CH^+ + CH^+$	Dissociative Ionisation	$f(\sigma)$, ε
E138	$e^- + C_2H_2^+ \Rightarrow 2e^- + C^+ + H + CH^+$	Dissociative Ionisation	$f(\sigma)$, ε
E139	$e^- + C_2H_2^+ \Rightarrow 2e^- + CH_2^+ + C^+$	Dissociative Ionisation	$f(\sigma)$, ε
E140	$e^- + C_2H_4 \Rightarrow e^- + C_2H_4$	Momentum Transfer	$f(\sigma)$, ε
E141-142	$e^- + C_2H_4 \Rightarrow e^- + C_2H_{4(V1\ \&\ 2)}$	Vibrational Excitation	$f(\sigma)$, ε
E143-144	$e^- + C_2H_4 \Rightarrow e^- + C_2H_{4(E1\ \&\ 2)}$	Electronic Excitation	$f(\sigma)$, ε
E145	$e^- + C_2H_4 \Rightarrow e^- + C_2H_3 + H$	Dissociative Excitation	$f(\sigma)$, ε
E146	$e^- + C_2H_4 \Rightarrow e^- + C_2H_2 + H_2$	Dissociative Excitation	$f(\sigma)$, ε
E147	$e^- + C_2H_4 \Rightarrow e^- + C_2H_2 + 2H$	Dissociative Excitation	$f(\sigma)$, ε
E148	$e^- + C_2H_4 \Rightarrow e^- + C_2H + H_2 + H$	Dissociative Excitation	$f(\sigma)$, ε
E149	$e^- + C_2H_4 \Rightarrow e^- + CH_3 + CH$	Dissociative Excitation	$f(\sigma)$, ε
E150	$e^- + C_2H_4 \Rightarrow e^- + CH_2 + CH_2$	Dissociative Excitation	$f(\sigma)$, ε
E151	$e^- + C_2H_4 \Rightarrow e^- + C + CH_4$	Dissociative Excitation	$f(\sigma)$, ε
E152	$e^- + C_2H_4 \Rightarrow 2e^- + C_2H_4^+$	Ionisation	$f(\sigma)$, ε

E153	$e^- + C_2H_4^+ \Rightarrow e^- + H + C_2H_3^+$	Dissociation of Ion	$f(\sigma)$, ε
E154	$e^- + C_2H_4^+ \Rightarrow e^- + H_2 + C_2H_2^+$	Dissociation of Ion	$f(\sigma)$, ε
E155	$e^- + C_2H_4^+ \Rightarrow e^- + H_2^+ + C_2H_2$	Dissociation of Ion	$f(\sigma)$, ε
E156	$e^- + C_2H_4^+ \Rightarrow e^- + CH_3^+ + CH$	Dissociation of Ion	$f(\sigma)$, ε
E157	$e^- + C_2H_4^+ \Rightarrow e^- + CH_3 + CH^+$	Dissociation of Ion	$f(\sigma)$, ε
E158	$e^- + C_2H_4^+ \Rightarrow e^- + CH_2 + CH_2^+$	Dissociation of Ion	$f(\sigma)$, ε
E159	$e^- + C_2H_4^+ \Rightarrow e^- + CH_4 + C^+$	Dissociation of Ion	$f(\sigma)$, ε
E160	$e^- + C_2H_4^+ \Rightarrow 2e^- + C_2H_3^+ + H^+$	Dissociative Ionisation	$f(\sigma)$, ε
E161	$e^- + C_2H_4^+ \Rightarrow 2e^- + C_2H_2^+ + H_2^+$	Dissociative Ionisation	$f(\sigma)$, ε
	$e^- + C_2H_4^+ \Rightarrow 2e^- + C_2H_2^+ + H +$		$f(\sigma)$, ε
E162	H^+	Dissociative Ionisation	
E163	$e^- + C_2H_4^+ \Rightarrow 2e^- + CH_3^+ + CH^+$	Dissociative Ionisation	$f(\sigma)$, ε
E164	$e^- + C_2H_4^+ \Rightarrow 2e^- + CH_2^+ + CH_2^+$	Dissociative Ionisation	$f(\sigma)$, ε
E165	$e^- + C_2H_4^+ \Rightarrow 2e^- + CH_4^+ + C^+$	Dissociative Ionisation	$f(\sigma)$, ε
E166	$e^- + C_2H_6 \Rightarrow C_2H_6^-$	Attachment	$f(\sigma)$, ε
E167	$e^- + C_2H_6 \Rightarrow e^- + C_2H_6$	Momentum Transfer	$f(\sigma)$, ε
E168-169	$e^- + C_2H_6 \Rightarrow e^- + C_2H_{6(V13\ \&\ 24)}$	Vibrational Excitation	$f(\sigma)$, ε
E170	$e^- + C_2H_6 \Rightarrow e^- + C_2H_5 + H$	Dissociative Excitation	$f(\sigma)$, ε
E171	$e^- + C_2H_6 \Rightarrow e^- + C_2H_4 + H_2$	Dissociative Excitation	$f(\sigma)$, ε
E172	$e^- + C_2H_6 \Rightarrow e^- + C_2H_3 + H + H_2$	Dissociative Excitation	$f(\sigma)$, ε
E173	$e^- + C_2H_6 \Rightarrow e^- + C_2H_2 + 2H_2$	Dissociative Excitation	$f(\sigma)$, ε
E174	$e^- + C_2H_6 \Rightarrow e^- + CH_4 + CH_2$	Dissociative Excitation	$f(\sigma)$, ε
E175	$e^- + C_2H_6 \Rightarrow e^- + CH_3 + CH_3$	Dissociative Excitation	$f(\sigma)$, ε
E176	$e^- + C_2H_6 \Rightarrow 2e^- + C_2H_6^+$	Ionisation	$f(\sigma)$, ε
E177	$e^- + C_2H_6^+ \Rightarrow e^- + C_2H_5^+ + H$	Dissociation of Ion	$f(\sigma)$, ε
E178	$e^- + C_2H_6^+ \Rightarrow e^- + C_2H_4^+ + H_2$	Dissociation of Ion	$f(\sigma)$, ε
E179	$e^- + C_2H_6^+ \Rightarrow e^- + CH_3^+ + CH_3$	Dissociation of Ion	$f(\sigma)$, ε
E180	$e^- + C_2H_6^+ \Rightarrow 2e^- + C_2H_5^+ + H^+$	Dissociative Ionisation	$f(\sigma)$, ε
E181	$e^- + C_2H_6^+ \Rightarrow 2e^- + C_2H_4^+ + H_2^+$	Dissociative Ionisation	$f(\sigma)$, ε
	$e^- + C_2H_6^+ \Rightarrow 2e^- + C_2H_4^+ + H +$		$f(\sigma)$, ε
E182	H^+	Dissociative Ionisation	
	$e^- + C_2H_6^+ \Rightarrow 2e^- + C_2H_3^+ + H_2 +$		$f(\sigma)$, ε
E183	H^+	Dissociative Ionisation	

	$e^- + C_2H_6^+ \Rightarrow 2e^- + C_2H_2^+ + H_2 +$		$f(\sigma)$, ε
E184	H_2^+	Dissociative Ionisation	
E185	$e^- + C_2H_6^+ \Rightarrow 2e^- + CH_4^+ + CH_2^+$	Dissociative Ionisation	$f(\sigma)$, ε
E186	$e^- + C_2H_6^+ \Rightarrow 2e^- + CH_3^+ + CH_3^+$	Dissociative Ionisation	$f(\sigma)$, ε
E187	$e^- + C_3H_6 \Rightarrow C_3H_6^-$	Attachment	$f(\sigma)$, ε
E188	$e^- + C_3H_6 \Rightarrow e^- + C_3H_6$	Momentum Transfer	$f(\sigma)$, ε
E189	$e^- + C_3H_6 \Rightarrow e^- + C_3H_{6(V)}$	Vibrational Excitation	$f(\sigma)$, ε
E190	$e^- + C_3H_6 \Rightarrow e^- + C_3H_5 + H$	Dissociative Excitation	$f(\sigma)$, ε
E191	$e^- + C_3H_6 \Rightarrow e^- + C_3H_4 + H_2$	Dissociative Excitation	$f(\sigma)$, ε
E192	$e^- + C_3H_6 \Rightarrow e^- + C_3H_3 + H + H_2$	Dissociative Excitation	$f(\sigma)$, ε
E193	$e^- + C_3H_6 \Rightarrow e^- + C_3H_2 + 2H_2$	Dissociative Excitation	$f(\sigma)$, ε
E194	$e^- + C_3H_6 \Rightarrow e^- + C_2H_4 + CH_2$	Dissociative Excitation	$f(\sigma)$, ε
E195	$e^- + C_3H_6 \Rightarrow e^- + C_2H_3 + CH_3$	Dissociative Excitation	$f(\sigma)$, ε
E196	$e^- + C_3H_6 \Rightarrow e^- + C_2H_2 + CH_4$	Dissociative Excitation	$f(\sigma)$, ε
E197	$e^- + C_3H_6 \Rightarrow 2e^- + C_3H_6^+$	Ionisation	$f(\sigma)$, ε
E198	$e^- + C_3H_6^+ \Rightarrow e^- + C_2H_5^+ + CH$	Dissociation of Ion	$f(\sigma)$, ε
E199	$e^- + C_3H_6^+ \Rightarrow e^- + C_2H_4^+ + CH_2$	Dissociation of Ion	$f(\sigma)$, ε
E200	$e^- + C_3H_6^+ \Rightarrow e^- + C_2H_3^+ + CH_3$	Dissociation of Ion	$f(\sigma)$, ε
E201	$e^- + C_3H_6^+ \Rightarrow e^- + C_2H_2^+ + CH_4$	Dissociation of Ion	$f(\sigma)$, ε
E202	$e^- + C_3H_6^+ \Rightarrow e^- + CH_4^+ + C_2H_2$	Dissociation of Ion	$f(\sigma)$, ε
E203	$e^- + C_3H_6^+ \Rightarrow e^- + CH_3^+ + C_2H_3$	Dissociation of Ion	$f(\sigma)$, ε
E204	$e^- + C_3H_6^+ \Rightarrow e^- + CH_2^+ + C_2H_4$	Dissociation of Ion	$f(\sigma)$, ε
E205	$e^- + C_3H_6^+ \Rightarrow 2e^- + C_2H_6^+ + C^+$	Dissociative Ionisation	$f(\sigma)$, ε
E206	$e^- + C_3H_6^+ \Rightarrow 2e^- + C_2H_5^+ + CH^+$	Dissociative Ionisation	$f(\sigma)$, ε
E207	$e^- + C_3H_6^+ \Rightarrow 2e^- + C_2H_4^+ + CH_2^+$	Dissociative Ionisation	$f(\sigma)$, ε
E208	$e^- + C_3H_6^+ \Rightarrow 2e^- + C_2H_3^+ + CH_3^+$	Dissociative Ionisation	$f(\sigma)$, ε
E209	$e^- + C_3H_6^+ \Rightarrow 2e^- + C_2H_2^+ + CH_4^+$	Dissociative Ionisation	$f(\sigma)$, ε
	$e^- + C_3H_6^+ \Rightarrow 2e^- + C_2H^+ + H +$		$f(\sigma)$, ε
E210	CH_4^+	Dissociative Ionisation	
	$e^- + C_3H_6^+ \Rightarrow 2e^- + C_2H^+ + H^+ +$		$f(\sigma)$, ε
E211	CH_4	Dissociative Ionisation	
	$e^- + C_3H_6^+ \Rightarrow 2e^- + C_2^+ + CH_4^+ +$		$f(\sigma)$, ε
E212	H_2	Dissociative Ionisation	

E213	$e^- + C_3H_8 \Rightarrow C_3H_8^-$	Attachment	$f(\sigma)$, ε
E214	$e^- + C_3H_8 \Rightarrow e^- + C_3H_8$	Momentum Transfer	$f(\sigma)$, ε
E215-216	$e^- + C_3H_8 \Rightarrow e^- + C_3H_{8(V1\ \&\ 2)}$	Vibrational Excitation	$f(\sigma)$, ε
E217	$e^- + C_3H_8 \Rightarrow e^- + C_3H_{8(E)}$	Electronic Excitation	$f(\sigma)$, ε
E218	$e^- + C_3H_8 \Rightarrow e^- + C_3H_7 + H$	Dissociative Excitation	$f(\sigma)$, ε
E219	$e^- + C_3H_8 \Rightarrow e^- + C_3H_6 + H_2$	Dissociative Excitation	$f(\sigma)$, ε
E220	$e^- + C_3H_8 \Rightarrow e^- + C_3H_4 + 2H_2$	Dissociative Excitation	$f(\sigma)$, ε
E221	$e^- + C_3H_8 \Rightarrow e^- + C_2H_6 + CH_2$	Dissociative Excitation	$f(\sigma)$, ε
E222	$e^- + C_3H_8 \Rightarrow e^- + C_2H_5 + CH_3$	Dissociative Excitation	$f(\sigma)$, ε
E223	$e^- + C_3H_8 \Rightarrow e^- + C_2H_4 + CH_4$	Dissociative Excitation	$f(\sigma)$, ε
E224	$e^- + C_3H_8 \Rightarrow 2e^- + C_3H_8^+$	Ionisation	$f(\sigma)$, ε
E225	$e^- + C_3H_8^+ \Rightarrow e^- + C_2H_5^+ + CH_3$	Dissociation of Ion	$f(\sigma)$, ε
E226	$e^- + C_3H_8^+ \Rightarrow e^- + C_2H_4^+ + CH_4$	Dissociation of Ion	$f(\sigma)$, ε
E227	$e^- + C_3H_8^+ \Rightarrow 2e^- + C_2H_6^+ + CH_2^+$	Dissociative Ionisation	$f(\sigma)$, ε
E228	$e^- + C_3H_8^+ \Rightarrow 2e^- + C_2H_5^+ + CH_3^+$	Dissociative Ionisation	$f(\sigma)$, ε
E229	$e^- + C_3H_8^+ \Rightarrow 2e^- + C_2H_4^+ + CH_4^+$	Dissociative Ionisation	$f(\sigma)$, ε
	$e^- + C_3H_8^+ \Rightarrow 2e^- + C_2H_3^+ + CH_4$		$f(\sigma)$, ε
E230	$+ H^+$	Dissociative Ionisation	
	$e^- + C_3H_8^+ \Rightarrow 2e^- + C_2H_3^+ + H +$		$f(\sigma)$, ε
E231	CH_4^+	Dissociative Ionisation	
	$e^- + C_3H_8^+ \Rightarrow 2e^- + C_2H_3^+ + H_2 +$		$f(\sigma)$, ε
E232	CH_3^+	Dissociative Ionisation	
	$e^- + C_3H_8^+ \Rightarrow 2e^- + C_2H_3^+ + H_2^+ +$		$f(\sigma)$, ε
E233	CH_3	Dissociative Ionisation	
	$e^- + C_3H_8^+ \Rightarrow 2e^- + C_2H_2^+ + CH_4^+$		$f(\sigma)$, ε
E234	$+ H_2$	Dissociative Ionisation	
	$e^- + C_3H_8^+ \Rightarrow 2e^- + C_2H_2^+ + CH_4$		$f(\sigma)$, ε
E235	$+ H_2^+$	Dissociative Ionisation	
E236	$e^- + CH_4^+ \Rightarrow CH_3 + H$	Recombination	[213-215]
E237	$e^- + CH_4^+ \Rightarrow CH_2 + 2H$	Recombination	[213-215]
E238	$e^- + CH_4^+ \Rightarrow CH + H_2 + H$	Recombination	[213-215]
E239	$e^- + CH_3^+ \Rightarrow CH_2 + H$	Recombination	[213-215]
E240	$e^- + CH_3^+ \Rightarrow CH + H_2$	Recombination	[213-215]

E241	$e^- + CH_3^+ \Rightarrow CH + 2H$	Recombination	[213-215]
E242	$e^- + CH_3^+ \Rightarrow C + H + H_2$	Recombination	[213-215]
E243	$e^- + CH_2^+ \Rightarrow CH + H$	Recombination	[213-215]
E244	$e^- + CH_2^+ \Rightarrow C + H_2$	Recombination	[213-215]
E245	$e^- + CH_2^+ \Rightarrow C + 2H$	Recombination	[213-215]
E246	$e^- + CH^+ \Rightarrow C + H$	Recombination	[213-215]
E247	$e^- + C_2H_6^+ \Rightarrow C_2H_5 + H$	Recombination	[213-215]
E248	$e^- + C_2H_6^+ \Rightarrow C_2H_4 + 2H$	Recombination	[213-215]
E249	$e^- + C_2H_5^+ \Rightarrow C_2H_4 + H$	Recombination	[213-215]
E250	$e^- + C_2H_5^+ \Rightarrow C_2H_3 + 2H$	Recombination	[213-215]
E251	$e^- + C_2H_5^+ \Rightarrow C_2H_2 + H + H_2$	Recombination	[213-215]
E252	$e^- + C_2H_5^+ \Rightarrow C_2H_2 + 3H$	Recombination	[213-215]
E253	$e^- + C_2H_5^+ \Rightarrow CH_3 + CH_2$	Recombination	[213-215]
E254	$e^- + C_2H_4^+ \Rightarrow C_2H_3 + H$	Recombination	[213-215]
E255	$e^- + C_2H_4^+ \Rightarrow C_2H_2 + 2H$	Recombination	[213-215]
E256	$e^- + C_2H_4^+ \Rightarrow C_2H + H_2 + H$	Recombination	[213-215]
E257	$e^- + C_2H_3^+ \Rightarrow C_2H_2 + H$	Recombination	[213-215]
E258	$e^- + C_2H_3^+ \Rightarrow C_2H + 2H$	Recombination	[213-215]
E259	$e^- + C_2H_2^+ \Rightarrow C_2H + H$	Recombination	[213-215]
E260	$e^- + C_2H_2^+ \Rightarrow CH + CH$	Recombination	[213-215]
E261	$e^- + O_2^+ + O_2 \Rightarrow O_2 + O_2$	Recombination	[213-215]
E262	$e^- + O_2^+ \Rightarrow O + O$	Recombination	[213-215]
E263	$e^- + CO_2^+ \Rightarrow CO + O$	Recombination	[213-215]
E264	$e + D_2O \Rightarrow D_2 + O^-$	Dissociative Attachment	$f(\sigma)$, ε
E265	$e + D_2O \Rightarrow D^- + OD$	Dissociative Attachment	$f(\sigma)$, ε
E266	$e + D_2O \Rightarrow OD^- + D$	Dissociative Attachment	$f(\sigma)$, ε
E267	$e + D_2O \Rightarrow e + D_2O^*$	Momentum Transfer	$f(\sigma)$, ε
E268	$e + D_2O \Rightarrow e + D_2O(V1)$	Vibrational Excitation	$f(\sigma)$, ε
E269	$e + D_2O \Rightarrow e + D_2O(V2)$	Vibrational Excitation	$f(\sigma)$, ε
E270	$e + D_2O \Rightarrow e + D_2O(V3)$	Vibrational Excitation	$f(\sigma)$, ε
E271	$e + D_2O \Rightarrow e + D + OD$	Dissociation	$f(\sigma)$, ε
E272	$e + D_2O \Rightarrow e + O + D_2$	Dissociation	$f(\sigma)$, ε
E273	$e + D_2O \Rightarrow e + e + D_2O^+$	Ionisation	$f(\sigma)$, ε

E274	$e + D_2 \Rightarrow e + D + D$	Dissociation	$f(\sigma), \varepsilon$

Table 9.10 Ion-neutral/ions involved in this model, and the corresponding reaction rate constant are adopted from the literature [213-215].

No.	Reaction	Rate constant (cm^3s^{-1})
I1	$CH_4^+ + C_2H_6 \Rightarrow C_2H_4^+ + CH_4 + H_2$	1.91×10^{-9}
I2	$CH_4^+ + C_2H_4 \Rightarrow C_2H_5^+ + CH_3$	4.23×10^{-10}
I3	$CH_4^+ + C_2H_4 \Rightarrow C_2H_4^+ + CH_4$	1.38×10^{-9}
I4	$CH_4^+ + C_2H_2 \Rightarrow C_2H_3^+ + CH_3$	1.23×10^{-9}
I5	$CH_4^+ + C_2H_2 \Rightarrow C_2H_2^+ + CH_4$	1.13×10^{-9}
I6	$CH_4^+ + H \Rightarrow CH_3^+ + H_2$	1.00×10^{-11}
I7	$CH_4^+ + O \Rightarrow CH_3^+ + OH$	1.00×10^{-9}
I8	$CH_4^+ + O_2 \Rightarrow CH_4 + O_2^+$	3.90×10^{-10}
I9	$CH_3^+ + CH_4 \Rightarrow CH_4^+ + CH_3$	1.36×10^{-10}
I10	$CH_3^+ + CH_4 \Rightarrow C_2H_5^+ + H_2$	1.20×10^{-9}
I11	$CH_3^+ + CH_2 \Rightarrow C_2H_3^+ + H_2$	9.90×10^{-10}
I12	$CH_3^+ + CH \Rightarrow C_2H_2^+ + H_2$	7.10×10^{-10}
I13	$CH_3^+ + C_2H_6 \Rightarrow C_2H_5^+ + CH_4$	1.48×10^{-9}
I14	$CH_3^+ + C_2H_4 \Rightarrow C_2H_3^+ + CH_4$	3.50×10^{-10}
I15	$CH_3^+ + C_2H_3 \Rightarrow C_2H_3^+ + CH_3$	3.00×10^{-10}
I16	$CH_2^+ + CH_4 \Rightarrow CH_3^+ + CH_3$	1.38×10^{-10}
I17	$CH_2^+ + CH_4 \Rightarrow C_2H_5^+ + H$	3.90×10^{-10}
I18	$CH_2^+ + CH_4 \Rightarrow C_2H_4^+ + H_2$	8.40×10^{-10}
I19	$CH_2^+ + CH_4 \Rightarrow C_2H_3^+ + H_2 + H$	2.31×10^{-10}
I20	$CH_2^+ + CH_4 \Rightarrow C_2H_3^+ + 2H_2$	3.97×10^{-10}
I21	$CH^+ + CH_4 \Rightarrow C_2H_4^+ + H$	6.50×10^{-11}
I22	$CH^+ + CH_4 \Rightarrow C_2H_3^+ + H_2$	1.09×10^{-9}
I23	$CH^+ + CH_4 \Rightarrow C_2H_2^+ + H + H_2$	1.43×10^{-10}
I24	$CH^+ + H_2 \Rightarrow CH_2^+ + H$	1.20×10^{-9}
I25	$C_2H_6^+ + C_2H_4 \Rightarrow C_2H_4^+ + C_2H_6$	1.15×10^{-9}
I26	$C_2H_6^+ + C_2H_2 \Rightarrow C_2H_5^+ + C_2H_3$	2.47×10^{-10}

I27	$C_2H_6^+ + H \Rightarrow C_2H_5^+ + H_2$	1.00×10^{-10}
I28	$C_2H_5^+ + H \Rightarrow C_2H_4^+ + H_2$	1.00×10^{-11}
I29	$C_2H_4^+ + C_2H_3 \Rightarrow C_2H_5^+ + C_2H_2$	5.00×10^{-10}
I30	$C_2H_4^+ + C_2H_3 \Rightarrow C_2H_3^+ + C_2H_4$	5.00×10^{-10}
I31	$C_2H_4^+ + H \Rightarrow C_2H_3^+ + H_2$	3.00×10^{-10}
I32	$C_2H_4^+ + O \Rightarrow C_2H_3^+ + HCO$	1.08×10^{-10}
I33	$C_2H_3^+ + C_2H_6 \Rightarrow C_2H_5^+ + C_2H_4$	2.91×10^{-10}
I34	$C_2H_3^+ + C_2H_4 \Rightarrow C_2H_5^+ + C_2H_2$	8.90×10^{-10}
I35	$C_2H_3^+ + C_2H_3 \Rightarrow C_2H_5^+ + C_2H$	5.00×10^{-10}
I36	$C_2H_3^+ + C_2H \Rightarrow C_2H_2^+ + C_2H_2$	3.30×10^{-10}
I37	$C_2H_3^+ + H \Rightarrow C_2H_2^+ + H_2$	6.80×10^{-11}
I38	$C_2H_2^+ + CH_4 \Rightarrow C_2H_3^+ + CH_3$	4.10×10^{-9}
I39	$C_2H_2^+ + C_2H_6 \Rightarrow C_2H_5^+ + C_2H_3$	1.31×10^{-10}
I40	$C_2H_2^+ + C_2H_6 \Rightarrow C_2H_4^+ + C_2H_4$	2.48×10^{-10}
I41	$C_2H_2^+ + C_2H_4 \Rightarrow C_2H_4^+ + C_2H_2$	4.14×10^{-10}
I42	$C_2H_2^+ + C_2H_3 \Rightarrow C_2H_3^+ + C_2H_2$	3.30×10^{-10}
I43	$C_2H_2^+ + H_2 \Rightarrow C_2H_3^+ + H$	1.00×10^{-11}
I44	$O_2^+ + CH_2 \Rightarrow CH_2^+ + O_2$	4.30×10^{-10}
I45	$O_2^+ + CH \Rightarrow CH^+ + O_2$	3.10×10^{-10}
I46	$O_2^+ + C_2H_4 \Rightarrow C_2H_4^+ + O_2$	6.80×10^{-10}
I47	$O_2^+ + C_2H_2 \Rightarrow C_2H_2^+ + O_2$	1.11×10^{-9}
I48	$O_2^+ + O^- \Rightarrow O + O_2$	2.90×10^{-8}
I49	$O_2^+ + O^- \Rightarrow 3O$	2.90×10^{-8}
I50	$O^- + CH_4 \Rightarrow OH^- + CH_3$	1.00×10^{-10}
I51	$O^- + C \Rightarrow e^- + CO$	5.00×10^{-10}
I52	$O^- + H_2 \Rightarrow e^- + H_2O$	7.00×10^{-10}
I53	$O^- + H_2 \Rightarrow OH^- + H$	3.00×10^{-11}
I54	$O^- + H \Rightarrow e^- + OH$	5.00×10^{-10}
I55	$O^- + O \Rightarrow e^- + O_2$	2.30×10^{-11}
I56	$O^- + CO \Rightarrow e^- + CO_2$	6.50×10^{-10}
I57	$CO_2^+ + CH_4 \Rightarrow CH_4^+ + CO_2$	5.50×10^{-10}
I58	$CO_2^+ + C_2H_4 \Rightarrow C_2H_4^+ + CO_2$	1.50×10^{-10}
I59	$CO_2^+ + C_2H_2 \Rightarrow C_2H_2^+ + CO_2$	7.30×10^{-10}

I60	$CO_2^+ + O_2 \Rightarrow O_2^+ + CO_2$	5.30×10^{-11}
I61	$CO_2^+ + O \Rightarrow O_2^+ + CO$	1.64×10^{-10}
I62	$OH^- + CH_3 \Rightarrow e^- + CH_3OH$	1.00×10^{-9}
I63	$OH^- + CH \Rightarrow e^- + CH_2O$	5.00×10^{-10}
I64	$OH^- + C \Rightarrow e^- + HCO$	5.00×10^{-10}
I65	$OH^- + H \Rightarrow e^- + H_2O$	1.40×10^{-9}